



**HAL**  
open science

# Development by 3D bioprinting and characterization of natural biomaterials for tissue engineering applications

Aurelia Poerio

► **To cite this version:**

Aurelia Poerio. Development by 3D bioprinting and characterization of natural biomaterials for tissue engineering applications. Materials. Université de Lorraine, 2021. English. NNT : 2021LORR0256 . tel-03669911

**HAL Id: tel-03669911**

**<https://hal.univ-lorraine.fr/tel-03669911v1>**

Submitted on 4 Dec 2023

**HAL** is a multi-disciplinary open access archive for the deposit and dissemination of scientific research documents, whether they are published or not. The documents may come from teaching and research institutions in France or abroad, or from public or private research centers.

L'archive ouverte pluridisciplinaire **HAL**, est destinée au dépôt et à la diffusion de documents scientifiques de niveau recherche, publiés ou non, émanant des établissements d'enseignement et de recherche français ou étrangers, des laboratoires publics ou privés.



## AVERTISSEMENT

Ce document est le fruit d'un long travail approuvé par le jury de soutenance et mis à disposition de l'ensemble de la communauté universitaire élargie.

Il est soumis à la propriété intellectuelle de l'auteur. Ceci implique une obligation de citation et de référencement lors de l'utilisation de ce document.

D'autre part, toute contrefaçon, plagiat, reproduction illicite encourt une poursuite pénale.

Contact : [ddoc-theses-contact@univ-lorraine.fr](mailto:ddoc-theses-contact@univ-lorraine.fr)

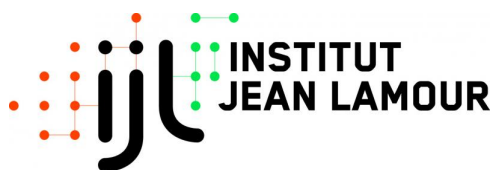
## LIENS

Code de la Propriété Intellectuelle. articles L 122. 4

Code de la Propriété Intellectuelle. articles L 335.2- L 335.10

[http://www.cfcopies.com/V2/leg/leg\\_droi.php](http://www.cfcopies.com/V2/leg/leg_droi.php)

<http://www.culture.gouv.fr/culture/infos-pratiques/droits/protection.htm>



## THÈSE

pour l'obtention du titre de  
DOCTEUR DE L'UNIVERSITÉ DE LORRAINE

SPÉCIALITÉ : SCIENCE DES MATÉRIAUX

Présentée par :  
AURELIA POERIO

---

# Élaboration par bio-impression 3D et caractérisation de biomatériaux naturels pour l'ingénierie tissulaire

---

Thèse soutenue publiquement le 30 Novembre 2021 devant le jury composé de:

Rapporteurs

**Mme Catherine Picart**

Professeur, Université de Grenoble

**Mme Catherine Levisage**

Directeur de recherche, Inserm, Université de Nantes

Examineurs

**M. Aldo Boccaccini**

Professeur, University of Erlangen-Nuremberg

**M. Christophe Drouet**

Directeur de recherche, CNRS, Université de Toulouse

**M. Frédéric Guittard**

Professeur, Université Côte d'Azur

**Mme Elmira Arab-Tehrany**

Professeur, Université de Lorraine

Directeurs

**M. Franck Cleymand**

Maître de Conférences, HdR, Université de Lorraine

**M. João F. Mano**

Professeur, University of Aveiro



# Abstract

## Development by 3D bioprinting and characterization of natural biomaterials for tissue engineering applications

3D bioprinting is a tissue engineering technology based on the combination of biomaterials, cells and bioactive molecules for the fabrication of tissue substitutes able to restore, replace and/or repair the damaged ones. Biomaterials act as a temporary extracellular matrix and promote the migration, proliferation and differentiation of cells. This ability is either due to the intrinsic properties of biomaterials or to their modification through the inclusion of biochemical cues, such as growth factors. The objective of this thesis is to develop new biomaterials allowing 3D printing and new strategies allowing for their application in tissue engineering, using, in particular, the technology of 3D bioprinting. In order to do that, we firstly extracted chitin from an unusual source, cicadas sloughs, and transformed it into its derivative chitosan. Chitin and chitosan were characterized from a physicochemical point of view. Furthermore, for the first time to our knowledge, we also characterized the raw material (*i.e.* cicada sloughs) and the intermediary products of the extraction process, which proved important to evaluate the stability of cicada sloughs as a source of chitin. Chitosan, a derivative of chitin, was then used to develop new biomaterial inks for extrusion 3D printing through its combination with two natural gums: guar gum and tamarind gum. These are polysaccharides derived from seed plants and widely used as thickening and gelling agents by the food industries. Their addition to chitosan improved its printability and, through a dual gelation mechanism, led to the fabrication of stable 3D constructs with improved mechanical properties. Subsequently, after reviewing the 3D bioprinting strategies used to control the release of growth factors from 3D printed and bioprinted constructs, PLGA microspheres were included into a 3D bioprinted skeletal muscle construct as a neurotrophic factor delivery system in order to improve and accelerate the innervation of the developed scaffold.

*Keywords:* 3D bioprinting, chitin, chitosan, cicada sloughs, guar gum, tamarind gum, growth factors delivery, neurotrophic factors, skeletal muscle regeneration.

## Élaboration par bio-impression 3D et caractérisation de biomatériaux naturels pour l'ingénierie tissulaire

La bio-impression 3D est une technologie d'ingénierie tissulaire basée sur la combinaison de biomatériaux, de cellules et de biomolécules pour la fabrication de substituts tissulaires capables de restaurer, remplacer et/ou réparer les tissus endommagés. Les biomatériaux agissent comme une matrice extracellulaire temporaire et favorisent la migration, la prolifération et la différenciation des cellules. Cette capacité peut être due aux propriétés intrinsèques des biomatériaux, ou à l'inclusion de signaux biochimiques, tels que des facteurs de croissance. L'objectif de cette thèse est de développer de nouveaux biomatériaux permettant l'impression 3D, mais également de trouver de nouvelles stratégies permettant leur application en ingénierie tissulaire, à l'aide de la technologie de la bio-impression 3D. Pour ce faire, nous avons d'abord extrait la chitine d'une source peu commune, les mues de cigales et nous l'avons transformé en son dérivé le chitosane. Chitine et chitosane ont ensuite été caractérisés d'un point de vue physico-chimique. Pour la première fois à

notre connaissance, nous avons également caractérisé la matière première (c'est à dire les mues de cigale) et les produits intermédiaires du procédé d'extraction, qui se sont avérés importants pour évaluer la stabilité des mues de cigales en tant que source de chitine. Le chitosane, un dérivé de la chitine, a ensuite été utilisé pour développer de nouvelles encres pour l'impression 3D grâce à sa combinaison avec deux gommes naturelles : la gomme de guar et la gomme de tamarin. Ces deux gommes sont des polysaccharides dérivés de plantes à graines et largement utilisés comme agents épaississants et gélifiants par les industries alimentaires. Leur combinaison avec le chitosane a amélioré son imprimabilité et, grâce à un mécanisme de double gélification, a conduit à la fabrication de constructions en 3D aux propriétés mécaniques améliorées. Par la suite, après avoir examiné les stratégies de bio-impression 3D utilisées pour contrôler la libération de facteurs de croissance à partir de constructions bio-imprimées, des microsphères de PLGA libérant des facteurs neurotrophiques ont été incluses dans une construction de muscle squelettique bio-imprimée afin d'améliorer et d'accélérer l'innervation de la structure 3D.

*Mots-clés* : bio-impression 3D, chitine, chitosane, mues de cigale, gomme de guar, gomme de tamarin, livraison de facteurs de croissance, facteurs neurotrophiques, régénération du muscle squelettique.

# Acknowledgements

At the end of this journey, I must thank the many people who have shared it with me and who have contributed to its achievement.

First of all, I would like to thank all the members of the jury: Ms. Catherine Picart, Ms. Catherine Levisage, Mr. Aldo Boccaccini, Mr. Christophe Drouet, Mr. Frédéric Guittard and Ms. Elmira Arab-Therany, for accepting to be members of my thesis committee and for their precious comments and suggestions. I would like to thank my supervisors, Franck Cleymand and João Mano for always supporting me and believing in me, even from miles away. Thanks for giving me the opportunity to travel for work or conferences, allowing me to broaden my cultural and scientific background.

I would like to thank Dr. James Yoo and all the members of the Wake Forest Institute for Regenerative Medicine, for welcoming me for a year. This has been a year of immense growth, both professionally and personally. For this, I also have to thank Dr. Ji Hyun Kim, Dr. Youngmin Ju and Dr. Dehui Lai for the trust they have placed in me and for their helpfulness. Thanks to Dr. Vladimir Mashanov for his precious teachings and his sincere friendship. Thanks to Diana for always being there for me, at any time of the day or night, for the deep discussions and all the great memories related to my stay in the USA. Thanks to Anastasiya, for sharing with me an amazing trip to New York and to Elham for our unforgettable and long walks. Thanks to my roommate Christina and her family for making me feel at home, even an ocean away. A special thanks to Maëlle for her friendship and her positive energy. Thanks for sharing with me the quarantine making it easier, for teaching me how to play squash and tennis and for the countless dinners based on French cheese and Italian wine.

These three years would have not been the same without the many friends and colleagues at the Institut Jean Lamour. In particular, my thanks go to Thomas and Solenne, who have always been there for me and who made the laboratory life easier and more fun. I also have to thank all the internship students who have been for more or less time in our team, for their help and funny moments of distraction. My thanks also go to all the people who have helped me perform experiments and solve administrative problems. In this regard, I would especially like to thank Sandrine Matthieu for teaching me how to use the scanning electron microscope, Christine Schwartz for her patience in organizing my internship in the USA and Christine Sartori for her kindness in answering my countless and repetitive questions. Thanks a lot to Mélanie for her support during the writing of my thesis and her friendship outside the laboratory and to Jean-Philippe, for his suggestions and explanations. A big thanks to Kathleen, Miguel, Sébastien, Kaushalya, Huyen, Thibaud, Pierre, Alexandre, Catalina, Thiago and Dominique for having lightened my working days between a coffee break and the sound of a guitar. A special thanks to Philippe, whose “disinterested interest” and passion for physics has been an inspiration to me and who, more than anyone else, has

patiently endured my mood swings.

I would also like to thank Sandra D., Sandra R., Clémence, Magali, Théo, Aseel, Stephania, François, Aurore, Giusi, Alessia, Francesca, Paola, Fabiana, Martina and Elisa for always being there for me, in Nancy or over the phone. A special thanks to Concetta for listening to my complaints from the beginning of my PhD and for always believing in me.

Lastly, I want to thank my family and in particular my parents for always supporting me and giving me all their unconditional love.



# Contents

<b>Abstract</b>	<b>iii</b>
<b>Acknowledgements</b>	<b>v</b>
<b>Introduction générale et objectifs de la thèse</b>	<b>1</b>
<b>General introduction and objectives of the thesis</b>	<b>7</b>
<b>1 Literature review</b>	<b>11</b>
1.1 Introduction to Tissue Engineering . . . . .	11
1.2 Cells in Tissue Engineering . . . . .	12
1.3 Biomaterial scaffolds . . . . .	14
1.3.1 Agro-resources based biomaterials for biomedical applications . . . . .	15
1.3.1.1 Chitin and chitosan . . . . .	16
1.3.1.2 Natural gums . . . . .	20
1.4 Growth factors . . . . .	21
1.5 3D bioprinting . . . . .	22
1.5.1 Development and optimization of bioinks or biomaterial inks . . . . .	25
1.5.2 Chitosan-based bioinks . . . . .	29
<b>2 Extraction and characterization of chitin and chitosan from <i>Cicada orni</i> sloughs</b>	<b>31</b>
2.1 <b>Extraction and Physicochemical Characterization of Chitin from <i>Cicada orni</i> Sloughs of the South-Eastern French Mediterranean Basin</b> . . . . .	<b>34</b>
2.2 <b>Comparison of the physicochemical properties of chitin extracted from <i>Cicada orni</i> sloughs harvested in three different years and characterization of the resulting chitosan</b> . . . . .	<b>48</b>
2.2.1 Abstract . . . . .	48
2.2.2 Introduction . . . . .	48
2.2.3 Materials and Methods . . . . .	50
2.2.3.1 Materials . . . . .	50
2.2.3.2 Extraction of chitin . . . . .	50
2.2.3.3 Deacetylation to obtain chitosan . . . . .	50
2.2.3.4 Fourier Transformed Infrared Spectroscopy (FTIR) . . . . .	50
2.2.3.5 X-Ray Diffraction (XRD) . . . . .	51
2.2.3.6 Scanning Electron Microscopy (SEM) . . . . .	51
2.2.4 Results . . . . .	51
2.2.4.1 Abbreviations . . . . .	51
2.2.4.2 FTIR spectra of chitin and degree of acetylation . . . . .	52

2.2.4.3	XRD spectra of chitin and evaluation of the cristallinity index	54
2.2.4.4	Scanning electron microscopy . . . . .	55
2.2.4.5	Characterization of the extracted chitosan . . . . .	56
2.2.5	Discussion . . . . .	59
2.2.6	Conclusions . . . . .	61
2.2.7	Supplementary information . . . . .	62
<b>3</b>	<b>Development of new biomaterial inks made of chitosan and guar gum or tamarind gum</b>	<b>67</b>
3.1	Initial screening of CH, CH-GG and CH-TG biomaterial inks . . . . .	71
3.2	<b>Development of self supported bioprinted constructs made of chitosan and guar gum or tamarind gum</b> . . . . .	<b>73</b>
3.2.1	Abstract . . . . .	73
3.2.2	Introduction . . . . .	73
3.2.3	Materials and methods . . . . .	74
3.2.3.1	Materials . . . . .	74
3.2.3.2	Preparation of the biomaterial inks . . . . .	74
3.2.3.3	Fourier Transformed Infrared Spectroscopy (FTIR) . . . . .	75
3.2.3.4	Viscosity measurement . . . . .	75
3.2.3.5	3D printing and evaluation of the printability . . . . .	75
3.2.3.6	Mass swelling ratio . . . . .	76
3.2.3.7	Degradation profile . . . . .	76
3.2.3.8	Nanoindentation . . . . .	76
3.2.3.9	Morphological characterization of 3D printed constructs . . . . .	77
3.2.3.10	<i>In Vitro</i> release profile of bovine serum albumin (BSA) . . . . .	77
3.2.3.11	Statistical analysis . . . . .	77
3.2.4	Results . . . . .	77
3.2.4.1	Spectroscopic characterization by FTIR . . . . .	77
3.2.4.2	Viscosity . . . . .	78
3.2.4.3	Evaluation of the printability . . . . .	79
3.2.4.4	Swelling and degradation profiles . . . . .	80
3.2.4.5	Nanoindentation . . . . .	81
3.2.4.6	Morphology of bioprinted constructs by SEM . . . . .	82
3.2.4.7	BSA release profile . . . . .	82
3.2.5	Discussion . . . . .	82
3.2.6	Conclusions . . . . .	85
3.2.7	Supplementary information . . . . .	86
3.3	Ongoing study: 3D printing of anisotropic cardiac patches . . . . .	88
<b>4</b>	<b>Advanced 3D bioprinting strategies for the controlled delivery of growth factors</b>	<b>95</b>
4.1	Abstract . . . . .	97
4.2	Introduction . . . . .	97
4.3	Importance of the dose-dependent efficiency . . . . .	99
4.4	Inclusion of GFs to bioinks for hard and soft tissue regeneration . . . . .	100
4.4.1	Hard biomaterial-based bioinks . . . . .	100
4.4.2	Soft biomaterial-based bioinks . . . . .	101
4.4.2.1	Natural polymer-based bioinks . . . . .	101

4.4.2.2	Synthetic polymer-based bioinks . . . . .	101
4.4.3	Heterogeneous materials . . . . .	101
4.4.4	Gene activated bioinks (GABs) . . . . .	102
4.5	Strategies adopted to temporally control the release of growth factors . . . . .	102
4.5.1	Physical entrapment . . . . .	102
4.5.2	Immobilization and covalent conjugation . . . . .	103
4.5.3	Encapsulation into nano- or micro-carriers . . . . .	105
4.5.3.1	Nanocarriers . . . . .	105
4.5.3.2	Microcarriers . . . . .	106
4.6	Spatial control of the release of growth factors from 3D bioprinted constructs	107
4.7	Conclusion and future perspectives . . . . .	112
<b>5</b>	<b>Towards innervation of bioengineered muscle constructs: Development of a sustained neurotrophic factor delivery and release system</b>	<b>115</b>
5.1	Abstract . . . . .	118
5.2	Introduction . . . . .	118
5.3	Methods . . . . .	120
5.3.1	Preparation of PLGA microspheres . . . . .	120
5.3.2	Characterization of PLGA microspheres . . . . .	120
5.3.3	Preparation and characterization of the acellular bioink-microsphere composite materials . . . . .	121
5.3.4	Encapsulation efficiency and <i>in vitro</i> release kinetics of cargo molecules	122
5.3.5	3D bioprinting of skeletal muscle constructs and human muscle progenitor cells (hMPCs) viability . . . . .	122
5.3.6	Dorsal root ganglia (DRGs) neurite growth assay . . . . .	123
5.3.7	Statistical analysis . . . . .	125
5.4	Results . . . . .	125
5.4.1	Optimization of the microsphere manufacturing protocol . . . . .	125
5.4.2	Effect of cargo encapsulation on the characteristics of the microspheres	126
5.4.3	Effect of microspheres on viscoelastic properties and morphology of the acellular bioink . . . . .	128
5.4.4	PLGA microspheres are capable of robust encapsulation efficiency and sustained release of cargo molecules . . . . .	129
5.4.5	Effect of PLGA microspheres on hMPC viability in bioprinted muscle constructs . . . . .	130
5.4.6	NFs released by PLGA microspheres retain their bioactivity and facilitate neurite outgrowth . . . . .	131
5.5	Discussion . . . . .	133
5.6	Conclusions . . . . .	135
5.7	Supplementary information . . . . .	136
<b>6</b>	<b>Conclusions and future perspectives</b>	<b>141</b>
6.1	Conclusions . . . . .	141
6.2	Future perspectives . . . . .	142
<b>A</b>	<b>Development of novel chitosan / guar gum inks for extrusion-based 3D bioprinting: Process, printability and properties</b>	<b>145</b>



# List of Figures

1	Schématization des trois principales étapes et plan de la thèse. . . . .	3
2	Schematization of the three main steps investigated and outline of the thesis. . . . .	8
1.1	Schematic representation of tissue engineering strategies . . . . .	13
1.2	Structural elements of the exoskeleton material (exocuticle, endocuticle) of <i>Homarus americanus</i> (lobster) . . . . .	17
1.3	Chemical structures of chitin and chitosan . . . . .	18
1.4	Chemical structures of guar gum and tamarind gum . . . . .	21
1.5	Components of inkjet, microextrusion and laser-assisted bioprinters . . . . .	24
1.6	Schematic representation of the biofabrication window . . . . .	26
1.7	Printing parameters that affect the printability . . . . .	27
1.8	Evaluation of printability (Pr) under three typical gelation statuses, namely under-, proper- and over-gelation . . . . .	28
2.1	FTIR spectra of CH-17, CH-19, CH-20 and of a commercial chitin . . . . .	53
2.2	FTIR spectra of raw material (cicada sloughs) harvested in 2017, 2019 and 2020 . . . . .	54
2.3	XRD spectra of CH-17 (a), CH-19 (b), CH-20 (c) and of a commercial chitin (d). . . . .	54
2.4	SEM images of raw material, demineralized and decolorized samples deriving from the extraction of chitin from cicada sloughs harvested in 2019 and 2020. . . . .	56
2.5	FTIR spectra of: (a) extracted chitosan, (b) CS-80, (c) CS-90 and (d) CS-95. . . . .	57
2.6	XRD of: extracted chitosan, CS-80, CS-90 and CS-95 . . . . .	58
2.7	SEM images of extracted chitosan (a), CS-80 (b), CS-90 (c) and CS-95 (d). . . . .	59
A1	FTIR spectra of raw material, demineralized, deproteinized and decolorized samples extracted in 2019 and 2020 . . . . .	62
A2	XRD spectra of raw material, demineralized, deproteinized and decolorized samples extracted in 2019 and 2020 . . . . .	62
3.1	Printability of chitosan-guar gum and chitosan-tamarind gum biomaterial inks. . . . .	71
3.2	FTIR spectra of the ink solutions in form of film and of the lyophilized 3D printed construct after incubation overnight at 37°C for 24 hours . . . . .	78
3.3	Viscosity of the three biomaterial inks: CH, CH-GG and CH-TG, containing gelatin, as a function of the shear rate, measured at 20°C . . . . .	79
3.4	Qualitative and semi-quantitative evaluation of the printability of the three ink formulations: CH, CH-GG and CH-TG . . . . .	80
3.5	(A) Mass swelling ratio of constructs made of chitosan (CH) and tamarind (CH-TG) or guar (CH-GG) gum. ***p<0.001. (B) Degradation profile of the same constructs (Black: CH, Green: CH-TG, Red: CH-GG) and representative images of the construct CH (B') after 3 weeks in lysozyme, CH-TG (B'') and CH-GG (B''') 7 weeks in lysozyme. . . . .	81

3.6	Nanoindentation of the samples CH, CH-GG and CH-TG . . . . .	82
3.7	SEM images of the bioprinted constructs made of CH, CH-GG and CH-TG .	83
3.8	Cumulative release of BSA from bioprinted construct made of CH (black squares), CH-GG (red circles) and CH-TG (green triangles). . . . .	83
B1	Summary of the FTIR spectra and characteristic absorption peaks of chitosan, gelatin, guar gum and tamarind gum. . . . .	87
B2	Schematic representation of the myofiber orientation . . . . .	89
B3	Schematization of the nanoindentation testing on the left ventricle of pig hearts	90
B4	Comparison of the nanoindentation results obtained on CH, CH-GG and CH-TG constructs vs dECM and myocardial with a longitudinal and radial orientation of rat myocardial fibers . . . . .	91
4.1	Schematic representation of the four level of optimization necessary to achieve the therapeutic effectiveness of GFs for tissue regeneration applications . . .	99
4.2	Strategies employed to temporally control the release of GFs from bioprinted scaffolds . . . . .	104
4.3	Nano-encapsulation for the temporal control of the release of GFs from bioprinted constructs . . . . .	106
4.4	Spatially controlled delivery of GFs . . . . .	109
4.5	Control of the spatial localization of GFs within 3D bioprinted constructs for bone regeneration . . . . .	111
5.1	Représentation schématique de la jonction neuromusculaire (NMJs). Figure reproduite de [242]. . . . .	116
5.2	Structure du copolymère PLGA . . . . .	117
5.3	Preparation of PLGA microparticles by the double emulsion solvent evaporation method. Adapted with permission [266]. . . . .	121
5.4	Representative image showing the design of a one layer bioprinted construct.	123
5.5	Design of the DRG neurite growth assay . . . . .	124
5.6	Empty PLGA microspheres produced with four different fabrication protocols	126
5.7	Characteristics of loaded microspheres. . . . .	127
5.8	FITC dextran-loaded PLGA microspheres before lyophilization (a), after lyophilization (b) and after lyophilization and subsequent immersion in water for 4 hours.	128
5.9	Viscoelastic properties and morphology of the microsphere-free hydrogels and the hydrogels loaded with microspheres at 5 mg/mL and 10 mg/mL . . . . .	129
5.10	Release kinetics of GDNF from bioprinted construct containing either CNTF/GDNF directly incorporated into the hydrogel or encapsulated in PLGA microspheres	130
5.11	Cell viability and microsphere distribution in bioprinted constructs . . . . .	131
5.12	Representative microscopic images of DRGs in the <i>in vitro</i> neurite outgrowth assay . . . . .	132
5.13	Quantitative analysis of the CNTF/GDNF either directly dissolved in the hydrogel or encapsulated in PLGA microspheres on the DRG neurite outgrowth.	133
C1	Neurite tracings (magenta) with the NeuronJ plugin on representative micrographs of DRGs in the <i>in vitro</i> neurite outgrowth assay . . . . .	136
C2	Ultrastructure (SEM) of the crosslinked microsphere-free and microsphere-laden (10 mg/mL) hydrogels after 7 days in PBS at 37°C . . . . .	137

# List of Tables

2.1	Résumé des protocoles utilisés pour l'extraction de la chitine ou de ses dérivés à partir des mues de cigale ou de leur du corps entier. . . . .	32
2.2	Average degree of acetylation (DA) of CH-17, CH-19 and CH-20. . . . .	53
2.3	Crystallinity index (CrI ) % of raw material, demineralized, deproteinized and decolorized samples extracted in 2017, 2019 and 2020. . . . .	55
2.4	Measured average degree of deacetylation (DD) of chitosan extracted form cicada sloughs harvested in 2020 and of three commercial chitosan with known DD (CS-80, CS-90 and CS-95). . . . .	57
2.5	Crystallinity index of the extracted chitosan and CS-80, CS-90 and CS-95. . . . .	58
5.1	Characteristic of empty ( <i>i.e.</i> without cargo) PLGA microspheres produced with different emulsification techniques (homogenization vs. vortexing) and different organic solvents (dichloromethane vs. chloroform). . . . .	125
C2	<i>In vitro</i> outgrowth assay. Total outgrowth. ANOVA summary table . . . . .	138
C3	<i>In vitro</i> outgrowth assay. Average neurite length. ANOVA summary table . . . . .	138
C4	<i>In vitro</i> outgrowth assay. Length of the longest neurite in DRGs. ANOVA summary table . . . . .	138
C5	<i>In vitro</i> outgrowth assay. Number of neurites per ganglion. ANOVA summary table . . . . .	138





# List of Abbreviations

2D	Two-dimensional
3D	Three-dimensional
BMP-2	Bone Morphogenetic Protein-2
BMP-4	Bone Morphogenetic Protein-4
CH	Chitosan
CPC	Calcium Phosphate Cements
CrI	Crystallinity Index
CTGF	Connective Tissue Growth Factor
DA	Degree of Acetylation
DD	Degree of Deacetylation
dECM	decellularized Extracellular Matrix
DPSCs	Dental Pulp Stem Cells
ECM	Extracellular Matrix
FGF	Fibroblast Growth Factor
FTIR	Fourier Transformed Infrared Spectroscopy
GAB	Gene activated bioinks
GDNF	Glial Cell line-derived Neurotrophic Factor
GelMA	Gelatin Methacrylate
GFs	Growth Factors
GG	Guar gum
HCl	Hydrochloric acid
MPs	Microparticles
MSs	Microspheres
MSCs	Mesenchymal Stem, Cells
NaClO	Sodium hypochlorite
NaOH	Sodium hydroxide
NFs	Neurotrophic factors
NGF	Nerve Growth Factor
NMJs	Neuromuscular Junctions
NPs	Nanoparticles
OCP	Octacalcium Phosphate
PBS	Phosphate buffer saline
PCL	Polycaprolactone
PDGF	Platelet-derived Growth Factor
PEG	Polyethylene Glycol
PGA	Poly Glycolic Acid
PLA	Poly Lactic Acid
PLGA	Poly Lactic-Gycolic Acid
PVA	Polyvinyl Alcohol
SEM	Scanning Electron Microscopy

TG	Tamarind gum
TGA	Thermogravimetric Analysis
TGF- $\beta$ 3	Transforming Growth Factor beta-3
TMJ	Temporomandibular Joint
VEGF	Vascular Endothelial Growth Factor
XRD	X-Ray Diffraction

# Introduction générale et objectifs de la thèse

L'utilisation de matériaux d'origine naturelle à des fins médicales remonte à l'Égypte ancienne, plus de 3000 ans av. J.-C. Des coquilles de noix de coco étaient alors utilisées pour guérir certaines blessures crâniennes, et le bois et l'ivoire servaient à créer des fausses dents [1]. Ces matériaux, utilisés ingénieusement, remplaçaient donc partiellement ou totalement certains tissus et, ce faisant, permettaient de maintenir ou d'améliorer la qualité de vie de l'individu. En conséquence, d'après la définition la plus largement acceptée, proposée en 1991 lors de la conférence de consensus de Chester, au Royaume-Uni, ils peuvent donc être qualifiés de biomatériaux [2]. Toutefois, il a fallu attendre la seconde moitié du XXe siècle pour que la science et l'ingénierie des biomatériaux se développent et en particulier ce n'est qu'au cours des ces dernières décennies que les biomatériaux, et plus spécifiquement leurs applications dans le domaine biomédical, connurent une réelle expansion [1]. Ceci vient non seulement de la découverte de nouveaux matériaux aux propriétés très prometteuses, mais également à l'augmentation de notre capacité à les modifier et/ou les synthétiser de manière contrôlée. Le développement de nouveaux biomatériaux ainsi que de nouvelles technologies ont conduit à la naissance de nouveaux domaines d'applications pour les biomatériaux, tels que l'administration de médicaments, les dispositifs médicaux ou encore l'ingénierie tissulaire [3].

L'ingénierie tissulaire est un domaine multidisciplinaire combinant les sciences biologiques et les sciences de l'ingénieur pour le développement de substituts fonctionnels permettant la restauration, le remplacement ou la régénération de tissus endommagés [4]. Différentes stratégies sont employées pour atteindre ces objectifs. Elles impliquent nécessairement un, ou plusieurs, de ces trois éléments : biomatériaux, cellules et/ou des facteurs de croissance. Le rôle des biomatériaux est d'imiter la matrice extracellulaire (ECM ou Extracellular Matrix en anglais), en fournissant un support aux cellules afin qu'elles puissent y adhérer, proliférer et se différencier pour former un tissu fonctionnel [4]. En raison de cette fonction de support, la structure faite de biomatériaux et ayant ce rôle, est aussi définie en tant qu'échafaudage, ou "scaffold" en anglais. Dans l'environnement tissulaire naturel l'ECM forme un micro-environnement contenant des signaux physiques (tels que son architecture ou son élasticité) et biochimiques (tels que les protéines d'adhésion ou les facteurs de croissance), auxquels les cellules répondent en modifiant leur comportement. En particulier, les facteurs de croissance sont des substances régulatrices, libérées à un moment précis (par exemple, suite à une lésion tissulaire pour permettre sa réparation) et qui induisent la prolifération ou la différenciation des cellules [5]. Par conséquent, afin d'accélérer ou de stimuler un comportement cellulaire spécifique, ces molécules sont souvent incorporées dans les scaffolds pour l'ingénierie tissulaire.

Dans ce contexte, l'élaboration de scaffolds devant remplir des rôles extrêmement précis

devient nécessaire, et pour ce faire, notre capacité à moduler leurs propriétés, à la fois mécaniques, de forme et physicochimiques est déterminante. Parmi les technologies d'ingénierie tissulaire utilisées pour la fabrication de scaffold, la bio-impression 3D est une des techniques les plus prometteuses, et est également la technique centrale de cette thèse. Cette technologie permet la fabrication de structures complexes, visant à mimer l'architecture tissulaire en déposant, couche par couche, un mélange de biomatériaux, de cellules et/ou de facteurs de croissance, souvent appelé "bio-encre" (ou "encre" si les cellules ne sont pas incluses [6]).

Pour répondre aux exigences de leur application en bio-impression 3D, les biomatériaux (utilisés comme encres ou bio-encres) doivent avoir des propriétés mécaniques et biologiques précises. En particulier, ils doivent avoir des propriétés mécaniques leur conférant la résistance nécessaire à leur superposition couche par couche sans que la structure 3D s'effondre, et des propriétés biologiques, tels que la biodegradabilité, la biocompatibilité et la présence de signaux biochimiques appropriées, leur permettant d'interagir avec les cellules. Les biomatériaux d'origine naturelle ou synthétique présentent généralement un comportement opposé vis-à-vis de ces deux exigences. En particulier, les biomatériaux d'origine naturelle présentent des similitudes avec l'environnement naturel, sont biodegradables et interagissent avec les cellules permettant leur croissance, leur prolifération et leur différenciation. Cependant, ils manquent souvent des propriétés mécaniques requises pour la fabrication de structures par impression 3D. D'autre part, les biomatériaux synthétiques permettent une meilleure imprimabilité, du fait de leurs propriétés mécaniques facilement ajustables, mais manquent souvent de fonctionnalités biologiques leur permettant d'interagir avec les cellules [7]. Cependant, les biomatériaux naturels sont souvent préférés aux synthétiques en raison de leurs propriétés biologiques intrinsèques mentionnées ci-dessus. Parmi les biomatériaux d'origine naturelle, dans cette thèse, nous nous intéressons au chitosane, un dérivé de la chitine. La chitine est le deuxième polymère naturel le plus abondant après la cellulose et se trouve dans les exosquelettes des arthropodes et dans la paroi cellulaire des champignons [8]. Au niveau commercial, la principale source de chitine et de chitosane est les déchets générés par les industries des fruits de mer, en particulier, des carapaces de crustacés. Compte tenu de l'intérêt croissant pour le chitosane en tant que biomatériau, et de la diminution concomitante de la disponibilité de la source principale, l'exploration de nouvelles sources représente un domaine de recherche très actif. Dans cette thèse, les mues de cigales ont été explorées comme une source peu commune de chitine et de chitosane. Ce dernier a ensuite été employé pour le développement de nouvelles encres pour des applications d'impression 3D.

En effet, l'objectif de ce travail est non seulement de développer de nouveaux biomatériaux permettant l'impression 3D, mais également de trouver de nouvelles stratégies permettant leurs applications en ingénierie tissulaire, à l'aide de la technologie de la bio-impression 3D. Pour ce faire, nous sommes passés par les trois étapes schématisés dans la figure ci-dessous (Figure 1), résumant l'organisation de cette thèse.

La première étape (Figure 1, A) concerne l'extraction et la caractérisation de deux polysaccharides: la chitine et le chitosane. Ces derniers sont obtenus à partir de mues de cigales, une nouvelle agro-ressource naturelle. Au cours de la deuxième étape (Figure 1, B), nous nous sommes intéressés à l'optimisation de l'utilisation du chitosane en tant que biomatériau de base pour le développement de nouvelles encres pour la bio-impression 3D. Pour ce faire, le chitosane est combiné à deux autres polysaccharides: la gomme de guar et la gomme de tamarin. La troisième étape vise à la fonctionnalisation des encres et/ou

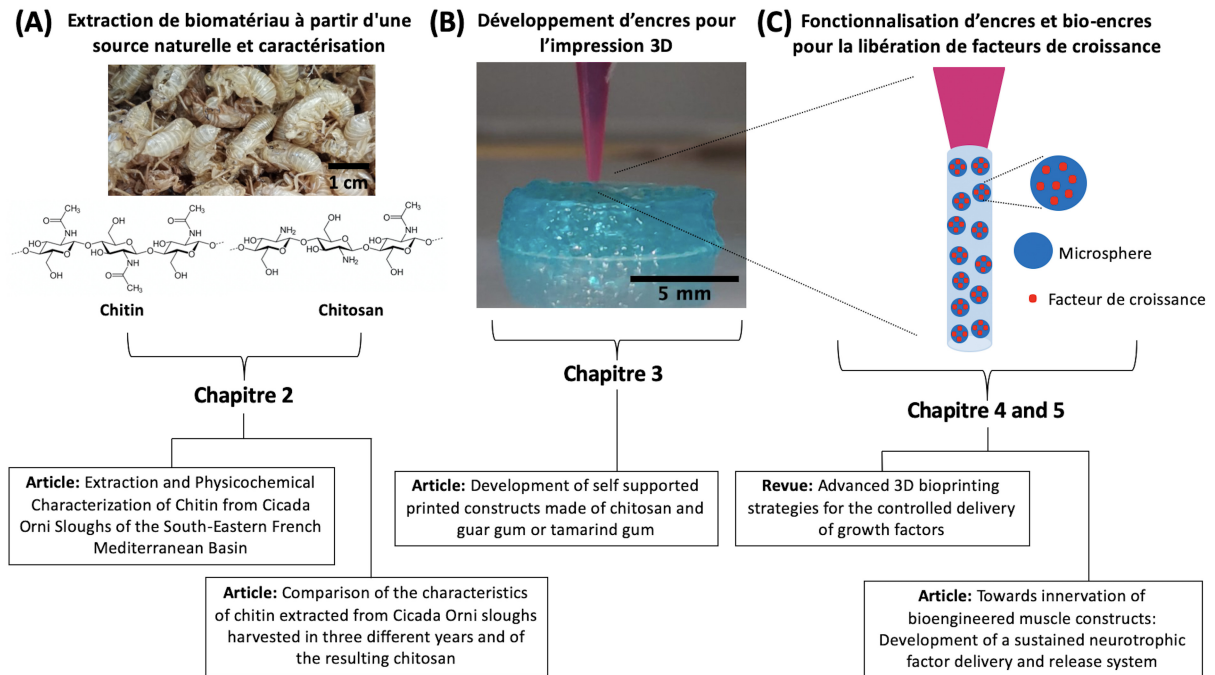


**Figure 1.** Schématisation des trois principales étapes et plan de la thèse.

bio-encre pour la libération de facteurs de croissance (Figure 1, C). Cette fonctionnalisation, réalisée au cours d'une mobilité internationale au laboratoire Wake Forest Institute for Regenerative Medicine (Caroline du Nord, USA), a pour objectif d'améliorer l'innervation d'un tissu musculaire bio-imprimé, grâce à un système de libération contrôlé de facteurs neurotrophiques (à base de PLGA) inclus dans une encre à base de fibrine.

Dans le Chapitre 1 les principaux concepts nécessaires à la compréhension des travaux de cette thèse sont expliqués. En particulier, nous y décrivons comment l'utilisation de cellules, de biomatériaux et de facteurs de croissance est mise au service de l'ingénierie tissulaire. Une attention particulière est portée aux biomatériaux naturels issus d'agro-ressources. Ensuite, nous décrivons la technologie de la bio-impression 3D et les méthodes employées pour le développement et l'optimisation d'encre et bio-encre, ainsi que certaines méthodes proposées dans la littérature pour évaluer leur imprimabilité. Nous passons finalement en revue les stratégies communément adoptées pour optimiser des encre et/ou des bio-encre à base de chitosane.

Le Chapitre 2 relate les résultats de deux études concernant l'extraction de la chitine à partir de mues de cigales, ainsi que la transformation de la chitine en chitosane. Il se base ainsi sur deux articles, dont l'un est publié et l'autre prêt à être soumis. Le premier article décrit l'extraction et l'évaluation des caractéristiques physico-chimiques, tels que le degré d'acétylation et le taux de cristallinité, de la chitine extraite des mues de cigale. En effet, bien que dans le cadre de cette thèse, nous nous intéressons principalement à l'utilisation de chitosane pour le développement d'encre, la chitine, à partir de laquelle est obtenue le chitosane, s'est également montrée utile dans un certain nombre d'applications [9]. Au cours de cette recherche, nous avons montré que les mues de cigales représentent une source riche en chitine (*i.e.* plus de 40% de la masse des mues, le reste étant composé de protéines et de minéraux). Pour la première fois, une même étude rassemble non seulement l'évaluation

des caractéristiques du produit final, (*i.e.* la chitine) mais également de la matière première (*i.e.* les mues de cigale) et des produits intermédiaires de l'extraction, tels que les matières déminéralisées et déprotéinisées. Ceci nous a permis de mieux comprendre les causes possibles induisant une variabilité entre différents prélèvements de la source première, sujet d'étude du deuxième article. Dans celui-ci, nous rapportons les caractérisations de deux extractions complémentaires effectuées sur des mues de cigales prélevées à différentes années (2017-2019 et 2020). La répétabilité du processus d'extraction et la stabilité de la source naturelle, que sont les mues de cigale, au fil des années ont été ainsi évaluées. Les propriétés physico-chimiques des produits finaux obtenus variaient d'une année sur l'autre et ces différences sont corrélées aux variabilités de la source (c'est à dire les mues de cigale), analysées par Spectroscopie Infrarouge à Transformée de Fourier (IRTF ou FTIR en anglais) et par Diffraction des Rayons X (DRX ou XRD en anglais). La chitine a ensuite été transformée en chitosane par désacétylation. Nous avons utilisé les mêmes méthodes de caractérisation pour évaluer l'efficacité du processus de transformation et pour déterminer les propriétés physicochimiques du chitosane.

Dans le Chapitre 3 nous présentons les résultats du développement d'encres pour la bio-impression 3D à base de chitosane et de gommages naturelles telles que la gomme de guar et la gomme de tamarin. En effet, le chitosane seul et non modifié n'est généralement pas adapté aux applications de bio-impression 3D en raison de ses faibles propriétés rhéologiques et mécaniques. La gomme de guar et la gomme de tamarin sont des polysaccharides dérivés de plantes à graines et largement utilisés comme agents épaississants et gélifiants par les industries alimentaires. Profitant de l'augmentation de viscosité qu'ils apportent, nous les avons initialement associés au chitosane afin d'améliorer ses propriétés rhéologiques et mécaniques des structures 3D résultantes. Bien que l'inclusion de ces gommages améliore les propriétés rhéologiques et l'imprimabilité du chitosane seul, elle n'est pas suffisante pour la fabrication de structures 3D stables dans le temps. Ces derniers ont été obtenus grâce à une double stratégie de gélification basée sur l'inclusion de gélatine dans les encres (qui modifie leur état de gélification en fonction de la température) et sur l'immersion des structures imprimées dans un bain de gélification (de NaOH et éthanol) immédiatement après l'impression (ce qui garantit leur stabilité à long terme et détermine leurs propriétés mécaniques).

Le Chapitre 4 est une revue des stratégies employées pour contrôler la libération de facteurs de croissance, aussi bien spatialement que temporellement, à partir de structures bio-imprimées en 3D. En particulier, dans cette revue, nous fournissons un aperçu général des fonctionnalités clés à optimiser afin de produire un système de libération de facteurs de croissance efficace et nous analysons les stratégies employées par les chercheurs pour les résoudre en utilisant la technologie de la bio-impression 3D.

Le Chapitre 5 est basé sur les travaux menés au cours d'une période d'un an passé en tant que doctorante visiteur au Wake Forest Institute for Regenerative Medicine. Le sujet de cette étude portait sur l'inclusion d'un système de libération de facteurs neurotrophiques à des constructions musculaires squelettiques bio-imprimées en 3D à base de fibrine, pour accélérer et améliorer leur innervation. Cette innervation, caractérisée par la formation de jonctions neuromusculaires, c'est-à-dire les points de contact entre le système nerveux périphérique et les fibres musculaires, est extrêmement importante car son absence conduirait à une atrophie musculaire et, plus généralement, à une perte des fonctions musculaires.

Enfin, dans le Chapitre 6, nous résumons les principaux résultats de cette thèse et nous présentons les développements et perspectives possibles.





# General introduction and objectives of the thesis

The use of naturally derived materials for medical purposes dates back to ancient Egypt (about 3000 BC) when coconut shells were used to heal head injuries, and wood and ivory were used to replace missing teeth [1]. These materials, ingeniously used to partially or totally replace certain tissues, made it possible to maintain or improve people's quality of life. Consequently, according to the most widely accepted definition, proposed in 1991 at the Chester Consensus Conference, in the United Kingdom, they can be qualified as biomaterials [2]. However, it was not until the second half of the 20th century, that the science and engineering of biomaterials started to be recognized and in particular, it was only in recent decades that their application in the biomedical field has experienced a real expansion [1]. This comes not only from the discovery of new materials with very promising properties, but also from the increase in our ability to modify and/or synthesize them in a controlled manner in the laboratory. The development of new biomaterials and of technologies able to tune their properties led to the appearance of new fields of application for biomaterials, such as drug delivery and tissue engineering [3].

Tissue engineering is a multidisciplinary field combining the principles of biology and the tools of engineering for the development of functional substitutes allowing for the restoration, replacement or regeneration of damaged tissues [4]. Different strategies are employed to achieve these goals and necessarily involve one or more of these three elements: biomaterials, cells and/or growth factors. The role of biomaterials is to mimic the Extracellular Matrix (ECM), providing support for cells so that they can adhere, proliferate and differentiate to form functional tissues [4]. In the natural tissue environment, the ECM contains physical signals (given, for example, by its architecture or its elasticity) and biochemical (such as the presence of adhesion proteins or growth factors), to which cells respond by modifying their behavior. In particular, growth factors are regulatory substances, which are released at a specific time (for example, following tissue damage to allow its repair) and induce the proliferation or differentiation of cells [5]. Therefore, in order to accelerate or stimulate specific cellular responses, these molecules are often incorporated into tissue-engineered scaffolds.

In this context, the development of biomaterial scaffolds that must fulfill extremely precise roles becomes necessary, and for this, our ability to modulate their mechanical, structural and physicochemical properties is decisive. Among the different tissue engineering technologies used for the development of scaffolds, 3D bioprinting is one of the most promising techniques and is the central one of this thesis. This technology allows for the fabrication of complex structures, aiming to mimic the tissue architecture by depositing, layer by layer, a mixture of biomaterials, cells and/or growth factors, often referred to as "bioink" (or "biomaterial ink" if cells are not included [6]). To fulfill the requirements for their application in 3D bioprinting, biomaterials used as ink or bioink must have specific mechanical and biological properties.

Based on their origin, either natural or synthetic, biomaterials usually show an opposite behavior regarding these two requirements. In particular, naturally derived biomaterials have similarities with the natural environment, are biodegradable and interact with cells allowing for their growth, proliferation and differentiation. However, they usually lack the mechanical properties required for the processing of 3D shapes. On the other hand, synthetic biomaterials allow for better printability, due to their tunable mechanical properties, but lack of biological functionalities allowing them to interact with cells [7]. However, natural biomaterials are often preferred over synthetic ones due to the above-mentioned intrinsic biological properties. Furthermore, they can be cheap and abundantly available in nature. Among naturally derived biomaterials, in this thesis, we are interested in chitosan, a derivative of chitin. Chitin is the second most abundant natural polymer after cellulose and is found in arthropods exoskeleton and the cell wall of fungi [8]. Commercially, the main source of chitin and chitosan is the waste generated by seafood industries (*i.e.* crustacean shells). Given the increasing interest in chitosan as a biomaterial, and the concomitant decrease in the availability of the main source, the exploration of new sources represents a very active field of research. In this thesis, cicada sloughs were explored as an uncommon source of chitin and chitosan. Chitosan has been then employed for the development of new biomaterial inks for 3D printing applications.

The objective of this thesis is not only to develop new biomaterials allowing for 3D printing but also to find new strategies allowing for their application in tissue engineering, using, in particular, the technology of 3D bioprinting. To do this, we went through the three steps schematized in the figure below (Figure 2), which summarizes the organization of this thesis.

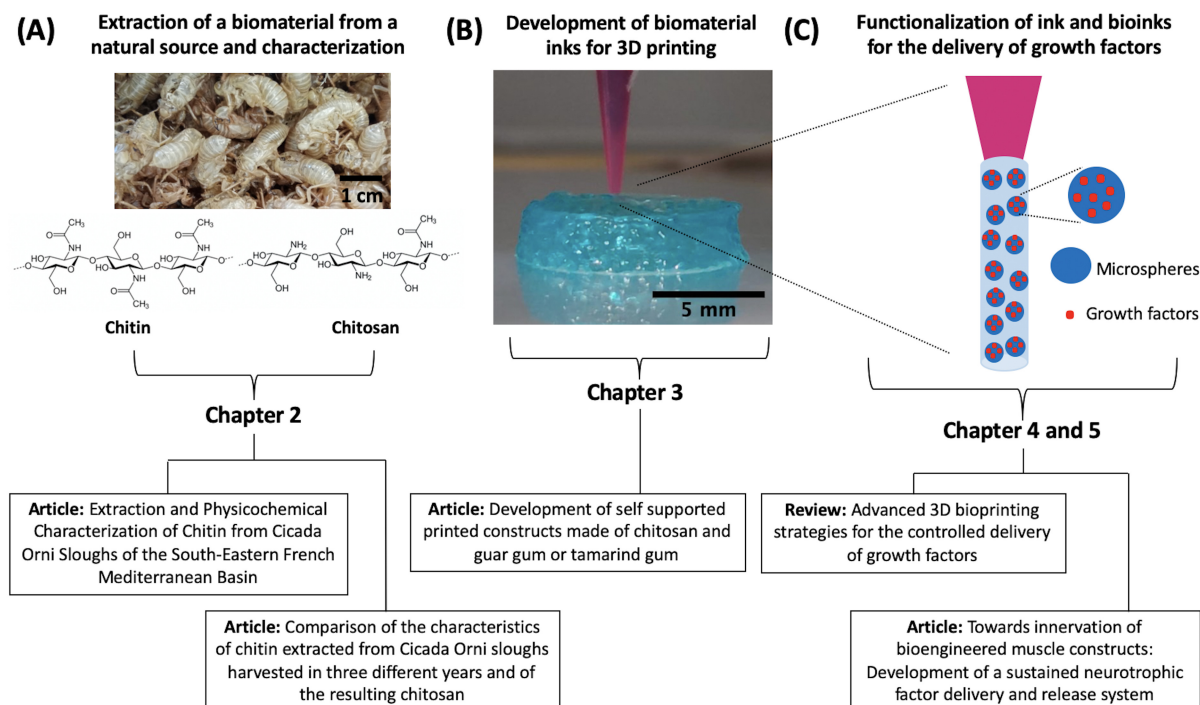


**Figure 2.** Schematization of the three main steps investigated and outline of the thesis.

The first step (Figure 2, A) is the extraction and characterization of chitin and chitosan obtained from cicadas sloughs, a new natural agro-resource. The second step (Figure 2,

---

B), is the development of new chitosan-based biomaterial inks obtained through its combination with two other natural polysaccharides: guar gum and tamarind gum, and the establishment of a dual gelation strategy. The third step aims at the functionalization of inks and/or bioinks for the release of growth factors (Figure 2, C). This functionalization, carried out during an international mobility at the Wake Forest Institute for Regenerative Medicine (North Carolina, USA), aims to improve the innervation of a bioprinted muscle tissue through the inclusion of PLGA microspheres as a neurotrophic factors delivery system within a fibrin-based bioink used for the bioprinting of the scaffold.

In Chapter 1 we present the main concepts necessary for understanding the work of this thesis. In particular, we introduce the three main components of tissue engineering: cells, biomaterials and growth factors and we give particular attention to natural biomaterials derived from agro-resources. Next, we describe the technology of 3D bioprinting and the methods used for the optimization of inks and bioinks, as well as some methods proposed in the literature to assess their printability. Finally, we review the strategies commonly adopted for the optimization of chitosan-based inks and/or bioinks.

Chapter 2 reports the results of two studies concerning the extraction of chitin from cicada sloughs, as well as the transformation of chitin into chitosan. It is based on two articles, one of which is published and the other ready for submission. The first article describes the extraction and evaluation of physicochemical characteristics, such as the degree of acetylation and index of crystallinity, of chitin extracted from cicada sloughs. Even though in the context of this thesis, we are mainly interested in the use of chitosan for the development of inks, chitin, from which chitosan is obtained, has also been shown to be useful in several applications [9]. In this study, we showed that cicada sloughs represent a source rich in chitin (constituting more than 40% of the slough mass while the rest is composed of proteins and minerals). For the first time, we evaluated not only the physicochemical characteristics of the final product (*i.e.* chitin) but also of the raw material (*i.e.* cicada sloughs) and the intermediate products of the extraction of chitin, such as the demineralized and the deproteinized material. This allowed us to better understand the possible causes inducing a variability between different harvesting of the source, which is the subject of the second article. In this one, we report the characterizations of two additional extractions performed on cicada sloughs harvested in different years in order to assess the repeatability of the extraction process and the stability of the natural source over the years. We found that the physicochemical properties of the final products obtained (*i.e.* chitin) varied from year to year, and that these differences could already be detected by analyzing the raw material (*i.e.* cicada sloughs) using simple techniques such as Fourier-transform infrared spectroscopy (FTIR) and X-ray diffraction (XRD). During this work, we also transformed chitin into chitosan through a process of deacetylation. We used the same characterization methods to assess the efficiency of the deacetylation process and to determine the physicochemical properties of chitosan in order to evaluate its possible applications (*e.g.* as ink for 3D bioprinting).

In Chapter 3 we present the results of the development of inks for 3D bioprinting based on chitosan and natural gums such as guar gum and tamarind gum. Chitosan alone, if not modified, is generally not suitable for 3D bioprinting applications due to its poor rheological properties and self-supporting capacity upon deposition. Guar gum and tamarind gum are polysaccharides derived from seed plants and widely used as thickening and gelling agents by

the food industries. Taking advantage of the increase in viscosity they provide, we firstly associated them with chitosan in order to improve its rheological properties. Even though the inclusion of these gums improves the rheological properties and printability of chitosan alone, it is still inadequate for the fabrication of 3D structures. These were obtained through a dual gelation strategy based on the inclusion of gelatin within the chitosan-gum inks (which modifies their gelation state according to the temperature) and on the immersion of the printed structures in a gelation bath immediately after printing (which guarantees their long-term stability and determines their mechanical properties).

Chapter 4 is a review of the strategies employed to control the release of growth factors, both spatially and temporally, from 3D bioprinted structures. In particular, in this review, we provide a general overview of the key functionalities to be optimized in order to produce an efficient growth factor delivery system and we analyze the strategies employed by researchers to solve them using the technology of 3D bioprinting.

Chapter 5 is based on the work carried out during a period of one year spent as a visiting doctoral student at the Wake Forest Institute for Regenerative Medicine. The subject of this study was the inclusion of a neurotrophic factor release system in 3D bioprinted skeletal muscle constructs based on fibrin, to accelerate and improve its innervation. This innervation, characterized by the formation of neuromuscular junctions (the points of contact between the peripheral nervous system and the muscle fibers) is extremely important because its absence would lead to muscle atrophy and, more generally, to a loss of muscle functions.

Finally, in Chapter 6, we summarize the main results of this thesis and we present the possible developments and perspectives.

# Chapter 1

## Literature review

### 1.1 Introduction to Tissue Engineering

Tissue engineering is a field of Regenerative Medicine, defined in 1993 by Robert Langer and Joseph Vacanti as “*an interdisciplinary field that applies the principles of engineering and the life sciences toward the development of biological substitutes that restore, maintain, or improve tissue functions*” [4]. The field of tissue engineering firstly appeared as a consequence of the organ shortage crisis with the “*big dream*” of fabricating, in the laboratory, full tissues and organs to be transplanted to overcome the lack of donors. In fact, the number of patients on transplant waiting lists was, and still is, exceedingly higher than the number of tissues and organs donors. While the fabrication of relatively simple tissue substitutes, such as skin, has been successfully achieved, the fabrication of full complex organs (*i.e.* kidney, heart, liver) to transplant remains a big challenge [10]. This is mainly due to the fact that many different cell types compose a tissue, each with its specific role, function and requirements, and many tissues work together to form an organ. Due to this hierarchical organization, tissues and organs show structural and functional complexities that are very difficult to reproduce *in vitro*. However, several attempts are being made every day, around the world, to develop biomaterials capable of mimicking these complex structures at a microscale level, in accordance with the concept of “*biomimicry*”, with a degree of complexity relative to the target application [11].

Even though several strategies have emerged since the beginning of tissue engineering, they all rely on the understanding of the tissue engineering paradigm according to which the three main components necessary for the fabrication of a tissue are:

1. **Cells**, the building blocks of tissues.
2. A **Scaffold** made of natural or synthetic biomaterials, whose role is to hold cells together and to induce their adhesion, migration, proliferation and differentiation.
3. **Biological factors**, such as growth factors (GFs), which instruct cells to express the phenotype typical of the tissue that they have to develop.

The simultaneous combination of all these three components is not mandatory. However, it is the basis of the “*traditional*” or “*ex vivo*” tissue engineering approach, according to which cells, ideally harvested from a patient, are combined to biomaterials and growth factors to generate a cell-laden scaffold. There exist two possibilities of incorporating cells into scaffolds: i) combining them to biomaterials before the fabrication process, or ii) seeding them on the surface of the scaffold following the scaffold fabrication [12]. The cell-laden

scaffold is then cultured in an appropriate environment (for example in a specific differentiation media and/or under specific mechanical stimulation) in order to induce cells to differentiate in a specific tissue. However, the use of the patient's own cells presents some limitations such as the difficulty in harvesting and expanding them. Furthermore, despite the possibility to create relevant size constructs through this strategy, it poses several challenges such as maintaining an extensive *in vitro* cell expansion under non-native conditions. As a consequence, other strategies emerged such as the *in situ* approach, which is based on the body's own capacity of regeneration and therefore, does not include cells within the scaffold prior to implantation. In this case, an acellular scaffold loaded with bioactive molecules (*i.e.* growth factors), is implanted and the patient's own stem- or tissue-specific progenitor cells are recruited into the scaffold and induced to proliferate and/or differentiate for the formation of a new tissue [13, 14]. However, the *in situ* strategy may be unsuccessful if the stem cells that should infiltrate the scaffold are damaged by the tissue defect or when this latter is too vast to rely only on the tissue's regenerative abilities. These two strategies are schematized in Figure 1.1). Even though these two strategies have long been the principal ones, they represent only a small portion of the existing approaches. Other possibilities have been explored such as the low-material based tissue engineering strategies that relies on the the fabrication of cell-rich devices containing a low amount of biomaterials (*i.e.* cell-only spheroids, cell-sheets, microparticles). In this approach, the regeneration processes depend on the inherent ability of cells to self-organize and can conduct to the repair of critical size defects via minimally invasive implantation [15]. Other strategies are based on the design of smart biomaterials able to guide stem cell differentiation without the help of growths factors but through biophysical cues (*i.e.* surface topography and stiffness) [16].

## 1.2 Cells in Tissue Engineering

Cells are the critical components for the success of any tissue engineering strategy. In fact, either harvested from a tissue, isolated, expanded and seeded on the top or within a scaffold (as in the *traditional* tissue engineering approach), or recruited by a biomaterial scaffold after implantation (as in the *in situ* tissue engineering approach), the development of a functional tissue depend on the activity of cells. Whether before or after implantation, cells interact with the biomaterials composing the scaffold and establish a complex network of signals that ultimately lead to the creation of a functional tissue [17]. Several sources of cells can be employed for tissue engineering applications. The ideal method would be the harvesting of autologous cells directly from the patient, followed by their expansion *in vitro*. Even though these cells present the advantage of not causing an immune response following transplantation, they are not always available and easy to collect and, in addition, can result in donor-site morbidity. Alternatively, cells can be obtained from another human source (called allogeneic source) which present the same limitation and, in addition, increases the risk of immune reaction. Lastly, cells can be harvested from different species (xenogenic sources) which present all the above mentioned limitations and include the risk of transmission of infectious agents other than ethical, moral and social issues [18].

The most widely used type of cells for tissue engineering application are adult stem cells, progenitor cells or primary cells. Primary cells are terminally differentiated cells, isolated from the tissue or organ of interest. These cells represent optimal cell type for the creation of

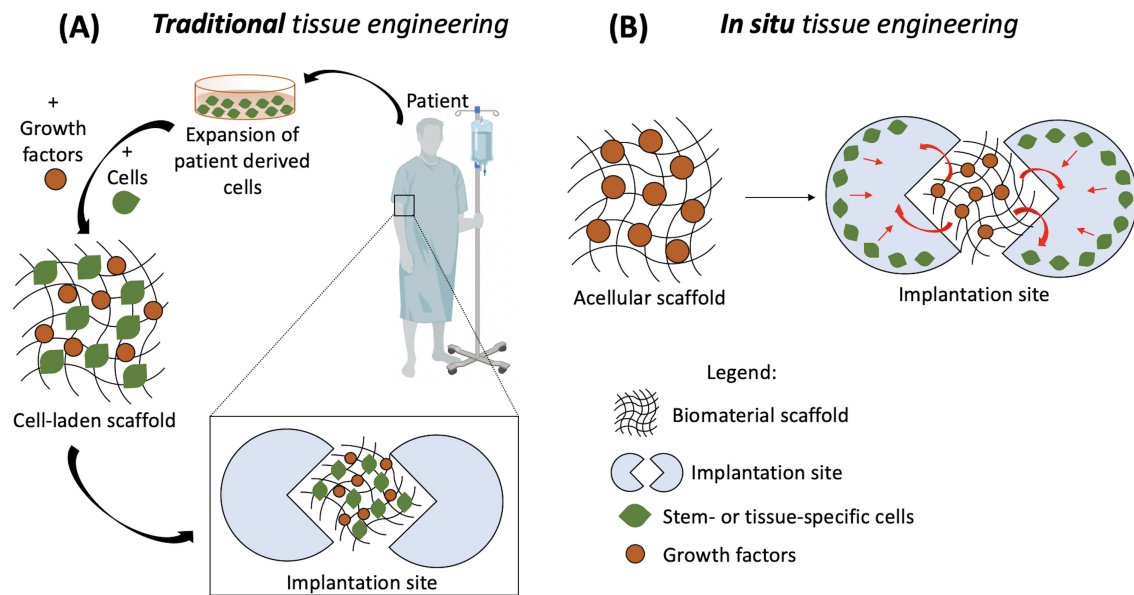


**Figure 1.1.** Schematic representation of tissue engineering strategies. (A) The *traditional* tissue engineering strategy is based on the harvesting of a patient’s own tissue to obtain cells. Cells are isolated, grown *in vitro* and subsequently seeded or encapsulated into a biomaterial-based scaffold together with growth factors. The cell-laden scaffold is then implanted into the site of injury of the patient. (B) The *in situ* strategy takes advantage of the body’s own regenerative capability. The biomaterial-based scaffold, loaded with growth factors, can recruit endogenous stem cells or tissue-specific progenitor cells at the site of implantation and direct their differentiation in a new tissue.

tissue constructs with respect to functionality. However, they have limited to no proliferative capacity [17]. Progenitor cells are the immediate descendant of stem cells. Unlike stem cells, progenitor cells can divide only a limited number of times and are more limited in what type of cell they can become. There exist different types of stem cells such as embryonic stem cells (ESCs), induced pluripotent stem cells (iPSCs) and adult stem cells, each with its advantages and disadvantages. For example, ESCs and iPSCs are pluripotent and could differentiate in every cell type. However, ESCs are associated with ethical issues and the risk of the formation of teratomas. Risk, this last, that concerns iPSCs as well. Adults stem cells are found in many adult tissues. They are multipotent and can differentiate into a wide variety of cell types composing that tissue. A particular type of adult stem cells are mesenchymal stem cells (MSCs) which reside mainly in the bone marrow and adipose tissue and can differentiate into bone (osteoblasts), muscle (myoblasts), fat (adipocytes) and cartilage (chondrocytes). Stem cells, in natural tissues, are induced to differentiate by the “niche” microenvironment, which contains several chemical, mechanical and topographical cues [19]. As a consequence, biomaterials can be designed using a biomimetic approach through the incorporation of these cues. Stem cells then, whether incorporated into the scaffold before its fabrication, seeded on the top of it, or recruited from their natural niche, are induced to form the desired tissue in response to these cues.

### 1.3 Biomaterial scaffolds

In native tissues, cells are immersed within an extracellular matrix (ECM), which provides mechanical support to tissues and influences cellular behavior, mainly through physical (*i.e.* surface topography, porosity, elasticity) or biochemical (*i.e.* adhesion molecules, growth factors) signals. The ECM microenvironment is tissue-specific and consequently, it contains the information inducing stem cells to develop that specific tissue. For instance, stem cells can differentiate in a type or another simply based on the stiffness and architecture of the scaffolds on which they adhere [20]. These concepts highlight the importance of the extracellular environment on the formation of tissues and implies that biomaterials used as scaffolds for tissue engineering should be able to “mimic” the natural ECM of the tissue to regenerate.

In general, biomaterials used as scaffolds should have specific requirements which can be summarized as follows:

- Biocompatibility, defined as the property of being compatible with living tissues.
- Biodegradability, meaning that the biomaterial scaffold has to act as a temporary ECM. Consequently, it must degrade in a timely manner to ensure proper regeneration of the tissue. If it degrades too fast, the developing tissue loses its mechanical support while if it degrades too slowly, it can prevent the proliferation and/or differentiation of cells.
- Mechanical properties comparable to those of the target tissue and that can be very different from one tissue to another (*i.e.* bone vs cartilage).
- A sufficient porosity, particularly important when scaffolds are of critical size, allowing for the exchange of oxygen and nutrients between the encapsulated cells and the environment.

Biomaterials used for tissue engineering applications can be classified into two main groups: natural and synthetic biomaterials. Natural biomaterials, such as proteins, decellularized tissue matrix and polysaccharides, usually derive from components that are already present within the living systems and therefore, they are engaged in a variety of biological processes. Furthermore, they are usually not toxic, present similarities with the extracellular matrix and, consequently, often assist cellular activities and are biodegradable [1]. In some cases, the biodegradability can prove to be a disadvantage since they are not very stable and, often, are not efficient in proving mechanical stability to implanted constructs. On the other hand, synthetic materials, such as organic and inorganic polymers, ceramics and metals, have very well controllable physicochemical, mechanical, and degradation properties, but they usually lack cell attachment sites [21]. Alternatively, natural and synthetic biomaterials can be combined for the creation of hybrid scaffolds which possess the properties of the other two categories.

Naturally-derived biomaterials are more attractive for tissue engineering applications since they present high similarity with natural tissues, favoring cell-matrix interactions. Furthermore, they can be cheap and abundantly available in nature. Among the naturally-derived biomaterials, great attention will be done, in this thesis, to biomaterials derived from agricultural or other natural wastes.



### 1.3.1 Agro-resources based biomaterials for biomedical applications

As the field of tissue engineering and biomaterials continues to evolve, the investigation of naturally-derived polymers to be used as scaffold materials evolves as well. In this context, particular attention has been done to the production of biomaterials from agricultural or industrial wastes. Agricultural or industrial wastes can be defined as solid or liquid materials produced from direct consumption of primary products or their industrialization, and that are no longer useful for the process that generated them [22]. However, the great advantages of naturally-derived products became so obvious that not only scientists investigated the potential applications of renewable and sustainable materials derived from wastes of the natural environment, but plants and animals started to be cultivated and bred specifically for biomedical applications [23].

Natural materials obtained from agro-resources can be grouped in three main categories: animal-derived, plant-derived and microbial-derived products, in turn being sources of two main classes of products: proteins and polysaccharides. In this part, we will briefly introduce few examples of animal- and plant-derived products. We will not discuss microbial-based products specifically but, since the plant-derived products that we present below are also produced by bacterias, we can refer to them as plant- and microbial-derived products.

Among the **animal-derived products**, of particular interest are collagen and its derivative gelatin which belong to the class of proteins and chitin and its derivative chitosan which belong to the class of polysaccharides.

*Collagen* is one of the key structural proteins found in the ECM of many connective tissues in mammals. It is rich in arginine-glycine-aspartic acid (RGD) sequences which are able to promote cell adhesion [24]. Collagen is usually extracted from bovine hide, pig skin or chicken waste. However since these sources have faced some constraints related to biological contaminants and ethical (religious) issues, alternative sources have been found for the commercial production of collagen and gelatin, such as fish skin [25]. Collagen is insoluble in water and is slightly immunogenic [25]. Hence, gelatin, which is the product of the thermal denaturation of collagen, is usually preferred to collagen. Based on the source of collagen and on the method used for its production, gelatin can have various molecular weights, which highly influence its rheological and mechanical properties. Gelatin is highly employed for biomedical applications due to its biocompatibility, biodegradability and high cell adhesion due to the fact that, as its precursor collagen, it is rich in RGD sequences [26]. In several applications, the main advantage of gelatin is due to its thermo-reversible sol-gel transformation, which makes gelatin liquid when heated and solid when it cools down [27]. Due to this tunable property, gelatin-based hydrogels are widely used in drug delivery and tissue engineering applications.

*Chitin* is a polysaccharide and represents the second most abundant natural polymer in the world after cellulose. The main industrial source of chitin is the waste of the fishing industry, which extracts it from crustacean shells (prawns, crabs, lobsters, etc.). The reuse of seafood wastes, especially in countries where the consumption of crustaceans is elevated, makes chitin and its derivative chitosan the most important renewable source in the food and

biomedical field. In fact, chitosan has FDA approval as a wound dressing, it is permitted as a food supplement in Japan, Italy and Finland, and is Generally Recognized As Safe (GRAS) in food in the USA [28]. Due to the success of their use, other sources, such as insects, are gaining strong attention for the production of chitin and chitosan [29]. Chitin and chitosan will be discussed more in detail below (section 1.3.1.1).

**Plant- and microbial-derived products** can, as well, be divided into two groups: proteins and polysaccharides. Plant-derived proteins mostly possess insignificant physicochemical and biological properties, even if after blending with synthetic polymers and/or crosslinking, they have found some applications which have been described elsewhere [30]. More popular are plant-derived polysaccharides such as alginate, cellulose and seed polysaccharides (also known as natural gums).

*Alginate* is a natural polysaccharide mainly derived from brown seaweed, but also from red seaweed and as exopolysaccharide synthesized by some bacteria. Alginate is composed of linear block copolymers of 1,4-linked  $\beta$ -D-mannuronic acid and  $\alpha$ -L-guluronic acid units. Its composition and molecular weight can vary between algae species and affect its viscosity, gelation, mechanical strength and other physicochemical and biological properties. Alginate is water-soluble at room temperature and in presence of certain divalent cations, such as calcium, it forms stable gels. This ability to form gels has been exploited for the production of alginate-based hydrogels, microparticles and nanoparticles for several biomedical applications [31] making alginate one of the most employed naturally-derived biomaterials.

*Cellulose* is a structural polysaccharide present in the primary cell wall of plants, algae, fungi and bacteria biofilms. It consists of a linear chain of  $\beta$ -1,4 linked G-glucose and is the most abundant organic polymer on the earth. Cellulose is insoluble in most solvents and consequently, if not chemically modified (for example in the form of carboxymethylcellulose) or combined with other molecules, cellulose has limited usages in tissue engineering. However, once modified or in combination with other materials, it has been successfully tested for several applications such as skin [32] and bone [33] regeneration.

*Natural gums* are polysaccharides obtained from plant seeds or exudates, or produced by bacterial fermentation. They are composed of different sugars other than glucose and are capable to increase the viscosity of solutions to which they are included, even at small concentrations [34]. For this reasons, as well as for their limited caloric contribution due to the fact that they act as fibers, natural gums have been widely used in food industry as thickening and gelling agents [35]. However, scientists soon realized that the above-mentioned properties might be beneficial also for pharmaceutical and biomedical applications. Consequently, due to their versatility and to the fact that they present large similarities with the ECM and excellent biological responses, natural gums have recently also been explored for new applications such as drug delivery and tissue engineering [36]. Natural gums will be discussed more in detail below (section 1.3.1.2).

### 1.3.1.1 Chitin and chitosan

After its isolation from mushrooms in 1811, the polysaccharide chitin gained strong attention in the biomedical and pharmaceutical fields. Other than in mushrooms, it is found in large quantities as a structural component of the exoskeletons, and in particular in cuticles (the

non living layer of the exoskeleton), of Arthropods (*i.e.* crustaceans and insects) [37, 8]. The cuticles of Arthropods consist of three layers: epicuticle, exocuticle, and endocuticle. The epicuticle does not contain chitin and is a very thin layer acting as a diffusion barrier. The exocuticle and endocuticle, responsible for the mechanical properties of cuticles consist of fibrous chitin–protein complexes containing variable amounts of minerals (typically calcium carbonate, or calcite) [38]. Within exocuticle and endocuticle, chitin is generally found as an ordered crystalline structure with a hierarchical organization, as shown in Figure 1.2.

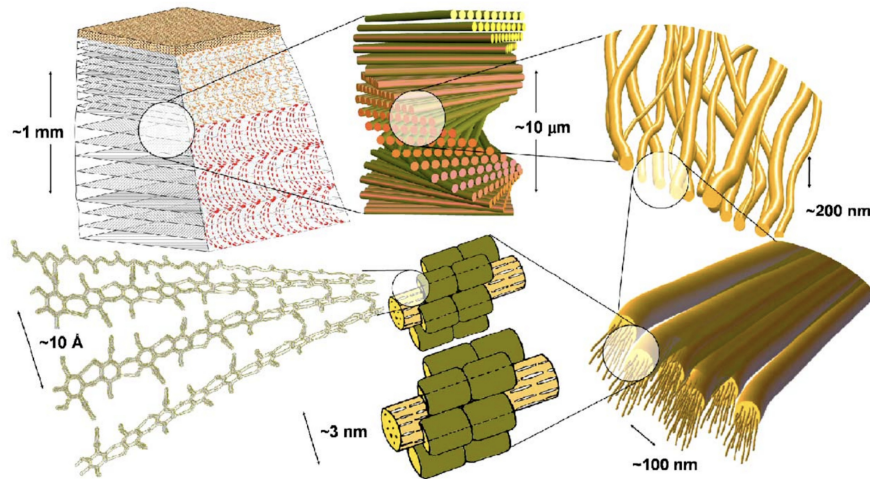


**Figure 1.2.** Structural elements of the exoskeleton material (exocuticle, endocuticle) of *Homarus americanus* (lobster). The hierarchical organization of chitin reveals six main different structural levels. From the bottom-left, the first level is the polysaccharide chitin. The antiparallel alignment of these molecules forms  $\alpha$ -chitin crystals. The second structural level is the arrangement of chitin chains in the form of narrow and long crystalline units, wrapped by proteins. These structures form nanofibrils of about 2–5 nm diameter and about 300 nm length. The third level is the clustering of some of these nanofibrils into long chitin–protein fibers of about 50–300 nm diameter. The fourth level is the formation of a planar woven and systematically branched network of such chitin–protein fibers. The spacing between these strands is filled by a variety of proteins and minerals. The fifth level is created from the woven chitin–protein planes. Their gradual rotation from one plane to the next creates complex structures (sixth level) that appear as an arched pattern when viewed in cross-sections. Figure reproduced from [38].

Chitin is a polymer of randomly distributed  $\beta$  (1 $\rightarrow$ 4)-linked N-acetyl-D-glucosamine (acetylated unit) and D-glucosamine (deacetylated unit) groups. To be called chitin, the number of acetylated units has to be higher than 50% [37]. Based on the source, chitin can exist in three different polymorphs called  $\alpha$ ,  $\beta$  and  $\gamma$ , depending on the antiparallel, parallel or alternated arrangements of the polymers chains, respectively [39].  $\alpha$ -chitin is the most abundant polymorph found in nature and the most used for biomedical applications [40]. The extraction of chitin from a source is made through a process consisting of three steps: the demineralization of the raw material for the removal of minerals, the deproteinization for the removal of proteins and the decolorization for the removal of pigments, which are responsible for coloring the cuticle of insects. Besides the removal of pigments, which is the less relevant step, either biological or chemical methods have been used to remove proteins and minerals [39]. Briefly, biological extraction methods are based on the use of lactic acid-producing bacteria for the demineralization. Lactic acid reacts with calcium carbonate to

form calcium lactate which can be removed by precipitation. Concerning the deproteinization, this employs proteolytic bacterias whose proteases are responsible for the elimination of proteins. Chemical extraction methods involve an acid treatment, mostly with hydrochloric acid (HCl) to dissolve the calcium carbonate, followed by alkaline treatment with sodium hydroxide (NaOH) to dissolve proteins. Chemical methods are more used than biological ones since the time of the extraction process is shorter and usually requires standard laboratory materials that are easily available. [39]. Due to the high number of acetyl groups, which form strong intra- and inter-molecular hydrogen bonds creating a rigid crystalline structure, chitin is insoluble in water and in the majority of organic solvents [41]. Although a high number of solvents have been investigated to dissolve chitin, such as calcium solvent systems [42] or ionic liquids [9], the use of chitin for tissue engineering applications is still limited. For most applications, chitin is transformed into chitosan, which is soluble in traditional organic solvents such as acetic acid. The deacetylation process is based on the transformation of the acetamide groups ( $\text{CH}_3\text{-CO-NH}$ ) present in chitin (and composing the acetylated unit) into primary amino groups ( $\text{NH}_2$ ) (composing the deacetylated unit). Consequently, chitosan is a derivative of chitin where the number of deacetylated units is higher than 50% [37]. The chemical structure of chitin and chitosan is shown in Figure 1.3.

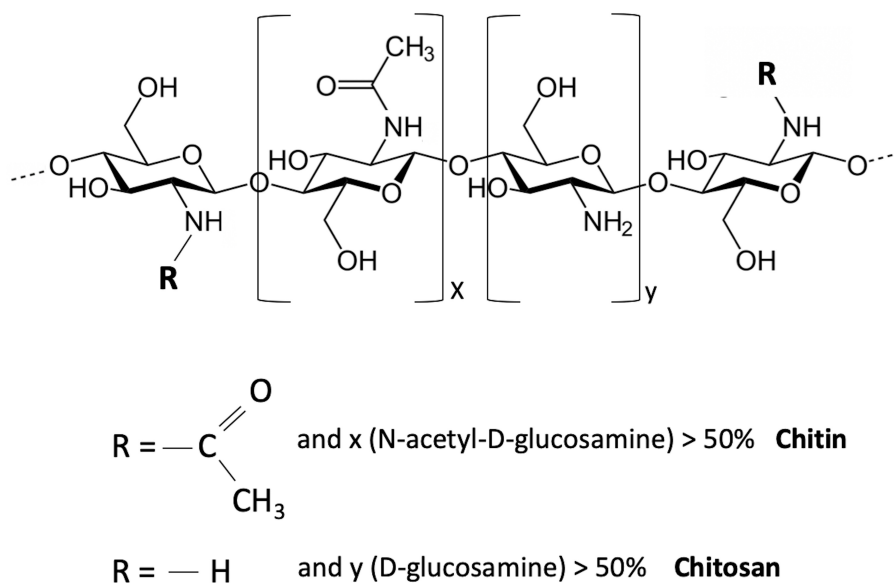
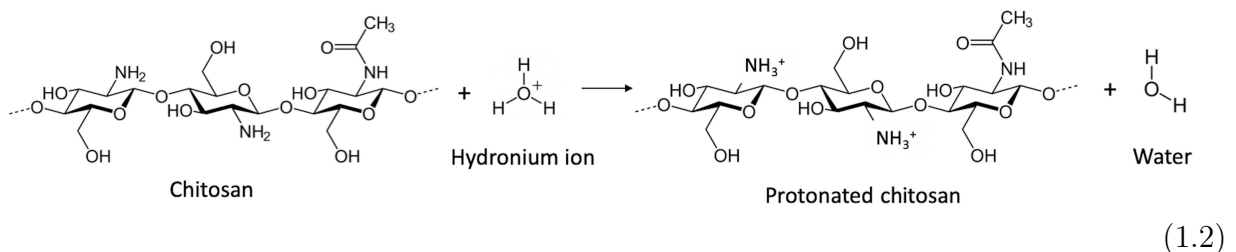
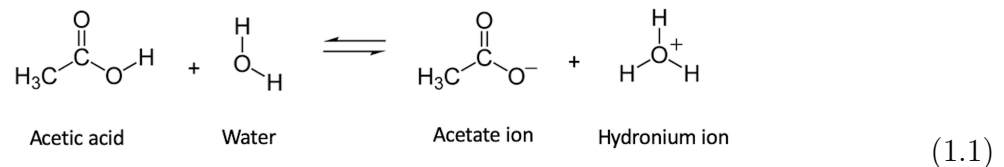


**Figure 1.3.** Chemical structures of chitin and chitosan. Figure reproduced from [43].

The deacetylation of chitin, which consists in the removal of acetyl groups, can, as well, be obtained through biological or chemical methods [39]. Biological methods involve the use of the enzyme chitin deacetylase, an enzyme present in bacteria, several fungi and a few insects. This enzyme recognizes the N-acetylglucosamine units and, through an hydrolytic process, generates glucosamine units and acetic acid. Chemical methods are based on an alkaline treatment using a concentrated base such as sodium (NaOH) or potassium hydroxide (KOH) solution at elevated temperatures [44]. Biological deacetylation usually produces chitosan with more controlled physicochemical properties. Contrarily, the chemical treatment with NaOH can cause the degradation of the polymer, other than its deacetylation. Consequently, the time of exposure to NaOH should be limited and for that reason it is difficult to obtain chitosan with high degrees of deacetylation. As a result, chemical methods often

produce randomly deacetylated chitosan oligomers with various degrees of polymerization. However, chemical deacetylation is a shorter process and more accessible in the laboratory, and thus, more common.

The deacetylation of chitin is almost never complete and the amount of acetamide groups remaining determines the so-called “degree of acetylation” (DA - usually employed for chitin) or “degree of deacetylation” (DD - usually employed for chitosan). When the DA is higher than 50% (or the DD lower than 50%), the product is still named chitin, while when the DD is higher than 50% (or the DA lower than 50%), the product is named chitosan. Chitosan has a pKa value of 6.2, meaning that when the pH is below this value, the amino groups (NH<sub>2</sub>) of chitosan chains are protonated (NH<sub>3</sub><sup>+</sup>), and the polymer becomes cationic and soluble, while at pH above 6.2 it remains insoluble [45]. In this process, the hydronium ions (H<sub>3</sub>O<sup>+</sup>) present in aqueous acetic acid (CH<sub>3</sub>-COOH) solutions (equation 1.1) transform chitosan into a polyelectrolyte by giving a proton (H<sup>+</sup>) to the NH<sub>2</sub> group and transforming it into (NH<sub>3</sub><sup>+</sup>), following the equilibrium reaction shown in equation 1.2 [46]:



Consequently, the higher the amount of NH<sub>2</sub> groups in chitosan, the higher its solubility.

The cationic nature of chitosan is rather special. In fact, the majority of polysaccharides are usually either neutral or negatively charged when dissolved in an acidic environment. This property allows chitosan to form electrostatic complexes or multilayer structures with negatively charged polymers [47]. Besides its cationic nature, chitosan has extraordinary properties which make it an excellent candidate in the field of tissue engineering. In fact, chitosan can have different molecular weights, degrees of deacetylation, viscosities and crystallinity which highly influence its physicochemical and biological properties. The influence of the molecular weight and the degree of deacetylation on physicochemical properties of chitosan for biomedical application has been reviewed elsewhere [48]. Furthermore, chitosan presents a high number of reactive amino (NH<sub>2</sub>) and especially hydroxyl (OH) groups, which can be easily chemically modified to produce chitosan derivatives [49]. These modifications are usually made either to improve its physicochemical properties [50] or to improve its biological properties (*e.g.* creating water-soluble chitosan that allows for cell encapsulation)

[51].

### 1.3.1.2 Natural gums

Natural gums are polysaccharides mostly obtained from plants and especially from three groups: (a) the endosperm of some seeds (*e.g.* guar gum, tamarind seed gum, locust bean gum); (b) plant exudate gums (*e.g.* gum tragacanth); and (c) tree or shrub exudates (*e.g.* gum arabic, karaya gum). Plant exudates are usually produced in response to a mechanism of protection against mechanical injury or microbial injury. Besides their origin, gums can be categorized based on their surface charges as anionic (*e.g.* gellan, agar, pectin, xanthan, ), cationic (*e.g.* modified guar gum), and non-ionic (*e.g.* guar gum, tamarind gum, cellulose), or based on their structure as linear chains (*e.g.* pectin, amylose, cellulose, and locust bean gum,) and branched chains (namely short branching as guar gum and long branching as amylopectin, gum arabic and tamarind gum) [36].

Natural gums, also known as hydrocolloids, are water-soluble polysaccharides consisting of long chains of sugar-building units, largely used as thickening and gelling agents in various industrial (mainly food) and biomedical applications. The main reason behind their successful use is their ability to modify the rheology of solutions, by increasing their viscosity, even at small concentrations, and/or the mechanical properties of the final product (such as the elasticity of resulting hydrogel, membranes etc.) [52]. Some natural gums have already been tested as components of inks or bioinks. For example, gellan gum has been added as rheology enhancer to poly (ethylene glycol) diacrylate (PEGDA). The success of PEGDA as inks is determined by its rapid UV cross-linking capability. However, if at the moment of crosslink, the structure does not retain its shape, this property can not be exploited to the fullest extent. The improved rheological properties due to the inclusion of gellan gum allow for high shape retention after printing without the need for additional support, making it possible to subsequently UV crosslink for mechanically property improvement and permanent stabilization [53]. Due to their low-cost, biocompatibility, non-toxicity and the fact that they have already been used for several applications such as drug delivery [54, 55] but not as components of inks and bioinks, we focused our attention in particular on two gums, guar gum and tamarind gum, as candidates to be combined with chitosan for the development of new natural-based biomaterial inks. (*NB: at the time this thesis started, neither guar gum nor tamarin gum had been used as components of inks or bioinks. Guar gum has been combined with chitosan to develop ink formulations firstly by our group during the course of this thesis. The resulting study has been published [56] and is discussed in Chapter 3. To our knowledge, after that, only one other study concerning the combination of guar gum with gelatin for the fabrication of bioinks has been published [57].*)

*Guar Gum (GG)* is a water-soluble and non-ionic polysaccharide extracted from the seed of the guar plant: *Cyamopsis tetragonolobus* seeds. GG is composed of linear chains of  $\beta$ -(1 $\rightarrow$ 4)-D-mannan with side chains of  $\alpha$ -(1 $\rightarrow$ 6) linked galactose (Figure 1.4(A)). It has been extensively used for pharmaceutical applications and in particular for drug delivery due to its biodegradability, biocompatibility and low toxicity. In combination with other polymers, GG has been prepared in form of nano- and micro-particles or hydrogels for the controlled release of therapeutics [54]. For example, among the others, GG has been combined with chitosan, in the presence of glutaraldehyde as crosslinker, to form microspheres encapsulating the antibiotic cefadroxil. Microspheres made with a higher amount of GG showed a

slower release of cefadroxil. According to the authors, this phenomenon is due to the higher swelling ability of chitosan compared to GG, which is, in tune, responsible for a faster release [58]. For its great role in controlling the release of molecules, GG-based formulations are emerging as new promising biomaterials for designing novel drug delivery systems as well as for tissue engineering applications, including 3D bioprinting and the controlled release of growth factors.

*Tamarind gum (TG)* is derived from the endosperm of seeds of the tree *Tamarindus indica* Linna. Its chemical structure consists of a branched structure containing main and side chains (Figure 1.4(B)). The main chain consists of a linear chain of (1→4)-β-D-glucan that is partially substituted with side chains of (1→6)-α-D-xylopyranose and β-D-galactopyranosyl linked with (1→2)-α-D-xylopyranose linked (1→6) to glucose residues. TG is a high molecular weight polysaccharide (about 720-880 kDa) that forms viscous solutions when dissolved in water [59]. TG has been declared safe (non-carcinogenic) and biocompatible, which results in its extensive applications with diverse pharmaceutical dosage forms [60]. As was the case with GG, also TG has been extensively applied, in particular, in the field of drug delivery due to its high drug holding capacity [55].

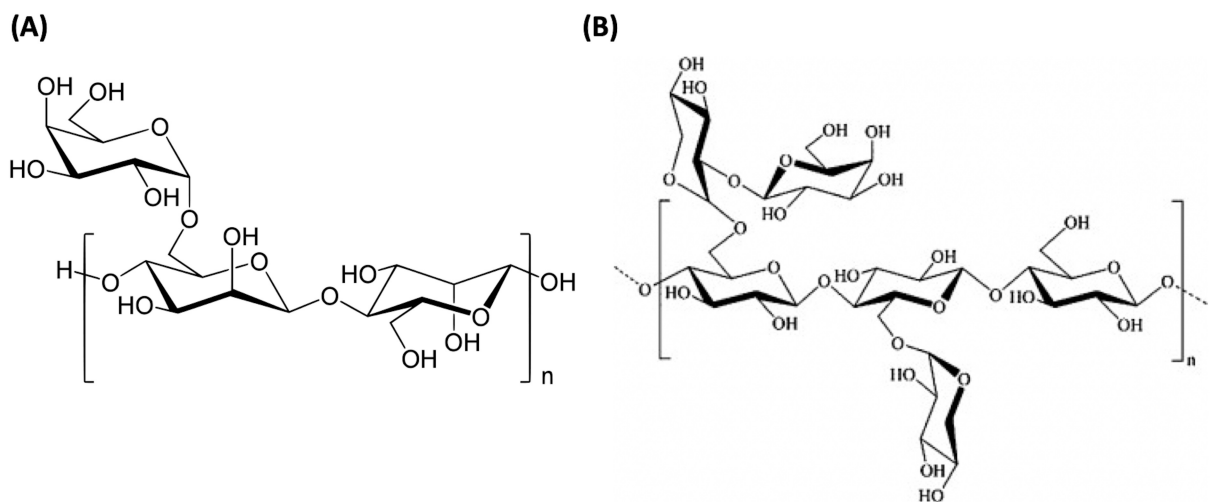


**Figure 1.4.** Chemical structures of (A) guar gum and (B) tamarind gum. Figure reused from [58] and from [59].

The ability of GG and TG to form hydrogels and modify the rheological properties of solutions makes them ideal candidates as components of a specific tissue engineering technology which is 3D bioprinting. In fact, both GG and TG present shear thinning properties [61] which represent one of the most important properties that should have inks and bioinks to be used for 3D printing. In Chapter 3 these two polysaccharides will be combined with chitosan for the development of three-dimensional constructs using an extrusion-based 3D bioprinter.

## 1.4 Growth factors

Growth factors represent the third essential component, with cells and biomaterials, of the tissue engineering “triad”. In fact, growth factors can be included within biomaterial-based

scaffolds in order to induce the proliferation and differentiation of cells seeded on the scaffold or to induce the migration of cells into an implanted acellular scaffold. In both cases, cells have to replace or regenerate a tissue. The understanding of how cells can be induced, *in vitro* or *in vivo* to form a specific tissue comes from the observation of what happens during normal development or normal wound healing [62]. Without going into details we can take as an example the normal wound healing, which is a complex process based on the coordinated interactions between molecules, including growth factors, and cells. Growth factors are endogenous signaling molecules able to influence cellular behavior and are usually expressed in a specific moment of the wound healing process and for a specific period of time [63]. An example is represented by angiogenic growth factors, such as the vascular endothelial growth factor (VEGF), which role is to promote the formation of new blood vessels from the existing ones. After injury, angiogenesis is necessary to restore the blood flow to damaged tissues and, consequently, to provide the oxygen and nutrients required to support the formation of a new tissue [64]. In some cases, once released, the growth factors bind to components of the ECM, whose role is probably to protect growth factors from degradation, and enhance their activity [65].

Considering the above, it is clear that the inclusion of growth factors within biomaterial scaffolds can significantly enhance and accelerate the formation of a new tissue *in vitro* and improve its integration *in vivo*. The emulation of natural strategies adopted to present growth factors to cells in order to maximize their actions in the fabrication of a tissue, is an active field of research that implies a deep understanding of the biology of growth factors and applies it to biomaterials design. Indeed, the precise control of the spatial and temporal release of growth factors, while preserving their bioactivity is the key to accelerate and improve the development of functional tissues. Several strategies have been developed in order to control the release of growth factors, including their encapsulation into nano- or micro-particles, or their chemical conjugation to biomaterial scaffolds, not only to protect them from degradation but also to temporally control their release [66]. 3D bioprinting offers the incredible advantage, over more traditional tissue engineering strategies which do not allow for the fabrication of micro-precise tissue-like structures, of a well-controlled spatial delivery of growth factors and/or of their delivery systems. The limitations associated with the clinical use of growth factors and the different strategies that have been adopted to spatiotemporally control their release using the technology of 3D bioprinting are the subject of a review paper, which is reported as Chapter 4 of this thesis.

## 1.5 3D bioprinting

In the previous sections we introduced the three main components of tissue engineering: cells, biomaterials and growth factors and highlighted the importance of recapitulating the complexity and heterogeneity of tissues and organs through the fabrication of scaffolds with hierarchical structural properties. In this context, the choice of the technology employed to design biomimetic scaffold is crucial. To this goal, 3D bioprinting represents one of the most promising. This technology is based on the printing of cells alone, cells contained in a liquid or viscous solution, or biomaterials without cells on the top of which cells are seeded in a second moment, with the ultimate goal of fabricating tridimensional biological structures [17, 11]. This technology has emerged to fabricate 3D tissues in the laboratory for two main applications: the first one is the fabrication of implantable tissue substitutes for the



replacement of damaged ones and the second one is the creation of “small-size” models of human tissues or organs, such as “organoids”, for the development of drugs or to improve disease knowledge [17].

3D bioprinting appeared, in the first place, with the objective of precisely locate cells alone. The first bioprinter was developed in 1988 by Klebe, which used a standard inkjet printer for the micro-positioning of cells and called this technology “Cytoscribing” [67]. Then, the interest in 3D bioprinting for the fabrication of living structures increased, especially to overcome the limitation of the size of constructs. In fact, it was already possible to grow cells in hydrogels, whose shape was given by a mold. However, with this approach, it was possible to fabricate only micro-metric structures, otherwise, the cells located in the inner part of the hydrogel would not receive oxygen and nutrients and would die [68]. In 2002 Landers *et al.* [12] presented the first example of hydrogel processed using the extrusion-based 3D printing technology with a free-form fabrication (FFF), indicating, with this term, auto-supported constructs with well-defined internal sub-structures and interconnected pores. Today, 3D bioprinting is the most attractive tissue engineering technology [11], allowing for the fabrication of high-resolution complex structures made of biomimetic biomaterials and containing multiple cell types. As mentioned above, cells may be included directly within the biomaterials and originate the so-called “bioink” or, materials may be printed and subsequently seeded with cells after printing are originate the so-called “biomaterial inks”. As a consequence, except for the cell-laden bioink, all the printed materials whose role is to support the fabrication of 3D constructs, belong to the category of biomaterial inks. Examples are the sacrificial materials that can help the bioprinting process or be used to create internal channels within printed constructs and are then removed, or structural materials, such as pillars, often made of synthetic materials, which only offer mechanical support to or within the construct and are removed before implantation [6]. 3D bioprinting also represents the main tissue engineering technology involved in personalized medicine. In fact, it is possible to acquire medical images of a patient’s damaged tissue, using magnetic resonance imaging (MRI) and computed tomography (CT) and to translate them in computer-aided design (CAD) models and STL files, which are used by the bioprinter to create tissues in a layer-by-layer manner [11].

There are three main bioprinting modalities known as inkjet-based, extrusion-based and laser-based bioprinting, (whose components are schematized in Figure 1.5) each one with its advantages and disadvantages and with different requirements for the inks and bioinks permitted.

1. **Inkjet-based bioprinting:** is based on the use of thermal or acoustic forces to eject drops of liquid onto a substrate. The small size of the droplets allows for the creation of high-resolution and intricate structures. Inkjet-based bioprinting is a non-contact technique, meaning that the risk of contamination is quite low. The main disadvantage, however, is that it only works for low viscosity bioinks with low cell density. Consequently, not only it limits the biomaterials that could be employed as bioinks, but it also prevents the fabrication of large structures, due to the higher risk of collapse. The development of low-viscosity materials able to quickly polymerize in order to stabilize the printed material is allowing the use of inkjet for the fabrication of more complex constructs [11].

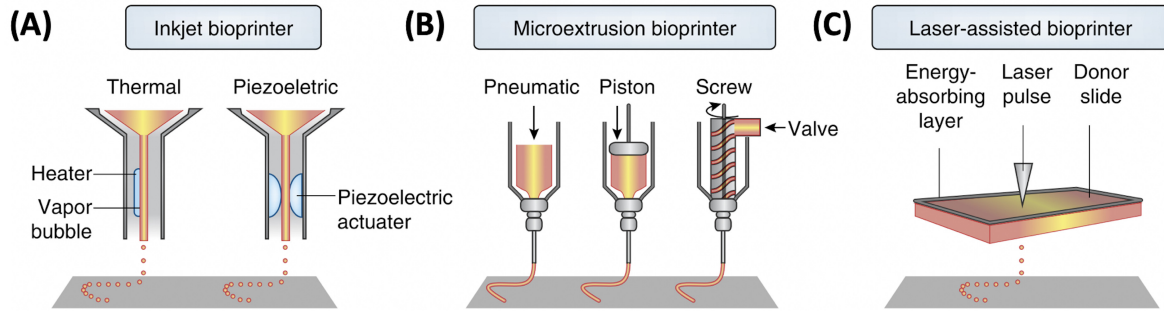


**Figure 1.5.** Components of inkjet, microextrusion and laser-assisted bioprinters. (A) Thermal inkjet printers electrically heat the printhead to produce air-pressure pulses that force droplets from the nozzle, whereas acoustic printers use pulses formed by piezoelectric or ultrasound pressure. (B) Microextrusion printers use pneumatic or mechanical (piston or screw) dispensing systems to extrude continuous beads of material and/or cells. (C) Laser-assisted printers use lasers focused on an absorbing substrate to generate pressures that propel cell-containing materials onto a collector substrate. Figure and caption reproduced with permission from [11].

2. **Extrusion-based bioprinting:** is the most common and most affordable printing modality. The extrusion of the bioink is driven by pneumatic pressure or mechanical pistons controlled by a computer that allows for the extrusion head or the stage to move in the x, y and z directions. Even if extrusion-based bioprinting has lower accuracy than other 3D bioprinting methods, its great advantage is the capability of using the broadest range of bioinks. Compared to the other methods, it allows for the printing of high viscosity bioinks which are more successful in leading to the fabrication of critical size and complex 3D structures. However, the shear stress to which cells are exposed during the extrusion might decrease their viability [11]. Besides the deposition of multiple layers on a surface exposed to air, which is often limited by the aqueous nature of bioinks, other strategies have emerged for the creation of self-supporting structures with high shape fidelity such the bioprinting into suspension baths [69] such as soft hydrogel-based [70] or granular baths [71].
3. **Laser-based bioprinting:** is based on the laser-induced forward-transfer (LIFT) technique. A laser-based bioprinter consists of three parts: a pulsed-laser source, a ribbon and the receiving substrate. The ribbon is a multilayer component containing a transparent glass, a thin layer of laser absorbing metal such as gold or titanium, and a suspended layer of bioink. The pulsed laser is used to induce the transfer of droplets of the bioink from the ribbon to the receiving substrate [72]. This bioprinting method can use high-viscosity bioinks with high cell density since it is nozzle-free. Being nozzle-free represents a great advantage since the problem of clogging with cells or materials, typical of other bioprinting technologies, is avoided. However, in order to obtain a highly precise shape, the gelation of the bioink should be fast. Since this is not often the case, laser-assisted bioprinting is a time-consuming process because of the relatively low flow rate for the crosslinking of the material. A long printing time could induce a decrease in the viability of cells encapsulated within the bioink. As a consequence, the challenge of building 3D constructs of clinically relevant size remains [73].

The technology of 3D bioprinting, independently from the method employed, has revolutionized the field of tissue engineering. Before the development of 3D bioprinting, the fabrication of critical-size constructs encapsulating cells was limited by the lack of internal porosity necessary for the oxygenation of cells encapsulated in the inner part of the constructs. 3D bioprinting made it possible to arrange the geometry of the constructs in order to generate self-supported porous structures allowing for the cells located in the center to stay alive. The presence of such pores improves the infiltration, within the constructs, of the host's vascular system promoting its vascularization and subsequent development of functional tissues. Furthermore, while more traditional tissue engineering approaches involve the fabrication of scaffolds where cells and growth factors are homogeneously seeded on, 3D bioprinting allows for a more controlled spatial and temporal distribution of cells and growth factors for the fabrication of multi-cellular and highly complex tissue structures [11].

### 1.5.1 Development and optimization of bioinks or biomaterial inks

The advent of 3D bioprinting led to the appearance of a new field of research that is the development and optimization of bioinks and biomaterial inks. Bioinks can be made of natural, synthetic or hybrid biomaterials. Natural and synthetic materials have characteristics that are usually opposite regarding their printability and cell viability. Natural-based biomaterials (*e.g.* made of natural proteins or polysaccharides) show great compatibility with cells since they usually present motifs that promote cell adhesion offering to cells an environment similar to their ECM. However, they often show poor printability. On the contrary, synthetic polymers usually show a better and controlled printability but they lack natural attachment sites that can interact with cells [52]. The concept of “printability”, although it seems intuitive, lacks a quantitative definition, which impedes the comparison among different inks or bioinks used in individual studies. In the context of extrusion-based 3D bioprinting, it could be defined as the ability of the bioink or biomaterial ink to generate objects as similar as possible to the theoretical ones (or with a high shape fidelity, itself defined as the shape retention of a single filament at a microscopic level) [7].

Printability and shape fidelity mainly depend on two parameters: the bioink properties and the printing parameters (such as the nozzle size and the speed and pressure used for extrusion). Rheological properties of bioinks, such as their viscosity, viscoelasticity and elastic recovery, are the parameters with the largest influence on printability. For example, biomaterials used as ink or bioink should have a shear thinning behavior, meaning that the viscosity has to decrease when a shear rate is applied such as its extrusion through a nozzle under applied pressure. However, after extrusion, when the shear rate ends, the viscosity of the ink should rise again in order to ensure shape retention [7]. The rheological properties and stiffness of bioinks can be optimized by tuning different parameters such as the concentration of the polymer composing the bioink or through the inclusions or crosslinkers or other components as rheology enhancers. The increase in the stiffness of a bioink usually results in improved printability. However, it could compromise the viability of encapsulated cells [7]. Previous studies identified the so-called “biofabrication window” which defines the relation between printability and the ability to maintain cells viable within the bioink [74] and is schematized in Figure 1.6.

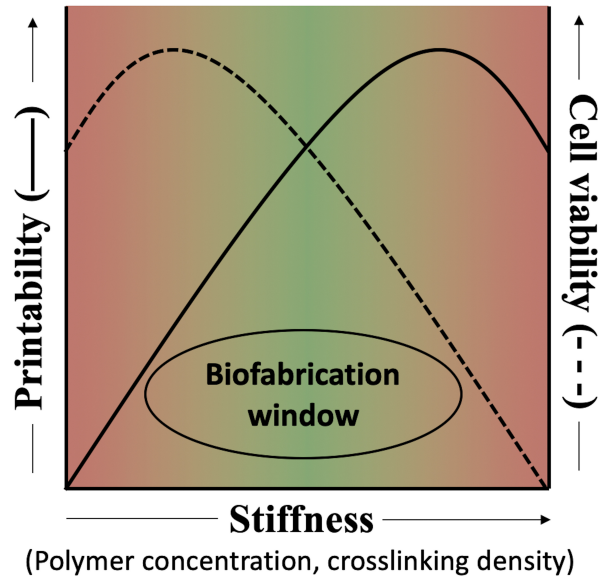


**Figure 1.6.** Schematic representation of the biofabrication window as introduced in 2013 by Malda *et al.* [74]. Figure adapted with permission from [74].

This graph shows that an increase in the stiffness of the bioink corresponds to an increase in printability until a certain point. In fact when the bioink became too stiff, it will not be easily extruded from the nozzle. On the contrary, when the stiffness of the bioink is low (and consequently the density of the polymer network is low) cell viability increases since the low density of the polymer network allows for cells to migrate and proliferate without mechanical impediments. However, if the stiffness is too low, it prevents the creation of a three-dimensional environment and thus, it prevents the correct development of a functional tissue.

Concerning the printing parameters, three of them are directly responsible for the shape fidelity: the size of the nozzle, the printing head speed and the pressure applied to extrude the bioink, which are summarized in Figure 1.7 (A). Nozzles can have different gauge sizes. Speed and pressure applied can be tuned from lower to higher values which depend on the bioprinter. If we aim to print a structure with a specific filament size, for example, 200  $\mu\text{m}$  (Figure 1.7 (B)), we can tune these three parameters knowing that, if we fix two parameters and change the third one we would obtain that: i) bigger nozzle size results in an increase in the filament size, ii) an increased head speed results in a smaller filament size and iii) an increased pressure results in a larger filament size (Figure 1.7 (C)). In some cases, thermoresponsive materials such as gelatin, are included as components of the ink or bioink to improve their gelation state [75, 76]. In that case, the temperature of bioprinting should be considered for the optimization process as an additional parameter. After printing with different combinations of these parameters, the filament size can be evaluated and compared to the theoretical one (*e.g.* 200  $\mu\text{m}$ ) in order to select the optimal combination of parameters for a specific bioink.

However, the optimization of the bioprinting parameters does not mean that the bioink can then lead to auto-supported 3D structures with high shape fidelity. Due to the lack

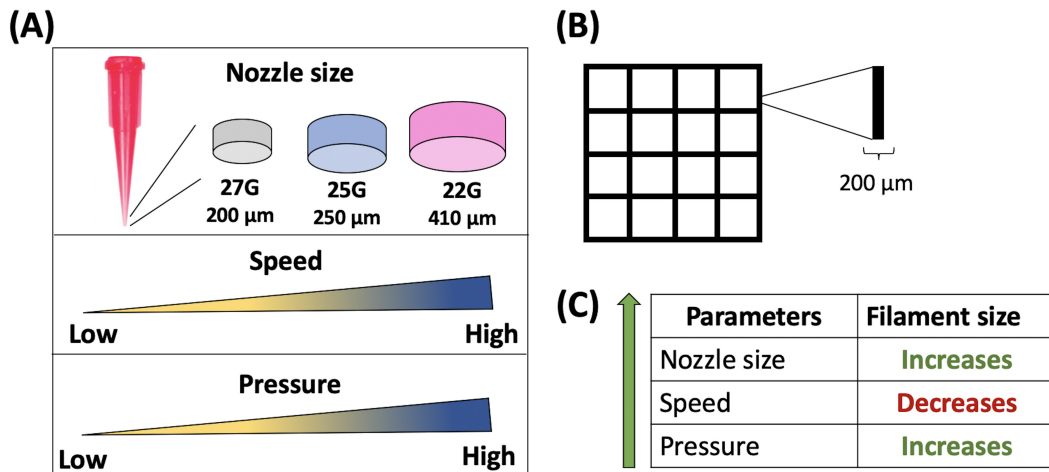


**Figure 1.7.** Printing parameters that affect the printability. A) Schematization of the three printing parameters: nozzle size, printing speed and applied pressure B). Representation of a hypothetical printed construct with a filament size of 200 μm. C) Effect of the increase of nozzle size, printing speed and applied pressure on the size of the printed filament.

of universal quantitative measures of their printability and to the fact that bioink optimization can be time-consuming, several methods have been proposed in order to simplify the identification of ideal bioink candidates. For example, some of them rely on the study of the rheological properties of bioink solutions before bioprinting [77] while others evaluate the quality of the printed objects (in terms of filament uniformity, pore geometry etc.) and still others suggest more quantitative or semi-quantitative methods for the evaluation of printability which have been excellently reviewed elsewhere [78, 7]. Here we will present only a few examples of these methods and in particular the ones that have been used in this thesis.

Ouyang *et al.* [79] proposed a method to determine the ideal bioink candidate and a semi-quantitative method to assess the bioink printability. In order to do that, they firstly evaluated the gelation state of their bioink, composed of alginate and gelatin, by defining it as in an under-gelation, proper-gelation or over-gelation state. This first evaluation of the bioink can be done by extruding a small quantity of bioink from the nozzle (Figure 1.8, top). If at the exit of the nozzle the bioink forms a drop, it means that the bioink is in an under-gelation state (too liquid). The formation of a smooth and uniform filament means that the bioink is in a proper gelation state while the formation of an irregular filament means that the bioink is in an over-gelation condition. Subsequently, they proposed to use the bioink to print 2 layers grid structures with square holes and look at the outcomes. If the bioink was in an under-gelation state, it would result in a grid whose pores would have a circular shape, if the bioink was in a proper-gelation state it would result in a grid with square pores, while if the bioink was in an over-gelation state it would result in a grid with irregular square edges (Figure 1.8, bottom). In order to quantify the results they proposed to measure the perimeter ( $L$ ) and the area ( $A$ ) of each pore and to apply the following formula in order to measure the printability value ( $Pr$  value):

$$Pr = \frac{L^2}{16A} \quad (1.3)$$

This measure can result in a value inferior, equal or superior to 1.  $Pr=1$  means that

the ink has the ideal gelation and subsequent ideal printability since it is able to create perfect square holes. Contrarily,  $Pr < 1$  means that the ink is too liquid and that holes have a more circular shape while  $Pr > 1$  means that the ink is over-gelled. Based on their experience, they suggest that bioinks should have a  $Pr$  value is comprised between 0.9 and 1.1.

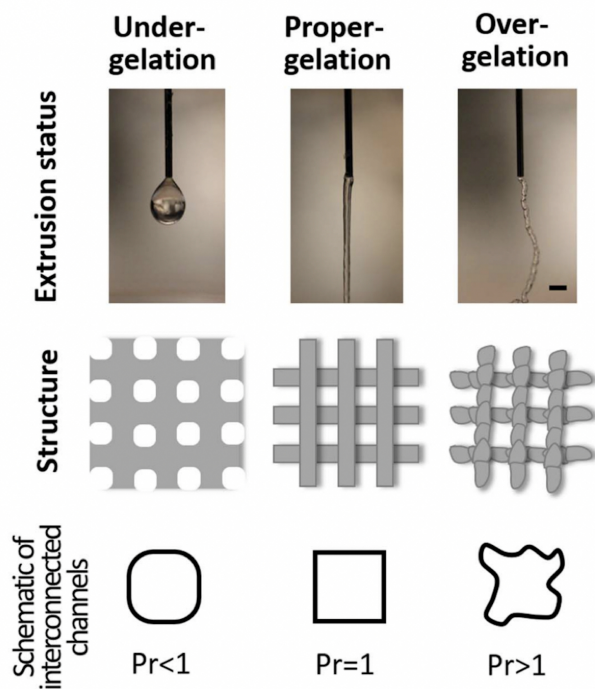


**Figure 1.8.** Evaluation of printability ( $Pr$ ) under three typical gelation statuses, namely under-, proper- and over-gelation. Scale bar is 1 mm. Figure reproduced from [79].

Paxton *et al.* [80], described a two-step method for the assessment of printability of inks for bioprinting. The first step is a screening of the ink formulations based on the evaluation of the shape of the extruded solution and the ability to print in three dimensions. The second step is based on the evaluation of the rheological properties of the ink in terms of yield point, shear-thinning properties and recovery behavior. The first screening of a material, to assess its “printability”, focuses on its ability to form fibers, rather than droplets, similarly to the method described above and proposed by Ouyang *et al.* [79]. The formation of fibers is then usually correlated to the ability of the material to be deposited layer-by-layer without collapsing, to form 3D constructs. The second method is based on the study of 3 rheological parameters which are: (A) a shear stress ramp to test if the material exhibits a yield stress, below which the material behaves like a solid rather than a liquid; (B) a shear viscosity tests to investigate the shear-thinning properties of the materials and (C) a recovery test applying an alternation of high and low shear rates to the material to see how it recovers after being exposed to high shear stress. However, all these rheological evaluations are not absolute criteria for the evaluation of printability nor they define any quantitative measure for printability. In fact, rheological measurements explain the behavior of a material under defined parameters, but due to the complexity and variability of printable materials, it is difficult to standardize these results.

Due to the absence of universal rules for the evaluation of bioinks printability, the method employed by each researcher is usually chosen based on its needs.

### 1.5.2 Chitosan-based bioinks

Biomaterials in form of gels (usually hydrogels), or more often in form of gel precursors which are crosslinked to form gels after printing, are among the most used biomaterials as inks or bioinks for 3D bioprinting applications [6]. Chitosan can form gels through different strategies such as the polyelectrolyte complexation, ionotropic gelation and physical or chemical crosslinking-mediated gelation [81]. Polyelectrolyte complexation is based on the association of particles, molecules or macromolecules with opposite charges. Since chitosan is the only natural polysaccharide to be charged positively, it is often employed for the formation of polyelectrolyte complexes. Ionotropic gelation is mediated by molecules such as tripolyphosphate (TPP) and  $\beta$ -glycerol phosphate ( $\beta$ -GP) and is based on the electrostatic interaction between the cationic polymer chains with the anionic TPP or  $\beta$ -GP. Chemical cross-linking is often performed with glutaraldehyde or genipin, with genipin preferred over glutaraldehyde due to its lower toxicity [82]. Physical cross-linking can be obtained by treating chitosan with a basic agent such as sodium hydroxide (NaOH) or potassium hydroxide (KOH). While this last method allows for an easy, fast and complete gelation, it reduces the control of some properties of chitosan gels such as their swelling behavior, porosity and mechanical properties, for example their strength and elasticity [81].

Despite its attractive properties of biodegradability, biocompatibility and low cost, chitosan has limited application as a bioink compared to other naturally-derived biomaterials, due to its limited solubility in water, which prevents the encapsulation of cells and its low stiffness, which usually leads to a poor printability and shape fidelity [45]. Concerning the limited solubility in water, it has to be noticed that water-soluble chitosan can be developed. For example, Lee *et al.* prepared a bioink through the conjugation of catechol to chitosan, creating a mussel-inspired adhesive polymer mainly to increase the adhesion of cells, since chitosan lack cell attachment sites. However, this modification simultaneously allowed for the encapsulation of cells since the modified chitosan can be dissolved at neutral pH [83]. Tonda *et al.* [84], methacrylated the chitosan to create a photocrosslinkable bioink and included  $\beta$ -glycerol phosphate salt ( $\beta$ -GP) to induce ionotropic gelation. The inclusion of  $\beta$ -GP allowed to adjust the pH around 7 by allowing the encapsulation of cells. This property has been exploited also by Demirtaş *et al.* [85] who added  $\beta$ -GP to a chitosan-hydroxyapatite ink to be able to include cells, and in particular of pre-osteoblasts, for bone tissue engineering applications. To do that, they firstly dissolved chitosan in an acetic acid solution, then mixed it with  $\beta$ -GP which led to a pH of 6.7. A pH of 7 was then reached by adding sodium hydroxide (NaOH). This strategy was adopted because NaOH leads to a fast gelation of chitosan while  $\beta$ -GP allows for a slower and temperature-dependent gelation that starts at around 32°C and leads to complete gels at 37°C.  $\beta$ -GP has also been included in the formulation of the only commercialized chitosan-bioink CHITOINK. Alternatively, other strategies can be adopted to include cells in a scaffold besides their encapsulation prior to fabrication. In fact, chitosan-based hydrogels or 3D printed constructs can be neutralized after processing, for example with NaOH, which plays a double role of neutralizing and gelling agent.

Concerning the printability of chitosan, some of the above-mentioned strategies used to allow for cell encapsulation, such as the inclusion of  $\beta$ -GP or other crosslinkers, also allow for a better printability of chitosan by modifying its rheological properties and gelation state. Another way to improve chitosan printability is to combine it with other macromolecules. As already mentioned, being the only cationic polysaccharide it can easily interact with negatively charged macromolecules. Consequently, it has been successfully combined with alginate [86] and gelatin [87]. The combination of chitosan with these materials usually leads only to more viscous solutions which can be printed more efficiently but also to improved mechanical properties of the bioprinted constructs. Chitosan has also been combined with other molecules, not necessarily of opposite charge, in order to improve its printability. For example, it has been combined with potato starch (which is made of amylose and amylopectin). Among the five combinations of chitosan-starch tested for biocompatibility, a 50:50 (or 1 to 1) starch-chitosan blend was determined to be the optimum bio-ink in terms not only of printability but also of biocompatibility of neural cells [88]. The combination of chitosan with other molecules is often advantageous because it can lead to a stable construct with no need for chemical crosslinking agents.

However, good printability does not necessarily mean good shape fidelity or ability to print complex 3D structures. In fact, after a few layers, the structure could start to collapse. One way to prevent the collapse of chitosan-based structures is to take advantage of its rapid gelation when treated with basic solvents, such as sodium hydroxide (NaOH), and perform the bioprinting into the so-called “gelation baths”. Aside from allowing for its fast gelation, NaOH is responsible for the neutralization of chitosan, which is necessary if a subsequent cell seeding is intended. Ang *et al.* [89], for example, extruded a bioink made of chitosan and hydroxyapatite into a dispensing medium made of NaOH and ethanol. The neutralization of the chitosan immediately after extrusion allows for the formation of a gel-like precipitate, keeping the scaffold in the desired shape. In another study, Elviri *et al.* [90], in order to keep the structure shape, bioprinted a chitosan bioink on a freezing plate and then transferred the frozen chitosan structures into a coagulation bath, made of a solution of KOH.



## Chapter 2

# Extraction and characterization of chitin and chitosan from *Cicada orni* sloughs

## Extraction et caractérisation de la chitine et du chitosan des mues de *Cicada orni*

Le premier objectif de cette thèse est l'identification d'une source alternative de chitine et chitosane. Notre choix s'est porté sur les mues de cigales pour deux raisons principales. Tout d'abord, l'intérêt des chercheurs pour les insectes comme source de chitine est en forte augmentation ces dernières années en tant qu'alternative aux déchets de la mer, qui représentent, à ce jour, la principale source commerciale de chitine et notamment de son dérivée le chitosane [91]. De plus, cette source a été peu étudiée mais les quelques études présentes dans la littérature suggèrent que les mues de cigales représentent une source importante de chitine [92, 93, 94, 95]. En effet, comme rapporté par Sajomsang et Gonil [93], qui ont été les premiers à montrer la possibilité d'extraire la chitine des mues de cigales, 36,6% de la masse de cette source est constituée de chitine, 39,8% de protéines et 11,7% de minéraux. La seule autre information disponible dans la littérature concernant la composition des mues de cigales est la teneur totale en chitosane obtenu à partir de chitine extraite des mues de cigales achetées chez Shanghai Traditional Chinese Medicine Co, mesurée par Luo *et al.* [92] qui est de 28,2%. Ces pourcentages de chitine sont relativement élevés comparés aux autres espèces (se référer à "Table 1" de l'article "Extraction and Physicochemical Characterization of Chitin from *Cicada Orni* Sloughs of the South-Eastern French Mediterranean Basin").

L'extraction de chitine et sa transformation en chitosane se fait en quatre étapes: 1) la déminéralisation de la source primaire pour l'élimination des minéraux (principalement le carbonate de calcium ou  $\text{CaCO}_3$ ); 2) la déprotéinisation pour l'élimination des protéines; 3) la décoloration pour l'élimination des pigments qui sont responsables de la coloration de la cuticule des insectes; 4) la désacétylation pour l'élimination des groupes acétyles et l'obtention de chitosane [96]. Afin de sélectionner le protocole le plus approprié pour l'extraction de la chitine et sa désacétylation pour produire du chitosane à partir des mues de cigale, nous avons évalué tous les protocoles utilisés pour extraire de la chitine ou ses dérivés des cigales, de leur mues ou de leurs cuticules. Au moment de la rédaction de cette thèse, la littérature ne comporte que six travaux concernant l'extraction de chitine ou de ses dérivés à partir des cigales et parmi eux, seulement quatre spécifiquement à partir des mues de cigale.

Toutes les extractions (résumées dans le tableau 2.1) ont été réalisées à l'aide d'acide chlorhydrique (HCl) pour l'élimination des minéraux et de la soude (NaOH) pour l'élimination des protéines. L'élimination des pigments n'est pas toujours réalisée. Quand c'est le cas, cela a été effectué par différents agents décolorants, comme l'hypochlorite de sodium (NaClO), le permanganate de potassium (KMnO<sub>4</sub>) ou un mélange méthanol (CH<sub>3</sub>OH) et chloroforme (CHCl<sub>3</sub>). La désacétylation de la chitine n'a été effectuée que par un seul auteur à partir des mues de cigale et, dans ce cas, elle a été obtenue par un traitement prolongé avec de la soude (NaOH).

Source	Déminéralisation	Déprotéinisation	Décoloration	Désacétylation	Ref
Mues de cigale	1M HCl 30°C (2 heures)	1M NaOH 90°C (2 heures)	2% KMnO <sub>4</sub> (2 heures) + 2% C <sub>2</sub> H <sub>2</sub> O <sub>4</sub> (2 heures)	60% NaOH (100°C 8 heures)	[92]
Mues de cigale	1N HCl 100°C (20 min)	1N NaOH 80°C (36 heures) + 0,4% Na <sub>2</sub> CO <sub>3</sub> (12 heures)	6% NaClO	ND	[93]
Mues de cigale	0,5M HCl TA (3 heures)	1M NaOH 100°C (2 heures)	ND	ND *	[94]
Mues de cigale	7% HCl TA (3 heures)	10% NaOH 60°C (24 heures)	ND	ND **	[95]
Cuticules de cigales	1M HCl 65°C (12 heures)	1M NaOH 65°C (12 heures)	ND	ND * * *	[97]
Cigales entières	2M HCl 100°C (2 heures)	10% NaOH 60°C (2 heures)	H <sub>2</sub> O, CH <sub>3</sub> OH, CHCl <sub>3</sub> (2 heures)	ND	[98]

**Table 2.1.** Résumé des protocoles utilisés pour l'extraction de la chitine ou de ses dérivés à partir des mues de cigale ou de leur du corps entier. *Abréviations* : HCl : acide chlorhydrique, NaOH : hydroxyde de sodium, Na<sub>2</sub>CO<sub>3</sub> : carbonate de sodium, NaClO : hypochlorite de sodium, KMnO<sub>4</sub> : permanganate de potassium, C<sub>2</sub>H<sub>2</sub>O<sub>4</sub> : acide oxalique, CH<sub>3</sub>OH : méthanol, CHCl<sub>3</sub> : chloroforme, TA : température ambiante, ND : données non disponibles.

\* L'extraction a été réalisée afin d'obtenir la D-glucosamine.

\*\* L'extraction a été réalisée afin d'obtenir des chitooligosaccharides.

\*\*\* Les cigales entières ont été traitées avec HCl et NaOH pour pouvoir observer l'organisation des fibres de chitine directement dans les cuticules des insectes par SEM.

Le choix des conditions utilisées pour les traitements de déminéralisation, déprotéinisation et désacétylation est très important. En effet, ces traitements, notamment les deux derniers, sont responsables de la qualité et des caractéristiques physicochimiques des produits finaux. Concernant l'étape de déminéralisation, il a été reporté que le temps nécessaire à l'élimination complète des minéraux, en traitant la source avec du HCl, est entre 2 et 3 heures [99]. Alors qu'aucune information n'est rapportée dans la littérature, à notre connaissance, concernant les effets d'un temps de déminéralisation prolongé, de nombreuses études ont été effectuées pour évaluer les effets des différentes conditions de déprotéinisation et de désacétylation sur la qualité de la chitine et du chitosane. En effet, un traitement prolongé au NaOH pour permettre la déprotéinisation, pourrait entraîner une désacétylation partielle de la chitine et une hydrolyse du polymère, abaissant son poids moléculaire [100]. Par conséquent, les informations obtenues concernant les propriétés de la chitine extraite pourraient dépendre du

processus d'extraction, ce qui empêcherait de tirer des conclusions. L'étape de désacétylation s'effectue avec un traitement prolongé au NaOH, à des hautes températures, pour permettre l'élimination des groupements acétyles contenus dans la chitine pour la transformer en chitosane. Toutefois, ce traitement est également responsable de l'hydrolyse du polymère et, en raison de ça, devrait être limitée.

En raison des considérations exposées ci-dessus, nous avons choisi d'utiliser pour nos études le protocole proposé par Luo *et al.* [92]. Ce chapitre présente deux articles. Le premier concerne l'extraction et caractérisation physicochimique de la chitine extraite des mues de cigale récoltées en 2017. Le deuxième compare la chitine extraite et caractérisée dans le précédent article avec celle extraite de mues de cigales récoltées en 2019 et 2020 ainsi que sur la transformation ultérieure de la chitine en chitosane.

## 2.1 Extraction and Physicochemical Characterization of Chitin from *Cicada orni* Sloughs of the South-Eastern French Mediterranean Basin

*The content of this part of the chapter is identical to the following published work:*



**Title:** Extraction and Physicochemical Characterization of Chitin from *Cicada orni* Sloughs of the South-Eastern French Mediterranean Basin

**Authors:** Aurelia Poerio, Chloé Petit, Jean-Philippe Jehl, Elmira Arab-Tehrany, João F. Mano and Franck Cleymand

**Reference:** Molecules 2020, 25(11), 2543 - Published: 29 May 2020

Article

# Extraction and Physicochemical Characterization of Chitin from *Cicada orni* Sloughs of the South-Eastern French Mediterranean Basin

Aurelia Poerio <sup>1</sup>, Chloé Petit <sup>1</sup>, Jean-Philippe Jehl <sup>1</sup>, Elmira Arab-Tehrany <sup>2</sup>, João F. Mano <sup>1,3</sup>   
and Franck Cleymand <sup>1,\*</sup> 

<sup>1</sup> Jean Lamour Institute, University of Lorraine, UMR 7198 CNRS, 2 allée André Guinier-Campus Artem, BP 50840, F-54011 Nancy CEDEX, France; aurelia.poerio@univ-lorraine.fr (A.P.); chloe.petit9@etu.univ-lorraine.fr (C.P.); jean-philippe.jehl@univ-lorraine.fr (J.-P.J.); jmano@ua.pt (J.F.M.)

<sup>2</sup> Laboratoire Ingénierie des Biomolécules, University of Lorraine, TSA 40602, F-54518 Vandoeuvre-lès-Nancy, France; elmira.arab-tehrany@univ-lorraine.fr

<sup>3</sup> Department of Chemistry, CICECO—Aveiro Institute of Materials, University of Aveiro, 3810-193 Aveiro, Portugal

\* Correspondence: franck.cleymand@univ-lorraine.fr

Academic Editors: Mohamed Samir Mohyeldin, Katarina Valachová and Tamer M Tamer

Received: 3 May 2020; Accepted: 25 May 2020; Published: 29 May 2020



**Abstract:** Chitin is a structural polysaccharide of the cell walls of fungi and exoskeletons of insects and crustaceans. In this study, chitin was extracted, for the first time in our knowledge, from the *Cicada orni* sloughs of the south-eastern French Mediterranean basin by treatment with 1 M HCl for demineralization, 1 M NaOH for deproteinization, and 1% NaClO for decolorization. The different steps of extraction were investigated by Fourier Transform Infrared Spectroscopy (FTIR), X-ray Diffraction (XRD), Thermogravimetric Analysis (TGA), and Scanning Electron Microscopy (SEM). Results demonstrated that the extraction process was efficiently performed and that *Cicada orni* sloughs of the south-eastern French Mediterranean basin have a high content of chitin (42.8%) in the  $\alpha$ -form with a high degree of acetylation of  $96\% \pm 3.4\%$ . These results make *Cicada orni* of the south-eastern French Mediterranean basin a new and promising source of chitin. Furthermore, we showed that each step of the extraction present specific characteristics (for example FTIR and XRD spectra and, consequently, distinct absorbance peaks and values of crystallinity as well as defined values of maximum degradation temperatures identifiable by TGA analysis) that could be used to verify the effectiveness of the treatments, and could be favorably compared with other natural chitin sources.

**Keywords:** *Cicada orni* sloughs; chitin; extraction; physicochemical characterization

## 1. Introduction

Chitin is a copolymer of *N*-acetyl-D-glucosamine and D-glucosamine units linked with  $\beta$ -(1–4) glycosidic bond, composed predominantly of *N*-acetyl-D-glucosamine units and represents the second most abundant polysaccharide after cellulose [1]. Due to their excellent properties, including biocompatibility, nontoxicity [2], and biodegradability [3], chitin and its derivatives, such as chitosan (deacetylated form of chitin), have recently become of great interest for medical and pharmaceutical applications [4,5]. Even though chitosan is mostly used for biomedical applications due to its higher solubility in water and other traditional solvents such as acetic acid [6], chitin can be solubilized in some other solvents, such as ionic liquids [7,8]. Due to the versatile properties of the material, it can be used to fabricate scaffolds [3], hydrogels [9], or microspheres [10], showing promising physicochemical, mechanical, and biological properties for different applications, such as in the biomedical field for wound healing [11], vascularization [12], and bone repair [7]. Chitin represents the primary structural

component of cell walls in fungi and of the exoskeletons of arthropods, such as crustaceans and insects [1]. Some species that belong to these subphyla are periodically forced to replace their old cuticle with a new one in a process called ecdysis. The lost cuticle is mainly made of chitin, but also of proteins and calcium carbonate, creating a rigid structure with the role of protecting the inner soft tissues from injury [13]. Therefore, these cuticles can represent a source of chitin. Depending on the source, the chitin can exist in three different forms:  $\alpha$ -,  $\beta$ -, and  $\gamma$ -chitin that present an antiparallel, parallel, and alternated arrangements of polymer chains, respectively [14].  $\alpha$ -chitin is mostly found in fungi [15], arthropod exoskeleton, and shells of crustaceans [1],  $\beta$ -chitin is mostly found in squid pens [16], and  $\gamma$ -chitin is mostly found in the beetle family Lucanidae [17]. Depending on the source and the extraction conditions, the obtained chitin can have different degree of acetylation (DA), molecular weight ( $M_w$ ) and crystallinity index (CrI), which influence its physicochemical and biological properties and therefore its applications [18]. Several methods have been developed to extract chitin from different natural sources, generally following a common protocol: the elimination of minerals (demineralization), proteins (deproteinization), and pigments (decolorization) until the final product: the chitin. These extraction methods can have either a biological or chemical nature [19]. Biological extraction methods are based on the use of lactic acid-producing bacteria for the demineralization, thanks to the reaction of lactic acid with calcium carbonate and the subsequent formation of calcium lactate that can be removed by precipitation, while the deproteinization is mainly based on the use of proteolytic bacteria, which produce proteases that eliminate proteins [20]. Interestingly, some bacteria have shown the advantage of taking part in both the deproteinization and demineralization processes [21]. Chemical extraction methods are the most used in both industrial and laboratory production and involve an acid treatment, mostly with hydrochloric acid (HCl) ranging from 0.5 to 2 M, to dissolve the calcium carbonate (demineralization), followed by alkaline treatment with sodium hydroxide (NaOH) to dissolve proteins (deproteinization) [22]. A recent alternative to the classic chemical extraction method is microwave-assisted extraction, which is based on the use of a different energy source to accomplish the same processes of demineralization, deproteinization, and decolorization, allowing enhanced reaction rates [23], but less information is available in the literature. Although chemical treatments can affect the physicochemical properties of the extracted chitin more than the biological ones, the short time of processing compared to the biological methods makes them the most commonly used treatments [18]. In industrial processing, chitin is mainly extracted from crustaceans (crab and shrimp shells), but different studies have demonstrated that chitin extracted from different sources has distinct characteristics [24]. For example, the chitin extracted from the cuticle of insects has lower levels of inorganic material compared to crustacean shells, making the demineralization process and the subsequent deacetylation process easier [25]. Even lower levels of inorganic materials are present in chitin extracted from fungal sources, making, in some cases, the demineralization process unnecessary [26,27]. Differences can also be present between the two sexes of the same species, such as in Grasshopper, where the chitin content is higher in males than female [28]. For this reason, it is important to characterize the chitin extracted from new sources. Furthermore, because of the high costs and increased demand, new sources of chitin are needed [29]. Cicadas are insects that belong to the order of Hemiptera and to the superfamily of Cicadoidea that lives in temperate climates [30]. *Cicada orni* represents the most abundant species of cicada in France (representing the 27% of all cicada species identified in the country), and especially in the south of France [31]. Despite the absence of updated information, there is no evidence of a decrease in the abundance of cicadas in the south of France [32]. The annual presence of *Cicada orni* could allow us to expect similar quantities of chitin every year. Their sloughs represent an important source of chitin. Extraction of chitin from cicada has been reported by a limited number of studies [30,33–37]. The aim of this study was not only the extraction and physicochemical characterization of the chitin obtained from *Cicada orni*, but, for the first time, we propose a detailed analysis of all the steps of the extraction process. In this study, we used a slightly modified version of Luo et al.'s extraction protocol [33]. The physicochemical properties of

chitin were characterized by Fourier transform infrared spectroscopy (FTIR), X-ray diffraction (XRD), thermogravimetric analysis (TGA), and scanning electron microscopy (SEM).

## 2. Results and Discussion

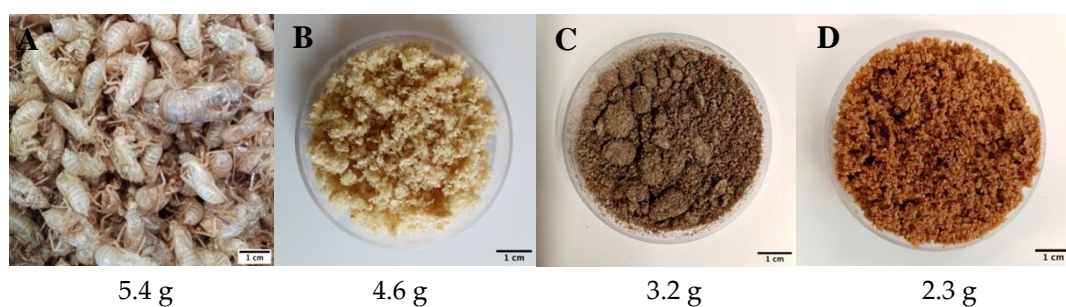
### 2.1. Chitin Extraction

Figure 1 shows pictures of the samples corresponding to all the steps of chitin extraction with their relative weights after each step. Raw material corresponds to cicada sloughs washed and dried at 50 °C for 24 h and represents the initial quantity (5.4 g). The decolorized samples correspond to the final product chitin. After each step, the powder was dried and weighed, and the difference of weight before and after the demineralization and deproteinization processes was used to calculate, as described in Equation (2), the percentage content of minerals and proteins present in the raw material. The mineral and protein contents were estimated to be 14.8% and 30.4%, respectively. The chitin content (%) of *Cicada orni* sloughs of the south-eastern French Mediterranean basin studied, defined in the following as *Cicada orni* (CO), and calculated using the Equation (1), was 42.6%. The chitin, protein, and mineral content of *Cicada orni* sloughs are similar to the only reported study on chitin extraction from cicada sloughs. According to Sajomsang and Gonil [35] cicada sloughs consist of approximately 37% chitin, 40% proteins, and 12% minerals. Only one other study reported the chitin content of cicada but, this time, from the whole body of six cicada species collected from the Mediterranean region of Turkey. The chitin content was in the range of 4.97–8.84% [30]. Table 1 summarizes some of the chitin content from different sources. The chitin content obtained in this study is higher compared to other sources, (Table 1), including seafood, which represent the primary sources of chitin. According to these results, extracting chitin from cicada sloughs offers the advantage of the production of higher quantities of final product for a given initial source biomass. However, a disadvantage of this source of chitin is that its availability is limited to a few months of the year. Comparable chitin contents have been reported for squid gladius but, in that organism, the chitin is type  $\beta$  [38].

**Table 1.** Chitin content from different sources.

Source	Chitin Content %	Ref.
<i>Cicada orni</i> sloughs (this study)	42.6	
Mushrooms	5.9–7.4; 4.31–9.66; 1.87–6.93	[15,39,40]
Grasshopper	4.71–11.84	[28]
Whole cicada body	4.97–8.84	[30]
Cicada sloughs	37	[35]
Squid gladius <sup>1</sup>	40–42; 31.27; 31	[37,41,42]
House cricket	4.3–7.1	[43]
Worm of giant flour	4.77–5.43	[44]
Colorado potato beetles	20	[45]
Beetle ( <i>H. parallela</i> )	15	[44]
Shrimp wastes	10.13; 3.12–17.36; 7.2	[46–48]
Crab shells	27.4; 17.35–20.62	[48,49]
Brine shrimp cysts	29.3–34.5	[50]
Hornet ( <i>Vespa velutina</i> )	11.7	[51]

<sup>1</sup> Chitin extracted from squid gladius is  $\beta$ -chitin.



**Figure 1.** Schematic illustration of the raw material and all the other samples after the extraction steps. The weight of the raw material (A) after washing and drying it in the oven at 50 °C for 24 h was 5.4 g. The weight of dried demineralized (B), deproteinized (C), and decolorized samples (chitin-D) was 4.6, 3.2, and 2.3 g, respectively.

## 2.2. FTIR Analysis

Since chitin is a copolymer of *N*-acetyl-*D*-glucosamine and *D*-glucosamine, DA is an important factor used to measure the quality of chitin, being obtained from the ratio of acetylated group (*N*-acetyl-*D*-glucosamine) to deacetylated (*D*-glucosamine) amino groups [15]. FTIR spectra were used to (1) to analyze the demineralization, deproteinization, and decolorization processes, (2) to characterize the extracted chitin, and (3) to calculate the degree of acetylation.

Figure 2 shows the FTIR spectra of raw material, demineralized, deproteinized, and decolorized samples. The trend of the absorbance of all samples is similar to the typical trend of chitin [52]. There is no remarkable difference between raw material and demineralized sample spectra. According to Gbenezor, [53], virgin crab and shrimp shell spectra present typical peaks for  $\text{CaCO}_3$  at 1473 and 874  $\text{cm}^{-1}$  and 1443 and 874  $\text{cm}^{-1}$ , respectively, and these peaks reduced in intensity after demineralization with 1 M HCl. Raw material spectra present only small peaks at these wavelengths. The absence of these peaks might be due to the lower mineral content cicada sloughs (12–14%) [35] compared with shrimp (30–40%) [34,48] and crab shells (30.3–44%) [14,48]. Instead, there are differences between the demineralized and deproteinized samples. According to Hassainia,  $\alpha$ -chitin presents two absorption peaks at about 1660 and 1627  $\text{cm}^{-1}$  (due to the C=O stretching vibration secondary amide stretch of the amide I), while  $\beta$ -chitin presents only one band at 1656  $\text{cm}^{-1}$  [15]. After deproteinization, the presence of two distinct peaks at about 1650 and 1621  $\text{cm}^{-1}$  confirms  $\alpha$ -chitin structure. These peaks are attributed to vibration modes of amide I, so their resolution in two separate peaks is probably due to the elimination of proteins [54]. In fact, only one peak is present in the raw material and demineralized sample. Deproteinized and decolorized samples present the same peaks, proving that pigments cannot be identified from these spectra. The degree of acetylation (DA) was calculated using the Brugnerotto expression (Equation (4)), which was the most reliable method in previous studies and in agreement with H-NMR and C-NMR data [55]. The peak at 1320  $\text{cm}^{-1}$  is specific of *N*-acetyl glucosamine and it is used for the determination of the DA with the peak at 1420  $\text{cm}^{-1}$  [52]. DA was calculated using the average of the absorption values at 1420 and 1320  $\text{cm}^{-1}$  (see Figure S1 in Supplementary Materials for details about the baselines used to calculate the DA). The resulting DA was  $96.3 \pm 3.4$ . Table 2 summarizes the DA and crystallinity index (CrI) (that will be discussed below) of chitin from different sources. The obtained DA was similar to that obtained by Sajomsang and Gonil from cicada sloughs [35] and comparable to that reported in the literature from different sources (Table 2). The DA is the parameter that affects the solubility of chitin and its derivatives the most. In fact, when the DA is below 50%, the product is already called chitosan, and its solubility in acidic solutions increases with the reduction of the DA [56].



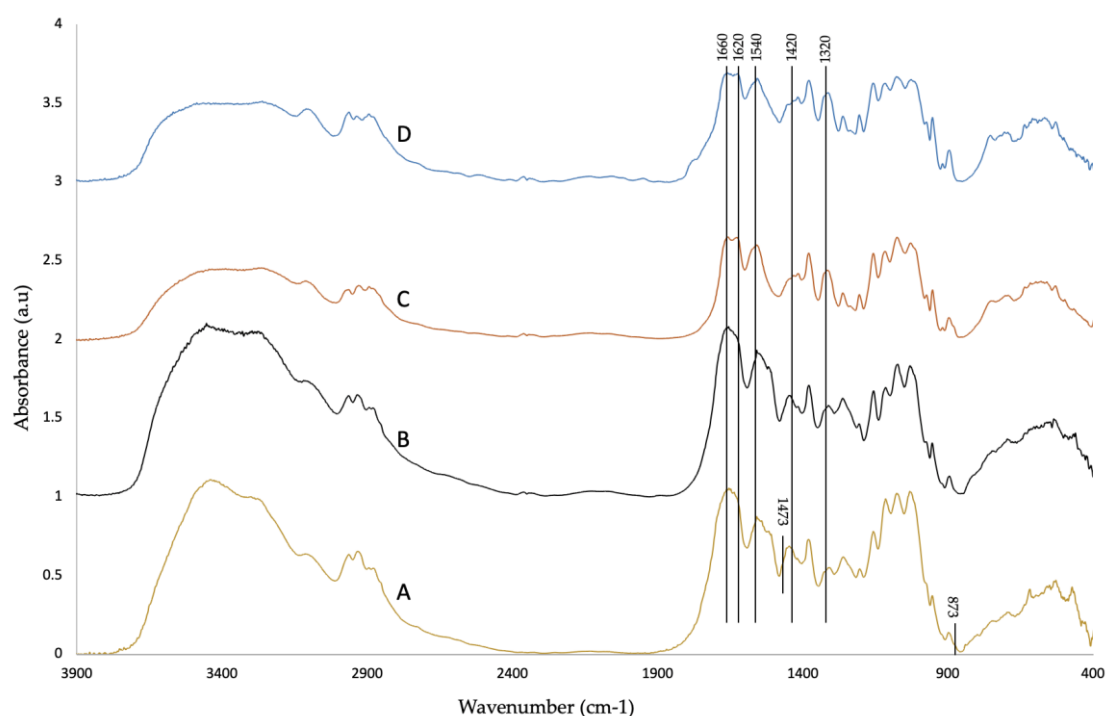


**Figure 2.** FTIR spectra of (A) raw material, (B) demineralized, (C) deproteinized, and (D) decolorized samples.

**Table 2.** Degree of acetylation (DA) and crystallinity index (CrI) of chitin from different sources.

Source	DA %	CrI %	Ref.
<i>Cicada orni</i> sloughs (this study)	96.3 ± 3.4	72.1	
Mushrooms	63.4–69.8	63	[15]
Grasshopper	108.5–180.7	75–80	[28]
Cicada sloughs	90.8–102.3	89.7	[35]
Squid gladius <sup>1</sup>	90.7–101.2; 96	72.3–85; 74.9	[38,42]
House cricket	108.1	88.02	[43]
Worm of giant flour	82.39–101.39	67.82–57.62	[44]
Beetle	93.1	89.05	[57]
Crab	78.5	67.8	[48]
Shrimp	88.5; 96; 65.6–99.4	64.1; 88; 79.4–87.4	[48,58,59]
Hornet ( <i>Vespa velutina</i> )	95.44		[51]

<sup>1</sup> Chitin extracted from squid gladius is  $\beta$ -chitin.

### 2.3. X-ray Diffraction

In nature, chitin is arranged in crystalline microfibrils [60]. The crystalline structure can be analyzed by X-ray diffraction (XRD). Figure 3 shows the XRD patterns of the demineralized, deproteinized, and decolorized steps of chitin extraction. All samples present six peaks at about 9.3°, 12.7°, 19.5°, 20.8°, 23.4°, and 26.3° that correspond to the six typical crystalline planes (020), (021), (110), (120), (101), and (130), respectively, except for the peak at 20.8° (120), which was decreased in the deproteinized sample and absent in the decolorized one. The positions and the amplitude of these peaks are in good agreement with those reported for five other sources of chitin, including cicada sloughs [33]. According to Jang [17],  $\alpha$ -chitin has four crystalline reflections at 9.6, 19.6, 21.1, and 23.7, while  $\beta$ -chitin has two crystalline reflections at 9.1 and 20.3. *Cicada orni* results indicate that the extracted chitin is the  $\alpha$  structure. Crystallinity index (CrI) is an important characteristic influencing the physical and biological properties of chitin, including solubility and biodegradability [59]. In particular, the higher the degree of crystallinity, the lower the solubility [60] and, accordingly, the biodegradability [61].

CrI was calculated using Equation (5). Results show that CrI was 68.6% for the raw material, 55.8% for the demineralized sample, 73.4% for the deproteinized sample, and 72.1% for the decolorized sample. Our hypothesis is that the removal of minerals may induce a diminution of CrI because of the absence of calcium carbonate crystals. After deproteinization, the increase of CrI may be due to a rearrangement of polymer chains after the removal of proteins. The CrI of chitin extracted from CO (72.1%) is within this range of chitin extracted in the literature from different sources, between 57.8% and 89.7% (Table 2).

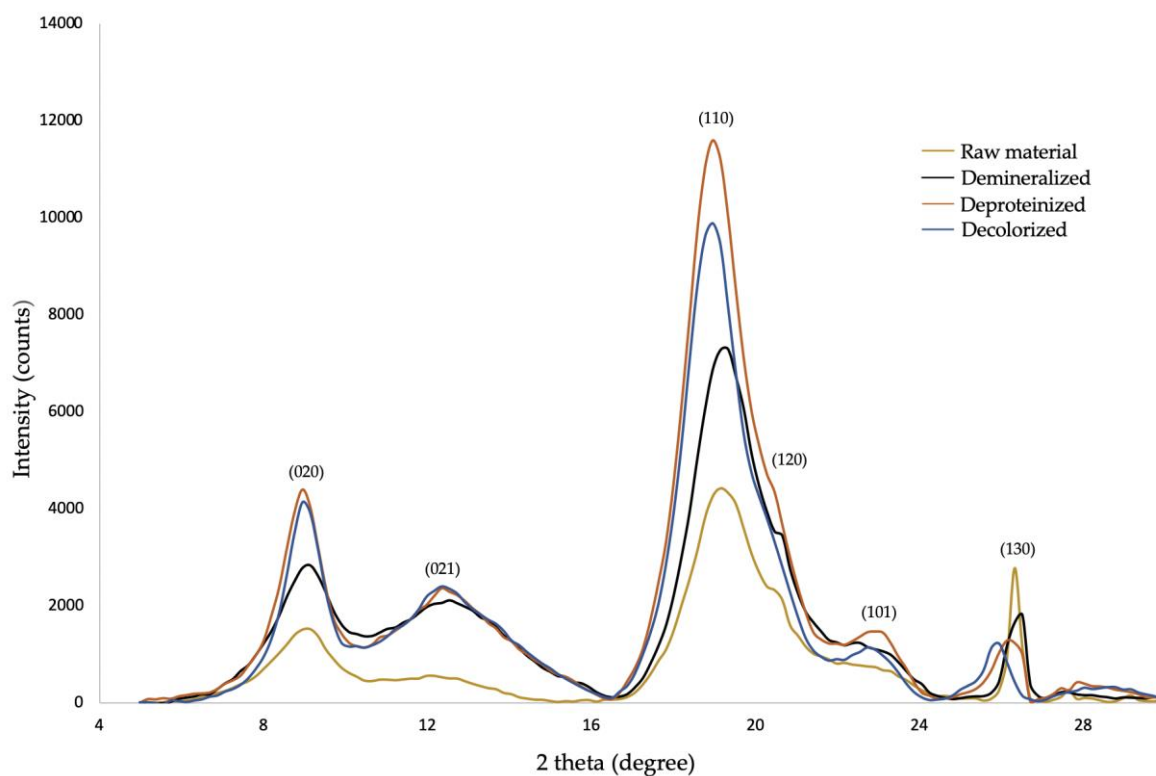


**Figure 3.** X-ray diffractograms of raw material, demineralized, deproteinized, and decolorized samples.

#### 2.4. Thermogravimetric Analysis

Thermogravimetric analysis (TGA), a measure of the change in mass of a substance as a function of temperature, is another important factor that defines the possible application of chitin [62] and helps to identify the type of chitin. TGA of raw material, demineralized, deproteinized, and decolorized samples is shown in Figure 4A. The maximum weight loss for all samples was obtained between 200 and 400 °C, and was 63.9% for the raw material, 68.4% for the demineralized sample, 55.8% for the deproteinized sample, and 63.9% for the decolorized sample. The maximum weight loss obtained from chitin extracted from cicada sloughs by Sajomsang and Gonil [37] was 66.4%, while the maximum weight loss obtained from chitin extracted from the whole body of cicadas was in the range of 72.2–88.3% [30]. Figure 4B shows the derivative thermogravimetric analysis (DTG) of the four samples. The thermal degradation of raw material occurs in at least four different degradation steps, that of demineralized and deproteinized samples in three steps, and that of decolorized samples in two steps. The temperature at which the maximum degradation of the samples occurred was 371.4, 357.6, 359.8, and 375.1 °C for raw material, the demineralized, deproteinized, and decolorized specimen steps, respectively. According to the literature, the maximum distortion temperature of  $\alpha$ -chitin is usually higher than 350 °C, while the value of for  $\beta$ -chitin is usually lower than 350 °C [16]. The maximum degradation temperature of chitin from CO was 375.1 °C, confirming that it is  $\alpha$ -chitin. This result is similar to the maximum degradation temperature of chitin extracted from cicada sloughs described by Sajomsang and Gonil [35], which was 362 °C, while for chitin extracted from the whole body of cicadas,

it was in the range of 339.9–412.7 °C [30]. All samples presented a peak around 100 °C corresponding to water evaporation. The peak around 306 °C in raw material decreased in the demineralized sample and disappeared in deproteinized and decolorized samples. This suggests that it could be related to the demineralization process.

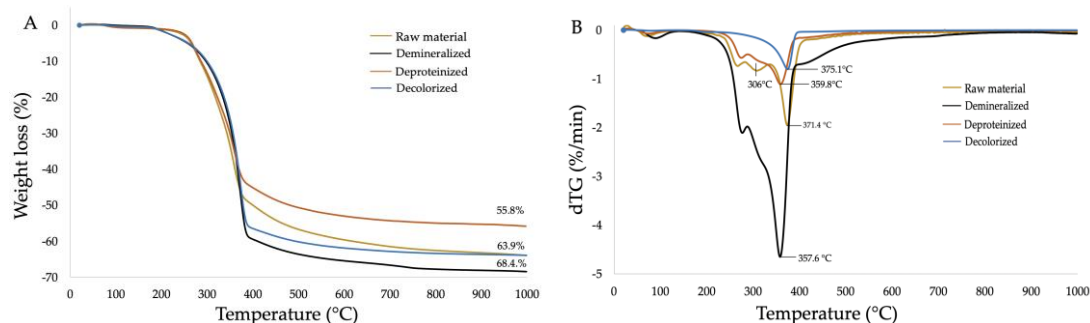


**Figure 4.** (A) TGA and (B) DTG of raw material, demineralized, deproteinized, and decolorized samples.

### 2.5. Scanning Electron Microscopy

Figure 5 shows scanning electron microscopy (SEM) images of the surface of the raw material (Figure 5A), and demineralized (Figure 5B) and decolorized (Figure 5C) specimens. Raw material surface exhibits a rough morphology. We hypothesize that chitin has a lamellar organization intercalated with some granular material (that could correspond to minerals and proteins) that seems to decrease in demineralized and in decolorized samples, where only the flat lamellar structure seems to remain. This decrease could demonstrate the effective removal of minerals and proteins, respectively [35].

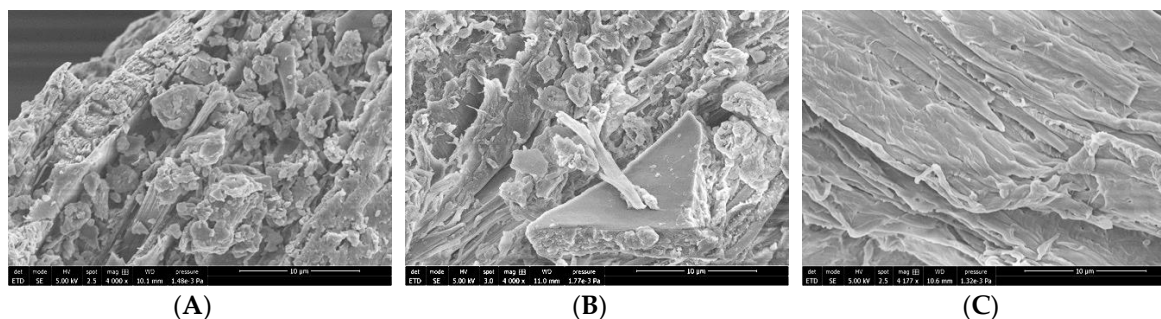


**Figure 5.** SEM images of (A) raw material, (B) demineralized, and (C) decolorized samples.

## 3. Materials and Methods

### 3.1. Extraction of Chitin from *Cicada orni*

*Cicada orni* sloughs were taken in August 2017 in the south-eastern French Mediterranean basin, especially in La Seyne sur Mer in a place called PinRolland. Chitin was extracted with a modified protocol based on Luo et al.'s work [33]. *Cicada orni* sloughs were washed with distilled water and dried in an oven at a temperature of 50 °C for 24 h. Then they were mechanically ground in a mortar. Specimen were demineralized with 1 M HCl aqueous solution (1:15 ratio of solid sample to solution) in a 30 °C water bath at 200 rpm for 2 h to remove calcium carbonate and other calcium salts. Then they were filtered out and washed with deionized water until neutral pH was detected. The reaction of demineralization is the following [63]:



In more detail, HCl reacts with calcium carbonate to produce an aqueous solution of calcium chloride (CaCl<sub>2</sub>) and CO<sub>2</sub>. Specimens were dried in the oven at 50 °C for 24 h and weighed to calculate the amount on minerals present in *Cicada orni* sloughs. For deproteinization, a treatment with 1 M NaOH solution (1:15 ratio of solid sample to solution) was done, and then refluxed at 90 °C for 2 h to remove proteins. The specimen was also dried in the oven at 50 °C for 24 h and weighed to calculate the amount of protein present in *Cicada orni* sloughs. Insoluble material was filtered and washed extensively with deionized water until neutral pH. For the decolorization, the sample was treated with 1% sodium hypochlorite (NaClO) (1:30 ratio of solid sample to solution) for 30 min at 25 °C room temperature, filtered, and washed with distilled water, and treated another two times with 1% NaClO for 10 min, until the water was transparent. After this last step, specimens were washed extensively to remove any residual chemicals.

### 3.2. Chitin Content

Chitin content was calculated by measuring the weight of samples before and after the extraction (always dried in an oven at 60 °C overnight). The chitin content (%) was calculated using the following formula:

$$\text{Chitin content (\%)} = \frac{\text{Dried chitin extracted (g)}}{\text{Raw material (g)}} \times 100 \quad (2)$$

The mineral content (%) of cicada sloughs was calculated using the following formula:

$$\text{Mineral content (\%)} = \frac{(W1 - W2)}{W1} \times 100 \quad (3)$$

where W1 is the raw material and W2 is the weight of the dried sample after demineralization. The protein content was calculated using the same formula, attributing the weight of the dried demineralized sample to W1 and the weight of the dried deproteinized sample to W2. The weight of the remaining material after the decolorization process represents the dried chitin extracted.

### 3.3. FTIR Analysis

Dried powder of raw material, demineralized, deproteinized, and decolorized *Cicada orni* samples were used for FTIR analysis. Spectra were collected in a range between 4000 to 400 cm<sup>-1</sup> with a Nicolet 6700 Spectrophotometer by accumulation of 64 scans with a resolution of 4 cm<sup>-1</sup> in KBr pellets (1 mg of the sample in 100 mg of KBr). The degree of acetylation (DA) was calculated from the Absorbance (A) ratios according to the Brugnerotto method [52]:

$$\text{DA (\%)} = \frac{\frac{A_{1320}}{A_{1420}} - 0.3822}{0.03133} \times 100 \quad (4)$$

where the values of the absorbance at 1420 cm<sup>-1</sup> and 1320 cm<sup>-1</sup> were calculated using the baselines shown in Figure S1. The DA was expressed as average of results from eight FTIR spectra.

### 3.4. X-ray Diffraction

Powder X-ray diffraction (XRD) (D8 Advance, Bruker, Billerica, MA, USA) analysis of demineralized, deproteinized, and decolorized steps were record using a D8 Advance X-ray diffractometer. Data were collected at a scan rate of 1°/min with the scan angle from 5–40°. The crystallinity indexes (CrI) were calculated using the following equation [57]:

$$\text{CrI (\%)} = \frac{I_{110} - I_{\text{am}}}{I_{110}} \times 100 \quad (5)$$

where I<sub>110</sub> is the maximum intensity of the crystalline region at 20° and I<sub>am</sub> is the maximum intensity of amorphous diffraction at 16°.

### 3.5. Thermogravimetric Analysis

The thermal degradation properties of demineralized, deproteinized, and decolorized powdered specimens were analyzed using a thermogravimetric analyzer equipped of a Setaram microbalance ((Setsys Ev. 1750, Setaram, Kep Technologies, Lyon, France). The samples (10 mg) were heated from 20 °C to 1000 °C at a constant heating rate of 10 °C/min under argon atmosphere.

### 3.6. Scanning Electron Microscopy

The surface morphologies of the samples were observed using a Quanta 650-FEG (FEI, Hillsboro, OR, USA) scanning electron microscope (SEM), model, manufacturer, city, country. The samples (raw material, demineralized, deproteinized, and decolorized) were dried, fixed on an adhesive tape, and coated with a gold layer. The images were taken at an acceleration voltage of 5 kV and with a magnification of 10 µm.

## 4. Conclusions

In this study, we extracted chitin from *Cicada orni* sloughs of the south-eastern French Mediterranean basin using a chemical method. We obtained a chitin yield of 42.6%, which is higher than that of other studies. FTIR, DRX, and TGA analysis confirmed that the chitin extracted from *Cicada orni* is in the  $\alpha$ -form, with a DA of  $99.6\% \pm 3.4\%$ , a CrI of 72.1%, and a maximum degradation temperature of 375.1 °C. *Cicada orni* sloughs of the south-eastern French Mediterranean basin show great potential as an ecological alternative source of chitin. Furthermore, for the first time, we analyzed and described all the steps of the extraction process to compare the effectiveness of the treatments and different extraction conditions. For example, FTIR spectra showed the formation of two distinct peaks at 1650 and 1621  $\text{cm}^{-1}$  after the deproteinization step that seem to be due to the elimination of proteins or, at least, to their decrease.

**Supplementary Materials:** The following are available online, Figure S1 Representation of the baselines used to calculate the DA.

**Author Contributions:** Conceptualization, F.C.; methodology, F.C. and J.-P.J.; investigations, A.P. and C.P.; writing—original draft preparation, A.P. and F.C.; writing—review and editing, A.P., F.C., E.A.-T., J.-P.J. and J.F.M.; supervision, F.C.; funding acquisition, F.C. All authors have read and agreed to the published version of the manuscript.

**Funding:** This work was supported partly by the French PIA project “Lorraine Université d’excellence”, reference ANR-15-IDEX-04-LUE. This work has been also supported by CNRS GDR 2088 <<BIOMIM>>.

**Acknowledgments:** F.C. would thanks Ilan, Timéo and Emmanuelle Cleymand for the cicada harvest.

**Conflicts of Interest:** The authors declare that they have no known competing for financial interests or personal relationships that could have appeared to influence the work reported in this paper. The authors declare no conflict of interest. The funders had no role in the design of the study; in the collection, analyses, or interpretation of data; in the writing of the manuscript, or in the decision to publish the results.

## References

1. Rinaudo, M. Chitin and chitosan: Properties and applications. *Prog. Polym. Sci.* **2006**, *31*, 603–632. [[CrossRef](#)]
2. Rejinold, N.S.; Nair, A.; Sabitha, M.; Chennazhi, K.P.; Tamura, H.; Nair, S.V.; Jayakumar, R. Synthesis, characterization and in vitro cytocompatibility studies of chitin nanogels for biomedical applications. *Carbohydr. Polym.* **2012**, *87*, 943–949. [[CrossRef](#)]
3. Onishi, H.; Machida, Y. Biodegradation and distribution of water-soluble chitosan in mice. *Biomaterials* **1999**, *20*, 175–182. [[CrossRef](#)]
4. Park, B.K.; Kim, M.M. Applications of Chitin and Its Derivatives in Biological Medicine. *Int. J. Mol. Sci.* **2010**, *11*, 5152–5164. [[CrossRef](#)]
5. Alves, N.M.; Mano, J.F. Chitosan derivatives obtained by chemical modifications for biomedical and environmental applications. *Int. J. Biolog. Macromol.* **2008**, *43*, 401–414. [[CrossRef](#)]

6. Shamshina, J.L. Chitin in ionic liquids: Historical insights into the polymer's dissolution and isolation. A review. *Green Chem.* **2019**, *21*, 3974–3993. [[CrossRef](#)]
7. Silva, S.S.; Duarte, A.R.C.; Oliveira, J.M.; Mano, J.F.; Reis, R.L. Alternative methodology for chitin-hydroxyapatite composites using ionic liquids and supercritical fluid technology. *J. Bioact. Compat. Polym.* **2013**, *28*, 481–491. [[CrossRef](#)]
8. Tolesa, L.D.; Gupta, B.S.; Lee, M.J. Chitin and chitosan production from shrimp shells using ammonium-based ionic liquids. *Int. J. Biolog. Macromol.* **2019**, *130*, 818–826. [[CrossRef](#)]
9. Nagahama, H.; Nwe, N.; Jayakumar, R.; Koiwa, S.; Furuike, T.; Tamura, H. Novel biodegradable chitin membranes for tissue engineering applications. *Carbohydr. Polym.* **2008**, *73*, 295–302. [[CrossRef](#)]
10. Wang, Y.; Li, J.; Li, B. Chitin microspheres: A fascinating material with high loading capacity of anthocyanins for colon specific delivery. *Food Hydrocoll.* **2017**, *63*, 293–300. [[CrossRef](#)]
11. Singh, R.; Chacharkar, M.P.; Mathur, A.K. Chitin membrane for wound dressing application-preparation, characterisation and toxicological evaluation. *Int. Wound J.* **2008**, *5*, 665–673. [[CrossRef](#)] [[PubMed](#)]
12. Sağlam, E.İ.; Kutlu, İ.C.; Haberal, O.E.; Yüksekaya, M.; Kılıçarslan, Ö.; Güran, Ş. Chitin increases the angiogenesis in chorioallantoic membrane model in the presence of testosterone and progesterone. *Gulhane Med. J.* **2019**, *61*, 20. [[CrossRef](#)]
13. Merzendorfer, H. Chitin metabolism in insects: Structure, function and regulation of chitin synthases and chitinases. *J. Exp. Biol.* **2003**, *206*, 4393–4412. [[CrossRef](#)] [[PubMed](#)]
14. El Knidri, H.; Belaabed, R.; Addaou, A.; Laajeb, A.; Lahsini, A. Extraction, chemical modification and characterization of chitin and chitosan. *Int. J. Biolog. Macromol.* **2018**, *120*, 1181–1189. [[CrossRef](#)]
15. Hassainia, A.; Satha, H.; Boufi, S. Chitin from *Agaricus bisporus*: Extraction and characterization. *Int. J. Biolog. Macromol.* **2018**, *117*, 1334–1342. [[CrossRef](#)]
16. Wu, Q.; Jungstedt, E.; Šoltésová, M.; Mushi, N.E.; Berglund, L.A. High strength nanostructured films based on well-preserved  $\beta$ -chitin nanofibrils. *Nanoscale* **2019**, *11*, 11001–11011. [[CrossRef](#)]
17. Jang, M.-K.; Kong, B.-G.; Jeong, Y.-I.; Lee, C.H.; Nah, J.-W. Physicochemical characterization of  $\alpha$ -chitin,  $\beta$ -chitin, and  $\gamma$ -chitin separated from natural resources. *J. Polym. Sci. A Polym. Chem.* **2004**, *42*, 3423–3432. [[CrossRef](#)]
18. Kumirska, J.; Weinhold, M.X.; Thöming, J.; Stepnowski, P. Biomedical Activity of Chitin/Chitosan Based Materials—Influence of Physicochemical Properties Apart from Molecular Weight and Degree of N-Acetylation. *Polymers* **2011**, *3*, 1875–1901. [[CrossRef](#)]
19. Pighinelli, L. Methods of Chitin Production a Short Review. *AJBSR* **2019**, *3*, 307–314. [[CrossRef](#)]
20. Arbia, W.; Arbia, L.; Adour, L.; Amrane, A. Chitin Extraction from Crustacean Shells Using Biological Methods—A Review. *Food Technol. Biotechnol.* **2013**, *51*, 12–25.
21. Sorokulova, I.; Krumnow, A.; Globa, L.; Vodyanoy, V. Efficient decomposition of shrimp shell waste using *Bacillus cereus* and *Exiguobacterium acetylicum*. *J. Ind. Microbiol. Biotechnol.* **2009**, *36*, 1123–1126. [[CrossRef](#)] [[PubMed](#)]
22. Hamed, I.; Özogul, F.; Regenstein, J.M. Industrial applications of crustacean by-products (chitin, chitosan, and chitoooligosaccharides): A review. *Trend. Food Sci. Technol.* **2016**, *48*, 40–50. [[CrossRef](#)]
23. El Knidri, H.; Dahmani, J.; Addaou, A.; Laajeb, A.; Lahsini, A. Rapid and efficient extraction of chitin and chitosan for scale-up production: Effect of process parameters on deacetylation degree and molecular weight. *Int. J. Biolog. Macromol.* **2019**, *139*, 1092–1102. [[CrossRef](#)] [[PubMed](#)]
24. Rameshthangam, P.; Solairaj, D.; Arunachalam, G.; Ramasamy, P. Chitin and Chitinases: Biomedical and Environmental Applications of Chitin and its Derivatives. *JEN* **2020**, *1*, 20–43. [[CrossRef](#)]
25. Badawy, R.M.; Mohamed, H.I. Chitin extraction, Composition of Different Six Insect Species and Their Comparable Characteristics with That of the Shrimp. *J. Am. Sci.* **2015**, *11*, 127–134.
26. Jones, M.; Kujundzic, M.; John, S.; Bismarck, A. Crab vs. Mushroom: A Review of Crustacean and Fungal Chitin in Wound Treatment. *Mar. Drug.* **2020**, *18*, 64. [[CrossRef](#)]
27. Abo Elsoud, M.M.; El Kady, E.M. Current trends in fungal biosynthesis of chitin and chitosan. *Bull. Natl. Res. Cent.* **2019**, *43*, 1–12. [[CrossRef](#)]
28. Kaya, M.; Lelešius, E.; Nagrockaitė, R.; Sargin, I.; Arslan, G.; Mol, A.; Baran, T.; Can, E.; Bitim, B. Differentiations of Chitin Content and Surface Morphologies of Chitins Extracted from Male and Female Grasshopper Species. *PLoS ONE* **2015**, *10*, e0115531. [[CrossRef](#)]

29. Dutta, P.K.; Dutta, J.; Tripathi, V.S. Chitin and chitosan: Chemistry, properties and applications. *J. Sci. Ind. Res.* **2004**, *63*, 12.
30. Mol, A.; Kaya, M.; Mujtaba, M.; Akyuz, B. Extraction of high thermally stable and nanofibrous chitin from *Cicada* (Cicadoidea). *Entomol. Res.* **2018**, *48*, 480–489. [[CrossRef](#)]
31. Puisasant, S. *Contribution à la Connaissance des Cigales de France: Géonomie et Écologie des Populations (Hemiptera, Cicadidae)*; Bédeilhac et Aynat: Perpignan, France, 2006.
32. Blondel, J.; Aronson, J. *Biology and Wildlife of the Mediterranean Region*; Oxford University Press: Oxford, UK, 1999.
33. Luo, Q.; Wang, Y.; Han, Q.; Ji, L.; Zhang, H.; Fei, Z.; Wang, Y. Comparison of the physicochemical, rheological, and morphologic properties of chitosan from four insects. *Carbohydr. Polym.* **2019**, *209*, 266–275. [[CrossRef](#)] [[PubMed](#)]
34. Bertuzzi, D.L.; Becher, T.B.; Capreti, N.M.R.; Amorim, J.; Jurberg, I.D.; Megiatto, J.D.; Ornelas, C. General Protocol to Obtain D-Glucosamine from Biomass Residues: Shrimp Shells, Cicada Sloughs and Cockroaches. *Glob. Chall.* **2018**, *2*, 1800046. [[CrossRef](#)] [[PubMed](#)]
35. Sajomsang, W.; Gonil, P. Preparation and characterization of  $\alpha$ -chitin from cicada sloughs. *Mater. Sci. Eng. C* **2010**, *30*, 357–363. [[CrossRef](#)]
36. Wu, S.-J.; Pan, S.-K.; Wang, H.-B.; Wu, J.-H. Preparation of chitooligosaccharides from cicada slough and their antibacterial activity. *Int. J. Biolog. Macromol.* **2013**, *62*, 348–351. [[CrossRef](#)]
37. Chandran, R.; Williams, L.; Hung, A.; Nowlin, K.; LaJeunesse, D. SEM characterization of anatomical variation in chitin organization in insect and arthropod cuticles. *Micron* **2016**, *82*, 74–85. [[CrossRef](#)]
38. Lavall, R.; Assis, O.; Campanafilho, S.  $\beta$ -Chitin from the pens of *Loligo* sp.: Extraction and characterization. *Bioresour. Technol.* **2007**, *98*, 2465–2472. [[CrossRef](#)]
39. Vetter, J. Chitin content of cultivated mushrooms *Agaricus bisporus*, *Pleurotus ostreatus* and *Lentinula edodes*. *Food Chem.* **2007**, *102*, 6–9. [[CrossRef](#)]
40. Ofenbeher-Miletić, I.; Stanimirović, D.; Stanimirović, S. On determination of chitin content in mushrooms. *Plant. Food Hum. Nutr.* **1984**, *34*, 197–201. [[CrossRef](#)]
41. Abdelmalek, B.E.; Sila, A.; Haddar, A.; Bougatef, A.; Ayadi, M.A.  $\beta$ -Chitin and chitosan from squid gladius: Biological activities of chitosan and its application as clarifying agent for apple juice. *Int. J. Biolog. Macromol.* **2017**, *104*, 953–962. [[CrossRef](#)]
42. Susana Cortizo, M.; Berghoff, C.F.; Alessandrini, J.L. Characterization of chitin from *Illex argentinus* squid pen. *Carbohydr. Polym.* **2008**, *74*, 10–15. [[CrossRef](#)]
43. Ibitoye, E.B.; Lokman, I.H.; Hezmee, M.N.M.; Goh, Y.M.; Zuki, A.B.Z.; Jimoh, A.A. Extraction and physicochemical characterization of chitin and chitosan isolated from house cricket. *Biomed. Mater.* **2018**, *13*, 025009. [[CrossRef](#)] [[PubMed](#)]
44. Soon, C.Y.; Tee, Y.B.; Tan, C.H.; Rosnita, A.T.; Khalina, A. Extraction and physicochemical characterization of chitin and chitosan from *Zophobas morio* larvae in varying sodium hydroxide concentration. *Int. J. Biolog. Macromol.* **2018**, *108*, 135–142. [[CrossRef](#)] [[PubMed](#)]
45. Kaya, M.; Baran, T.; Erdoğan, S.; Mentş, A.; Aşan Özusağlam, M.; Çakmak, Y.S. Physicochemical comparison of chitin and chitosan obtained from larvae and adult Colorado potato beetle (*Leptinotarsa decemlineata*). *Mater. Sci. Eng. C* **2014**, *45*, 72–81. [[CrossRef](#)] [[PubMed](#)]
46. Tokatlı, K.; Demirdöven, A. Optimization of chitin and chitosan production from shrimp wastes and characterization. *J. Food Process. Preserv.* **2018**, *42*, e13494. [[CrossRef](#)]
47. Hossain, M.; Iqbal, A. Production and characterization of chitosan from shrimp waste. *J. Bangladesh. Agric. Univ.* **2014**, *12*, 153–160. [[CrossRef](#)]
48. Hajji, S.; Younes, I.; Ghorbel-Bellaaj, O.; Hajji, R.; Rinaudo, M.; Nasri, M.; Jellouli, K. Structural differences between chitin and chitosan extracted from three different marine sources. *Int. J. Biolog. Macromol.* **2014**, *65*, 298–306. [[CrossRef](#)]
49. Youn, D.K.; No, H.K.; Prinyawiwatkul, W. Physicochemical and functional properties of chitosans prepared from shells of crabs harvested in three different years. *Carbohydr. Polym.* **2009**, *78*, 41–45. [[CrossRef](#)]
50. Tajik, H.; Moradi, M.; Rohani, S.; Erfani, A.; Jalali, F. Preparation of Chitosan from Brine Shrimp (*Artemia urmiana*) Cyst Shells and Effects of Different Chemical Processing Sequences on the Physicochemical and Functional Properties of the Product. *Molecules* **2008**, *13*, 1263–1274. [[CrossRef](#)]

51. Feás, X.; Vázquez-Tato, M.P.; Seijas, J.A.; Pratima, G.; Nikalje, A.; Fraga-López, F. Extraction and Physicochemical Characterization of Chitin Derived from the Asian Hornet, *Vespa velutina* Lepelletier 1836 (Hym.: Vespidae). *Molecules* **2020**, *25*, 384. [[CrossRef](#)]
52. Brugnerotto, J.; Lizardi, J.; Goycoolea, F.M.; Argüelles-Monal, W.; Desbrières, J.; Rinaudo, M. An infrared investigation in relation with chitin and chitosan characterization. *Polymer* **2001**, *42*, 3569–3580. [[CrossRef](#)]
53. Gbenedor, O.P.; Adeosun, S.O.; Adegbite, A.A.; Akinwande, C. Organic and mineral acid demineralizations: Effects on *crangon* and *Liocarcinus vernalis*-sourced biopolymer yield and properties. *J. Taibah Univ. Sci.* **2018**, *12*, 837–845. [[CrossRef](#)]
54. Zhao, D.; Huang, W.C.; Guo, N.; Zhang, S.; Xue, C.; Mao, X. Two-Step Separation of Chitin from Shrimp Shells Using Citric Acid and Deep Eutectic Solvents with the Assistance of Microwave. *Polymers* **2019**, *11*, 409. [[CrossRef](#)] [[PubMed](#)]
55. Czechowska-Biskup, R.; Jarosińska, D.; Rokita, B.; Ulański, P.; Rosiak, J.M. Determination of degree of deacetylation of chitosan-comparison of methods. *Prog. Chem. Appl. Chitin Deriv.* **2012**, *16*, 5–20.
56. Roy, J.C.; Salaün, F.; Giraud, S.; Ferri, A.; Chen, G.; Guan, J. Solubility of Chitin: Solvents, Solution Behaviors and Their Related Mechanisms. In *Solubility of Polysaccharides*; Xu, Z., Ed.; InTech: Vienna, Austria, 2017.
57. Liu, S.; Sun, J.; Yu, L.; Zhang, C.; Bi, J.; Zhu, F.; Qu, M.; Jiang, C.; Yang, Q. Extraction and Characterization of Chitin from the Beetle *Holotrichia parallela* Motschulsky. *Molecules* **2012**, *17*, 4604–4611. [[CrossRef](#)]
58. Vázquez, J.; Ramos, P.; Mirón, J.; Valcarcel, J.; Sotelo, C.; Pérez-Martín, R. Production of Chitin from *Penaeus vannamei* By-Products to Pilot Plant Scale Using a Combination of Enzymatic and Chemical Processes and Subsequent Optimization of the Chemical Production of Chitosan by Response Surface Methodology. *Mar. Drug.* **2017**, *15*, 180. [[CrossRef](#)]
59. Gbenedor, O.P.; Adeosun, S.O.; Lawal, G.I.; Jun, S.; Olaleye, S.A. Acetylation, crystalline and morphological properties of structural polysaccharide from shrimp exoskeleton. *Eng. Sci. Technol. Int. J.* **2017**, *20*, 1155–1165. [[CrossRef](#)]
60. Ioelovich, M. Crystallinity and Hydrophilicity of Chitin and Chitosan. *J. Chem.* **2014**, *3*, 7–14.
61. Elieh-Ali-Komi, D.; Hamblin, M.R. Chitin and Chitosan: Production and Application of Versatile Biomedical Nanomaterials. *Int. J. Adv. Res. (Indore)* **2016**, *4*, 411–427.
62. Klapiszewski, Ł.; Bula, K.; Sobczak, M.; Jesionowski, T. Influence of Processing Conditions on the Thermal Stability and Mechanical Properties of PP/Silica-Lignin Composites. *Int. J. Polym. Sci.* **2016**, *2016*, 1–9. [[CrossRef](#)]
63. Fadli, A.; Drastinawati; Komalasari; Afriani, Y.; Maulana, S.; Huda, F. Demineralization kinetics of chitin isolation from shrimp shell waste. *Ces* **2017**, *10*, 1409–1418. [[CrossRef](#)]

**Sample Availability:** Samples of the compounds are not available from the authors.



© 2020 by the authors. Licensee MDPI, Basel, Switzerland. This article is an open access article distributed under the terms and conditions of the Creative Commons Attribution (CC BY) license (<http://creativecommons.org/licenses/by/4.0/>).



## Supplementary Materials

# Extraction and physicochemical characterization of chitin from *Cicada orni* sloughs of south-eastern French Mediterranean basin

Aurelia Poerio<sup>1</sup>, Chloé Petit<sup>1</sup>, Jean-Philippe Jehl<sup>1</sup>, Elmira Arab-Tehrany<sup>2</sup>, João F. Mano<sup>1,3</sup>, Franck Cleymand<sup>1\*</sup>

<sup>1</sup> University of Lorraine, Jean Lamour Institute, UMR 7198 CNRS, 2 allée André Guinier-Campus Artem, BP 50840, F-54011 Nancy Cédex, France.

<sup>2</sup> University of Lorraine, Laboratoire Ingénierie des Biomolécules, TSA 40602, Vandoeuvre-lès-Nancy, F-54518, France.

<sup>3</sup> University of Aveiro, CICECO—Aveiro Institute of Materials, Department of Chemistry 3810-193 Aveiro, Portugal

\* Correspondence: franck.cleymand@univ-lorraine.fr

Figure S1 shows how we traced the baselines for the calculation of the degree of acetylation, as proposed by Brugnerotto [49]. The values at 1420 and 1320  $\text{cm}^{-1}$  were given by the length of the lines between the point of the peaks and the intersection with the baselines. These two values were then used in the Eq. (4). (See materials and methods).

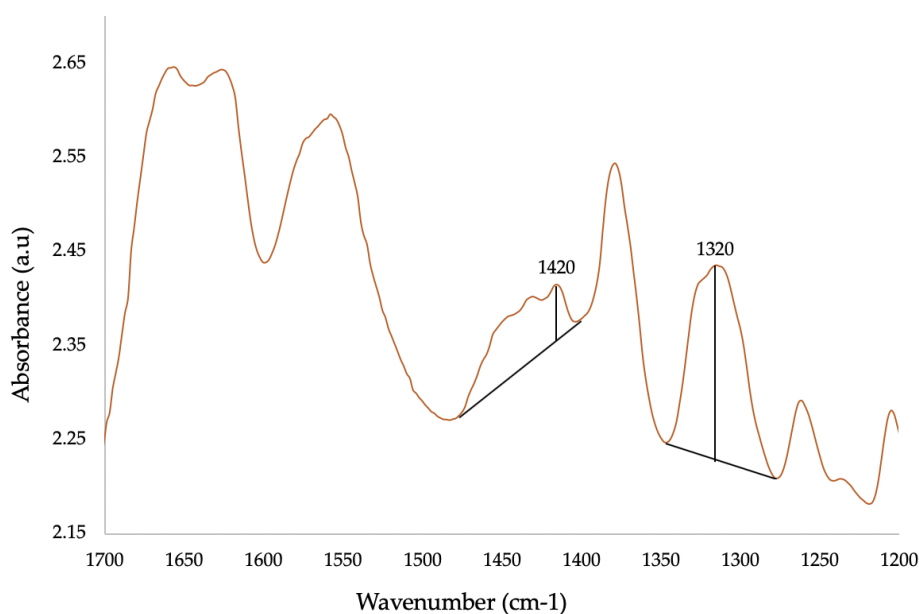


Figure S1. Representation of the baselines used to calculate the DA.

### References

49. Brugnerotto, J.; Lizardi, J.; Goycoolea, F.M.; Argüelles-Monal, W.; Desbrières, J.; Rinaudo, M. An infrared investigation in relation with chitin and chitosan characterization. *Polymer* **2001**, *42*, 3569–3580.

## 2.2 Comparison of the physicochemical properties of chitin extracted from *Cicada orni* sloughs harvested in three different years and characterization of the resulting chitosan

*The content of this part of the chapter is identical to the following published work:*

**Title:** Comparison of the physicochemical properties of chitin extracted from *Cicada orni* sloughs harvested in three different years and characterization of the resulting chitosan

**Authors:** Aurelia Poerio, Thomas Girardet, Chloé Petit, Solenne Fleutot, Jean-Philippe Jehl, Elmira Arab-Tehrany, João F. Mano and Franck Cleymand

**Reference:** Appl. Sci. 2021, 11(23), 11278 - Published: 29 November 2021

### 2.2.1 Abstract

Chitin and its derivative chitosan are among the most used polysaccharides for biomedical and pharmaceutical applications. Most of the commercially available chitin is obtained from seafood wastes. However, the interest in alternative renewable sources of chitin and chitosan, such as insects, is growing. When new sources are identified, their stability over time has to be evaluated to allow for their commercialization. The aim of this study is to compare the physicochemical properties of chitin extracted from *Cicada orni* sloughs harvested in three different years (2017, 2019 and 2020) in order to assess the stability of the source and the repeatability of the extraction process. Chitin and its derivative chitosan were characterized by simple techniques such as Fourier transform infrared spectroscopy (FTIR) and X-ray diffraction (XRD). Results suggest that the physicochemical properties of the extracted chitin varied from year to year, and that these differences are not due to the extraction process but rather to intrinsic differences within the source. We showed that these differences could already be detected by analyzing the raw material (*i.e.* cicada sloughs) using the above-mentioned simple methods. The chitosan obtained from deacetylation of chitin had a low degree of deacetylation ( $66.2 \pm 1.6$ ). This low degree of deacetylation can be attributed to the deacetylation process which is probably not appropriate for this source of chitin.

### 2.2.2 Introduction

Chitin is a linear polymer composed of units of N-acetyl-D-glucosamine (acetylated unit) and D-glucosamine (deacetylated unit), found in natural sources (*i.e.* the exoskeleton of Arthropods, cell wall of fungi) in association with proteins, minerals and pigments. The removal of these elements, in order to obtain pure chitin, is realized in three steps: the demineralization of the raw material, its deproteinization and its decoloration [39]. Through a process of deacetylation, which consists in the removal of acetyl groups, chitin can be transformed into its derivative chitosan. The amount of acetylated units remaining reveals the efficiency of the transformation of chitin into chitosan and determines their so-called degree of acetylation (DA - usually employed for chitin) or degree of deacetylation (DD - usually employed for chitosan). If the product resulting from this transformation contains more than 50% of acetylated units (DA>50% and DD<50%), it is called chitin, while if it

contains more than 50% of deacetylated units (DA < 50% and DD > 50%) is it called chitosan [39]. Within a source, chitin can be found in three different polymorphs:  $\alpha$ ,  $\beta$  and  $\gamma$ , depending on the parallel, antiparallel or alternated orientation of the fibers, respectively [41].  $\alpha$ -chitin is the most abundant polymorph and if found in fungi, insect exoskeleton and shells of crustaceans, while  $\beta$ - and  $\gamma$ -chitin are uncommon and are found in squid pens and in beetles (family *Lucanidae*), respectively [101]. Both chitin and chitosan, due to their biodegradability, biocompatibility and low toxicity, are widely studied in the biomedical and pharmaceutical research fields. However due to the high number of acetyl groups, which form strong hydrogen bonds, chitin is insoluble in water and in most of the common organic solvents such as acetic acid [41]. As a consequence, the use of chitin is limited, and it is often converted to its derivative chitosan. Chitosan has a pKa value of 6.2, meaning that when the pH is above this value, its amino groups ( $\text{NH}_2$ ) are protonated ( $\text{NH}_3^+$ ) and chitosan becomes cationic and soluble. The cationic nature of chitosan is rather special, since most of the natural polysaccharide are either neutral or negatively charged when dissolved in acidic environment. This property allows chitosan to form electrostatic complexes with negatively charged polymers [47]. Furthermore, chitosan presents a high number of reactive amino ( $\text{NH}_2$ ) and hydroxyl ( $\text{OH}$ ) groups, which can be easily chemically modified to produce chitosan derivatives [49]. Commercially, chitin is mainly extracted from crustaceans and, in a minor part, from fungi. However, the interest in insects as an alternative source of chitin and chitosan is growing [91]. The investigation of alternative renewable sources is an active field of research that could not only lead to their commercialization but also the identification of products with different properties and applications. When new sources are identified, it is necessary to characterize the physicochemical properties of the resulting product chitin and investigate its stability over the years. In fact, all the sources (*i.e.* the exoskeleton of arthropods) are usually composed of the same elements (*i.e.* chitin, proteins, minerals and pigments), whose relative abundance is usually source-specific. However, the precise amounts can vary due to environmental causes and lead to chitin with different physicochemical properties. Green *et al.* [102], for example, reported that within the same source (in this case crustacean shells), the content in minerals, proteins and chitin, as well as the physicochemical properties of the latter, can differ based on the season when the shells are collected. In another study, Youn *et al.* [103] compared the chitosan obtained from shells of crabs harvested in three different years and seasons showing that their physicochemical characteristics slightly differed depending on the harvest year. Among the physicochemical characteristics, the DA/DD and the crystallinity index (CrI) are the ones that mostly influence the physical, chemical and biological properties of chitin and its derivative chitosan. In a previous study, we extracted chitin from *Cicada orni* sloughs harvested in the south-eastern French Mediterranean basin in 2017 and we characterized its physicochemical properties (*i.e.* its DA and CrI) using two simple techniques such as Fourier-transform infrared spectroscopy (FTIR) and X-Ray Diffraction (XRD) [104]. For the first time to our knowledge, we used the same techniques to analyze the raw material (*i.e.* cicada sloughs) and the intermediary products of the extraction process (*i.e.* demineralized and deproteinized products) to assess the efficiency of the extraction process. We suggested that these analyses could be used to compare different extractions among them [104]. Here, we compare the physicochemical properties of chitin extracted from cicada sloughs harvested in two different years (2019 and 2020) in order to evaluate the repeatability of the extraction process and the stability of the source. We found that the physicochemical properties of the chitin obtained varied from year to year, and that these differences are not due to the extraction process but rather to

intrinsic variations within the source. Furthermore, we found that these differences could already be detected by analyzing the raw material (*i.e.* cicada sloughs) using the above-mentioned simple methods. Subsequently, we deacetylated the chitin extracted from cicada sloughs harvested in 2020, to obtain chitosan, and compared it to three commercially available chitosan, in order to assess the effectiveness of the deacetylation process. We found that it has a low degree of deacetylation, which can be attributed to the extraction process which is probably not appropriate for the deacetylation of this source.

## 2.2.3 Materials and Methods

### 2.2.3.1 Materials

*Cicada orni* sloughs were harvested during the summer of 2017, 2019 and 2020 in the south-eastern French Mediterranean basin (PinRolland - La Seyne sur Mer). Chitosan 80/200 (ref. 23405), chitosan 90/10 (ref. 23601), chitosan 95/500 (ref. 23706) were obtained from Heppe Medical Chitosan GmbH. Chitin (ref. C7170), Acetic acid (ref. 33209) and Hydrochloric acid (HCl) (ref. 30721) were obtained from Sigma-Aldrich. Sodium hypochlorite (ref. 33369) was purchased from Alfa Aesar. Sodium hydroxide (NaOH) (ref.28244) was purchased from VWR Chemicals.

### 2.2.3.2 Extraction of chitin

Chitin was extracted from *Cicada orni* sloughs as previously described [104]. Briefly, cicada sloughs were washed with distilled water, dried at 50°C for 24 hours in a drying oven and then mechanically grounded in a mortar. The powder (raw material) was then demineralized using 1M HCl aqueous solution under agitation at 30°C at 200 rpm for 2 hours. The sample was then filtered and washed with deionized water until neutral pH was detected. Subsequently, the demineralized sample was treated with a solution 1M NaOH heated at 90°C under reflux for 2 hours to remove proteins. Again, the sample was filtered and washed extensively with deionized water until neutral pH was reached and dried in a drying oven at 50°C for 24 hours. Finally, the deproteinized sample was treated with a solution 1% of sodium hypochlorite (NaClO) for 30 minutes at 25°C, filtered, washed with distilled water, and treated two additional times with 1% NaClO for 10 minutes, until the solution was transparent. After this last step, the decolorized sample (chitin) was extensively washed to reach neutral pH and remove any residual chemicals and dried again in a drying oven at 50°C for 24 hours.

### 2.2.3.3 Deacetylation to obtain chitosan

The deacetylation process was performed according to Luo *et al.* [92]. Briefly, the chitin extracted from cicada sloughs harvested in 2020 has been treated with a 60% NaOH solution, at 100°C (oil bath) for 8 hours under continuous stirring. The sample was then filtered, washed with deionized water until neutral pH was reached and placed in a drying oven at 50°C for 24 hours.

### 2.2.3.4 Fourier Transformed Infrared Spectroscopy (FTIR)

Powdered samples (demineralized and deproteinized products and chitin obtained from the extractions performed on cicada sloughs harvested in 2019 and 2020, commercial chitin, as well as extracted and commercial chitosan) were used for the preparation of KBr pellets

(1 mg of the sample with 100 mg KBr). FTIR spectra were collected in a range of 400 to 4000  $\text{cm}^{-1}$  with a Nicolet 6700 Spectrophotometer, by the accumulation of 64 scans, with a resolution of 4  $\text{cm}^{-1}$ . However, only peaks from 400 to 2000  $\text{cm}^{-1}$  are shown in the results, since they are important for the calculation of the degree of deacetylation (DD) and for the investigation of the differences among the samples.

The DD was calculated according to the following equation:

$$DD(\%) = 100 - DA \quad (2.1)$$

where DA is the degree of acetylation. DA was calculated as proposed by Brugnerotto *et al.* [105] as following:

$$DA(\%) = \frac{\frac{A_{1320}}{A_{1420}} - 0.3822}{0.03133} \times 100 \quad (2.2)$$

where A1320 and A1420 are the absorbance values at 1320 and 1420  $\text{cm}^{-1}$  obtained by the FTIR spectra. For each type of chitin and chitosan were produced three KBr pellets and the results were presented as mean  $\pm$  standard deviation of three measurements.

### 2.2.3.5 X-Ray Diffraction (XRD)

Powdered samples (demineralized and deproteinized products and chitin obtained from the extractions performed on cicada sloughs harvested in 2019 and 2020, commercial chitin, as well as extracted and commercial chitosan) were used to collect X-ray diffraction (XRD) spectra. Data were collected at a scan rate of 1°/min and a scan angle from 5 to 40°, using a D8 Advance (Bruker, Billerica, MA, USA). The Crystallinity Index (CrI) was determined using the formula:

$$CrI(\%) = \frac{I_{110} - I_{am}}{I_{110}} \quad (2.3)$$

where  $I_{110}$  is the maximum intensity of the (110) diffraction peak in the crystalline region at 20° and  $I_{am}$  is the maximum intensity of amorphous diffraction at 16°.

### 2.2.3.6 Scanning Electron Microscopy (SEM)

The morphology of the samples were imaged using a Quanta 650-FEG (FEI, Hillsboro, OR, USA) scanning electron microscope. The samples in form of powder were dried in a drying oven at 50°C for 24 hours, fixed on an adhesive tape, gold sputter-coated and then imaged using an acceleration voltage of 5 kV.

## 2.2.4 Results

### 2.2.4.1 Abbreviations

Through the text, the samples will be abbreviated as follows: CH will refer to chitin and the following numbers 17, 19 and 20 will refer to the year on which the cicada sloughs were harvested. Therefore, CH-17 will refer to chitin extracted from cicada sloughs harvested in 2017 and CH-19 and CH-20 in 2019 and 2020, respectively. CS will refer to chitosan and the numbers 80, 90 and 95 will refer to their degree of deacetylation (DD) which was obtained

from the product specification sheet. Consequently, the three commercial chitosan will be labeled CS-80, CS-90 and CS-95.

#### 2.2.4.2 FTIR spectra of chitin and degree of acetylation

In a previous study [104], we analyzed the different steps of the extraction process (*i.e.* demineralization, deproteinization and decoloration) from cicada sloughs collected in 2017. The FTIR characterization showed that the raw material and the demineralized sample presented a single peak at approximately  $1660\text{ cm}^{-1}$ , while after the deproteinization two individual peaks appeared at  $1620\text{ cm}^{-1}$  and  $1660\text{ cm}^{-1}$ . This phenomenon was attributed to the removal of proteins since the peak at  $1660\text{ cm}^{-1}$  might be assigned to the amide I vibrational modes [106]. Furthermore, the presence of two individual peaks also suggested that the extracted chitin was the  $\alpha$ -polymorph (while the presence of a single peak was attributed to the  $\beta$ -polymorph [107]). In order to validate these observations, we collected the FTIR spectra of the raw material and of the intermediary products of the extraction of chitin from cicada sloughs harvested in 2019 and 2020 - see Supplementary Figure A1. We found that the FTIR spectra for the extractions performed on cicada sloughs harvested in 2019 and 2020 are very similar to each other. In both the extraction processes, the raw material and the demineralized product present only one peak at  $1660\text{ cm}^{-1}$  while two peaks appear at  $1620\text{ cm}^{-1}$  and  $1660\text{ cm}^{-1}$  for the deproteinized and decolorized products, confirming that proteins were efficiently removed, and that chitin is in its  $\alpha$ -polymorph. According to Jang *et al.* [101]  $\alpha$ -chitin has two types of hydrogen bonding: intra-sheet and inter-sheet. The absorption band at  $1660\text{ cm}^{-1}$  correspond to hydrogen bonding between the carbonyl groups (C=O) of amide I and amide II (NH) while the absorption band at  $1620\text{ cm}^{-1}$  correspond to the hydrogen bonding between the  $\text{CH}_2\text{OH}$  side chain and the carbonyl group (C=O). Since the amide I of proteins absorbs at wavelengths comprised between  $1600$  and  $1700\text{ cm}^{-1}$ , the presence of proteins and the interactions of the latter with chitin, lead to the appearance of a single peak, at wavelengths comprised between  $1620$  and  $1660\text{ cm}^{-1}$ , in the samples before deproteinization (*i.e.* raw material and demineralized sample). Here, in order to evaluate the quality of the final product (*i.e.* chitin extracted from cicada sloughs harvested in three different years, we compare the FTIR spectra (shown in Figure 2.1) of the samples CH-17, CH-19, and CH-20 among them and with a commercial chitin. The three extracted chitin present similar spectra and, in particular, very similar to the spectrum of the commercial chitin.

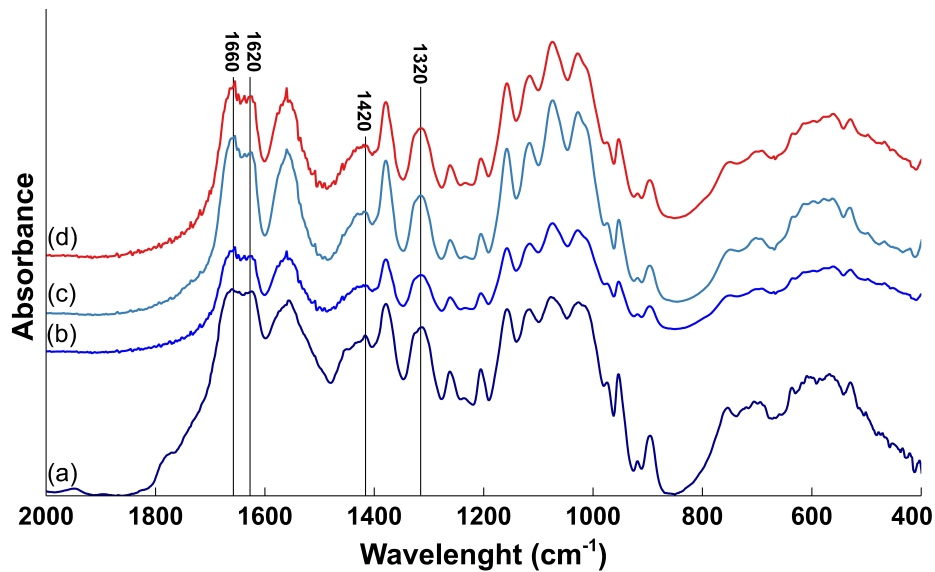


**Figure 2.1.** FTIR spectra of CH-17 (a), CH-19 (b), CH-20 (c) and of a commercial chitin (d).

The FTIR spectra were used for the measurements of the degree of acetylation (DA). In table 2.2 are presented the average DA of CH-17, CH-19 and CH-20. The results show that chitin extracted from cicada sloughs collected in three different years had a different degree of acetylation. In particular, CH-17 and CH-19 were more acetylated than CH-20, suggesting that chitin extracted from cicada sloughs harvested in 2020 was different from the others.

	CH-17	CH-19	CH-20
DA %	$96.3 \pm 3.4$	$102.7 \pm 5.5$	$74.7 \pm 3.1$

**Table 2.2.** Average degree of acetylation (DA) of CH-17, CH-19 and CH-20.

To better understand if the difference in the DA is due to the extraction process or to an intrinsic difference within the source, we compared the FTIR spectra of the raw materials (cicada sloughs) harvested in 2017, 2019 and 2020. Results (shown in Figure 2.2) evidence a major difference in the peaks at  $1420 \text{ cm}^{-1}$  and  $1375 \text{ cm}^{-1}$ . In fact, these two peaks show an opposite conformation in the three spectra with the peak at  $1375 \text{ cm}^{-1}$  being less intense than the peak at  $1420 \text{ cm}^{-1}$  for CH-20 compared to CH-17 and CH-19. The peak at  $1375 \text{ cm}^{-1}$  can be attributed to  $\text{CH}_3$  deformations typical of chitin (in particular, typical of the acetyl group) while the peak at  $1420 \text{ cm}^{-1}$  can be attributed to the  $\text{CH}_2$  bending. Since the amount of  $\text{CH}_2$  groups does not change according to the degree of acetylation, we can suppose that the different conformation of these two peaks is only given by a change in the amount of  $\text{CH}_3$  groups and, consequently, in the amount of acetyl groups which is lower in CH-20 compared to CH-17 and CH-19. As a result, the DA of the final product, chitin, is lower for CH-20 compared to CH-17 and CH-19.

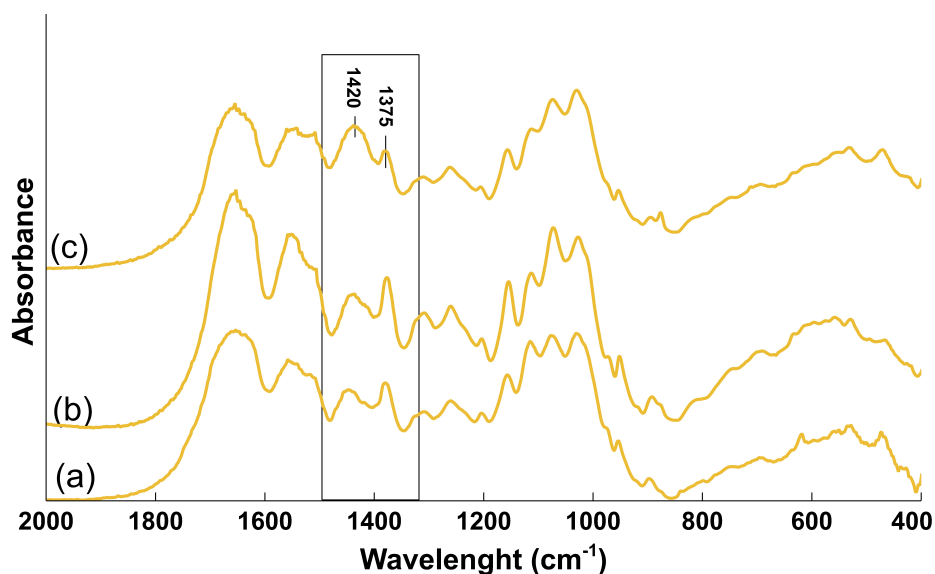


**Figure 2.2.** FTIR spectra of raw material (cicada sloughs) harvested in 2017 (a), 2019 (b) and 2020 (c).

### 2.2.4.3 XRD spectra of chitin and evaluation of the cristallinity index

As resulted from studies based on their supramolecular structure, chitin and chitosan, in solid state, are linear semicrystalline polymers [108]. Chitin macromolecules interact through hydrogen bonds to form nanofibrillar bundles called microfibrils, characterized by alternated ordered crystallites and non-ordered (amorphous) domains [109]. Figure 2.3 shows the XRD spectra of chitin extracted from cicada sloughs harvested in 2017, 2019 and 2020 as well as the spectrum of commercial chitin. All samples present similar spectra with peaks at  $2\theta$  of about  $8.9^\circ$  from (020) planes,  $12.5^\circ$  from (021) planes and  $18.9^\circ$  for from (110) planes of crystalline unit cells and some additional weak peaks (*i.e.*  $25.9^\circ$  from (130) planes).

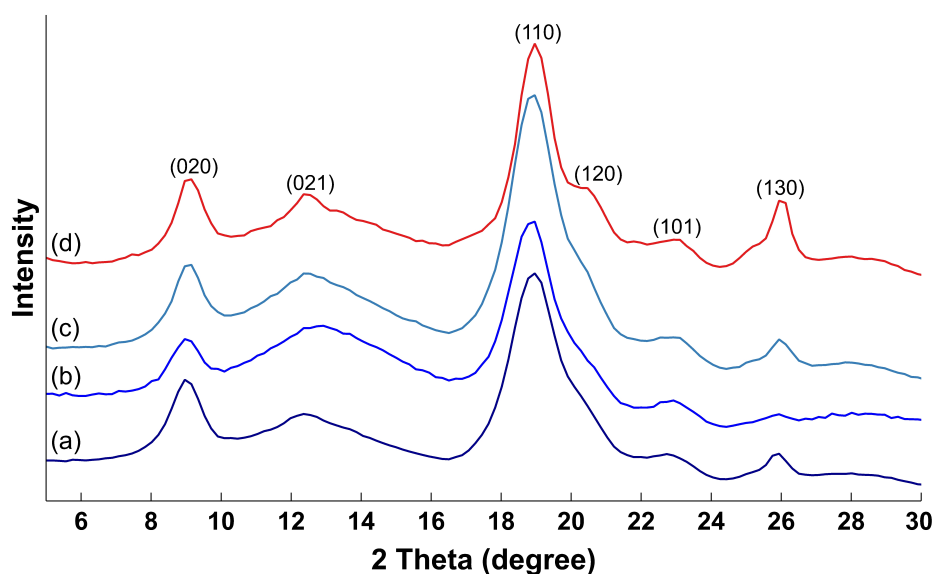


**Figure 2.3.** XRD spectra of CH-17 (a), CH-19 (b), CH-20 (c) and of a commercial chitin (d).



In a previous study [104] we analyzed the XRD spectra and measured the CrI not only of the final product chitin, but also of the intermediary products of the extraction process (demineralization, deproteinization and decoloration) performed on cicada sloughs harvested in 2017. Here, we do the same with cicada sloughs harvested in 2019 and 2020. The XRD spectra of raw material, demineralized, deproteinized and decolorized samples extracted from cicada sloughs collected in 2019 and 2020 are shown in Supplementary Figure A2. We evidenced no particular differences among the XRD spectra of the intermediary products deriving from the extractions performed on the three different lots. Nevertheless, the measure of the CrI value shows interesting results concerning the evolution of the crystallinity of the products during the extraction processes. Table 2.3 shows the CrI values for the intermediary products of the extraction performed on cicada sloughs collected in 2017 (data reused from [104]), 2019 and 2020. The three lots (2017, 2019 and 2020) showed the same trend with the crystallinity slightly decreasing from the raw materials to the demineralized ones, increasing from the demineralized to the deproteinized and being almost stable from the deproteinized to the decolorized (chitin). According to these results, chitin extracted from cicada sloughs collected in 2017 has a greater crystallinity (72.1) compared to the chitin extracted from sloughs collected in 2019 and 2020 (61.5 and 61.6 respectively). However, it has to be noticed that the decrease in the value of crystallinity for the chitin extracted from cicada sloughs harvested in 2019 and 2020, compared to the one extracted from cicada sloughs collected in 2017, is due to a different initial value of crystallinity in the raw materials (that was 68.6, 56.4 and 56.1 for chitin 2017, chitin 2019 and chitin 2020, respectively). The trend of the crystallinity value through the extraction process suggests that the extraction process produces coherent results, even if the sources (*i.e.* raw materials) differ among them.

	2017	2019	2020
Raw material	68.6	56.4	56.1
Demineralized	55.8	54.2	49.4
Deproteinized	73.4	65.2	62.5
Decolorized	72.1	61.5	61.6

**Table 2.3.** Crystallinity index (CrI) % of raw material, demineralized, deproteinized and decolorized samples extracted in 2017, 2019 and 2020.

#### 2.2.4.4 Scanning electron microscopy

Figure 2.4 shows the SEM images of raw material, demineralized and decolorized (chitin) samples from extractions performed on cicada slough harvested in 2019 and 2020 (for SEM images of extraction performed on cicada sloughs harvested in 2017, refer to the previously published paper [104]). Raw materials present a high amount of granular material, which could be attributed to calcium carbonate crystals. In fact, after the demineralization process, the surfaces appear smoother, suggesting an efficient removal of minerals. On the surface of the final decolorized product (chitin) is possible to observe the thick chitin micro- and nano-fibers.

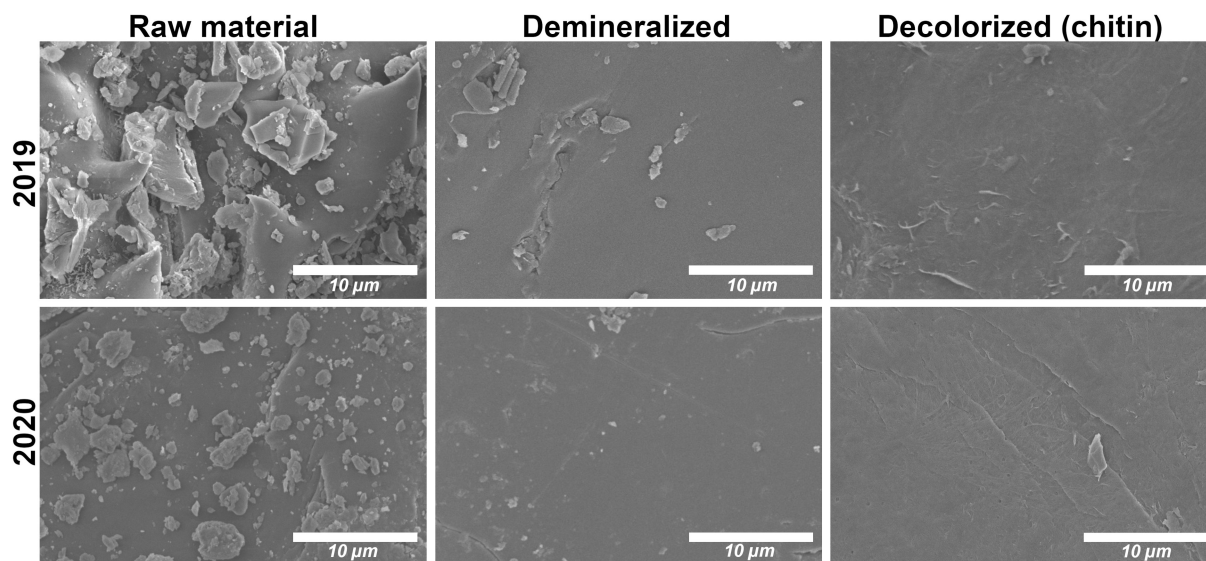


**Figure 2.4.** SEM images of raw material, demineralized and decolorized samples deriving from the extraction of chitin from cicada sloughs harvested in 2019 and 2020.

#### 2.2.4.5 Characterization of the extracted chitosan

Chitin extracted from cicada sloughs collected in 2020 has subsequently been deacetylated to obtain chitosan. In order to assess the effectiveness of the deacetylation process and to characterize the extracted chitosan, the FTIR spectrum of the latter has been compared to the spectra of three commercial chitosan (CS-80, CS-90 and CS-95). Even though the spectra (shown in Figure 2.5) present high similarities among them, the extracted chitosan shows two additional peaks at  $1556$  and  $1631\text{ cm}^{-1}$ . According to Dahmane *et al.*, [110] the peak at  $1631\text{ cm}^{-1}$  may indicate a specific hydrogen bond between  $\text{C}=\text{O}$  and the hydroxymethyl group ( $\text{CH}_2\text{-OH}$ ) of the next chitin residue of the same chain. Since  $\text{C}=\text{O}$  belong to the acetyl group, which is characteristic of chitin rather than chitosan, its presence suggests that a high amount of acetyl groups are still present in the extracted chitosan. Dahmane *et al.*, [110] also report that after the deacetylation of chitin, the peak at  $1556\text{ cm}^{-1}$ , corresponding to amide II (N-H bending), disappeared along with the appearance of a new sharp peak at  $1595\text{ cm}^{-1}$  ( $\text{NH}_2$  bending). Since these two peaks (*i.e.*  $1556$  and  $1631\text{ cm}^{-1}$ ) are more characteristics of chitin rather than chitosan, their presence suggests that the deacetylation process was only partially efficient. This can be confirmed by observing the peak at  $1320\text{ cm}^{-1}$  which is more intense for the extracted chitosan while its intensity decreases as the DD increases (CH-95 has the less intense peak). This is due to the fact that the peak at  $1320\text{ cm}^{-1}$  corresponds to the N-acetyl-D-glucosamine which belongs to chitin (and for this reason included in the calculation of the DA/DD [105]).

The degree of deacetylation of the four chitosan samples has been calculated using the equation 2.1 and 2.2 from their FTIR spectra. In order to assess the accuracy of the calculation of the DD for the extracted chitosan, we used the same method to calculate the DD of the three commercial chitosan (whose DD was stated in the product specification sheet obtained from Heppel Medical Chitosan, HMC<sup>+</sup> (refer to section 2.2.3.1)). Table 2.4 shows the measured average DD of the extracted chitosan, CS-80, CS-90 and CS-95 as well as their DD obtained from the product specification sheets. The results show that the FTIR method employed for the calculation of the DD is highly efficient for chitosan with high

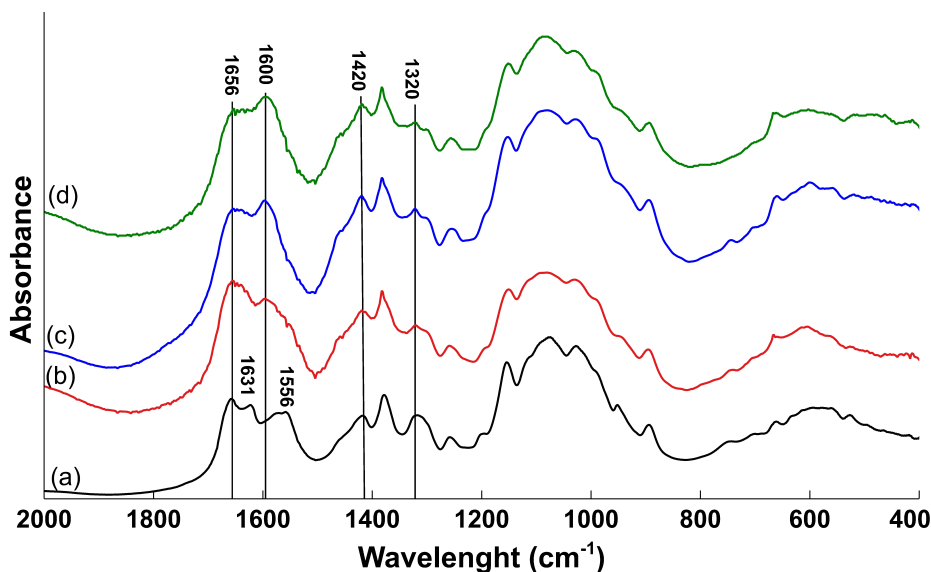


**Figure 2.5.** FTIR spectra of: (a) extracted chitosan, (b) CS-80, (c) CS-90 and (d) CS-95.

DD. In fact, the measured value of DD for CS-90 and CS-95 ( $91.1 \pm 1.1$  and  $93.7 \pm 0.7$ , respectively) falls in the expected values of DD indicated by the company HMC<sup>+</sup> ( $87.6-92.5$  % and  $\geq 92.6$  %, respectively). However, for the CS-80, we measured a higher DD ( $89.9 \pm 1.6$  %) compared to the expected one ( $77.6-82.5$  %). According to the employed method, the extracted chitosan has a degree of deacetylation of  $66.2 \pm 1.6$  %. The low DD measured is not surprising considering the presence of the peaks at  $1320$ ,  $1556$  and  $1631$   $\text{cm}^{-1}$  described above.

	Extracted chitosan	CS-80	CS-90	CS-95
DD %	$66.2 \pm 1.6$	$89.9 \pm 1.6$	$91.1 \pm 1.1$	$93.7 \pm 0.7$
Expected DD %		$77.6 - 82.5$	$87.6 - 92.5$	$\geq 92.6$

**Table 2.4.** Measured average degree of deacetylation (DD) of chitosan extracted from cicada sloughs harvested in 2020 and of three commercial chitosan with known DD (CS-80, CS-90 and CS-95).

We then looked at the crystallinity of the extracted chitosan. The XRD spectra of the extracted chitosan, CS-80, CS-90 and CS-95 are shown in figure 2.6. All the spectra are very similar and present peaks at approximately  $12^\circ$  from (020) plane and  $19.5^\circ$  from (110) plane, which are characteristics of chitosan. The peak at approximately  $12^\circ$  is indicative of the efficiency of the deacetylation process. In fact, while chitin (which is more crystalline than chitosan) present two distinct peaks at  $8.9^\circ$  and  $12.5^\circ$  (see Figure 2.6), chitosan only presents one large peak between  $11.6$  and  $12.7^\circ$  [111]. Our result shows that the extracted chitosan still presents a small peak at  $8.9^\circ$  from (020) plane, suggesting that the deacetylation process was not totally efficient. The peak at approximately  $19.5^\circ$  from (110) reflection is representative of the DD and it moves to higher angles while the DD increases. In fact, the peak at  $18.9^\circ$  of chitin (see Figure 2.3), moves to  $19.1^\circ$  for the extracted chitosan, to  $19.7^\circ$  for CS-80, to  $19.9^\circ$  for CS-90 and to  $20^\circ$  for CS-95. These results confirm that chitin was only partially deacetylated using this deacetylation process and that the extracted chitosan has a lower DD compared to the commercial ones.

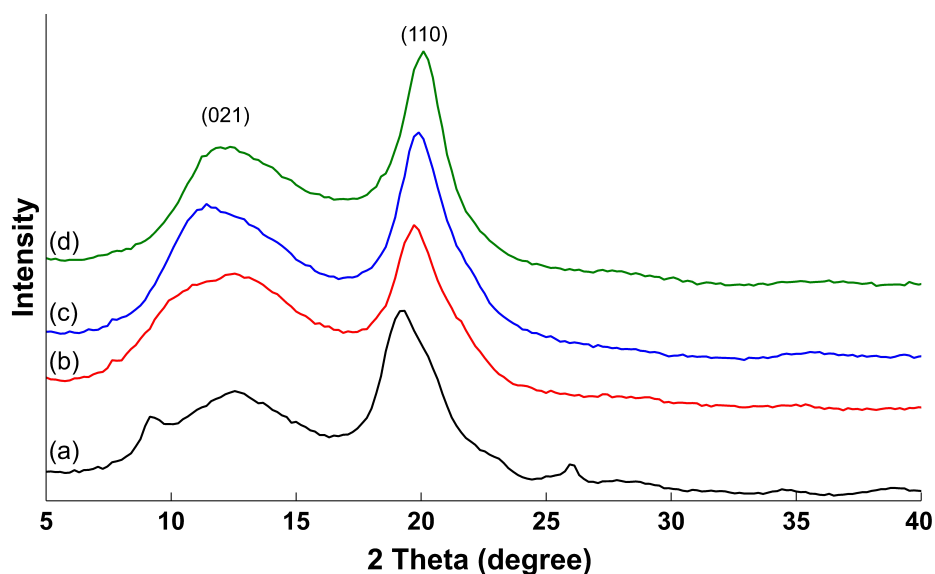


**Figure 2.6.** XRD of: (a) extracted chitosan, (b) CS-80, (c) CS-90 and (d) CS-95.

Subsequently, we calculated the crystallinity index (CrI) of the extracted chitosan, CS-80, CS-90 and CS-95. The results are shown in Table 2.5. The extracted chitosan presented a higher CrI compared to CS-80, CS-90 and CS-95. Several studies report that there is an indirect correlation between the DD and CrI with the CrI decreasing with increased DD [112, 113], while other studies show opposite trends [114, 115]. According to Wu *et al.* [116], this is due to the fact that fewer acetyl groups are present, more randomly they are distributed and, consequently, the development of broad crystalline regions is not allowed, while other studies show opposite trends [113]. We found that the CrI increased with increased DD for the commercial chitosan (CS-80 has a lower CrI compared to CS-90 and CS-95). However, the extracted chitosan does not follow the same trend. On the contrary, the CrI of the extracted chitosan was more similar to the CrI found for chitin (CH-20, which was 61.6%), suggesting that the deacetylation was only partially efficient.

	<b>Extracted chitosan</b>	<b>CS-80</b>	<b>CS-90</b>	<b>CS-95</b>
CrI (%)	53.7	42.8	49.4	49.4

**Table 2.5.** Crystallinity index of the extracted chitosan and CS-80, CS-90 and CS-95.

Figure 2.7 shows SEM images of extracted chitosan, CS-80, CS-90 and CS-95. The surface morphology of the four samples is similar and presents a fibrillar structure. However, the nano-fibers of the extracted chitosan are less evident compared to the commercial samples.

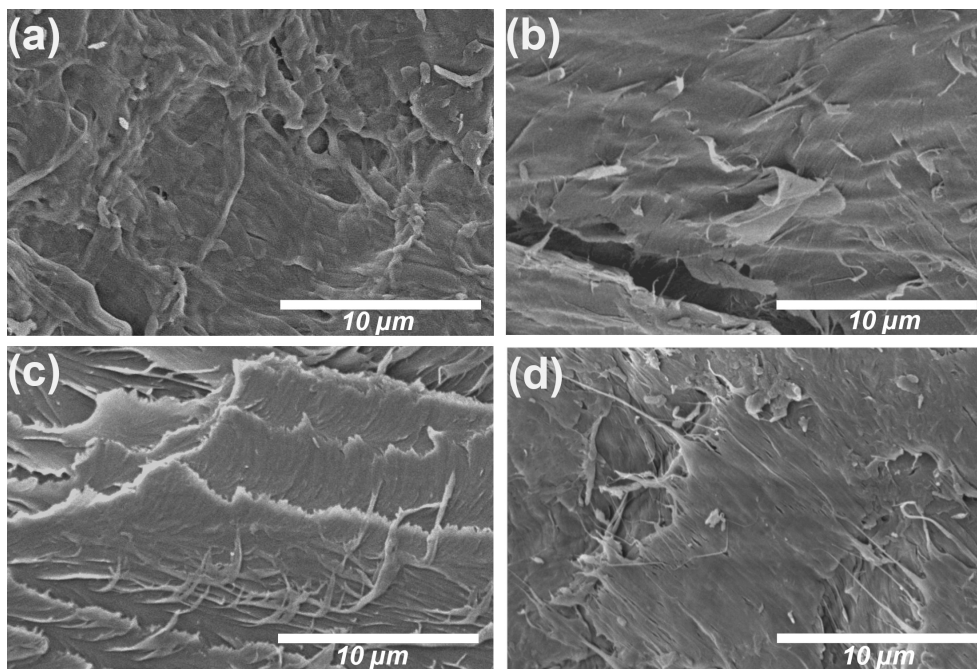


**Figure 2.7.** SEM images of extracted chitosan (a), CS-80 (b), CS-90 (c) and CS-95 (d).

### 2.2.5 Discussion

In this study, chitin extracted from cicada sloughs harvested in two different years (2019 and 2020) has been characterized from a physicochemical point of view and compared to the chitin extracted from cicada sloughs harvested in 2017, the results of which are reported in a previous study [104]. The main objective of this comparison was to assess the stability of cicada sloughs as a source of chitin and to evaluate the efficiency of the extraction process. For that, we evaluated two of the parameters that mostly influence the chemical, physical and biological behavior of chitin and its derivative chitosan: the degree of acetylation/deacetylation (DA/DD) and the index of crystallinity (CrI) using simple techniques such as FTIR and XRD (see the supplementary information (2.2.7) for clarification on the methods used for the calculation of DD/DA and CrI).

Our results show that chitin extracted from cicada sloughs harvested in 2020 has a significantly lower degree of acetylation compared to chitin extracted from cicada sloughs collected in 2017 and 2019. Other authors reported variabilities within the source harvested in different years or seasons. For example, Youn *et al.* [103] reported that the degree of deacetylation of chitosan obtained from the transformation of chitin extracted from shells of crabs harvested in three different seasons and years (July 2004, January 2005, and September 2007) was slightly different: 89.01%, 84.11% and 82.49% for the three seasons, respectively. However, in addition to having been harvested in three different years and seasons, samples (crab shells) were stored for different time before being characterized, and in particular for 3.5 years, 3 years and 3 months, respectively for shells harvested in July 2004, January 2005, and September 2007. The results showed that chitosan having longer storage time presented higher DD. However, the authors of the study were unable to conclude if the differences were due to the storage time or to the season or year of collection of crab shells. In another study, Green *et al.* [102], reported that within the same source (that in their case was crustacean

shells), the content in minerals, proteins and chitin and the physicochemical properties of the latter can differ based on the season when the shells are collected. However, again, there is no information about how the different compositions in minerals, proteins and chitin would influence the characteristics of the final product chitin, in terms of degree of acetylation. In order to better analyze the differences that we found in the degree of acetylation of chitin extracted from cicada sloughs in different years, we compared the FTIR spectra of the raw materials (*i.e.* cicada sloughs). We found that two specific peaks (at 1420 and 1375  $\text{cm}^{-1}$ ) have an opposite conformation in the sample CH-20 as compared to CH-17 and CH-19 which might justify the lower degree of acetylation of CH-20. However, the reasons for the lower degree of acetylation are unknown and further investigations are needed to understand the relation between DA/DD and, for example, abundance and structural organization of proteins and minerals within the source.

Concerning the crystallinity, we found that chitin extracted from cicada sloughs collected in 2017 has a greater crystallinity compared to the ones extracted from cicada sloughs harvested in 2019 and 2020. The evaluation of the CrI measured for the raw material showed that also the raw material of cicada sloughs harvested in 2017 had a greater crystallinity compared to the raw materials of cicada sloughs collected in 2019 and 2020. This result suggests that, within the source, chitin might be organized differently, or sloughs have a different composition (in terms of proteins and minerals) giving rise to a more or less crystalline structure [97]. The evaluation of the CrI and for the intermediary products resulting from the extraction of chitin (*i.e.* demineralized, deproteinized) gave us some important information about the repeatability of the extraction process. In fact, the trend of crystallinity displayed by these products (*i.e.* decreasing after demineralization, increasing after deproteinization being almost stable after decoloration) suggests that the extraction process produces coherent results.

We then performed the deacetylation of chitin in order to obtain chitosan using a previously published protocol [92]. We compared the FTIR and XRD spectra and the resulting measured DD and CrI values of the extracted chitosan to three commercial chitosan with known DD. We found that the method employed in this study for the calculation of the DD was efficient for chitosan with high DD (90 and 95 %) while it was less precise for chitosan with lower DD (80 %). Using this method, the DD that we measured for the extracted chitosan was  $66.2 \pm 1.6$  %. Even if the molecule extracted could be considered as chitosan (since the DD is higher than 50 %), this result suggests that the deacetylation process was not the most appropriate for the deacetylation of this source. Luo *et al.* [92], by using the same protocol for the deacetylation of chitin extracted from cicada sloughs, obtained a chitosan with a DD of 84.1%. However, in their study, the DD was calculated using different absorbance peaks of the FTIR spectra which might lead to different results. Concerning the crystallinity, we found that the extracted chitosan had a higher CrI compared to the commercial chitosan. Several studies show a tendency of the DD and CrI to be indirectly related with higher DD showing lower CrI [112, 116]. However, other studies show an opposite trend [114, 115] and this relation is still an object of discussion. The methods employed in this study for the calculation of the DA/DD and CrI present some limitations. In fact, more sophisticated techniques such as Nuclear Magnetic Resonance (NMR) spectrometry and X-ray photoelectron spectroscopy (XPS) would allow us to obtain more precise measurements of the degree of acetylation and alternative methods for the calculation of the CrI have been proposed in the literature (*i.e.* the use of the peak  $I_{020}$  in the Equation (2.3) instead of  $I_{110}$

[112]). However, when applied uniformly, the FTIR and XRD methods employed in this study are highly efficient to compare multiple samples among them. The characterization, in particular, of the DD of chitosan, is essential since it influences its possible applications [117]. In the biomedical field, DD is one of the most important properties of chitosan since most of its biological properties are attributed to its cationic behavior, which depends on its DD. In fact, in acidic solutions, the amine groups ( $\text{NH}_2$ ) of chitosan acquire a positive charge ( $\text{NH}_3^+$ ) [50]. This property makes chitosan the only naturally cationic polysaccharide, allowing it to form polyelectrolyte complexes with negatively charged polymers [47]. Several studies investigated the effect of different DD for different applications. Some authors report that chitosan with high DD is more suitable for tissue engineering [118] because usually constructs made of chitosan with lower DD degrade faster, leading to less supportive healing. However, other studies reported the higher the DD of chitosan, the lower was the adhesion of keratinocytes and fibroblasts on chitosan films [119]. Chitosan is also highly used as a vehicle for nucleic acid or drug delivery (in form of nano- or micro-particles). Sizovs *et al.* [120] reported that a degree of deacetylation of at least 65% is required for an efficient transfection with the desirable value being in the range of 65–80%. Gupta *et al.* [121] showed that microspheres prepared using chitosan with a DD comprised between 48–62% presented a higher drug loading capacity.

### 2.2.6 Conclusions

In this work, we compared the physicochemical properties (*i.e.* degree of deacetylation and crystallinity index) of chitin extracted from *Cicada orni* sloughs harvested in three different years in order to assess the repeatability of the extraction process and the stability of cicada sloughs as a source of chitin. We found that the extracted chitin presented different physicochemical characteristics from one year to another and that this variability seems not to be dependent on the extraction process, but rather on intrinsic differences within the source, as suggested by the results obtained on the raw material (*i.e.* cicada sloughs) through FTIR and XRD analysis. The methodology employed in this study, based on the evaluation of the raw material and the resulting intermediary products of the extraction (*i.e.* demineralized and deproteinized products) in terms of FTIR spectra and trends of crystallinity, could be extended to the evaluation of the quality of other sources and the effectiveness of different extraction protocols. We then determined the physicochemical properties of chitosan and found that it has a low degree of deacetylation ( $66.2 \pm 1.6$ ), which can be attributed to the deacetylation process which is probably not appropriate for this source. Further studies should be conducted to understand the causes of the variability in cicada sloughs over the years and to optimize the protocol of deacetylation in order to obtain chitosan with a higher degree of deacetylation.

## 2.2.7 Supplementary information

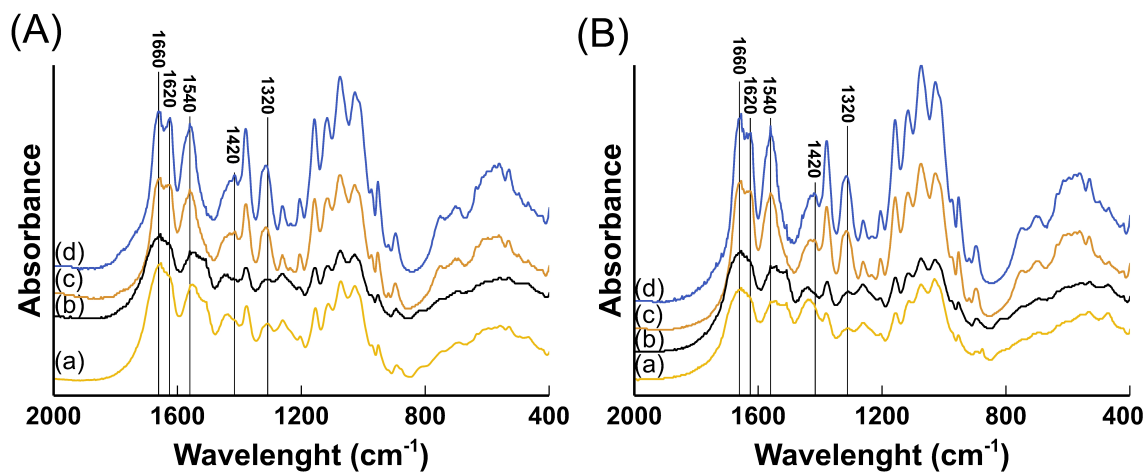


**Figure A1.** FTIR spectra of raw material (a), demineralized (b), deproteinized (c) and decolorized (d) samples extracted in (A) 2019 and (B) 2020.

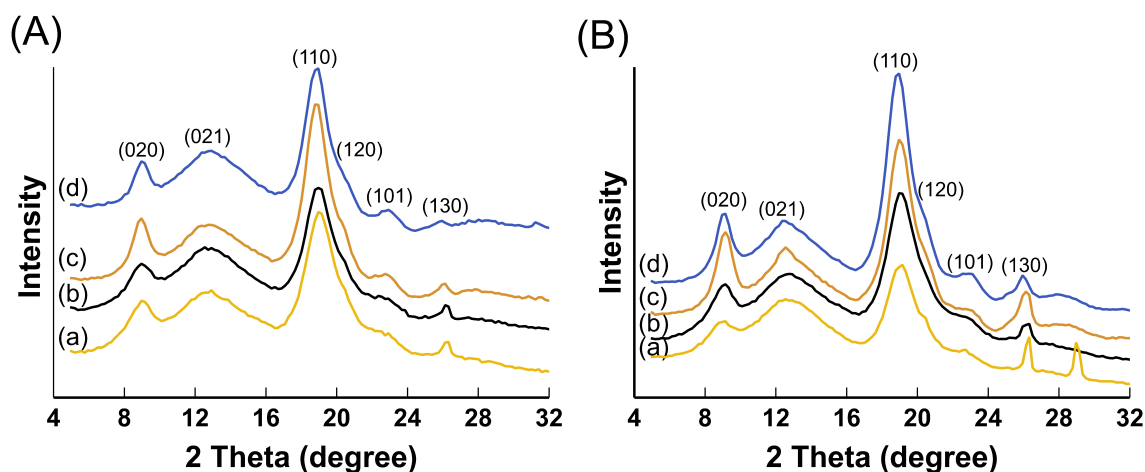


**Figure A2.** XRD spectra of raw material (yellow), demineralized (black), deproteinized (orange) and decolorized (blue) samples extracted in (A) 2019 and (B) 2020.

### Clarification on the methods used for the calculation of DD/DA and CrI:

The methods employed for the determination of DA/DD and crystallinity are still object of discussion since different methods often show different results. The most precise measurement of DA/DD can be done using NMR (nuclear magnetic resonance) spectrometer. However, it is a sophisticated and expensive instrument and not always available. The easiest and economical method for the determination of DA/DD is Fourier Transformed Infrared Spectroscopy (FTIR). Brugnerotto *et al.* [105] conducted a detailed infrared spectroscopy study in order to select the absorbance bands optimal for the determination of the DA/DD. They used FTIR technique to individually analyze, the spectra of N-acetyl-D-glucosamine (acetylated unit) and of D-glucosamine (deacetylated unit) which are the repeated units of chitin and chitosan, and found the specific peaks for each of them. Comparing both spectra,



they found that a band, specific for N-acetyl-D-glucosamine appears at  $1320\text{ cm}^{-1}$  while different reference peaks were evaluated, including the peak at  $1420\text{ cm}^{-1}$ . Subsequently, they measured the ratio of selected absorbance peaks and calculated the degree of acetylation and compared the results to the ones obtained by NMR. They found that the result obtained using the ratio between the absorbance bands at  $1320\text{ cm}^{-1}$  and  $1420\text{ cm}^{-1}$  was the one most in agreement with the results obtained by the NMR. In this and the previous study, the absorbance bands proposed by Brugnerotto were employed for the measurement of the DA/DD.

The crystallinity index (CrI) represents the easiest evaluation of the crystallinity properties. This is usually based on calculations of the ratio of the peak  $I_{110}$ , which represents the maximum intensity of the (110) diffraction plane in the crystalline region at  $20^\circ$  and  $I_{am}$ , which represents the maximum intensity of amorphous diffraction at  $16^\circ$ . Since the evaluation of the CrI is dependent on the method employed for its calculation, results about the crystallinity values based on estimation of CrI are doubtful [109]. CrI only indicates which of the samples has greater crystallinity and which less crystallinity but it does not give any further information about the crystalline properties. However, when no deep information is required for the study, selecting one method for the calculation of the CrI and applying it uniformly, represent a good method to compare the content of crystalline fraction in different samples [109].

## Conclusions clé

- La chitine a été extraite des mues de *Cicada orni* récoltées dans le bassin méditerranéen du sud-est de la France (Var) et représente le 42,6 % de leurs poids, ce qui signifie qu'il s'agit d'une souche riche de chitine.
- Nous avons proposé, pour la première fois à notre connaissance, une analyse détaillée de la chitine extraite des mues de cigale ainsi que de toutes les étapes de l'extraction. En effet, la matière première (*i.e.* les mues de cigale) et les produits intermédiaires de l'extraction tels que le produit déminéralisé et déprotéinisé ont été caractérisés afin d'évaluer l'efficacité du procédé d'extraction et de pouvoir comparer différentes extractions entre elles.
- Nous avons ensuite comparés les produits obtenus de l'extraction de chitine à partir des mues de cigale collectées en trois années différentes (2017, 2019 et 2020). Nous avons trouvé que les propriétés physico-chimiques de la chitine obtenue, en termes de degré de désacétylation et d'indice de cristallinité, variaient d'une année sur l'autre. Ces différences ne semblent pas être dues au processus d'extraction, en considérant qu'elles pouvaient déjà être détectées par l'analyse de la matière première (c'est-à-dire les mues de cigale). Nos résultats suggèrent que ces différences sont dues à une variabilité intrinsèque des sources qui pourrait dépendre de plusieurs facteurs, tels que les changements climatiques, ou encore la disponibilité alimentaire. En effet, bien que généralement chaque espèce ait un nombre défini de mues, pour certaines d'entre elles, ce nombre peut varier en fonction des caractéristiques environnementales et être par exemple plus rapides si les disponibilités alimentaires sont abondantes ou plus lentes si elles sont plus rares. Par conséquent, on peut imaginer que toutes les mues n'aient pas la même composition en chitine, minéraux et protéines et que la chitine elle-même n'ait pas toujours les mêmes caractéristiques physicochimiques.
- La désacétylation de la chitine a conduit à la production d'un chitosane avec un faible degré de désacétylation ( $66.2 \pm 1.6$  %). Cela semble être dû au processus de désacétylation qui n'est pas optimal pour notre source.

## Perspectives

Les méthodes de caractérisation utilisées dans l'évaluation de la stabilité temporelle des mues de cigales comme source de chitine, pourrait également être étendu à l'évaluation de la qualité d'autres sources, ou à l'efficacité de différents procédés d'extraction. Concernant la transformation de chitin en chitosane, celle-ci a conduit à un chitosane avec un faible degré de désacétylation, qui a une faible solubilité dans les solvants communément utilisés pour le dissoudre. Par conséquent, il serait nécessaire d'évaluer des différentes conditions de désacétylation tels que l'utilisation de concentrations plus élevées de NaOH, des températures plus élevées ou un temps de réaction plus long. Cependant, un tel environnement conduirait à l'hydrolyse du chitosane et abaisserait son poids moléculaire. Celui-ci, avec le degré d'acétylation, influence fortement les propriétés rhéologiques, biologiques et physico-chimiques du chitosane telles que sa biodégradabilité. Par conséquent, l'évaluation du poids moléculaire devrait être envisagé à l'avenir. La mise en œuvre de plans d'expérience

impliquant différentes conditions d'extraction pourrait être réalisée afin de relier le degré de désacétylation et le poids moléculaire et de sélectionner les caractéristiques souhaitées.



## Chapter 3

# Development of new biomaterial inks made of chitosan and guar gum or tamarind gum

## Développement de nouvelles encres pour la bio-impression 3D à base de chitosane et gomme de guar ou gomme de tamarin

Dans le chapitre précédent, nous avons montré que les mues de cigale représentent une source intéressante et riche en chitine. La chitine, suite à un processus de désacétylation, peut être transformée en chitosane qui, en raison de sa biocompatibilité, sa biodégradabilité et sa faible toxicité [47], est largement utilisée pour différentes applications d'ingénierie tissulaire. Dans le cadre de cette thèse nous nous sommes intéressés à l'utilisation du chitosane pour une technologie en particulier, la bio-impression 3D par extrusion. *(NB: Notre objectif initial était d'utiliser le chitosane précédemment extrait des mues de cigales en tant que matériel de base pour le développement de nouvelles encres. Cependant, étant donnée que la quantité de matière première n'était pas suffisante et que le bas degré de désacétylation ( $66.2 \pm 1.6$  %) de ce chitosane limite sa solubilité dans des solvants organiques tels que d'acide acétique, nous avons utilisé un chitosane commercial (avec un DD compris entre 87.6 - 92.5 %) pour les études ultérieures.)*

La technologie de la bio-impression 3D se base sur l'utilisation de biomatériaux, cellules et/ou des facteurs de croissance (et appelées bio-encres ou encres, si elles contiennent ou non des cellules, respectivement [6]). En superposant ces encres ou bio-encres couche par couche, la bio-impression 3D permet de fabriquer de structures complexes, visant à mimer l'architecture tissulaire. Afin d'être utilisés en tant qu'encres ou bio-encres, les biomatériaux doivent avoir des propriétés rhéologiques précises et une tenue nécessaire à permettre leur superposition couche par couche. Par exemple, l'impression par extrusion nécessite des encres ayant un comportement d'amincissement par cisaillement, dont la viscosité diminue sous contrainte de cisaillement. Cependant, à la sortie de la buse d'impression, le matériel devrait augmenter de nouveau sa viscosité pour que, après dépôt, l'objet imprimé en 3D soit stable, ce que signifie que le matériel doit être thixotrope [7]. En effet, bien que la stabilité à long terme est généralement pris en charge par la réticulation (ou en anglais "crosslinking") après impression [80], il est nécessaire que l'objet conserve sa forme avant que la réticulation soit

faite, et donc, que l'impression soit terminée.

Le chitosane seul, et non modifié, de même que la majorité de biomatériaux d'origine naturelle, présente des faibles propriétés rhéologiques qui ne font pas de lui un très bon candidat en tant qu'encre pour la bio-impression 3D. Toutefois, comme nous l'avons vu dans l'introduction de cette thèse (section 1.5.2) de nombreuses stratégies ont été adoptées pour améliorer ses propriétés rhéologiques et son imprimabilité, telles que sa combinaison avec d'autres molécules, l'inclusion d'un crosslinker ou son impression dans un bain de réticulation [45]. Parmi ces stratégies, dans cette thèse, nous combinons le chitosane avec des gommes naturelles: la gomme de guar et la gomme de tamarin. Le choix d'utiliser des gommes naturelles est motivé du fait que ces polysaccharides i) ont la capacité d'augmenter la viscosité des solutions ii) ont la capacité de former des hydrogels dont les propriétés mécaniques dépendent de leur structure [36]; iii) de nombreuses études présentes dans la littérature ont démontré leur biocompatibilité [36, 60, 57]. Le choix spécifiquement de la gomme de guar et de tamarin provient principalement de leur structure (représentées dans la figure 1.4). En effet, la gomme de guar présente une ramification courte alors que la gomme de tamarin présente une ramification longue. Ce différent degré de ramification pourrait influencer les propriétés rhéologiques des encres développées ainsi que les propriétés mécaniques des constructions 3D imprimées. Au delà de deux études (dont une menée par un étudiant au sein de notre équipe et détaillée ci-dessous), basées sur la combinaison de la gomme de guar avec du chitosane [56] ou de la gélatine [57], ces deux gommes n'ont pas été utilisées en tant qu'encres.

La première de ces deux études, qui reporte le développement d'encres à base de chitosane et gomme de guar, a été menée par un étudiant de l'école des Mines de Nancy ayant effectué son stage de Master au sein de notre équipe et que j'ai co-encadré. (Se référer à l'article suivant [56] dont la première page est jointe en annexe (Annexe A)). Cinq formulations différentes d'encres ont été préparées en combinant une solution de chitosane et une solution de gomme de guar en différentes proportions. Les encres obtenues, appelées C100, C95, C85, C75 and C65 (où C indique le chitosane et le numéro représente la proportion (v/v) de chitosane vs. gomme de guar), ont été ensuite utilisées pour des tests d'imprimabilité à l'aide d'une bioimprimante à extrusion. L'imprimabilité des cinq formulations a été évaluée en mesurant le diamètre des filaments extrudés sous diverses conditions d'impression, en faisant varier la taille de buse, la vitesse d'impression et la pression appliquée pour permettre l'extrusion. En quantifiant la différence entre la taille obtenue expérimentalement et la taille théorique que les filaments auraient dû avoir, il a été possible de conclure que la meilleure imprimabilité s'obtient en utilisant l'encre C85, la buse 27G (correspondant à 200  $\mu\text{m}$ ), une pression de 1,7 bar et une vitesse d'impression de 25 mm/s, ces conditions permettant d'obtenir des filaments ayant la taille la plus proche de celle théorique. La raison de la meilleure imprimabilité de l'encre C85 par rapport aux autres a été attribuée à l'évaporation plus rapide du solvant, limitant ainsi le phénomène d'élargissement du filament. Concernant les propriétés rhéologiques, toutes les formulations d'encres ont montré un comportement d'amincissement par cisaillement, se montrant approprié au mécanisme d'impression par extrusion. Bien que l'inclusion de gomme de guar a conduit à une augmentation de la viscosité de la solution de chitosane, cette augmentation, n'était pas proportionnelle à la quantité de gomme de guar ajoutée. L'encre ayant la meilleure imprimabilité a ensuite été utilisée pour l'impression de membranes qui ont été neutralisées et caractérisées pour leurs propriétés mécaniques (la résistance à la traction et la déformation). Bien que cette étude ait montré que la gomme de

guar est capable d'augmenter la viscosité de la solution de chitosane et que sa combinaison avec le chitosane permet d'obtenir des encres qui peuvent être extrudées, ces dernières ne conduisent pas à la fabrication de structures 3D en raison de leur faible tenue qui empêche leur superposition couche par couche.

L'une des stratégies les plus simples pouvant être utilisées pour améliorer ultérieurement l'imprimabilité d'une encre et permettre sa déposition couche par couche est l'ajout de gélatine suivi par une stabilisation des structures après impression. En effet, la gélatine, en fonction de la température, peut se comporter comme un solide ou comme un liquide. En particulier, à basses températures la gélatine est solide alors qu'à des températures plus élevées, notamment à la température du corps (37°C) elle est liquide[27]. Cette propriété peut être exploitée en introduisant la gélatine dans l'encre et en adaptant la température d'impression pour que l'encre soit dans le bon état de gélification permettant sa superposition couche par couche [75].

Avant de conduire une nouvelle étude incluant la gélatine, nous avons testé l'imprimabilité de deux nouvelles encres, une à base de chitosane et gomme de guar dans un rapport 1:1 (ou 50:50), et une à base de chitosane et gomme de tamarin dans un rapport 1:1 (ou 50:50), en comparaison au chitosane seul. La raison de ce choix est basée sur le fait que, à ce stade, nous voulions comparer l'effet de ces gommes non seulement sur l'imprimabilité, mais également, dans un deuxième temps, sur d'autres propriétés physicochimiques du chitosane seul telles que la dégradabilité et les propriétés mécaniques. Par conséquent, le choix s'est porté sur la préparation d'encres composées à part égales de chitosane et d'une des deux gommes. Une deuxième raison de ce choix est que les encres à base de chitosane et gomme de guar développées dans l'étude précédente ont été obtenues en utilisant une solution de chitosane 10%, préparée en dissolvant le chitosane dans une solution d'acide acétique à 40%, ce qui pourrait en réduire la biocompatibilité. Bien qu'il est possible de traiter les structures imprimées avec une solution basique, tel que le NaOH, pour neutraliser et rendre les structures imprimées biocompatibles, l'utilisation d'une si forte concentration d'acide acétique n'est pas nécessaire à la bonne dissolution du chitosane et rend la neutralisation du chitosane plus difficile à obtenir. En effet, pour garantir la biocompatibilité du produit, la concentration d'acide acétique à utiliser devrait être la plus faible nécessaire pour dissoudre le chitosane. Par conséquent, dans l'étude suivante, nous avons préparé du chitosane 2% dans une solution 1% d'acide acétique. Étant donné que la concentration d'acide acétique utilisée pour dissoudre le chitosan influence sa viscosité, il aurait été nécessaire d'effectuer une nouvelle optimisation de l'imprimabilité également pour la combinaison chitosane-gomme de guar. Toutefois, la méthode employée lors de la première étude (évaluation de la taille du filament obtenu par rapport à la taille théorique) est une méthode d'évaluation qui demande beaucoup de temps et qui n'a pas permis de conclure sur la possibilité de fabriquer des structures 3D. Nous aurions pu utiliser, pour ces nouvelles encres, la proportion qui dans l'étude précédente avait donné la meilleure imprimabilité, c'est-à-dire la combinaison chitosane:gomme de guar 85:15. Toutefois, nous avons décidé d'évaluer l'imprimabilité à travers deux méthodes plus simples et plus rapides proposées par Ouyang *et al.* and Paxton *et al.* [79, 80], détaillées dans la section suivante (section 3.1). Dans cette section nous évaluons l'imprimabilité des trois encres à base de chitosane seul (CH), de chitosane et gomme de guar (CH-GG) et de chitosane et gomme de tamarin (CH-TG) dans un rapport 1:1. Bien que l'ajout de celles-ci, notamment de la gomme de guar, entraîne une meilleure

imprimabilité, celle-ci n'est pas encore suffisante pour la fabrication de structures 3D. Ces dernières ont été obtenues, comme mentionné précédemment et comme présenté dans l'article suivant (section 3.2) grâce à l'ajout de gélatine en tant que matériel capable de modifier l'état de gélification des encres. La stabilité à long terme des structures 3D imprimées a été obtenue à travers l'immersion de ces dernières dans une solution gélifiant à base de NaOH et éthanol, immédiatement après impression.



### 3.1 Initial screening of CH, CH-GG and CH-TG biomaterial inks

As mentioned in the Introduction (section 1.5.1), an easy, initial screening of new inks or bioinks, can be done as proposed Ouyang *et al.* and Paxton *et al.* [79, 80]. Briefly, a “candidate” ink or bioink can be selected through two experimental methods. The first one consists in the extrusion of a small quantity of bioink from the nozzle. If it results in a drop, it means that the bioink is in an “under-gelation state” while if it results in an irregular filament, it is in an “over-gelation state”. Contrarily, the formation of a smooth and uniform filament indicates that the bioink is in a “proper gelation state”. A second evaluation can be done by printing a multi-layer structure with square holes and by evaluating the ability of the printed fibers to retain their shape or, rather, the merging between layers.

According to the above, we initially evaluated, through the proposed methods, the gelation state of inks made of chitosan alone (CH) and chitosan with either guar gum (CH-GG) or tamarind gum (CH-TG) at a ratio 1:1. These inks were prepared as follows. Briefly, chitosan (20 mg/mL) was dissolved in a solution of acetic acid (1%, v/v) under continuous stirring for 2 hours. Then either guar gum (20 mg/mL) or tamarind gum (20 mg/mL) was added and the solutions were heated at 37°C until complete dissolution. The resulting inks were then loaded into sterile syringes and kept at 20°C until printing. A 4th generation 3D-Bioplotter from EnvisionTEC was used to design 2 layers or 10 layers 10x10 mm<sup>2</sup> scaffold. The constructs were printed using a 250 µm inner diameter needle and a constant speed of 5 mm/s, while the pressure was adapted to each formulation: approximately 0.6 bars for CH, 0.8 bars for CH-TG and 1.0 bars for CH-GG. Figure 3.1(A), shows the results obtained by extruding a small droplet of ink through a nozzle.

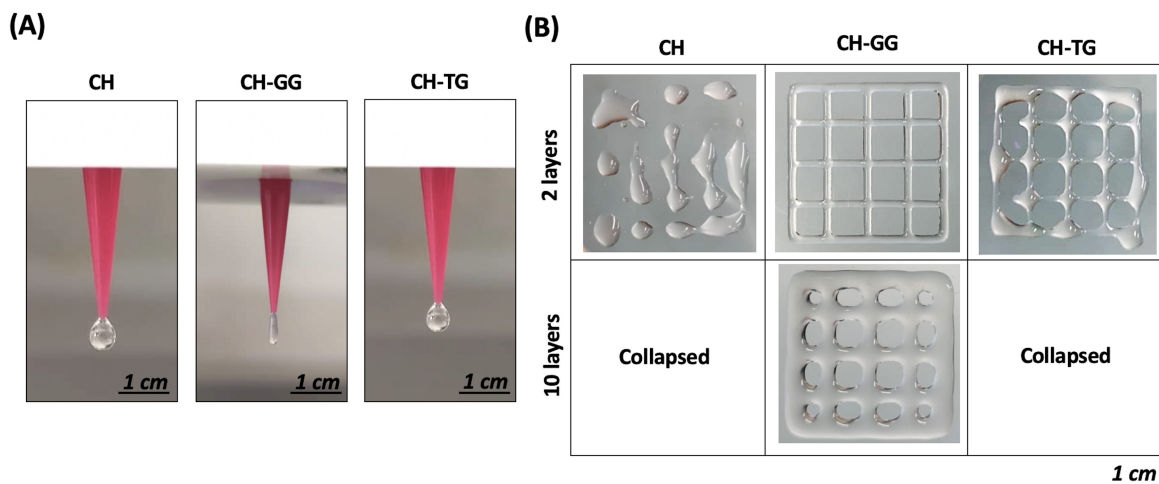


**Figure 3.1.** Printability of chitosan-guar gum and chitosan-tamarind gum biomaterial inks. (A) Initial screening of ink formulations through the extrusion of a small droplet and (b) printing of 2 and 10 layers in order to assess the successful layer stacking or the merging between layers.

Results show that CH alone was in an “under-gelation state”, which was not improved by the presence of TG. Contrarily, the combination CH-GG led to ink with a “proper gelation state”. These assumptions are confirmed by the results shown in Figure 3.1(B). If we look at the 2 layers constructs, we can see that the ones made of CH alone and CH-TG

did not retain their shape since the ink solutions were too liquid (even if this phenomenon was less evident for CH-TG compared to CH alone). Instead, CH-GG led to the fabrication of a well-organized 2 layer grid with square holes and it was the only ink to allow for the fabrication of 10 layers constructs without totally collapsing. However, the square shape of the holes was almost completely lost at 10 layers meaning that not even this ink formulation was ideal for the fabrication of complex structures.

In the next step, described in the following article we decided to include gelatin as a thermoresponsive material to the CH, CH-GG and CH-TG inks and we printed at a temperature of 20°C.

## 3.2 Development of self supported bioprinted constructs made of chitosan and guar gum or tamarind gum

*The content of this part of the chapter is nearly identical to the following work which will be submitted shortly:*

**Authors: Development of self supported bioprinted constructs made of chitosan and guar gum or tamarind gum**

**Authors: Aurelia Poerio, Jean-Philippe Jehl, Sandrine Hoppe, Philippe Marchal, Elmira Arab-Tehrany, Nguyen Tran, João F. Mano and Franck Cleymand**

### 3.2.1 Abstract

Chitosan has been widely used for tissue engineering applications. However, its application as ink or bioink for 3D bioprinting is limited due to the soft stiffness, which usually significantly reduces the printability and shape fidelity of the printed scaffolds. In this study, we prepared three ink formulations based on chitosan and either guar gum or tamarind gum for the fabrication of self-supporting 3D printed objects using a dual gelation strategy. This is based on the inclusion of gelatin as a thermoresponsive component of the ink formulations in order to improve their printability and on the immersion of the printed constructs in a gelation bath of ethanol and sodium hydroxide (NaOH) to allow for their long term stability. The inclusion of gums had a significant effect of printability as well as on other properties of chitosan, such as its degradability and mechanical properties.

### 3.2.2 Introduction

Tissue engineering is a field of regenerative medicine that aims to replace, repair and regenerate damaged tissues or organs through the fabrication of biomaterials-based scaffolds. Biomaterials can be modified and modulated for different tissue engineering applications according to two major strategies. The first one is based on the implantation of cell-laden scaffolds that already present some similarities with the natural tissue to be replaced. The second one is based on the recruitment of patient's own cells to migrate into the implanted acellular scaffolds due to the release of cytokines or growth factors in order to create a new tissue *in situ* [122]. In both cases, the role of the scaffold is to provide the structural support for cell attachment, proliferation and differentiation, in order to facilitate tissue healing and regeneration [123]. Among the different strategies used for the manufacturing of biomaterial-based scaffolds, 3D bioprinting has emerged due to its great advantages of high resolution, repeatability and personalized reproduction of patient's tissues and organs [124]. This technology is based on the precise positioning of the so-called "bioink", which is a mixture of biomaterials, cells and biological molecules, in order to create complex architectures with well-interconnected pores [11]. The primary limitation of this technology is the lack of biomaterials that meet the requirements of good printability, and subsequent good shape fidelity, and high cell viability during or after the bioprinting process. Therefore, there is always a need of new ink and bioinks, based on natural or synthetic polymers [125]. Natural polymers, such as polysaccharides, have gained strong attention as components of bioinks thanks to their morphological similarity to the extracellular matrix (ECM) and their distinct behavior in water which depends on monosaccharide's composition, ramification and interaction. Furthermore, the high number of hydroxyl groups present in their structure allows for several chemical modifications, making them really versatile components [126]. Among the polysaccharides, chitosan (CH) has been vastly used

for different tissue engineering applications due to its biocompatibility, biodegradability and low toxicity [127]. However, its lack of strong mechanical properties (as low stiffness) prevents its use for some applications such as 3D bioprinting. In fact, in most conditions, chitosan alone is not self-supporting meaning that it has low printability and low shape fidelity [45]. Guar gum (GG) and tamarind gum (TG), are natural polysaccharides extracted from the endosperms of *Cyamopsis Tetragonoloba* [128] and *Tamarindus indica* [129], respectively. These natural gums have already been used for food, drug delivery and tissue engineering applications [130]. They are well known for their capability to increase the viscosity of solutions even at small concentrations and to form hydrogels [36]. In a previous work, GG has been added to chitosan, at different concentrations, in order to improve the printability of newly developed inks for extrusion-based bioprinting [56]. This study showed that GG was able to increase the viscosity of chitosan solutions, improve the printability of the ink and lead to a better shape fidelity after printing. However, the improvement of these properties was not related to a better ability to build complex structures in three dimensions. The fabrication of self-supporting bioinks, able to create large-scale scaffolds, that also present high biocompatibility, biodegradability and mechanical properties appropriate for the target tissue, is one of the current challenges of 3D bioprinting [131]. In this study, we combined CH to GG or TG to develop new biomaterial inks for the fabrication of self-supporting 3D printed objects using a dual gelation strategy. The first one was obtained by the inclusion of gelatin, as a thermoresponsive component. Since gelatin is solid at room temperature ( $\sim 25^{\circ}\text{C}$ ), it allows the fabrication of well-defined 3D printed objects. However, if not chemically bonded, gelatin dissolves when constructs are incubated at body temperature ( $\sim 37^{\circ}\text{C}$ ), a phenomenon that could lead to the collapse of the structure. A second gelation mechanism was obtained by immersing, immediately after printing, the constructs in a solution made of ethanol and NaOH. This treatment, other than allowing for the neutralization of chitosan, necessary for the subsequent cell seeding, leads to the gelation of the constructs [132]. Here, we evaluated the viscosity and the printability of biomaterial inks based on chitosan (CH), chitosan-guar gum (CH-GG) and chitosan-tamarind gum (CH-TG). We assessed the swelling ratio and degradation profile of the bioprinted constructs, as well as their mechanical properties, internal morphology and their ability to release BSA as model protein *in vitro*.

### 3.2.3 Materials and methods

#### 3.2.3.1 Materials

Chitosan (degree of deacetylation: 87.6 - 92.5%, viscosity: 8 - 15 mPas) was purchased from Hepepe medical chitosan (ref. 23601). Gelatin (ref. 42043) was purchased from Honeywell Fluka. Tamarind gum (ref. T0909) was purchased from TCI. Guar gum (ref. G4129), acetic acid (ref. 33209M), lysozyme from chicken egg white (ref. 629709), bovine serum albumin (BSA, ref. A2153) were purchased from Sigma Aldrich. Ethanol absolute (ref. 20821) and sodium hydroxide (NaOH, ref. 28244) were purchased from VWR.

#### 3.2.3.2 Preparation of the biomaterial inks

Chitosan (CH), chitosan-tamarind gum (CH-TG), and chitosan-guar gum (CH-GG) inks were prepared as following. Chitosan (20 mg/mL) was dissolved in a solution of acetic acid (1%, v/v) under continuous stirring for 2 hours. Then, gelatin (35 mg/mL) and either guar gum (20 mg/mL) or tamarind gum (20 mg/mL) were added and the solutions were heated at  $37^{\circ}\text{C}$  until complete dissolution. The resulting inks were then loaded into sterile syringes and kept at  $20^{\circ}\text{C}$  until printing. For the *in vitro* release studies, bovine serum albumin (BSA) was added to the ink formulations at a concentration of 0.8 g/mL.

### 3.2.3.3 Fourier Transformed Infrared Spectroscopy (FTIR)

FTIR spectra were collected using a Thermo Scientific Nicolet machine on dried films made of ink solutions and on lyophilized 3D printed constructs after incubation at 37°C. Briefly, a small amount of the ink solution was placed on a petri dish and treated for 10 minutes with a solution of ethanol (80%) containing 2% of NaOH (in the following called Et-NaOH or gelation bath). The resulting wet film was washed 3 times with deionized water and left to dry at room temperature. The dried films were then used for the FTIR analysis. To investigate the effect of incubation at 37°C (and assess the effect of the dissolution of gelatin), constructs were 3D printed (see section 3.2.3.5), treated for 10 minutes with Et-NaOH, washed 3 times with deionized water and incubated overnight at 37°. The constructs were then lyophilized for 48 hours and the resulting lyophilized structures were grounded and used to create KBr pellets (ratio samples to KBr 1:100), which were then used for FTIR analysis. The FTIR spectra of each individual component (Supplementary figure B1) were obtained on dried films created by pouring a solution 1% w/v of each component into Petri dishes. For chitosan, the solvent was a solution 1% v/v of acetic acid while for gelatin and both guar and tamarind gum was water. The spectra were collected in the range from 400 to 4000  $\text{cm}^{-1}$  at a resolution of 4  $\text{cm}^{-1}$ .

### 3.2.3.4 Viscosity measurement

The shear viscosity of the CH, CH-GG and CH-TG inks (containing gelatin) was assessed by a shear sweep analysis (between 0.1 and 100  $\text{s}^{-1}$ ) at 20°C (that is the temperature used for the printing process). The test was performed with a rotational rheometer (ARES, G2, TA Instruments) equipped with a plate geometry of 25 mm diameter.

### 3.2.3.5 3D printing and evaluation of the printability

A 4th generation 3D-Bioplotter from EnvisionTEC was used to perform the 3D printing processes. The syringe temperature controller for all the ink formulations was adjusted at 20° and a computer-aided design (CAD) software was used to design 2 layers or 10 layers 10x10  $\text{mm}^2$  scaffold. The 2 layers and 10 layers constructs were used to measure the Printability (see below) while all the other tests were performed using 10 layers scaffolds. All the scaffolds were printed using a 250  $\mu\text{m}$  inner diameter needle and a constant speed of 5 mm/s, while the pressure was adapted to each formulation: approximately 0.6 bars for CH, 0.8 bars for CH-TG and 1.0 bars for CH-GG. To improve the visualization of the printed scaffolds and to facilitate measurements, a blue colorant was added to the inks.

The printability was evaluated using the Printability (Pr) measure proposed by Ouyang *et al.* [79]. Basically, since the fabricated object resulted in regular grids and square holes, the area (A) and perimeter (L) of the pores of each construct can be measured.

The following formula:

$$Pr = \frac{L^2}{16A} \quad (3.1)$$

results in a value inferior, equal or superior to 1. When  $Pr=1$ , the ink possesses the ideal gelation and subsequent ideal printability since it is able to create grids with perfect square holes. Contrarily,  $Pr < 1$  means that the ink is too liquid and the holes have a more circular shape while  $Pr > 1$  means that the ink is over-gelled. Images of 2 or 10 layer constructs were analyzed using Fiji image processing software [133]. Results are presented as average  $\pm$  standard deviation of 25 measurements per condition.

### 3.2.3.6 Mass swelling ratio

The mass swelling ratio of the 3D printed scaffolds was evaluated as follows. The printed constructs, formerly gelled with Et-NaOH as previously described (see section 3.2.3.3), were immersed in PBS (Phosphate Buffer Saline) at 37 °C for 24 h to reach equilibrium swelling. After being removed from PBS, the excess of water was gently removed using a paper tissue, and the swollen weight ( $W_s$ ) of the samples was measured using a precision balance. The samples were then lyophilized for 48 hours and their dry weight ( $W_d$ ) was measured. The mass swelling ratio was calculated as:

$$\text{Mass swelling ratio} = \frac{W_s - W_d}{W_d} \quad (3.2)$$

Results are presented as average  $\pm$  standard deviation of 6 measurements per condition.

### 3.2.3.7 Degradation profile

For the degradation studies, 3D printed constructs were immersed in the Et-NaOH solution for 10 minutes and washed 3 times with PBS. After the third washing step, the excess of PBS was removed using a tissue paper and the samples were weighed to obtain the initial weight ( $W_i$ ). They were then immersed in a solution of PBS containing 10 mg/L of lysozyme and incubated at 37°C. At each time point (once a week from 1 to 9 weeks) samples were removed from the lysozyme solution, wiped with a tissue paper and weighted again to obtain the final weight ( $W_f$ ). At each time point, lysozyme solution was replaced with a fresh one. The percentage of degradation was determined as:

$$\text{Weight loss (\%)} = \frac{W_i - W_f}{W_i} \cdot 100 \quad (3.3)$$

Results are presented as average  $\pm$  standard deviation of at least 3 measurements.

### 3.2.3.8 Nanoindentation

The indentation curves were collected using an ultra nanoindenter (Anton-Paar, Peseux, Switzerland), at a penetration range comprised between few  $\mu\text{m}$  and 100  $\mu\text{m}$ , using loads of 10  $\mu\text{N}$ –300  $\mu\text{N}$ . Samples were tested in the form of hydrogels, prepared by placing a certain amount of CH, CH-GG and CH-TG ink solutions into 30 mm plastic round molds and treating them with Et-NaOH solution for 10 minutes. The hydrogels were then washed 3 times with PBS and incubated overnight in PBS at 37°C. Prior to indentation, PBS was removed and replaced with a fresh amount and placed again 1 hour at 37°C. Samples were tested in the liquid environment (PBS) at 37°C. The reduced Young's modulus was calculated at the end of the loading curve (between 70 and 90 % of penetration depth) using the contact theory (Hertz formula). As previously described [134], this theory establishes the relationship between the force applied ( $F$ ), the relative approach distance of the two elements ( $h$ ). These formulae also involve the radius of the indenter's curve ( $R_c$ ) and the mechanical characteristics of the sample and indenter, *i.e.* their Young's moduli and Poisson ratios, using the reduced elasticity modulus:

$$h = \left( \frac{9 \cdot F^2}{16 \cdot R_c \cdot E_c^{*2}} \right)^{(1/3)} \quad (3.4)$$

with the bend radius  $R_c$  defined as:

$$\frac{1}{R_c} = \frac{1}{R_i} + \frac{1}{R_s} \quad (3.5)$$

and the reduced Young's modulus  $E^*$  given by:

$$\frac{1}{E_c^*} = \frac{(1 - \nu_i^2)}{E_i} + \frac{(1 - \nu_s^2)}{E_s} \quad (3.6)$$

where  $E_s$ ,  $E_i$ ,  $\nu_s$ ,  $\nu_i$ ,  $R_s$  and  $R_i$  are the Young's moduli, the Poisson ratios, and the bend radius of the sample and the indenter, respectively.

The values are presented as mean  $\pm$  standard deviation of at least 6 measurements per sample.

### 3.2.3.9 Morphological characterization of 3D printed constructs

The internal morphologies of the printed constructs were assessed using a Quanta 650-FEG (FEI, Hillsboro, OR, USA) scanning electron microscope (SEM). To assess the morphology at day 0, constructs were immersed in Et-NaOH, immediately after printing, for 10 minutes. They were then washed 3 times with PBS frozen overnight at  $-80^\circ\text{C}$  and lyophilized for 48 hours. To assess the effect of time and lysozyme treatment on the morphology of the constructs, at 3 (CH) or 7 weeks (CH-GG and CH-TG), samples were removed from the lysozyme solution, washed 3 times with PBS and lyophilized as previously described. Prior to observation, the samples were cut in half to observe the internal morphology. They were then placed on SEM stubs, and gold sputter-coated.

### 3.2.3.10 *In Vitro* release profile of bovine serum albumin (BSA)

The *in vitro* release studies were conducted using BSA as a model protein. BSA was added at a concentration of 0.8 g/mL within the three ink formulations. The BSA-loaded constructs were printed, immersed for 10 minutes in the gelation solution (Et-NaOH) and washed 3 times with PBS. Each construct was then incubated in 1 mL of PBS at  $37^\circ\text{C}$ . At each time point (day 1, 4, 7 and 14), the entire release medium was collected and replaced with an equal volume of fresh medium. The release medium was then used to measure the total protein content with the BCA Protein Assay kit (ThermoFisher, 23225). The release values were corrected by subtracting the absorbance measured on the release medium collected from constructs that did not contain BSA. Results are presented as average  $\pm$  standard deviation of 3 measurements per condition at each time point.

### 3.2.3.11 Statistical analysis

Statistical analyses were performed using R studio software [135]. All data were expressed as mean  $\pm$  standard deviation. The differences between groups were explored by one-way ANOVA followed by Tukey post-hoc test and significance was determined at  $p < 0.05$ .

## 3.2.4 Results

### 3.2.4.1 Spectroscopic characterization by FTIR

FTIR analysis was conducted to investigate the permanence of gelatin after gelation and incubation of the 3D printed constructs at  $37^\circ\text{C}$ . In fact, since gelatin was not chemically bonded, we expect it to dissolve once the constructs are incubated at body temperature. To do that, each of the components of the inks (*i.e.* chitosan, gelatin, guar gum and tamarind gum) was characterized by FTIR in order to attribute the peaks found in the inks to each individual component (spectra and peak identification shown in the supplementary information B1). To investigate the permanence of gelatin we conducted FTIR analysis on two types of samples: biomaterials inks (CH, CH-GG and CH-TG containing gelatin) in form of films and on lyophilized scaffolds after incubation overnight at  $37^\circ\text{C}$ . As shown in Figure 3.2, among the three samples (CH, CH-GG and CH-TG) in the same

state (films, represented by continuous lines or after incubation at 37°C, represented by dashed lines), there were no significant differences. All the spectra present the typical absorption bands of polysaccharides (between 800 and 1200  $\text{cm}^{-1}$ ) and a large peak from 3000 to 3700  $\text{cm}^{-1}$ , which corresponds to N-H and O-H stretching and to the intramolecular hydrogen bonds. However, it can be noticed that this peak is larger, for CH-GG and CH-TG films compared to lyophilized samples, demonstrating that this peak is influenced by the residual water, which is certainly inferior after lyophilization [136]. However, CH does not show any difference among the film or lyophilized state. This might be explained by the fact that the lower amount of -OH groups of chitosan as compared to guar gum or tamarind gum, leads to fewer hydrogen bonds and, consequently, to less residual water even in the film state. As showed in the supplementary Figure B1, the peak at 1560 $\text{cm}^{-1}$ , is attributed to amide II vibrations of N-H groups and stretching vibrations of N-C groups, belonging to chitosan and gelatin, while it is absent in guar and tamarind gum. Consequently, we suppose that the decrease in its intensity after incubation at 37°C might be attributed to the dissolution of gelatin. Similarly, the peak at 1460  $\text{cm}^{-1}$ , which was found in gelatin alone (see supplementary Figure B1), had a reduced intensity after incubation at 37°C for the three inks CH, CH-GG and CH-TG. Together, these results suggest that gelatin dissolves after incubation at 37°C.

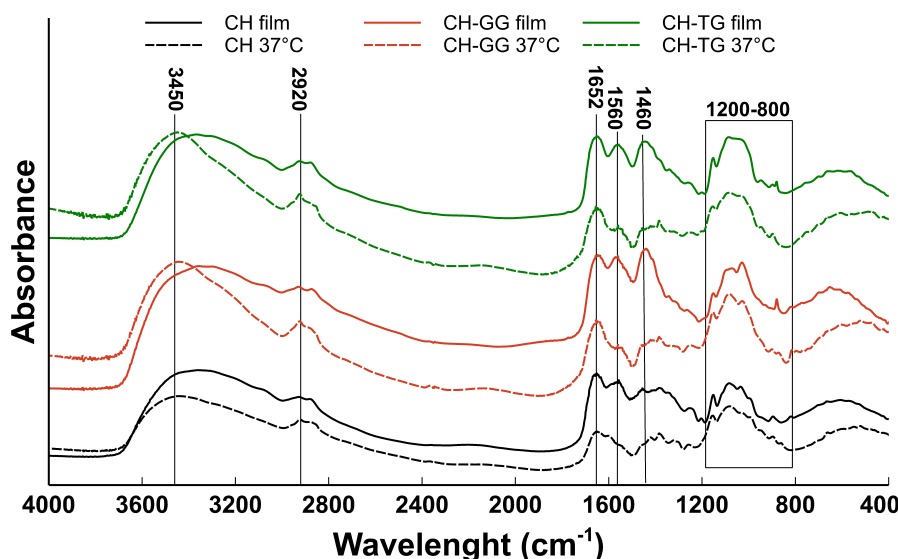


**Figure 3.2.** FTIR spectra of the ink solutions in form of film (discontinuous line) and of the lyophilized 3D printed construct after incubation overnight at 37°C for 24 hours (continuous line). Black curves correspond to the sample CH, red to CH-GG and green to CH-TG.

### 3.2.4.2 Viscosity

Viscosity is one of the most important parameters to consider when developing new inks or bioinks. In fact, during bioprinting, bioinks should be easily extruded through a nozzle under applied pressure [76]. Consequently, they should present a shear-thinning behavior, meaning that viscosity decreases when the shear rate increases. Figure 3.3 shows the shear viscosities of the inks CH (black squares), CH-GG (red circles) and CH-TG (green triangles) as a function of the shear rate measured at 20°, since it represents the temperature used for the bioprinting process. The three inks showed a shear-thinning behavior, which is not surprising since GG and TG, present a shear-thinning behavior on their own [61]. At each shear rate, the viscosity of CH-GG and CH-TG inks is higher than the viscosity of CH. However, at low shear rates, CH-GG shows a slightly higher viscosity than CH-TG while at higher shear rates, CH-TG shows increased values of viscosity compared to CH-GG. This behavior demonstrates that CH-GG has a more pronounced shear-thinning



behavior than CH-TG, which might result in a better print fidelity. In fact, the decrease of the viscosity of the ink due to the applied pressure facilitates the deposition of the ink [131]. However, when the shear stress is removed, the more pronounced shear-thinning behavior could lead to a more rapid increase of the viscosity after the removal of the stress applied and consequently, to an improved shape fidelity after deposition. The decrease in the viscosity of polymers under a shear rate depends on the disentanglement of polymer chains. The different shear-thinning behavior might depend on the molecular weight of the polysaccharides [61] or on the fact that tamarind gum has a more branched structure compared to guar gum, which might resist more to disentanglement.

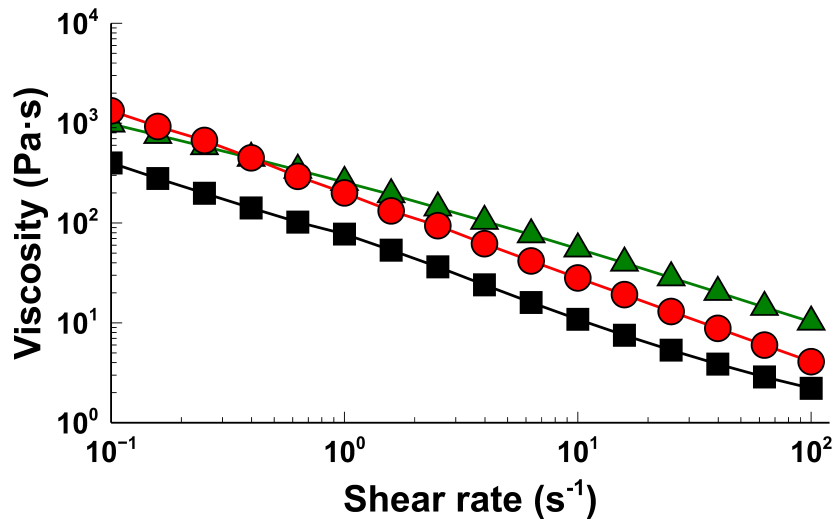


**Figure 3.3.** Viscosity of the three biomaterial inks: CH (black squares), CH-GG (red circles) and CH-TG (green triangles), containing gelatin, as a function of the shear rate, measured at 20°C.

### 3.2.4.3 Evaluation of the printability

When new inks or bioinks are developed, it is essential to assess their printability and shape fidelity. The latter can be defined as the ability to form 3D printed structures with high similarity to the initial design. Here, a qualitative and semi-quantitative evaluation of the printability has been conducted. Figure 3.4(A) shows representative images of 2 and 10 layers constructs made of CH, CH-GG and CH-TG. The top view of 2 and 10 layers square constructs with four holes each have been used for the semi-quantitative evaluation of the printability. A qualitative evaluation of the ability of the inks to be deposited layer-by-layers, without collapsing, can be done by observing the side view of the 10 layers square or cylindrical constructs. These pictures show that constructs made of CH and CH-GG retain better their shape compared to CH-TG, which is more inclined to collapse. Figure 3.4(B) shows the theoretical design of the constructs (2 layers) and evidences the Area (A) and the perimeter (L) of the pores used for the measurements of the Pr value. Figure 5.9(C) shows the Pr values of 2 layers (full bars) or 10 layers (dotted bars) constructs printed using CH, CH-GG and CH-TG inks. Our results showed no significant difference, within the same group, between the Pr value measured for the 2 layers constructs and the 10 layers one for the three groups CH, CH-GG and CH-TG, suggesting that these inks could be efficiently used for the fabrication of relevant size constructs without collapsing.

However, some differences were evident among the three groups (CH, CH-GG and CH-TG) for both 2 and 10 layers constructs, among the three groups. According to Ouyang *et al.* [79], the ideal gelation condition and ideal printability values are comprised between 0.9 and 1.1. Our results show that CH constructs have a Pr value superior to 1 (1.19 and 1.22 for the 2 and 10 layers, respectively) meaning that the ink solution was in an over-gelation condition. CH-TG constructs have a Pr value

inferior to 1 (0.89 and 0.93 for the 2 and 10 layers, respectively) meaning that the solution was too liquid. In contrast, CH-GG constructs have a printability value equal to 1 (1.03 and 1.06 for the 2 and 10 layers, respectively), showing the ideal gelation state and ideal printability. These results are corroborated by the qualitative images showed in Figure 3.4(A), where it is clear that CH-TG constructs are more inclined to collapse. These results seem to confirm our observations that inks with a more pronounced shear-thinning behavior lead to a better shape fidelity. Furthermore, they also suggest that the inclusion of gums reduces the gelation of the inks. In fact, it seems that it is higher for CH (over-gelation state), lower for CH-GG (proper-gelation state) and even lower for CH-TG (under-gelation state).

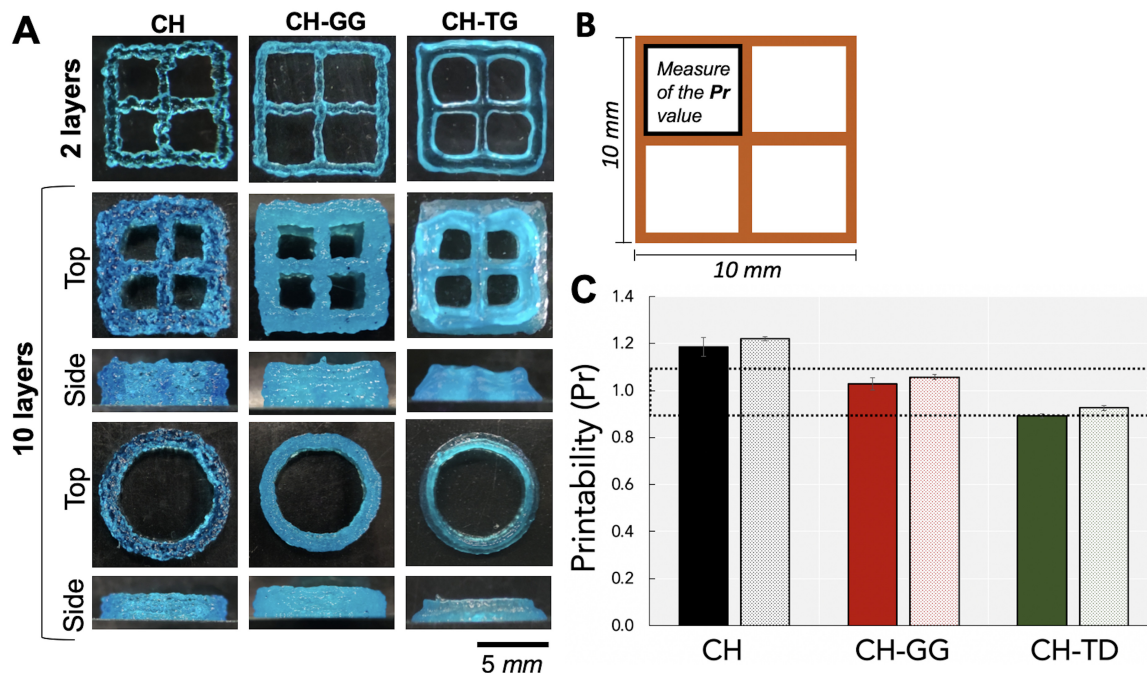


**Figure 3.4.** Qualitative and semi-quantitative evaluation of the printability of the three ink formulations: CH, CH-GG and CH-TG. (A) Qualitative images of 10 mm x 10 mm square and 10 mm circular constructs printed in 2 or 10 layers view from the top and from the side. (B) Representative image evidencing the pores used for the calculation of the Pr value. (C) Quantification of the printability (Pr value) of constructs made of 2 layers (full bars) or 10 layers (dotted bars) using the Pr value.

### 3.2.4.4 Swelling and degradation profiles

Figure 3.5(A) shows the swelling mass ratio of the gelled 3D printed constructs, One-way ANOVA detected a significant variability in the mass swelling ratio among different printed constructs ( $F(2, 13) = 168, p = 5.13 \times 10^{-10}$ ). In particular, CH showed a significantly higher swelling compared to CH-GG and CH-TG, while there was no significant difference between CH-GG and CH-TG ( $p = 0.86$ ). While the sample CH absorbed  $\sim 21$  times its dry weight, CH-GG and CH-TG absorbed it  $\sim 13$  times. The ability of swelling is a characteristic of hydrogels which is essential since it would allow for the absorption of the surrounding fluids (and consequently, nutriment for encapsulated cells). It usually depends on the density of the three-dimensional network (less pores means less space that can be occupied by fluids). However, high swelling is not always related to enhanced properties of the hydrogel since it could lead to faster degradation.

Figure 3.5(B) shows the degradation profile of the CH, CH-GG and CH-TG constructs during 9 weeks in a solution of 10 mg/L of lysozyme. The concentration of lysozyme was chosen to mimic

the average concentration contained in the human serum [137]. After 3 weeks, the sample CH still retained 64% of its weight. However, at that time point, samples made of CH were very fragile and they could not be used for the measurements. Interestingly, the presence of tamarind gum (CH-TG) and guar gum (CH-GG) reduced the degradation of the constructs which, except for an initial weight loss, were stable for at least 3 weeks to slowly degrade during the subsequent time points but still maintained their structure for at least 9 weeks. Representative images of the macroscopic appearance of the construct after 3 weeks (CH) and 7 weeks (CH-TG and CH-GG) can be seen in the magnifications B', B'' and B''', respectively. Taken together, these results suggest that the higher absorbance of water (evaluated as mass swelling ratio) of the constructs CH, as supposed, leads to faster degradation.

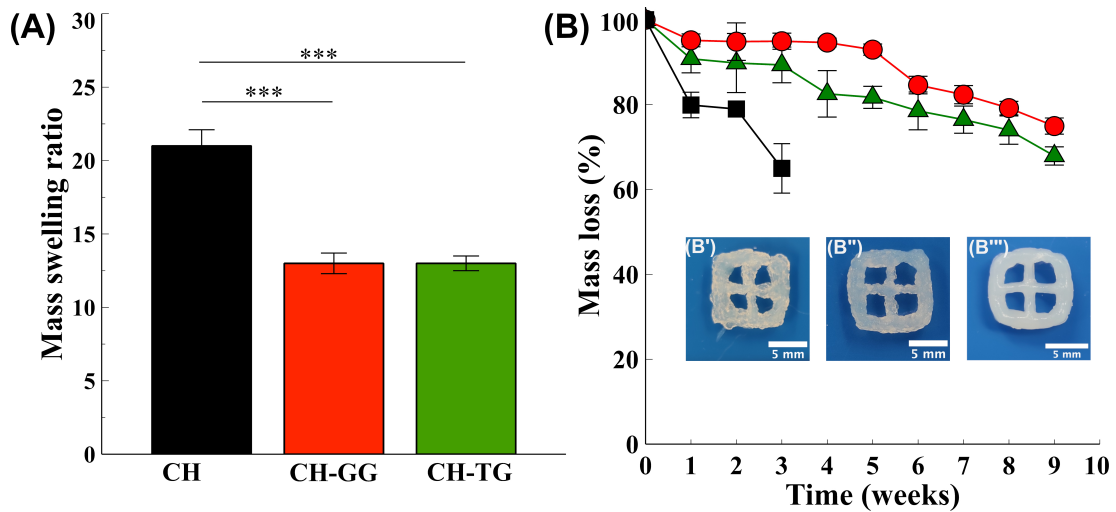


**Figure 3.5.** (A) Mass swelling ratio of constructs made of chitosan (CH) and tamarind (CH-TG) or guar (CH-GG) gum.  $***p < 0.001$ . (B) Degradation profile of the same constructs (Black: CH, Green: CH-TG, Red: CH-GG) and representative images of the construct CH (B') after 3 weeks in lysozyme, CH-TG (B'') and CH-GG (B''') 7 weeks in lysozyme.

### 3.2.4.5 Nanoindentation

Nanoindentation is a technique used commonly to measure nanomechanical properties of materials. Figure 3.6(A) shows the evolution of the Reduced Young's modulus of CH, CH-GG and CH-TG constructs, in form of hydrogels, versus penetration depth. At the beginning of the curve (between 0 and 1 % of penetration depth), the three samples have similar and high  $E^*$  values ( $1.46 \times 10^5$  Pa for CH,  $1.55 \times 10^5$  Pa for CH-GG and  $1.56 \times 10^5$  Pa for CH-TG). For the three groups, as the penetration depth increases, the  $E^*$  decreases until reaching the asymptotic limit of  $E^* = 2.67 \times 10^4 \pm 4.7 \times 10^3$  Pa for CH,  $E^* = 44.2 \times 10^4 \pm 2.8 \times 10^3$  Pa for CH-GG and  $E^* = 33.7 \times 10^4 \pm 2.4 \times 10^3$  Pa for CH-TG, as shown in Figure 3.6(B). These results suggest that the mechanical properties were significantly enhanced in the CH-GG hydrogel compared to CH and CH-TG ( $F(2, 25) = 26.79, p = 0.002$ ), which presented more similar curves and Young's modulus values. In particular, the  $E^*$  value of CH-GG, measured between 70 and 90 % of penetration depth, was significantly higher ( $p = 0.002$ ) compared to CH as well as to CH-TG ( $p = 0.02$ ). In contrast, CH and CH-TG were not significantly different between them ( $p = 0.2$ ). The higher  $E^*$  values at low penetration depth might be due to the effect of the gelation with Et-NaOH which creates a rigid superficial layer that, becoming hydrophobic, prevents the additional infiltration of Et-NaOH, leaving the inner part of the hydrogel less rigid.

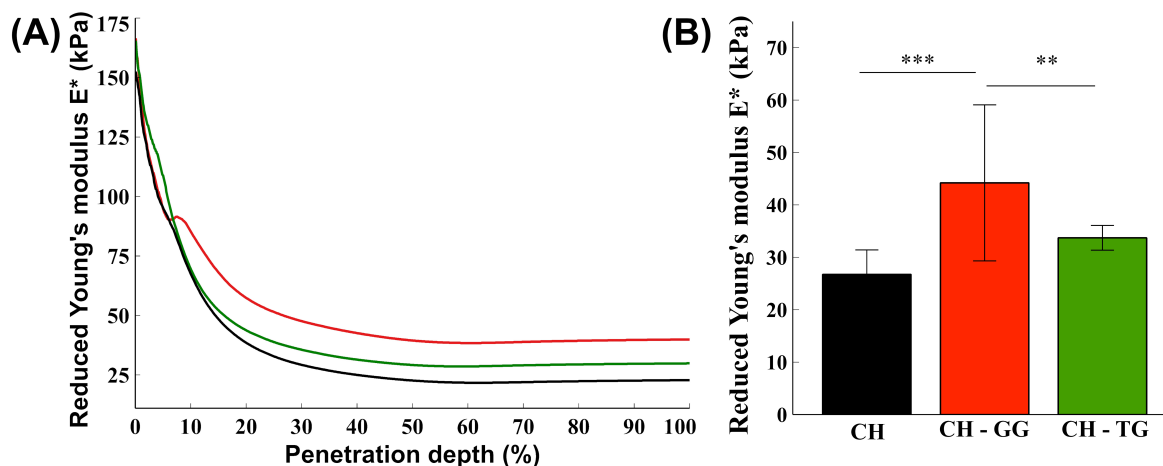


**Figure 3.6.** Nanindentation of the samples CH, CH-GG and CH-TG. (A) Reduced Young's modulus vs indenter penetration depth for the samples CH (black), CH-GG (red) and CH-TG (green). (B) Average reduced Young's modulus values for the samples CH, CH-GG and CH-TG measured between 70 and 90% of penetration depth. \*\*\* $p < 0.001$ .

#### 3.2.4.6 Morphology of bioprinted constructs by SEM

Figure 5.12 shows the SEM images of the internal morphology of the constructs before (day 0) and after incubation in lysozyme at 37°C for 21 (CH) or 35 days (CH-GG and CH-TG). Hydrogel-based constructs should have good porosity to allow cell attachment, migration and proliferation. At day 0 (Figure 5.12 A, B and C) all the constructs present high porosity CH-TG that seems to present larger pores compared to CH and CH-GG. Even if quantitative studies should be performed in order to affirm that, we suppose that this is due to the fact that guar gum and chitosan have a less branched structure compared to tamarind gum. The construct made of CH and TG, in tune, is more voluminous and might result in larger pores. After 21 (CH) or 49 days in lysozyme (CH-GG and CH-TG), all the constructs showed signs of internal degradation represented by the loss of defined pores (Figure 5.12 D, E, F).

#### 3.2.4.7 BSA release profile

Bioactive molecules, such as growth factors, can be encapsulated within 3D printed or printed objects and released with a kinetic that depends on the material the constructs are made of. Here, we used BSA as a model protein to assess how encapsulated factors would be released from 3D printed constructs made of CH, CH-GG and CH-TG. As shown in Figure 5.13, the three samples display a similar release kinetic. At day 1, the three samples showed a burst release, which was slightly lower for CH-TG compared to CH and CH-GG. This trend of release was maintained for the subsequent time points. In fact, CH and CH-GG released higher percentages of BSA at each time point compared to CH-TG. The 100 % of release was not obtained from any construct due to the fact that a certain amount of BSA probably dissolved out of the construct during the incubation with Et-NaOH and subsequent washing steps. These results suggest that either CH-TG retains BSA more efficiently and release it slowly or loses a higher amount of BSA during the incubation with Et-NaOH and washing.

### 3.2.5 Discussion

In this study, new biomaterial inks based on chitosan and guar gum (GG) or tamarind gum (TG) were developed. While some results have already been obtained by using GG as ink, combined with

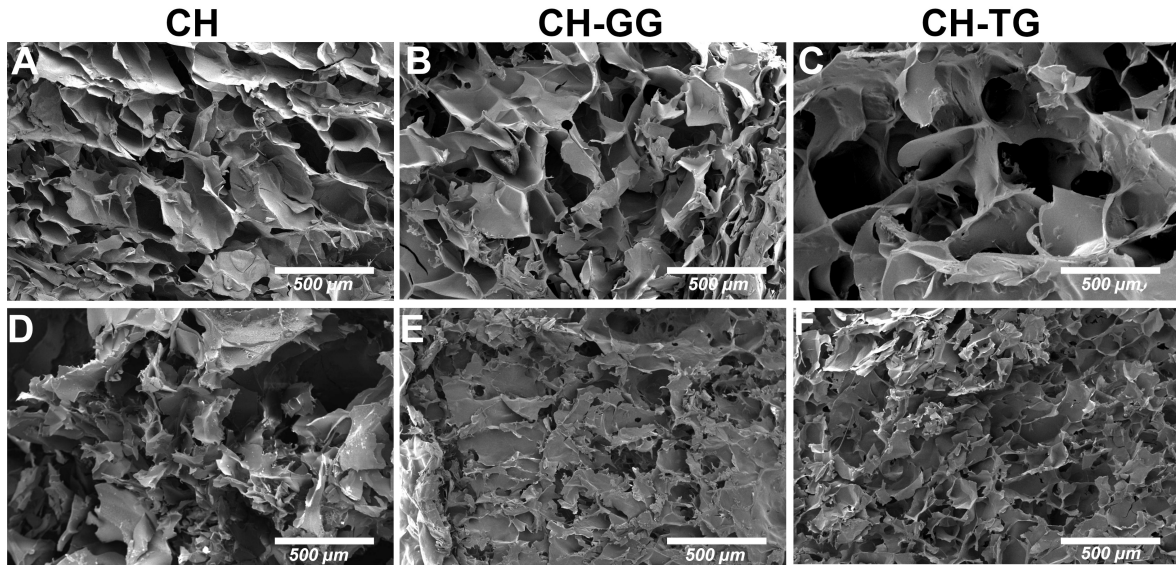


**Figure 3.7.** SEM images of the bioprinted constructs made of CH (A and D) at day 0 (A) and after 21 days in lysozyme (D), CH-GG (B and E) at day 0 (B) and after 49 days in lysozyme (E) and CH-TG (C and F) at day 0 (C) and after 49 days in lysozyme (F).

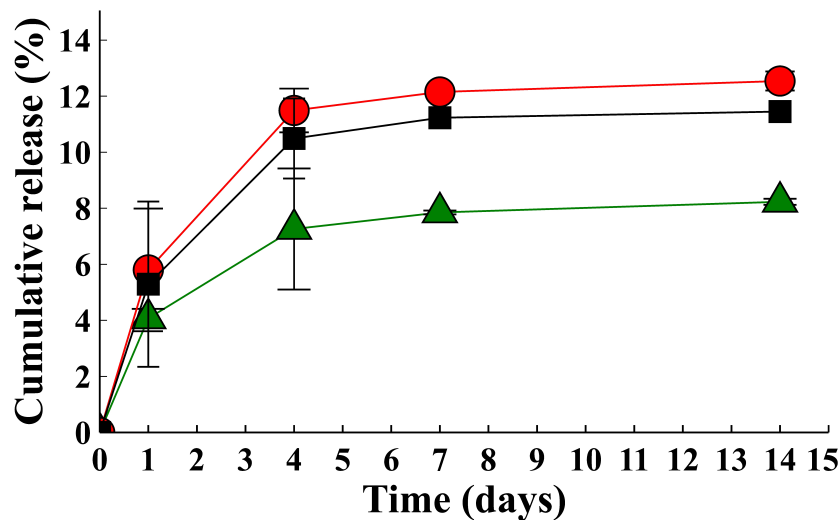


**Figure 3.8.** Cumulative release of BSA from bioprinted construct made of CH (black squares), CH-GG (red circles) and CH-TG (green triangles).

chitosan [56] or gelatin [57], TG has never been included as a component of inks or bioinks, to our knowledge. Here, these two natural polysaccharides have been combined with chitosan to develop self-supporting 3D bioprinted constructs without the use of chemical crosslinkers. Even if chemical crosslinking is mechanically stronger than the physical one, it can lead to cytotoxicity [138]. To avoid the use of chemical crosslinkers, gelatin has been included as a thermoresponsive component during the 3D printing and a solution of ethanol and NaOH has been used to induce the gelation of the printed constructs. As reported by other studies [139, 140, 79] the inclusion of gelatin is very helpful during the bioprinting process since, due to its reversible thermal gelation, it allows for the achievement of the right viscosity by tuning the temperature and highly improve the shape fidelity of the printed structures. To assess the permanence of gelatin after the gelation of the constructs, we performed FTIR analysis on the inks before printing and on 3D printed scaffolds after overnight incubation at 37°C and subsequent lyophilization. The decrease in the intensity of the peaks related

to gelatin evidence the dissolution of gelatin after incubation of the constructs at 37°C. Yin *et al.* [141] showed that, in hydrogels made of methacrylate gelatin (GelMA)/gelatin, between 2.9 and 11.6 % of the non crosslinked gelatin (depending on the composition of the hydrogel) dissolved away from scaffolds after incubation at 37°C for 24 hours. After printing, a solution of ethanol 80% containing 2% of NaOH was used to induce the gelation of the 3D printed constructs. NaOH other than inducing the gelation of chitosan improves cell compatibility due to the neutralization of chitosan surfaces [142]. Ethanol has been widely used to induce the gelation of polysaccharides to avoid the use of chemical crosslinkers [132]. The mixture Et-NaOH has been previously utilized [89] in a ratio NaOH to ethanol 7:3, where, a bioink made of chitosan and hydroxyapatite was dispensed into a bath mixture of Et-NaOH to form a hydrated gel-like precipitate immediately after printing, keeping the scaffold in the desired shape. To assess the feasibility of the developed inks to be good candidates for extrusion-based 3D bioprinting, we determined their shear viscosity. We showed that CH, CH-GG and CH-TG had a shear-thinning behavior, which is appropriate for extrusion bioprinting. Furthermore, since expected, the inclusion of either GG or TG with CH led to values of viscosity constantly higher compared to the CH alone, confirming that these natural gums have an important role in increasing the viscosity of solutions. We then evaluated the printability of the developed inks. Over the past years, different methods have been proposed to assess the printability, as already reviewed elsewhere [78, 7]. Most of these methods evaluate the ability to extrude filaments or the shape fidelity of 1 or 2 layers constructs. However, one of the main challenges in the biomanufacturing of cell-laden or acellular scaffolds is the fabrication of constructs with clinically relevant dimensions [143]. In this study, we evaluated the printability by determining the Pr value, as proposed by Ouyang *et al.* [79] either on 2 or 10 layers constructs. We showed that this semi-quantitative measurement could be also used to evaluate the ability to print multiple layers without collapsing. In fact, by demonstrating that the Pr values of 2 or 10 layers constructs printed using the same bioink are not significantly different, we can insinuate that the developed inks lead to a good shape fidelity, due to the fact the square holes were still evident after 10 layers and they maintained their shape without collapsing. The ability of hydrogels to absorb water is essential to ensure the transport of nutrients, oxygen and growth factors for cell survival and proliferation. However, since polymeric biomaterials are usually degraded by the hydrolysis of backbone bonds, an excessive absorption of water could also be related to a faster degradation [144, 145]. In line with this statement, CH constructs showed the highest mass swelling ratio and the fastest degradation compared to CH-GG and CH-TG which had very similar swelling ratios and degradation profiles. Despite the presence of lysozyme which could accelerate the degradation rate, CH-GG and CH-TG showed excellent stability in this environment by maintaining their shape for at least 9 weeks. Controlling the degradation of the manufactured constructs is crucial for tissue engineering applications and it is highly dependent on the target tissue or organ. In fact, if it degrades too fast, its role in supporting the new tissue formation is lost. On the other hand, if it degrades too slowly it can hinder the regeneration process [10]. Similarly, based on the application, engineered constructs should have the desired mechanical properties [146]. In this study, we investigated Young's moduli of hydrogels made of CH, CH-GG and CG-TG. We found that the inclusion of GG, but not of TG to chitosan, led to an increase of this value, representative of the stiffness of the hydrogels. SEM images showed that the three constructs have a highly porous structure, typical of hydrogels, that could efficiently support cell proliferation and migration [147], with no significant difference among the three samples. After 21 (CH) or 49 (CH-GG and CH-TG) days in lysozyme, signs of internal degradation were evident for the three samples. These results are promising if the inclusion of cells within the constructs is considered. In fact, cells would be able to produce their own ECM while scaffold degrades, supporting the regeneration of tissues which could require a relatively long time to occur. We finally evaluated the ability of the developed constructs to release BSA as a model protein. Results showed that all constructs were able to release BSA

with similar kinetics. However, CH and CH-GG released BSA in higher amounts compared to CH-TG. Surprisingly, the release profile of BSA from CH-GG constructs did not follow its degradation profile. In fact, even if CH alone degrades faster compared to CH-GG, they were able to release BSA with the same kinetic.

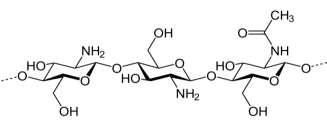
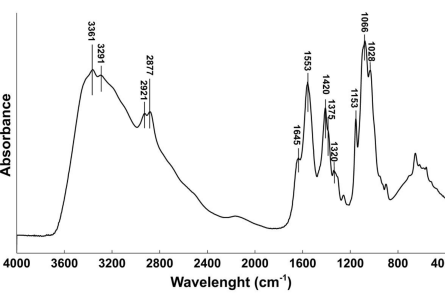
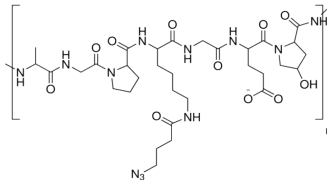
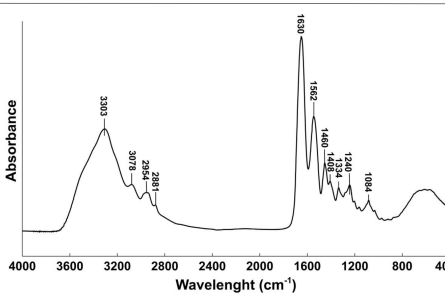
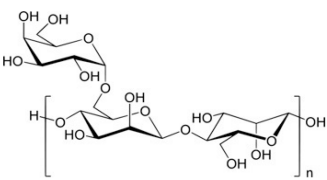
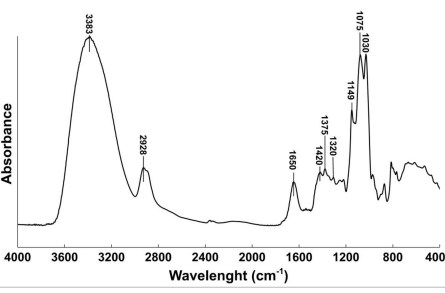
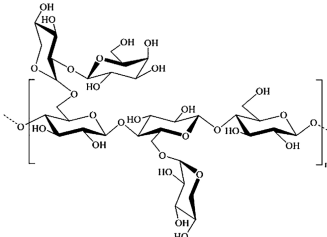
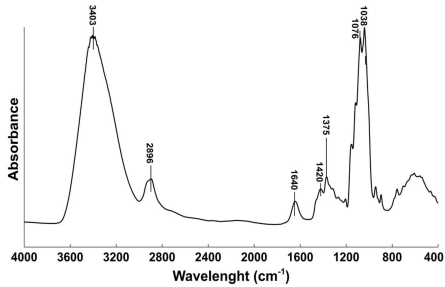
### 3.2.6 Conclusions

In this study we developed new self-supporting 3D printed constructs based on chitosan (CH) and either guar gum (GG) or tamarind gum (TG) through a dual gelation strategy, based on the inclusion of gelatin to improve the printing process and on the immersion of the 3D printed constructs into a gelation bath (ethanol-NaOH), after printing, to induce their long term-stability. We showed that the inclusion of GG or TG improved some of the properties of CH alone, such as its degradability and stiffness (only GG). In fact, while CH constructs were weak and almost completely degraded after 3 weeks, CH-GG and CH-TG were stable in lysozyme for at least 9 weeks. Further studies are needed to investigate the ability of these printed constructs to allow and support cell growth, migration and differentiation. Further investigations are also needed to better understand the interactions occurring between GG, TG and CH, in order to interpret, for example how the size of the branching (which is longer in TG and shorter in GG) could influence the rheological and mechanical properties of the biomaterial inks and the 3D printed constructs, respectively.

### 3.2.7 Supplementary information

Figure B1 shows the chemical structure of chitosan, gelatin, guar gum and tamarind gum, their FTIR spectra and their characteristic absorption peaks. Most of the peaks for chitosan, gelatin and guar gum (reported in black characters) were attributed based on other studies [148, 149, 150], while others, and in particular for tamarind gum, were proposed in this study (reported in blue characters). Looking at the four spectra we can notice that they are quite similar to each other and that they all present a large peak between 3000 and 3700  $\text{cm}^{-1}$ . This peak is attributed to N-H and/or O-H stretching and to intramolecular hydrogen bonding. This peak is present in all the FTIR spectra, due to the presence of N-H or O-H groups in the four molecules. Furthermore, since the spectra were collected on films, these peaks are also characteristic of the bound residual water. The region between 2850 and 2960  $\text{cm}^{-1}$  is due to the C-H stretching, which is also present in the backbone of the four molecules. The peak around 1650  $\text{cm}^{-1}$  is characteristic either of the C=O stretching (which is present in chitosan and gelatin molecules) or of the C-N stretching of the amide group (which is present, again, in chitosan and gelatin) or to residual water [151], which is certainly the case for guar gum and tamarind gum since they both lack double bonds or amide groups. The peak around 1560  $\text{cm}^{-1}$  is due to the N-H bending vibration and from the C-N stretching vibration of the amide group. As expected, these two peaks are not present in the spectra of guar gum and tamarind gum since they do not present amide groups. The peak at 1320  $\text{cm}^{-1}$  is the CH<sub>2</sub>-OH. In chitosan, it is attributed to the presence of the acetyl group of the N-acetyl-glucosamine and it is the reason why it is employed for the calculation of its degree of deacetylation. Even if the peak at 1375  $\text{cm}^{-1}$  is usually typical of the C-H bending of the methyl group (CH<sub>3</sub>), this must be true for the chitosan and gelatin, which have methyl functions but it can not be true for guar and tamarind gum. In these two gums, peaks around 1370 and 1385  $\text{cm}^{-1}$  are more probably related to the presence of methylene groups (CH<sub>2</sub>). Peaks from 1200 to 800  $\text{cm}^{-1}$  are attributed to C-C-O, C-OH and C-O-C stretching modes of the polymer backbone and are typical of polysaccharides. These peaks are in fact present in chitosan, guar gum and tamarind gum which, not surprisingly, are very similar to each other.



Molecules	FTIR spectra	Characteristic absorption peaks
<p><b>Chitosan</b></p> 		<ul style="list-style-type: none"> <li>- 3291–3361: N-H and O-H stretching and intramolecular hydrogen bonds</li> <li>- 2921 and 2877: C-H symmetric and asymmetric stretching, respectively</li> <li>- 1645 and 1320: C=O stretching of amide I and C-N stretching of amide III (presence of residual N-acetyl groups)</li> <li>- 1553: N-H bending</li> <li>- 1420 and 1375: CH<sub>2</sub> bending and CH<sub>3</sub> symmetrical deformations</li> <li>- 1153: asymmetric stretching of the C-O-C bridge</li> <li>- 1066 and 1028: C-O stretching</li> <li>- 1200-800: C-C-O, C-OH and C-O-C stretching modes of polymer backbone</li> </ul>
<p><b>Gelatin</b></p> 		<ul style="list-style-type: none"> <li>- 3433: N-H stretching and intramolecular hydrogen bonds</li> <li>- 2954 and 2881: C-H stretching modes</li> <li>- 1630: amide I (C=O stretching/hydrogen bond coupling with COO)</li> <li>- 1562: amide II (bending vibration of N-H groups and stretching vibrations of N-C groups)</li> <li>- 1460-1380: symmetric and asymmetric bending vibrations of methyl and methylene groups (CH<sub>2</sub> and CH<sub>3</sub>)</li> <li>- 1240: amide III (vibrations in plane of C-N and N-H groups of bound amide)</li> <li>- 1084: C=O stretching</li> </ul>
<p><b>Guar gum</b></p> 		<ul style="list-style-type: none"> <li>- 3300: O-H stretching vibration of polymer and water involved in hydrogen bonding</li> <li>- 3000-2800: C-H stretching modes</li> <li>- 1650: Associated water molecule</li> <li>- 1420: CH<sub>2</sub> deformation (methylene group)</li> <li>- 1375: vibration of CH<sub>2</sub> (methylene group)</li> <li>- 1200-800: C-C-O, C-OH and C-O-C stretching modes of polymer backbone</li> <li>- 1079: CH<sub>2</sub>-OH stretching mode</li> </ul>
<p><b>Tamarind gum</b></p> 		<ul style="list-style-type: none"> <li>- 3403: O-H stretching vibration of polymer and water involved in hydrogen bonding</li> <li>- 2896: C-H stretching modes</li> <li>- 1640: Associated water molecule</li> <li>- 1420: CH<sub>2</sub> deformation (methylene group)</li> <li>- 1375: vibration of CH<sub>2</sub> (methylene group)</li> <li>- 1200-800: C-C-O, C-OH and C-O-C stretching modes of polymer backbone</li> </ul>

**Figure B1.** Summary of the FTIR spectra and characteristic absorption peaks of chitosan, gelatin, guar gum and tamarind gum. The characteristic absorption peaks for chitosan, gelatin and guar gum have been obtained from previous studies [148, 149, 150] and are reported in black. The characteristic peaks of tamarind gums were not found in the literature and are extracted from the graph and the comparison with guar gum and chitosan spectra. These and others derived peaks are reported in blue.

### 3.3 Ongoing study: 3D printing of anisotropic cardiac patches

One of the applications that we are currently investigating and that involves the 3D printing of the previously developed inks based on chitosan and guar gum or tamarind gum, is the fabrication of anisotropic cardiac membranes (or patches) for the treatment of myocardial infarction (MI).

The heart has limited capacity of regeneration. Once cardiomyocytes (the contractile cells of the cardiac muscle) of an adult heart are damaged, they are replaced by non-contractile fibrotic scar tissue. The loss of the contractile capacity of the cardiomyocytes leads to the dysfunction of heart and causes, eventually, heart failure [152]. A promising approach for the treatment of the MI is the application of cardiac patches, which can be two-dimensional (2D) membranes or three-dimensional (3D) constructs. In order to be efficient in restoring the cardiac function, these patches should i) have mechanical properties similar to those of the heart and ii) release therapeutic ingredients, which can be cells and/or growth factors.

For now, we only focused on the mechanical behavior of the cardiac tissue, which is given by its particular structure.

The heart walls are composed of three layers: the outer epicardium, the middle myocardium, and the inner endocardium. Myocardium consists of cardiac muscle fibers, also called “myofibers”, which are aligned in a specific orientation. This orientation was first quantified by Streeter *et al.* [153] who showed a transition in the orientation of myocytes of the left ventricle, from a left-handed helix at the epicardium to a right-handed helix at the endocardium, by observing histologic slices through the ventricular wall, as shown in Figure B2 (A). However, cardiac muscle fibers are oriented differently not only from epicardium to endocardium but also from the base to the apex of the heart. In fact, the myocardium has been described as a continuous muscle band that wraps up both the left and right ventricles, with bands oriented spatially as a helix formed by basal and apical loops [154] (schematized in Figure B2). Consequently if we look at a longitudinal cross section of the left ventricle (Figure B2 (C)) we can see that the orientation of fibers differ from the base to the apex. The simultaneous contraction of muscle fibers with different orientations allows for the pumping capabilities of the left ventricle. Because of the particular myofiber orientation, myocardium is defined as a highly anisotropic tissue. Anisotropy, as opposed to isotropy, is the property of being dependent on the direction. Considering the mechanical properties of the heart wall, and particularly of the left ventricle, being an anisotropic tissue means that the stiffness of the heart tissue is not uniform, but it depends on the fiber orientation.

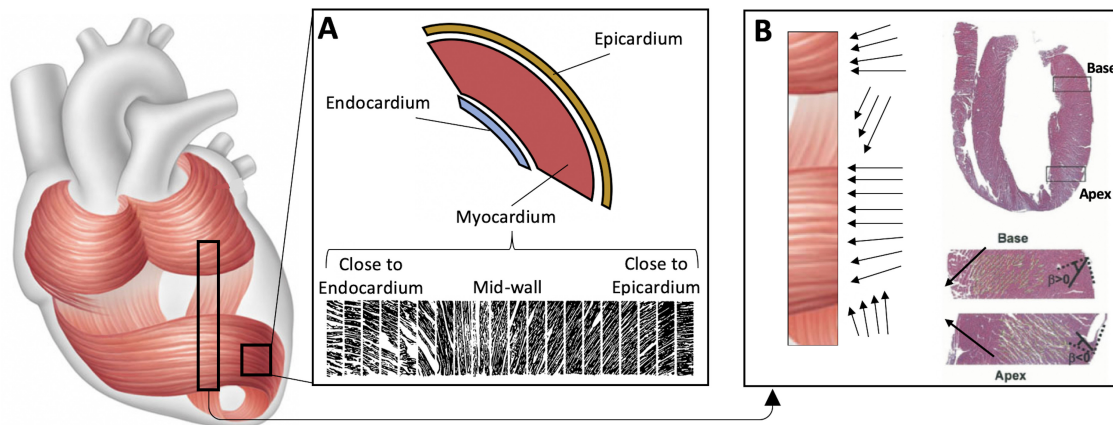


**Figure B2.** Schematic representation of the myofiber orientation showing (A) the cross-section of the left ventricle wall. The figure in the lower part is reused from [153] and indicates the sequence of photomicrographs showing fiber angles in successive sections are parallels to the epicardial plane of the canin heart. (B) Higher magnification of the schematic representation of the myocardium helicoidal orientation from base to apex. The figure in the right part shows the hematoxylin and eosin stain of the longitudinal cross-section of left ventricle of a porcine heart. Figure reused from [155].

When a cardiac patch is applied on the heart wall, it is subjected to strain and shear stress caused by the heart beating. Similarly, the mechanical behavior of the region of the heart in contact with the patch can be modified if the mechanical characteristics of the patch are higher than those of the native tissue. The patch can then rigidify the area, by applying an inappropriate force to the heart, ultimately causing a restriction effect. As a consequence, a major challenge for engineering cardiac patches is represented by the recapitulation of the fibrillar structural organization and in particular of the anisotropic mechanical behavior of native myocardial muscle [134].

In order to be able to fabricate cardiac patches with the appropriate mechanical characteristics, Jehl *et al.* [134] characterized the mechanical properties of the myocardial wall of pig cardiac tissue by performing nanoindentation measures on tissues slices of the long axis of the left ventricle, as shown in Figure B3A). Their results showed variations in stiffness according to the local orientation of the myocardial tissue. In fact, by knowing that the tissue is less stiff (and consequently results in a lower Young's modulus) when the indentation is parallel to fibers, meaning that the latter are longitudinally oriented (Figure B3,B top) while the tissue is stiffer (and consequently results in higher Young's modulus), when the indentation is perpendicular to fibers, meaning that the latter are radially oriented (Figure B3B, bottom), they were able to describe and model the overall fiber orientation.

Subsequently, we evaluated the possibility of using the previously developed ink formulations based on chitosan and natural gums for the fabrication of anisotropic cardiac patches. As previously shown (3.2.4.5), we characterized by nanoindentation, hydrogels composed by the three ink formulations based on chitosan (CH), chitosan/guar gum (CH-GG) and chitosan/tamarind gum (CH-TG), which resulted in different values of Young's moduli. In a preliminary study, in collaboration with the Ecole de Chirurgie de Nancy, we compared the mechanical properties of the developed bioinks with the mechanical properties of the rat cardiac tissue. Three samples were characterized by nanoindentation: i) the cardiac tissue-derived extracellular matrix (decellularized ECM or dECM), ii) the myocardium with a longitudinal myofiber orientation and iii) the myocardium with a radial myofiber orientation. In the myocardium, myofibers are immersed in an extracellular matrix mainly composed of collagen fibers aligned in parallel to cardiac myocytes to

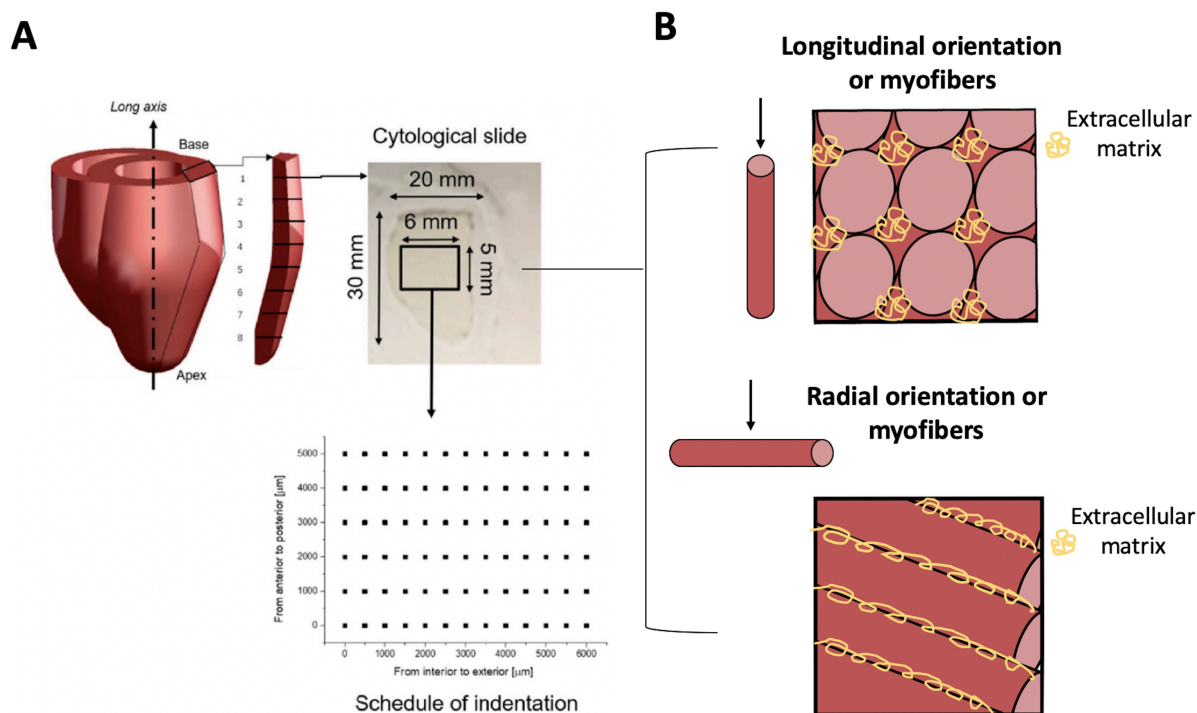


**Figure B3.** Schematization of the nanoindentation testing conducted by Jehl *et al.* [134]. A) Schematization of the tissue slices obtained from the left ventricle of pig hearts and of nanoindentation mapping (Figure reused from [134]). B) Representative images showing the direction of the indentation (arrows) and the two opposite myofiber orientations: longitudinal or radial respectively in the top and bottom images. By knowing that the lower Young's modulus was attributed to the longitudinally oriented one and the higher Young's modulus to the radially oriented one, it was possible to understand the possible orientations between these two and to model the overall fiber orientation.

provide structural stability and tensile strength [156]. The mechanical properties of the decellularized cardiac ECM were evaluated in order to assess the contribution of ECM components, and in particular of collagen fibers, to the general mechanical properties of the myocardium after the removal of cells. Figure B4 (A) shows the evolution of the reduced Young's modulus versus penetration depth of CH, CH-GG and CH-TG hydrogels (data reused from figure 5.11 (A)), as well as the evolution of the dECM and of the myocardium with longitudinal and radial orientation of the fibers. Figure B4 (B) shows the average Reduced Young's modulus measured between 70 and 90% of penetration depth of the same samples (data reused from figure 5.11 (B) for the samples CH, CH-GG and CH-TG). These preliminary results show that i) dECM and the myocardium with a longitudinal orientation of the fibers have a similar stiffness, which is not surprising since having an ECM with higher Young modulus would create a resistance to the normal heart beating; ii) the myocardium with a radial orientation of the fibers has, at lower percentages of penetration depth (between 0 and 75%), similar values to the CH-GG hydrogel, while after 75% of penetration depth it shows more similarities with CH-TG; iii) CH hydrogels present values of reduced young modulus that are too high compared to dECM and myocardium with a longitudinal orientation of the fibers. As a consequence, a study is also in progress in order to find the appropriate candidate to mimic the mechanical properties of the myocardium with a longitudinal myofiber orientation.

According to these preliminary results, CH-GG and CH-TG represent good candidates for the fabrication of an anisotropic cardiac patch in the reproduction of the mechanical properties of the

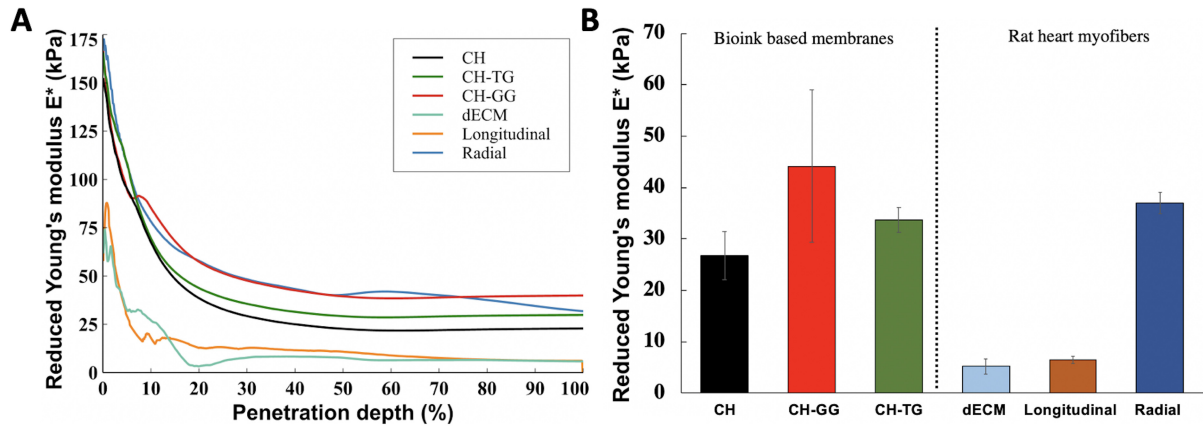


**Figure B4.** Comparison of the nanoindentation results obtained on CH, CH-GG and CH-TG constructs vs dECM and myocardial with a longitudinal and radial orientation of rat myocardial fibers. (A) Reduced Young's modulus vs indenter penetration depth for the samples CH, CH-GG, CH-TG, dECM and myocardial with a longitudinal and radial orientation of the fibers. (B) Average reduced Young's modulus values for the same samples measured between 70 and 90% of penetration depth.

myocardium with a radial orientation of the myofibers. Our further experiments will include the use of 3D bioprinting for the recapitulation of the anisotropic properties of a specific zone of the heart walls by combining the different biomaterial inks that have mechanical characteristics similar either to the myocardium with a longitudinal orientation of the fibers or to the myocardium with a radial orientation of the fibers. 3D bioprinting will allow to test easily different pattern designs in order to find the one that has the mechanical behavior closest to the native heart. In a second moment, we will functionalize the cardiac patches for the delivery of cells and/or growth factors necessary for the treatment of the myocardial infarction.

## Conclusions principales:

- Le chitosane et deux gommes naturelles, de guar (GG) et de tamarin (TG), ont été associés pour le développement d'encre pour l'impression 3D par extrusion. L'ajout de GG et TG au chitosane (CH), en améliore l'état de gélification, ce qui permet une meilleure impression. Cependant, la seule combinaison de ces deux polysaccharides n'est pas suffisante pour la fabrication de constructions tridimensionnelles.
- L'ajout de gélatine aux encres constituées de CH, CH-GG et CH-TG permet leur utilisation pour l'impression de structures 3D. Cette imprimabilité a été évalué à travers une méthode semi-quantitative, le "Pr value". Les encres ayant un "Pr value" compris entre 0,9 et 1,1 sont considérées comme des bons candidats en tant qu'encres. Bien que seulement l'encre CH-GG à montré un valeur de Pr comprise entre 0,9 et 1,1 montrant l'état de gélification idéal à 20°C et une imprimabilité optimale toutes les trois encres ont permis la fabrication de structures 3D.
- Une étape de gélification à l'éthanol et NaOH des constructions 3D imprimées en utilisant CH-GG et CH-TG a rendu ces constructions très stables et robustes sans l'utilisation de crosslinkers chimiques. L'inclusion de GG et TG à augmenté la biodegradabilité des constructions imprimées d'au moins 6 semaines, par rapport à celles imprimées en utilisant seulement CH.
- Les constructions CH-GG ont montré un module de Young plus élevé par rapport aux structures de CH-TG et CH seuls. Les différentes propriétés mécaniques de ces constructions sont actuellement exploitées pour la fabrication de patches cardiaques anisotropes.
- Les constructions imprimées en utilisant les encres CH, CH-GG et CH-TG peuvent libérer la BSA utilisée ici en tant que protéine modèle. CH-TG montre une libération de BSA plus soutenue par rapport aux constructions CH et CH-GG qui pourrait toutefois dépendre d'une perte plus importante de cette protéine lors de la gélification des constructions imprimées.

## Perspectives:

Bien que ces études montrent de potentielles applications de ces encres, des études plus approfondies sont nécessaires afin d'optimiser l'utilisation de chitosane en combinaison avec la gomme de guar et la gomme de tamarin en tant qu'encres ou bio-encres. En particulier, différentes proportions de ces composants devraient être évaluées pour mieux comprendre les interactions entre ces macromolécules, ce qui pourrait nous permettre d'identifier les raisons de certains comportements obtenus (*i.e.* un module de Young plus élevée pour la construction CH-GG par rapport aux autres etc.). Par exemple, une analyse détaillée des propriétés viscoélastiques pourrait contribuer à une meilleure compréhension des contributions de chaque composante. Les propriétés mécaniques des constructions 3D, ainsi que leur capacité à encapsuler ou retenir des facteurs d'une manière plus efficace, ou de les libérer d'une manière plus ou moins soutenue, sont également influencées par le processus de gélification (impliquant le temps d'immersion, la concentration de NaOH, la proportion éthanol:NaOH). Différents protocoles pourraient ainsi être testés pour obtenir des constructions 3D avec des propriétés mécaniques ou de libération désirées. Pour finir, des études sont nécessaires pour évaluer la biocompatibilité des structures imprimées en 3D ainsi que leur habilité à soutenir la croissance, la migration et la différenciation cellulaires. Étant donné que le GG et le TG sont acceptés comme additifs alimentaires, nous nous attendons à ce qu'ils soient compatibles avec les cellules de même que les matériaux résultants de leur combinaison avec le chitosane. L'une des limites de cette étude, et de manière plus générale, de l'utilisation du chitosane en tant qu'encre,

est que son insolubilité dans l'eau empêche l'encapsulation des cellules directement dans l'encre. Pour contourner cette limitation il est toutefois possible d'utiliser du chitosane soluble dans l'eau ou d'inclure dans l'encre des molécules comme le  $\beta$ -Glycerol phosphate qui, souvent utilisé pour induire une gelification, peut également diminuer le pH d'une solution de chitosane. Alternative-ment, la neutralisation des structures après impression est généralement suffisante pour les rendre biocompatibles.





## Chapter 4

# Advanced 3D bioprinting strategies for the controlled delivery of growth factors

## Stratégies avancées de bio-impression 3D pour la libération contrôlée de facteurs de croissance

Dans le chapitre 3 nous avons vu que la libération de l'albumine de sérum bovin (BSA en anglais pour Bovine Serum Albumin) à partir de structures 3D (faites de chitosane, chitosane et gomme de guar ou chitosane et gomme de tamarin), dépend du type des macromolécules composant la structure 3D (ou "scaffold"). Cette protéine est souvent utilisée comme protéine modèle en raison de son faible coût et de sa bonne stabilité, ce qui la rend plus facilement quantifiable par rapport à d'autres molécules. Toutefois si on imagine encapsuler maintenant une protéine différente, ayant une masse moléculaire plus grande ou plus petite ou ayant une charge de surface lui permettant de créer des interactions électrostatiques avec le polymère composant le scaffold, on obtiendra très probablement une cinétique de libération différente. De manière similaire, si l'on modifie la composition des scaffolds en utilisant des biomatériaux qui se dégradent plus ou moins rapidement, ou qui forment un réseau plus ou moins dense sur la base de leur concentration ou, par exemple, de la présence et la densité de cross-linkers, on obtiendra aussi des cinétiques de libération différentes. Il est donc clair que de nombreux facteurs influencent la libération des molécules, ce qui représente aussi un avantage. En effet, les matériaux peuvent être modifiés pour obtenir le profil de libération désiré [157].

La possibilité de contrôler la libération de facteurs à travers leur encapsulation dans des biomatériaux est un domaine de recherche très actif, surtout en pharmacologie, pour la libération de médicaments mais aussi en ingénierie tissulaire, pour la libération de facteurs de croissance. Ces derniers sont des molécules sécrétées par des cellules, qui ont la capacité d'influencer la migration, la prolifération et la différenciation d'autres cellules. C'est en grande partie l'activité de ces molécules qui est responsable de la formation de tissus et organes pendant le développement normal et la formation de nouveaux tissus pendant les processus naturels de régénération (par exemple après une blessure) [5]. En imitant les processus naturels, l'ingénierie tissulaire vise à inclure les facteurs de croissance pour améliorer et accélérer la formation de nouveau tissu selon deux stratégies principales, décrites dans le chapitre 1 (section 1.1) et ci-dessous brièvement résumées. Une première stratégie, appelée ingénierie tissulaire *in situ* se base sur l'implantation de scaffolds de biomatériaux qui, grâce à la libération de facteurs de croissance, attirent les cellules du patient dans la structure implantée et les induisent à développer un nouveau tissu. Une deuxième stratégie, plus traditionnelle et appelée ingénierie tissulaire *ex vivo*, se base sur l'inclusion de facteurs de croissance avec les cellules dans les biomatériaux avant la fabrication du scaffold, pour induire des cellules à

développer un nouveau tissu avant l'implantation [14].

Quelle que soit la stratégie adoptée, la présence des facteurs de croissance est essentielle pour le bon développement d'un tissu ou sa régénération. Toutefois, l'utilisation des facteurs de croissance présente des limites telles qu'une courte demi-vie, une efficacité dépendante de la dose utilisée ainsi qu'une activité très dépendante de leur localisation spatiale et temporelle. Il est essentiel que les facteurs de croissance soient libérés à un moment précis et à l'endroit nécessaire à l'accomplissement de leur action [158]. En effet, la présence de facteurs de croissance dans un tissu différent de sa cible peut conduire à de graves effets secondaires, comme la formation de tissu ectopique et le développement d'un cancer [159]. De la même manière, la présence d'une quantité trop élevée de facteurs de croissance peut conduire aux susmentionnés effets indésirables [160], alors qu'une quantité inférieure à celle nécessaire peut produire une réponse insuffisante. Comme la régénération tissulaire est un processus lent par nature, souvent l'exposition des tissus aux facteurs de croissance doit être prolongée dans le temps. Pour ce faire, de nombreuses stratégies pour contrôler la libération temporelle des facteurs de croissance ont été développées telles que leur conjugaison chimique aux biomatériaux constituant le scaffold ou leur inclusion dans des systèmes de libération tels que les nano- ou micro-particules [161]. L'application clinique de produits d'ingénierie tissulaire libérant des facteurs de croissance est encore problématique en raison des limites mentionnées ci-dessus. Toutefois, parmi toutes les technologies d'ingénierie tissulaire, la bio-impression 3D est celle qui semble la plus prometteuse pour surmonter ces limites. En effet, en permettant un dépôt spatiale précise des biomatériaux et la fabrication de géométries haute résolution, la bio-impression 3D permet, également, un dépôt précise des facteurs de croissance et de leurs systèmes de libération.

Dans le chapitre suivant (article de revue), nous présentons les limites liées à l'utilisation clinique des facteurs de croissance et nous proposons une revue des différentes stratégies qui ont été proposées dans la littérature pour surmonter ces limites à travers la bio-impression 3D.

# Advanced 3D bioprinting strategies for the controlled delivery of growth factors

*The content of this Chapter is identical to the following work which will be submitted shortly:*

**Title:** Advanced 3D bioprinting strategies for the controlled delivery of growth factors

**Authors:** Aurelia Poerio, João F. Mano, Franck Cleymand

## 4.1 Abstract

The controlled delivery of growth factors (GFs) from tissue-engineered constructs represents a promising strategy to improve tissue repair and regeneration. However, despite their established key role in tissue regeneration, the use of GFs is limited by their short half-life in the *in vivo* environment, their dose-dependent effectiveness and their space- and time-dependent activity. Promising results have been obtained both *in vitro* and *in vivo* in animal models. Nevertheless, the clinical application of tissue-engineered constructs releasing GFs is still ambiguous due to the several limitations and risks associated with their use. Three-dimensional (3D) bioprinting, by allowing the micro-precise spatial deposition of multiple materials and the fabrication of high-resolution geometries, offers advanced strategies for an optimal release of GFs from 3D constructs. This review summarizes the strategies that have been employed to include GFs and their delivery system within bioinks used for 3D bioprinting applications, in order to optimize their controlled release and to improve both the *in vitro* and *in vivo* regeneration processes. The approaches adopted to overcome the above-mentioned limitations are presented, showing the potential of the technology of 3D bioprinting to get one step closer to clinical applications.

## 4.2 Introduction

The engineering of three-dimensional biological constructs in the laboratory, with the aim to replace damaged tissues in patients and overcome the shortage of donor organs, is one of the primary goal of 3D bioprinting. Through the precise deposition of a biomaterial ink, which can contain living cells (and thus called “bioinks”) and/or biological molecules, 3D printing or bioprinting (if cells are included) allows for the fabrication of structures able to closely reproduce the complex architecture of natural tissues and organs [11]. Natural regeneration processes are highly complex and require the coordinated action of different cell types and signaling molecules, such as growth factors (GFs) [162]. GFs play a key role in tissue regeneration by controlling the proliferation, migration and differentiation of stem cells [5]. With the aim of better mimic the natural regeneration processes, the integration of GFs and their delivery system within 3D bioprinted constructs has become essential [17]. However, the optimal delivery of GFs from tissue-engineered constructs present several difficulties. A first difficulty is due to the fact that multiple GFs take part in the complex sequence of molecular and cellular events involved in the regeneration processes [163]. The inclusion of multiple exogenous growth factors within a tissue-engineered construct, however,

would result in high cost and increased risk of adverse effects, such as ectopic tissue formation or cancer [159]. Secondly, the concentration of the delivered exogenous GFs has to be maintained in the physiological range. In fact, under-physiological doses lead to an insufficient response, while supra-physiologic doses cause the above-mentioned undesirable effects [160]. Finally, to exert their therapeutic role, GFs have to be released with a specific spatio-temporal pattern [158] and have to maintain their biological activity in the target location, besides their typical short-life in the *in vivo* environment [164]. Based on the above considerations, it is clear that the clinical application of GFs is particularly problematic and that their therapeutical efficiency is totally dependent on the efficiency of the delivery system employed. Consequently, it is essential to design delivery systems or to develop strategies able to provide stability, optimal activity and tunable release for GFs [160]. As well-reviewed elsewhere [160, 158, 165], many biomaterial-based strategies have been developed to achieve a controlled delivery of GFs. However, compared to traditional tissue engineering methods, 3D bioprinting offers extraordinary advantages such as the precise positioning of biomaterials, cells and GFs in target areas [166] and the creation of complex personalized geometries [167]. The optimal release of single or multiple GFs can be achieved by controlling different steps of the bioprinting process, starting from the choice of the biomaterials used as bioinks. In fact, several parameters, such as the nature of the biomaterial, its molecular weight, its concentration and the crosslinking chemistry, can influence the bioactivity and the release of the encapsulated factors [168]. Unless incompatible with the printing process, due, for example, to a drastic reduction of the printability or the clogging of the nozzle, bioinks can usually be easily functionalized by the inclusion of GFs and/or their delivery systems. GFs can be simply be mixed with the bioink upon formation or conjugated to the polymers constituting the bioink through chemical modifications. Alternatively, GFs can be encapsulated within a delivery system, such as nano- or micro-particles, which can be, in turn, incorporated into the bioink [161]. The entrapment, conjugation and nano- or micro-encapsulation are not only primarily responsible for protecting GFs from the environment but play also a major role in controlling their temporal release. The spatial localization of GFs, instead, is usually achieved by tuning the bioprinting parameters and by creating specific and complex designs. For example, most of the currently available bioprinters allow for the fabrication of hybrid structures, by using multiple bioinks. Each part of the construct could individually release a different GF in order to spatially guide the regeneration of complex tissues [169].

This review aims to discuss and summarize the strategies employed to functionalize inks and bioinks with GFs and their delivery system to control their release from 3D bioprinted constructs and improve their efficiency. To obtain the desired therapeutical effect, four level of optimization, schematized in Figure 4.1 and discussed in the following sections, should be taken into account. We will briefly introduce the importance of choosing the optimal dosage of GFs, to obtain the desired function and avoid side effects. We will then review the strategies adopted to include single or multiple GFs within two classes of biomaterials, for hard and soft tissue regeneration, in order to preserve their bioactivity during the preparation of the bioink and the bioprinting process. Here, we will also describe a more recent strategy that combines 3D bioprinting and gene therapy giving rise to a particular class of bioinks, named GAB or “gene activated bioinks”, which aim to overcome some limitations of the direct use of GFs. We will then summarize the strategies employed to temporally control the release of the encapsulated GFs, such as the physical entrapment, chemical conjugation and nano- or micro-encapsulation. Finally, we will review the advantages of the use of 3D bioprinting technologies to control the spatial deposition of GFs presenting showcasing representative examples, with a particular emphasis on bone regeneration, due to the higher number of studies about the spatially controlled release of GFs using 3D bioprinting concerning this tissue, compared to others.

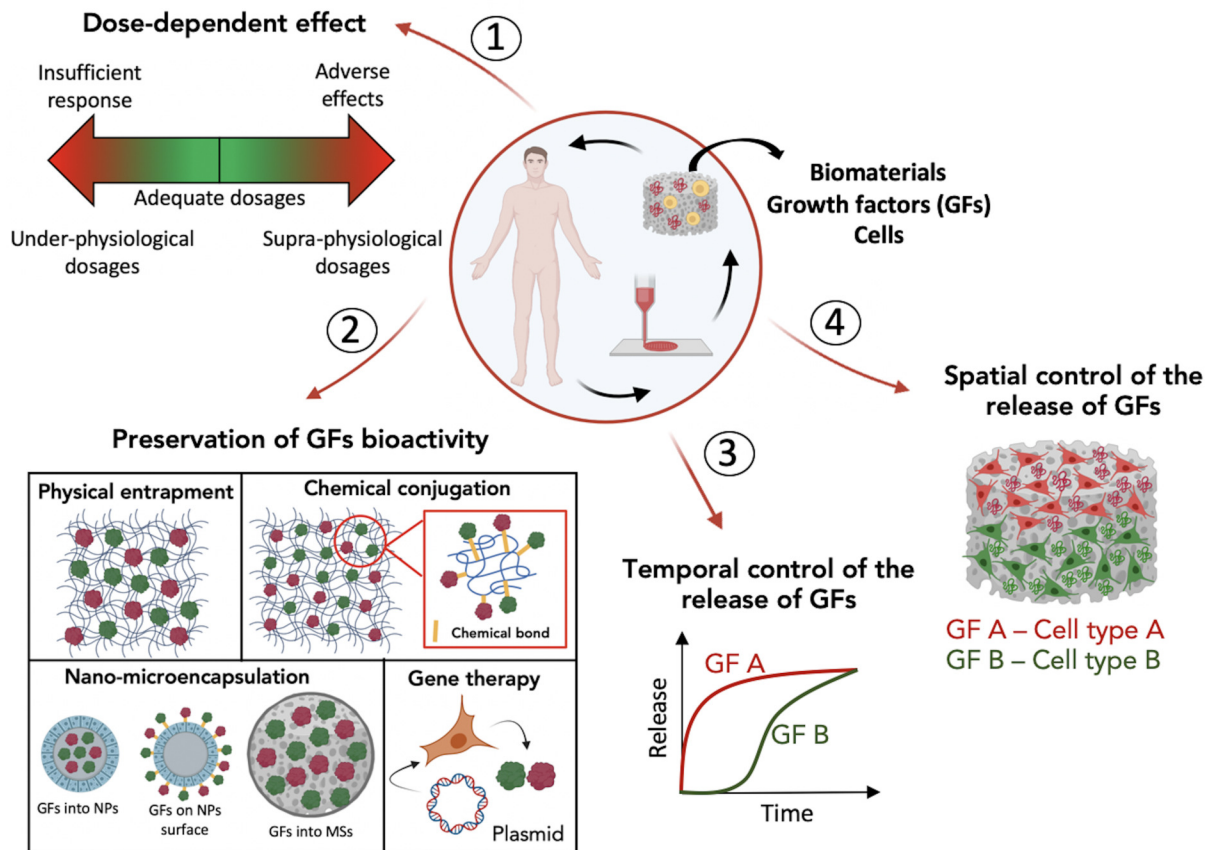


**Figure 4.1.** Schematic representation of the four level of optimization necessary to achieve the therapeutic effectiveness of GFs for tissue regeneration applications. Firstly, the optimal dose of GFs has to be carefully selected in order to avoid an insufficient response or side effects. Subsequently, based on the type of bioink and on the bioprinting process employed, a strategy should be adopted in order to preserve GFs bioactivity. In particular, GFs can be simply mixed within biomaterials composing bioinks, be chemically conjugated to the polymer network, be encapsulated or conjugated to the surface of nanoparticles (NPs) as well as of microspheres (MSs), or their production can be induced in cells by the transfection with plasmids encoding GFs. The strategies adopted to protect GFs from the environment and preserve their bioactivity can also advantageously control their temporal release. As a consequence, the same strategy is often chosen in order to both protect GFs bioactivity and temporally control their release. Controlled temporal release and coordination among multiple GFs are important since several GFs take part in the regeneration processes (e.g growth factor A: green and growth factor B: red) and their action is often time-dependent (an example is bone regeneration where angiogenesis usually precedes osteogenesis and each process is guided by different GFs). Furthermore, the spatial distribution of GFs allows for the fabrication of complex constructs by inducing, for example, the differentiation of multiple cell types to recreate the hierarchical architecture of natural tissues. Figures created with <https://biorender.com/>.

### 4.3 Importance of the dose-dependent efficiency

The selection of the appropriate concentration of GFs that need to be delivered from tissue engineered constructs is of primary importance if the developed tissue-engineered constructs aim to reach clinical applications. GFs are characterized by poor stability in the physiological environment and can easily undergo enzymatic degradation. Consequently, supra-physiological concentrations are usually delivered in order to overcome these limitations. However, supra-physiological doses

have been shown to lead to serious side effects [164, 159]. As for traditional tissue engineering applications, controlling the amount of loaded and delivered amount of GFs, as well as their bioactivity, from a 3D bioprinted construct, still present several difficulties. A loss of GFs or a decrease in their bioactivity can occur during the preparation of the bioink, the bioprinting process or the crosslinking of the printed constructs. For example, the crosslinking step sometimes requires the immersion of the constructs in a liquid solution for a specific amount of time that could lead to a diffusion of GFs. Different methods can then be employed to quantify the precise amount of GFs loaded into a construct, their biological activity after processing, or their release kinetic. However, these tests are mostly carried out in an *in vitro* environment. For example, the release kinetic is usually studied by immersing the constructs in PBS and quantifying the GFs released in the media at specific time points. It is then clear that the results obtained from these studies are not representatives of the same events occurring in the *in vivo* environment, where, many other parameters, such as the presence of enzymes, could affect the bioactivity and the dose-effect response of the delivered GFs. Although there is still a lot of work to be done, the technology of 3D bioprinting is showing promising results in controlling the release of GFs with the objective of using the appropriate doses of GFs and, hopefully, reducing the risk of side effects.

## 4.4 Inclusion of GFs to bioinks for hard and soft tissue regeneration

Once the appropriate dosage of GFs has been selected, their bioactivity inside biomaterials has to be preserved in order to obtain the desired response. Biomaterials used as bioinks can be divided into two categories, hard and soft, according to their mechanical properties, which also determine their use for specific target tissues. Hard biomaterials, such as bioceramics, metals and thermoplastic polymers, have strong mechanical properties (e.g., high elastic modulus), which are suitable for the regeneration of hard tissues, such as bones and teeth [170, 171]. Soft biomaterials, such as hydrogels, have poor mechanical properties, due to the high content in water, and are mainly employed for the regeneration of soft tissues [172]. Based on the nature of the bioink, different strategies have to be employed to include GFs during the bioink preparation and the bioprinting process, in order to protect them from the environment and to spatio-temporally control their release [173].

### 4.4.1 Hard biomaterial-based bioinks

The fabrication of bioprinted constructs using bioceramics (e.g. calcium phosphate cement (CPC), metals and thermoplastics (e.g. polycaprolactone (PCL) or poly lactic-glycolic acid (PLGA)) usually requires melting and curing during the fabrication steps. The use of high temperatures is usually incompatible with the inclusion of living cells and biological molecules. Consequently, different strategies have to be adopted to include GFs within high temperature bioprinted constructs in order to preserve their bioactivity. For example, Tarafder *et al.* [174] individually encapsulated the transforming growth factor  $\beta 3$  (TGF- $\beta 3$ ), the connective tissue growth factor (CTGF) and the bone morphogenetic protein-2 (BMP-2) into PLGA microspheres (MSs) to demonstrate that the spatially controlled delivery of multiple GFs, from the same scaffold, can induce the formation of multi-tissue interfaces, like the temporomandibular joint (TMJ) disc, which is made of fibrocartilage covering the bone. PLGA MSs were lyophilized and subsequently filled into a high temperature cartridge containing PCL, and the constructs were printed at a temperature of 120°C. Since the melting temperature of PLGA is around 200°C, the encapsulated GFs were efficiently protected by the denaturation and their bioactivity preserved, as confirmed by the induced *in vitro* differentiation of mesenchymal stem cells (MSCs) into fibrogenic, chondrogenic and osteogenic cells, when exposed to CTGF, TGF- $\beta 3$  and BMP-2, respectively.

## 4.4.2 Soft biomaterial-based bioinks

Hydrogels are the principal biomaterials used as bioinks thanks to their high content of water, which supports the viability of cells and the bioactivity of the entrapped GFs. Hydrogel-based bioinks can be made of natural or synthetic polymers [131, 175, 176]. Natural polymers, such as proteins and polysaccharides, are advantageous thanks to their similarity to extracellular matrix (ECM) composition and structure, to their biocompatibility and biodegradability characteristics [177]. However, hydrogels based on natural polymers usually present poor mechanical properties and need to be modified to allow the fabrication of complex three-dimensional bioprinted structures. On the other hand, synthetic materials, such as pluronic, polyethylene glycol (PEG) or polyvinyl alcohol (PVA), allow for controlled printing processes, leading to high-resolution bioprinted objects [78, 178].

### 4.4.2.1 Natural polymer-based bioinks

Natural biomaterials-based bioinks (e.g. alginate, chitosan, collagen, fibrinogen, gelatin, hyaluronic acid or laminin) offer several advantages regarding the inclusion of GFs. In fact, some of them are constituents of the ECM and, consequently, naturally present GFs-binding domains. Accordingly, GFs can be directly mixed within the bioink upon formation and their release depends on the diffusion and degradation profile of the hydrogel. Alternatively, GFs can be physically or chemically immobilized/conjugated to the polymer network through different strategies, such as the inclusion of heparin, which is able to bind several GFs and protect them from degradation [179]. Furthermore, some biomaterials naturally contain GFs. One relatively recent strategy adopted to preserve the naturally present endogenous GFs, is the use of decellularized ECM (dECM) as bioink [180]. Several studies showed a positive effect on tissue regeneration when using dECM with a high content of naturally present GFs [181, 182, 183] compared to other biomaterials containing exogenous GFs. This can be explained by the fact that natural ECM contains a high variety of GFs, which are rarely included in bioinks from an exogenous source, due to the high cost and possible side effects. Another interesting recent strategy employed to include multiple GFs and avoid side effects is the inclusion of platelet-rich plasma (PRP) to hydrogel-based bioinks as a source of autologous GFs, which positive effects have been shown by several studies [184, 185, 186, 187, 188, 189]. The use of dECM as bioinks or the inclusion of PRP could represent fascinating strategies to overcome the limitations of the delivery of multiple GFs in the adequate dosages from bioprinted objects, allowing a better mimic of the *in vivo* repair and regeneration processes [163].

### 4.4.2.2 Synthetic polymer-based bioinks

Synthetic polymers are less used as components of bioinks, compared to natural ones, since they usually lack biological cues for cell attachment [190]. The most used synthetic polymers are polyglycolic acid (PGA), polylactic acid (PLA) and their co-polymers PLGA, PCL, PVA and PEG [191]. Since their bioprinting process often involves the use of organic solvents or high temperatures, synthetic polymers-based bioinks are usually not compatible with the incorporation of cells or GFs [192]. However, thanks to their excellent printability properties, they are usually used in combination with natural-based hydrogels loaded with cells or GFs [193]. Alternatively, they are excellently employed as delivery systems thanks to their degradation properties which can be easily modulated.

## 4.4.3 Heterogeneous materials

In some cases, the simple mixing of GFs within bioinks is not possible or not appropriate. For example, bone regeneration often requires the use of solid materials such as CPC, which, because

of the setting reaction and subsequent leaching once the material is hydrated, can lead to the loss of the encapsulated GFs [194, 195]. As a consequence, GFs can be released from CPC-based materials using different strategies such as the inclusion of a delivery system or the combination with another material compatible with the bioactivity of GFs. To overcome this limitation, Akkineni *et al.* [195] encapsulated the vascular endothelial growth factor (VEGF) within dextran sulfate-chitosan microspheres which were subsequently mixed to CPC paste in a freeze-dried state, while Ahlfeld *et al.* [196, 197] created a biphasic scaffold through the combination of CPC-based bioink and VEGF-loaded alginate-gellan gum bioink. Shim *et al.* [193] used a dual-head printing system to print BMP2-loaded collagen/gelatin solution into hollow cylindrical PCL/PLGA scaffolds.

#### 4.4.4 Gene activated bioinks (GABs)

An interesting strategy employed to overcome the limitations of the short half-life of GFs and/or to sustain their release is to combine 3D bioprinting with gene therapy to induce cells to produce GFs autonomously. Viral or non-viral gene therapy allows the delivery of plasmid DNA (pDNA) and the consequent transfection of cells in a time- and space-dependent manner within the constructs. Gene therapy combined with 3D bioprinting has been especially used for bone regeneration and the inclusion of genes, with or without their vectors, to a bioink, rise to the so-called “gene activated bioinks (GABs). Different strategies have been developed in order to increase the transfection efficiency or to induce a sustained production of GFs from cells. Some of them include the modification of the bioink characteristics, the inclusion of delivery systems or the use of multiple materials. For example, Loozen *et al.* [198] included a naked plasmid DNA encoding for BMP-2 in a bioink composed of alginate, multipotent stromal cells/mesenchymal stem cells (MSCs) and calcium phosphate particles. Using a lower concentration of alginate, they obtained a higher transfection efficiency and consequently, higher production of BMP-2 by MSCs within the bioprinted construct and enhanced osteogenetic differentiation *in vivo*. Cunniffiee *et al.* [199] complexed plasmid DNA encoding for BMP-2 and TGF- $\beta$ 3 to hydroxyapatite nanoparticles, embedded in an RGD- $\gamma$ -irradiated alginate bioink containing bone marrow-derived MSCs. The expression of the transgenes BMP-2 and TGF- $\beta$ 3 was maintained for 14 days post-bioprinting leading to enhanced osteogenesis of the encapsulated MSCs. In order to increase the transfection efficiency, Gonzalez-Fernandez *et al.* [200] used a sacrificial bioink to create pores within the bioprinted constructs. The porosity modulates the transfection of cells which is faster when the porosity is higher and slower when the porosity is lower. By using either pro-osteogenic or pro-chondrogenic bioinks, with different porosity, they were able to direct the differentiation of encapsulated bone marrow-derived MSCs to recapitulate the native osteochondral unit. Bozo *et al.* [201] bioprinted a construct based on octacalcium phosphate (OCP) and plasmid DNA encoding for VEGF-A. This gene-activated implant induced the differentiation of the patient’s own cells in the implantation site leading to improved vascularization and osteointegration.

## 4.5 Strategies adopted to temporally control the release of growth factors

### 4.5.1 Physical entrapment

The simple mixing of GFs with the hydrogel-based bioinks is the most common and simple method for their delivery from bioprinted constructs. The release kinetic of the entrapped GFs is usually characterized by an initial burst followed by a slower release which depends on the diffusion and degradation profile of the hydrogel. The diffusion process is, in turn, controlled by the matrix



properties such as the type of polymer, its molecular weight and concentration, and the characteristics of gelation [157]. Also, the crosslinking density affects the degradation rate and the water content, and consequently the release of the encapsulated molecules, generally without influencing their bioactivity [202]. Usually, fast degradation of the polymer is related to a fast release of the GFs. The strategies adopted to temporally control the release of GFs from hydrogel-based scaffolds, mainly based on the optimization of the above-mentioned parameters, have been excellently reviewed [158, 66, 165] and can be applied to hydrogel-based 3D bioprinted objects. However, the use of this technology offers several advantages compared to traditional tissue engineering strategies. 3D bioprinting, in fact, allows for a fast and reproducible deposition of single or multi-materials containing one or more GFs for the creation of complexes bioprinted geometries with high resolution [203]. For example, Park *et al.* [204] bioprinted a multi-material construct to allow for the release of VEGF and BMP-2 with two different kinetics by loading VEGF into a alginate/gelatin-based bioink, which degrades faster and BMP-2 in a crosslinked collagen bioink, which degrades slower (Figure 4.2A). The faster release of VEGF from the implanted construct facilitated early vasculogenesis and is promising in enhancing bone formation, even in the core of a large structure. Furthermore, the release kinetic of the entrapped molecules can be modified by tuning the printing parameters such as the geometry of the bioprinted construct, the size of the filaments and the distance between filaments, responsible of the macro-porosity [205, 206]. However, if GFs are simply physically entrapped, they can more easily diffuse out of the construct or undergo enzymatic degradation [161]. Consequently, especially when long exposures are required, other methods can be employed to include GFs into bioinks and control their delivery, such as their immobilization or chemical conjugation to the hydrogel.

## 4.5.2 Immobilization and covalent conjugation

An attractive strategy employed to increase the half-life of GFs and avoid their burst release is to mimic the natural interactions between the GFs and the components of the ECM. With the aim of mimic the natural environment and particularly the ECM functions, that is where the activity of GFs is localized, different studies have reported the inclusion of heparin or heparin-sulfate within hydrogel-based bioinks [205] or the use of decellularized ECM as bioink [180]. GFs that exhibit ECM-binding domains can bind the matrix and can be presented to cells in spatio-temporal gradients that provide essential cues to elicit specific cellular responses [179, 207]. For example, the prolonged release of BMP-2 has been obtained by chemically modifying alginate, in order to produce alginate-sulfate (Figure 4.2B). The latter, which structurally and functionally mimics the heparin, highly enhances its binding affinity to BMP-2. Furthermore, as evidenced by the release curve shown in Figure 4.2C, the higher the concentration of alginate-sulfate, the slower the release of BMP-2. The authors suggest that this is due to the strong electrostatic interactions occurring between BMP-2 and alginate-sulfate which, in addition, protect the GF from degradation and increase its bioactivity [208]. Covalent conjugation is a common strategy used to strongly immobilize GFs to biomaterials [209]. The release of GFs mainly depends on the degradation rate of biomaterials and/or on the cleavage (hydrolytic and enzymatic) of the bonds between GFs and biomaterials. This strategy improves the stability of GFs as it may reduce the exposure of GFs to a proteolytic microenvironment at the delivery site [164]. Byamba *et al.* [210] chemically conjugated different concentrations of VEGF to GelMA (structure shown in Figure 4.2D). The binding of VEGF to the polymer (GelMA-VEGF) led to a slower release of the GF, compared to the same simply mixed to the bioink (GelMA+VEGF (Figure 4.2E)). This result is corroborated by the higher amount of VEGF still present in the hydrogel GelMA-VEGF after 7 days, compared to the hydrogel GelMA+VEGF (Figure 4.2F). The slower release and consequent longer exposition to VEGF, in turn, improved the vascularization of a bone scaffold.

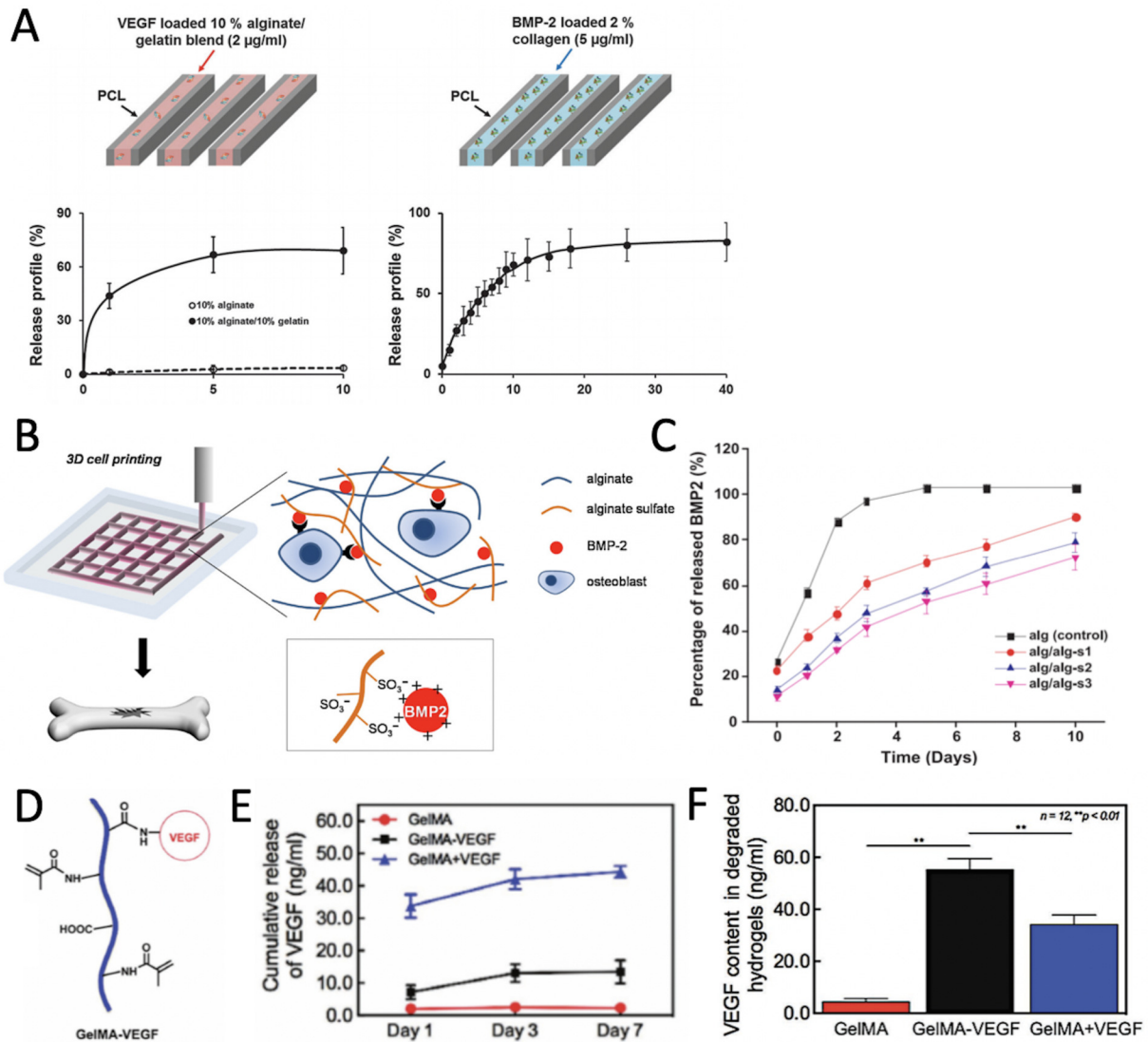


**Figure 4.2.** Strategies employed to temporally control the release of GFs from bioprinted scaffolds. A) Release kinetics of VEGF and BMP-2. The first one, entrapped in an alginate/gelatin-based bioink (pink) is released faster compared to BMP-2, entrapped in crosslinked collagen bioink (blue). Reproduced with permission. [204] Copyright 2015, The Royal Society of Chemistry. B) By mimicking the natural interactions occurring between ECM and GFs, Park *et al.* chemically modified alginate, in order to produce alginate-sulfate which resulted in a sustained release of BMP-2. Furthermore, as shown in C), the higher the concentration of alginate sulfate (which increases from s1 to s3), the slower the release of BMP-2, due to the higher number of electrostatic interactions. Reproduced with permission. [208] Copyright 2018, Elsevier. D) Structure of VEGF-conjugated GelMA hydrogels. E) Release of bioactive VEGF from VEGF conjugated GelMA hydrogel (GelMA-VEGF), physically mixed GelMA/VEGF hydrogel (GelMA + VEGF), and GelMA hydrogel only (GelMA). F) Quantification of VEGF remaining in different hydrogels after 7 days of release experiments and after the degradation of the hydrogels. Reproduced with permission. [210] Copyright 2017, John Wiley and Sons.

### 4.5.3 Encapsulation into nano- or micro-carriers

Nano- or micro-encapsulation refers to the entrapment of GFs within nano- or micro-carriers, usually based on biodegradable polymers [161]. The encapsulation of GFs within a nano- or micro-carrier has several advantages. First of all, it protects the GFs from the environment, increasing their half-life, and allows for the encapsulation of a more precise amount of GFs, avoiding under- or over-dosing which can cause undesirable effects. Furthermore, by turning the fabrication method and the polymer properties (such as the molecular weight, the concentration etc.), the temporal release of the entrapped factors can be significantly controlled. Nano-carriers, due to their small size, can be easily incorporated into bioinks. For micro-carriers, contrariwise, the size should be carefully considered in order to avoid the clogging of the nozzle during printing [76]. The inclusion of nano- or micro-carriers could also affect the viscoelastic properties of the bioinks and the resolution of the resulting biofabricated constructs in terms of printability and shape fidelity [211]. For example, laponite, a nanosilicate commonly applied for bioink reinforcement, can play the dual role of bioink reinforcer and GFs delivery system [212]. The structure of 3D bioprinted objects, (e.g. filament size, geometry, macroporosity), allows for further control of the temporal release of GFs. Furthermore, taking advantage of the ability of 3D bioprinting to precisely localize a specific amount of bioink, the release of the GFs entrapped in nano- or micro-carriers can take place under a well-controlled spatial localization.

#### 4.5.3.1 Nanocarriers

Due to their small size, nanoparticles (NPs) are an extremely advantageous carrier for GFs. They can provide a controlled release and great ability to target the desired cells thanks to their high penetration abilities [213]. NPs are generally classified as hard and soft, with the first one having high compressive modulus and the soft ones with mechanical properties more similar to natural hydrogels [214]. In both cases, the methods usually employed to include GFs for their controlled release are their encapsulation into core-shell NPs or their conjugation/absorption to the NPs surface [213]. For example, nanosilicates have a particular surface charge with negatively charged faces and positively charged edges. Consequently, they can interact with a wide range of GFs including BMP-2, VEGF, platelet-derived growth factor (PDGF) and fibroblast-derived growth factor (FGF) and result in their sustained release. Peak *et al.* [215] included nanosilicates to a poly(ethylene glycol)-dithiothreitol (PEGDTT) bioink in order to both improve its shear-thinning properties and act as a sustained delivery system for GFs (Figure 4.3A). In a first moment, they used fluorescein-conjugated bovine serum albumin (FITC-BSA) as a model protein to demonstrate that nanosilicate-loaded 3D bioprinted scaffolds were able to release the desired molecules for 28 days (Figure 4.3B). Subsequently, they demonstrated that VEGF and FGF released from 3D printed structures were able to induce the migration of human vascular endothelial cells (HUVEC) compared to the negative control groups that did not contain the GFs (Figure 4.3C). Similarly, nanospheres made of polydopamine present many active functional groups on the surface that can be used to graft the GFs. Polydopamine nanospheres were used to sustain the release of CTGF and TGF- $\beta$ 3 up to 30 days which led to a significant regeneration of the intervertebral disc [216]. The use of different populations of NPs allows for the bioprinting of constructs where each part has a distinct growth factor release pattern. Freeman *et al.* [217] investigated the release profile of VEGF from a bioink made of RGD  $\gamma$ -irradiated alginate and methylcellulose in presence of laponite NPs or hydroxyapatite NPs (nHA). Their results showed that laponite NPs markedly slowed down the release of VEGF (that was less than 50% at day 10) while nHA led to a faster and more gradual release profile (100% at day 10). Aiming to obtain a near-complete release of VEGF over 10 days, in order to mimic the release observed during normal fracture healing, they included nHA to the “vascular” bioink. Contrarily, aiming to release BMP-2 from the bioprinted constructs slowly, they included laponite NPs to the “osteoinductive” bioink. The two bioinks were used to create

a composite scaffold able to release BMP-2 and VEGF in a well-controlled temporal and spatial manner, which enhanced angiogenesis and bone regeneration *in vivo*. The encapsulation of GFs in the core of nanoparticles, allows for a controlled temporal release which is dependent on their size and the properties of the polymers NPs are made of. Lee *et al.* [218] showed that the release of nerve growth factors (NGF) encapsulated into PLGA nanoparticles and subsequently embedded in PEG-based 3D bioprinted constructs, was consistently lower, for at least 7 days, compared to the release of NGF directly sprayed on the scaffolds [218]. The sustained released of NGF from the 3D bioprinted scaffold led to enhanced neurite outgrowth compared to the NGF sprayed of the surface of the scaffold.

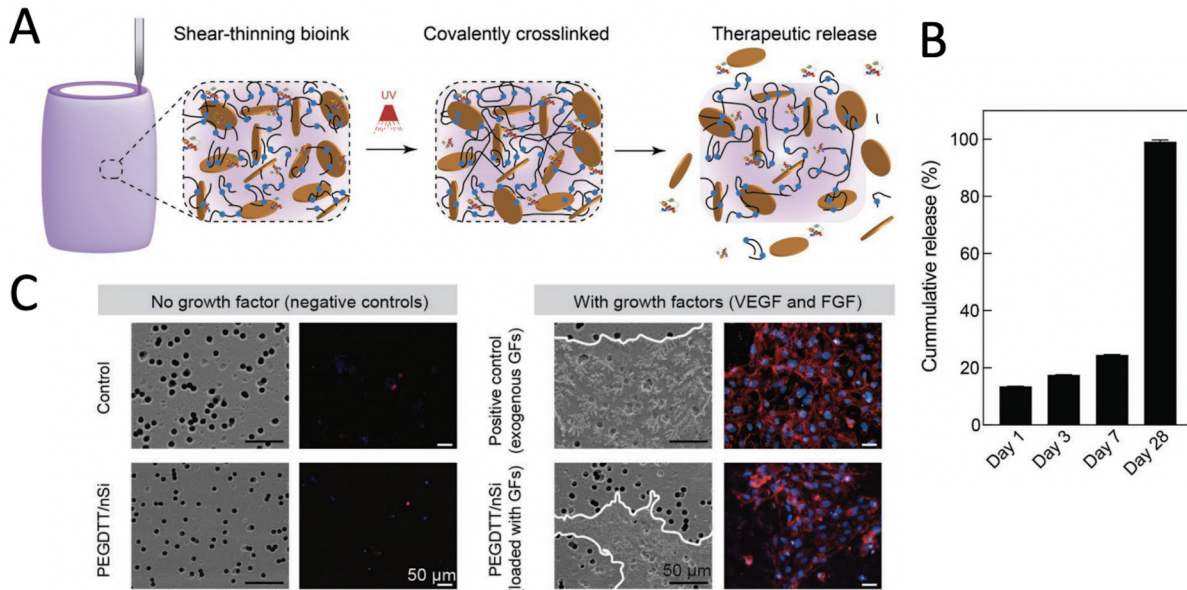


**Figure 4.3.** Nano-encapsulation for the temporal control of the release of GFs from bioprinted constructs. A) The high surface area and charge characteristics of nanosilicates are able to sequester protein therapeutics within 3D printing structure. The degradation of printed network results in the release of therapeutics. B) The release of fluorescently labeled protein (FITC from 3D printed structure) was monitored over 28 d in PEGDTT/nSi hydrogels. C) Actin and nuclei staining of migrating HUVECs across transwell. The addition of growth factors (VEGF and FGF) to PEGDTT/nSi influences cell migration. SEM images of deposited extracellular matrix (outlined in white) due to cell migration. Reproduced with permission. [215] Copyright 2021, John Wiley and Sons.

#### 4.5.3.2 Microcarriers

The encapsulation of GFs into microcarriers is mostly referred to their inclusion in spherical structures of micrometrical size, usually labeled as microparticles (MPs) or microspheres (MSs) [165]. Similarly to NPs, MPs can be made of natural materials such as chitosan, alginate and gelatin or synthetic materials such as PLA, PLGA or PCL [219]. Either using natural or synthetic materials, the microencapsulation present the great advantage of preserving GFs from the environment, increasing their half-life by maintaining their bioactivity, and control their temporal release [220]. The release profile of the encapsulated GFs is influenced by the type of material MPs are made of, its molecular weight and concentration and by its degradation profile [221]. Furthermore, it is also influenced by the material used as bioink, its degradation properties and the geometry of the printed construct. As an example, VEGF, encapsulated into gelatin MPs embedded in a bioink

composed of Matrigel and alginate was released continuously for 3 weeks *in vitro* and with a slower kinetic compared to VEGF simply mixed into the bioink. The sustained release of VEGF led to a significant vasculogenic capacity *in vivo* compared to the control group (containing empty gelatin MSs) and the fast-release group (containing empty MSs and VEGF mixed in the bioink) [222]. Among the synthetic materials, MSs made of PLGA, a co-polymer of PLA and PGA, are the most used FDA-approved delivery system thanks to their versatility [223]. In fact, different properties such as the size of the MSs and their internal and external porosity can be easily modulated to obtain the desired release profile over periods ranging from a few days up to several months [224, 225]. Furthermore, the different ratios of PLA to PGA composing the co-polymer (labeled as 50/50, 75/25, 95/5, etc.), highly influence its degradation, which is responsible for the release profile of the encapsulated molecules [226]. In particular, higher relative contents of PLA lead to a slower degradation and consequently to a slower release [223]. Based on the above, Lee *et al.* [227] used two different co-polymers of PLGA to prepare MSs able to release CTGF and TGF- $\beta$ 3 with two different release profiles. In order to improve meniscus regeneration, CTGF was encapsulated into PLGA MSs 50/50 so that it would be released faster and TGF- $\beta$ 3 into PLGA MSs 75/25 so that it would be released slower. They showed that the sequential application, *in vitro*, of CTGF for 2 weeks, followed by the application of TGF- $\beta$ 3 for another 2 weeks, induced the differentiation of mesenchymal stem cells into fibrochondrocyte-like cells. Subsequently, they replaced the sheep meniscus with the bioprinted scaffold able to spatiotemporally release in a sequential manner CTGF and TGF- $\beta$ 3. Their *in vivo* study showed that the delivered GFs were able to stimulate the recruitment of stem cells to the scaffold, to induce their differentiation and *in situ* regeneration. The resulting multi-layer tissue was composed of either fibrous or cartilaginous tissues, connected by an intermediate zone presenting comparable characteristics to the native one. Tarafder *et al.* [174], contrarily, used the same type of PLGA MSs (50/50) to obtain a sustained release, *in vitro*, of three different GFs namely CTGF, TGF- $\beta$ 3 and BMP-2, up to 42 days. The temporally controlled delivery of CTGF and TGF- $\beta$ 3, *in vivo*, allowed for the formation of fibrocartilaginous tissue, similar to the native TMJ disc. Sun *et al.* [228] encapsulated TGF- $\beta$ 3 and BMP-4 into PLGA MSs and printed a cartilage scaffold showing that these two GFs (that were released *in vitro* up to 60 days), significantly improved *in vivo*, cartilage repair.

## 4.6 Spatial control of the release of growth factors from 3D bioprinted constructs

Natural tissue and organs are complex structures composed of multiple types of cells, whose activity is influenced by specific macro- and micro-environments and by specific biochemical signals, such as GFs. Through the coordinated deposition of multiple bioinks, 3D bioprinting allows for the creation of structures where the distribution of cells and GFs is highly comparable to that of natural tissues [229]. A controlled spatial presentation of GFs is essential for the development of heterogeneous tissues, made of multiple cell types. For example, Sun *et al.* [216] used three materials to create a complex intervertebral disc (IVD) scaffold (Figure 4.4A-C). PCL was used to print the framework necessary to provide mechanical support to the IVD scaffold. The other two materials consisted of a hydrogel made of gelatin, alginate, hyaluronic acid and glycerol and containing both BMSCs and polydopamine nanospheres carrying either TGF- $\beta$ 3 or CTGF. A specific design was then created in order to spatially control the release of TGF- $\beta$ 3 and CTGF, with the first one printed in the inner part of the scaffold and the second one in the periphery. This spatial localization of these two GFs induced the corresponding BMSCs to differentiate into nucleus pulposus like cells (in the inner part) and annulus fibrous-like cells (in the periphery). Lee *et al.* [227] fabricated an acellular meniscus scaffold whose inner region released CTGF and the outer region released TGF- $\beta$ 3. After implantation, they found that the outer zone of the regenerated

meniscus was populated by fibroblast-like cells, the inner one by chondrocyte-like cells while mixed fibroblast- and chondrocyte-like cells were found in the intermediate zone. 3D bioprinting is also showing progress in the field of neural tissue regeneration by improving the traditional nerve guidance conduits through the micro-precise deposition of single or multiple GFs gradients [230]. For example, Johnson *et al.* [203] fabricated a bifurcate pathway where one path was loaded with a gradient of NGF in order to induce the growth of sensory nerves while the other path was loaded with a gradient of GDNF in order to induce the growth of motor nerves, as shown in Figure 4.4D-G. Sun *et al.* [228] developed a dual-factor releasing system with a well defined spatial organization for cartilage regeneration. The native joint cartilage is characterized by multiple layers (Figure 4.4H) with a precise zonal-dependent chondrogenic differentiation and ECM deposition (which is higher in the superficial zone and lower in the deep zone). In order to obtain this gradient, they encapsulated TGF- $\beta$ 3 and BMP-4 into PLGA MSs, to sustain their release for 60 days (*in vitro*) and created a four-layers construct (Figure 4.4I). Three of the layers contained a combination of MSCs and TGF- $\beta$ 3 loaded PLGA MSs while the fourth one contained a combination of the MSCs and BMP-4-loaded MSs. Furthermore, in order to improve the integration of the cartilaginous constructs, the fourth layers were fabricated with increasing spacing between the printed filaments for each layer (Figure 4.4J), ranging gradually from 150  $\mu$ m (in the superficial zone) to 750  $\mu$ m (in the deepest zone) to maximize the diffusion of nutrients. The spatiotemporally controlled delivery of TGF- $\beta$ 3 and BMP-4, combined to a strategical design with a controlled microporosity, allowed for the fabrication of a highly complex anisotropic cartilage construct which showed, *in vivo*, high similarity to the native tissue.

Due to the incidence of bone disorders worldwide, many studies are focusing on the regeneration of large bone defects through the controlled delivery of GFs using 3D bioprinting strategies [231]. Bone is a complex highly vascularized tissue. Vascularization is of great importance since, during bone regeneration, osteogenesis is preceded by angiogenesis [232, 233]. For the regeneration of large size defects of bone, is then essential that both processes occur [234, 235]. For this reason, several studies focused on the delivery of VEGF, which is the most potent inducer of angiogenesis and BMP-2, known to strongly promote osteogenesis [236, 237]. The positive effect of their delivery, either in combination or alone, has been largely demonstrated through traditional tissue engineering approaches [238, 239, 240]. However, significant improvements in bone regeneration were obtained using 3D bioprinting technologies since they allow for the use of multiple materials and the fabrication of high-resolution geometries. For example, Park *et al.* [204] obtained a temporal control on the delivery of VEGF and BMP-2 by using two different biomaterials as bioink. In particular, they printed human dental pulp stem cells (DPSCs), that have both osteogenic and vasculogenic potential, with VEGF in the center of the 3D constructs and BMP-2 in the peripheral zone (Figure 4.5A). The results of their *in vivo* study showed that the pre-vascularized implanted scaffolds, due to the presence of VEGF and DPSCs, led to an improved bone regeneration compared to the same scaffold non pre-vascularized (Figure 4.5B). Contrariwise, Freeman *et al.* [217] functionalized the same bioink with these two different GFs-loaded nanoparticles (hydroxyapatite for VEGF and laponite for BMP-2) as a delivery system. Similarly, they placed the bioink containing VEGF in the inner part of the structure and BMP-2 in the periphery. They showed that the spatial patterning of VEGF and BMP-2 enhanced angiogenesis *in vivo* leading to improved large bone defect healing. Byambaa *et al.* [210] printed cylinders with different concentrations of VEGF (covalently conjugated to GelMA) gradients, arranging them from higher on the center of the structure to lower on the periphery (Figure 4.5C). The faster degradation of the inner core created a lumen functioning as central blood vessels in the construct. Ahlfeld *et al.* [196, 197] created a biphasic scaffold based on a combination of CPC paste and VEGF-loaded alginate-based hydrogel and established a gradient of VEGF by increasing the number of VEGF-loaded hydrogel strands per layer in the center of the construct and by lowering it in the periphery (Figure 4.5D).

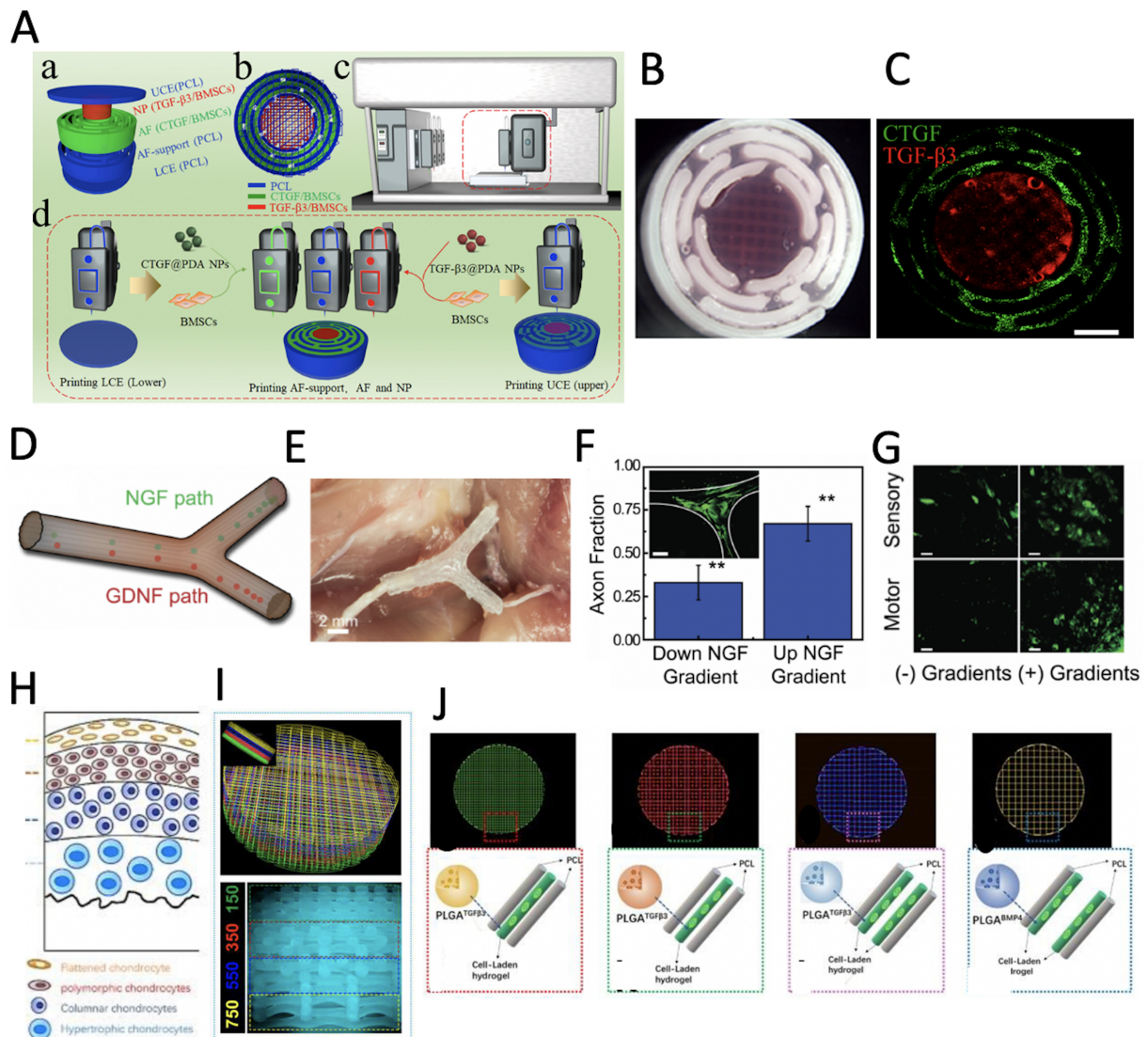


**Figure 4.4.** Spatially controlled delivery of GFs. A) Schematic representation of the fabrication design for a dual GFs-releasing intervertebral disc (IVD) scaffold by multi-head 3D bioprinting. B) Macroscopic image showing the PCL framework (white) and the hydrogel loaded with GFs (pink) and C) fluorescence images of CTGF (green) and TGF- $\beta$ 3 (red) showing their spatial distribution within the IVD bioprinted construct. Reproduced under terms of the CC-BY license.[216] Copyright 2018. Elsevier. D) Functionalization of nerve pathways with path-specific biochemical gradients. In particular, the spatial distribution was obtained by printing NGF to create the sensory path, and GDNF to create the motor paths. E) Photograph of the implanted 3D printed nerve guide prior to suturing. F) Effect of the diffusive NGF gradient on the guidance of the sensory neurite network growth. G) Histology of regenerated nerve showing cross-sections of regenerated nerves stained for tubulin (green) confirming that the presence of GFs induced the formation of different pathways. Reproduced with permission. [203] Copyright 2015, John Wiley and Sons. H) Schematization of the four-layer structure of native articular cartilage. I) CAD model of the gradient cartilage scaffold for the hydrogel part (upper) and for the PCL pillar (lower). J) CAD of the four-layer with 150  $\mu$ m spacing (green); 350  $\mu$ m spacing (red); 550  $\mu$ m spacing (blue) and 750  $\mu$ m spacing (yellow), deposited between PCL paths. Reproduced with permission. [228] Copyright 2020, Science Advances.

The spatial organization of VEGF showed a significant enhancement of the vascularization of the implanted scaffold compared to the groups that did not contain VEGF.



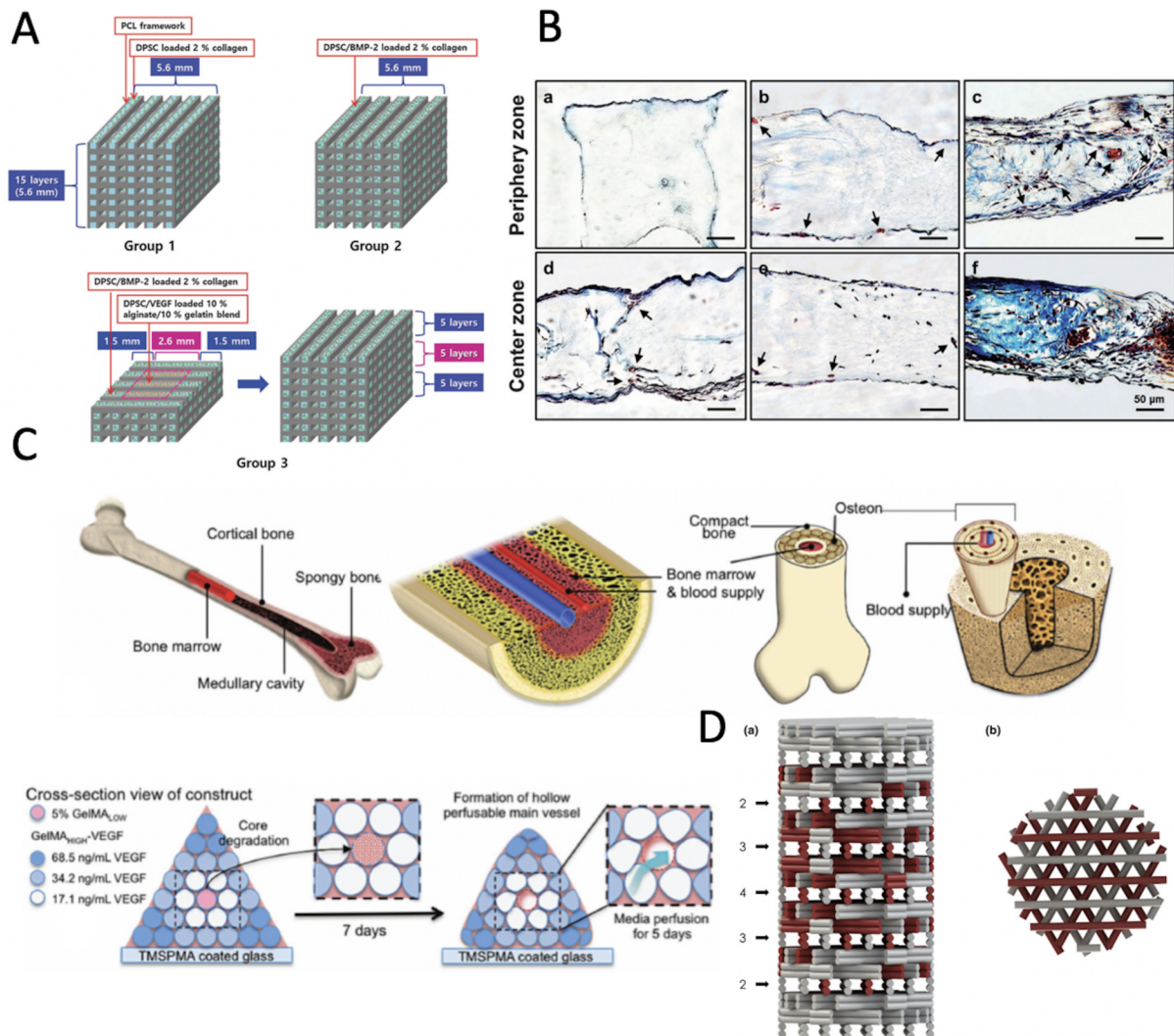


**Figure 4.5.** Control of the spatial localization of GFs within 3D bioprinted constructs for bone regeneration. A) Schematic representation of the strategy employed by Park *et al.* to release VEGF from the inner part of the construct and BMP-2 from the periphery. B) Masson's trichrome staining confirming bone regeneration. Blue-positive staining, indicating that the encapsulated cells secreted collagenous proteins, was seldom observed in groups 1 and 2, while group 3 showed strong blue staining, showing the importance of pre-vascularization for large-volume bone regeneration. Reproduced with permission. [204] Copyright 2015, The Royal Society of Chemistry. C) Illustrations of bone tissue structure, with particular attention to the structure of an osteon followed by a representation of the design developed by Byambaa *et al.* [210]. The cylindrical design aims to mimic the cylindrical structure of the osteon containing gradients of VEGF, arranged from the more concentrated on the center of the structure to the less concentrated on the periphery. Reproduced with permission. [210] Copyright 2017, John Wiley and Sons. D) Model of the biphasic scaffolds with CPC (white) and the growth factor loaded hydrogel (red). The number of VEGF-loaded strands at each layer is indicated on the left side. In the center of the scaffold, four strands are consisting of hydrogel, which is half of the scaffold's profile. Reproduced with permission [196]. Copyright 2016, Springer Nature.

## 4.7 Conclusion and future perspectives

The therapeutical efficiency of growth factors in tissue repair and regeneration has been largely demonstrated. However, several limitations for the clinical applications of biomaterials releasing GFs still remain, due to the many difficulties related to their complex mechanism of action and high risk of side effects. The number of growth factors intervening, *in vivo*, in tissue repair and regeneration is very high and their action is strictly regulated by the activity of cells and extracellular matrix components, which determine their precise spatio-temporal release. Currently, a growing number of studies are focusing on the improvement of bioinks properties and on the development of new delivery systems to be able to reproduce, *in vitro*, the complex natural mechanism of action of GFs. Many strategies for a more controlled delivery of GFs can be developed using 3D bioprinting, which currently represents the most promising tissue engineering technology, thanks to the ability to fabricate micro-precise structures. The deposition of multiple and specialized biomaterials, able to release single or multiple GFs in a temporal and spatial controlled manner, could allow for the use of appropriate dosages of GFs, increasing the efficacy and safety of bioprinted constructs. More work will be needed from the biomaterials side to improve the control of the release kinetics of the proteins, including the use of multi-scale delivery systems (e.g. nanoparticles in microparticles or stratified structures) and improved methodologies for stabilizing the structure of GFs compliant with the bioprinting process. Furthermore, the utilization of modeling tools to predict the release of the factors from complex structures will most probably gain relevance in the future; by reversing engineering this could be useful in the design of customizable bioprinted devices with the required release of the cargo in time and space.

## Conclusions clé:

- La libération contrôlée des facteurs de croissance est un sujet de recherche très importante dans le domaine de la médecine régénérative. En effet, malgré leurs rôles essentiels et reconnus pour la régénération tissulaire, l'application clinique de scaffolds libérant des facteurs de croissance est encore limitée en raison des risques associés à leur libération, tels qu'une libération spatiale incontrôlée, qui pourrait conduire à la formations de tissus ectopiques, ou le surdosage qui pourrait induire le développement d'un cancer.
- Par conséquent, le contrôle spatio-temporel de la libération des facteurs de croissance représente un défi pour permettre la regeneration de tissus complexes pour des applications cliniques. La bio-impression 3D, grâce à sa capacité à contrôler le dépôt de biomatériaux, cellules et facteurs de croissance avec une haute précision, permet un contrôle plus efficace, notamment spatiale, de la libération des facteurs de croissance. En effet, le contrôle temporel de la libération des facteurs de croissance, ainsi que leur protection de l'environnement, sont surtout dépendant de la qualité et de l'efficacité du système de libération adopté. Ces systèmes de libération, tels que les nano- ou micro-particules peuvent être facilement inclus dans la composition d'encres et/ou bio-encres utilisées pour la bio-impression 3D.
- La combinaison de ces stratégies de contrôle temporel et spatial font de la bio-impression 3D la technologie la plus prometteuse pour relever le défi mentionné ci-dessus. De plus, le contrôle de la libération spatiale des facteurs de croissance à travers la bio-impression 3D pourrait également permettre une meilleure sélection des dosages des facteurs de croissance à délivrer, et, par conséquent, une augmentation de l'efficacité des constructions bio-imprimées pour la formation ou régénération d'un tissu.



## Chapter 5

# Towards innervation of bioengineered muscle constructs: Development of a sustained neurotrophic factor delivery and release system

## Vers l'innervation des structures musculo-squelettiques bioimprimées : développement d'un système de libération de facteurs neurotrophiques soutenue

Une analyse bibliographique des différentes méthodes permettant la libération contrôlée de facteurs de croissance à l'aide de l'impression 3D, a permis de définir un projet d'étude effectué en tant que doctorante invitée au laboratoire Wake Forest Institute of Regenerative Medicine. Ce projet concerne l'accélération de l'innervation de structures 3D musculo-squelettique bio-imprimées. Le tissu musculaire est responsable du mouvement de l'organisme. Bien que le tissu musculaire ait une capacité de régénération limitée pour des petites blessures, des blessures plus étendues peuvent entraîner des lésions nerveuses entraînant une atrophie et une incapacité fonctionnelle permanente [241]. Les fibres musculaires sont innervées et contrôlées par les motoneurones. Les motoneurones, dont le corps cellulaire est situé dans le système nerveux central, ont des axones qui pénètrent dans le muscle. À ce niveau, chaque axone du motoneurone se divise en branches appelées terminaisons axonales qui établiront ce que l'on appelle des jonctions neuromusculaires (NMJs en anglais pour Neuromuscular Junctions). Les NMJs sont donc le point de contact entre les cellules musculaires et les motoneurones (schématisé en figure 5.1) et sont responsables de la conversion des impulsions électriques générées par les motoneurones en contraction musculaire à travers la libération du neurotransmetteur acétylcholine [242]. Il est donc clair que l'implantation d'un scaffold musculaire squelettique nécessite que ce tissu soit correctement innervé par le système nerveux périphérique du patient pour générer un tissu fonctionnel. Au contraire, une mauvaise innervation entraînerait une atrophie du tissu musculaire et une perte de la fonction contractile.

Le groupe que j'ai rejoint au WFIRM avait déjà développé des structures 3D de muscle squelettiques bio-imprimées à l'aide d'un système de bio-impression 3D à trois composants, qui est détaillé à la fois dans un article publié précédemment [243] et dans la section Matériaux et méthodes du chapitre suivant (5.3.5). Kim *et al.* [243] ont montré que ces structures 3D avaient les caractéristiques structurelles et cellulaires du muscle natif, représentant une stratégie prometteuse

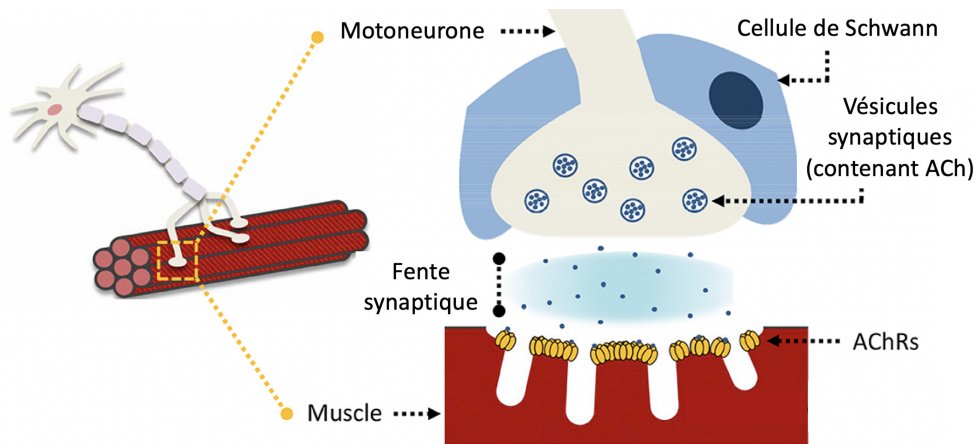


**Figure 5.1.** Représentation schématique de la jonction neuromusculaire (NMJs). Figure reproduite de [242].

pour la restauration de la fonction musculaire. Cependant, l'accélération de l'intégration du muscle squelettique bio-imprimé par le système nerveux périphérique de l'hôte est le facteur le plus important pour le succès clinique. En effet, la capacité de régénération des nerfs est influencée par la distance entre les deux terminaisons nerveuses et le délai entre le moment de la lésion nerveuse traumatique et celui de la réparation chirurgicale, pouvant conduire à la formation de tissu cicatriciel [244].

Notre objectif ici est d'inclure dans un scaffold musculo-squelettique bio-imprimée, un système de libération prolongée de facteurs neurotrophiques (NFs en anglais pour Neurotrophic Factors) pour accélérer l'intégration des nerfs de l'hôte dans la structure 3D. Les NFs sont des substances endogènes capables de contrôler la migration, la prolifération et la différenciation cellulaires dans le système nerveux [245]. Après une lésion nerveuse, ces NFs sont libérés et régulent le processus de réparation. Cependant, leur dégradation rapide et, donc, leur possible perte de l'activité biologique *in vivo*, posent plusieurs limitations à leur utilisation. La stratégie adoptée pour surmonter ces limites est d'encapsuler deux facteurs neurotrophiques (CNTF et GDNF), précédemment sélectionnées pour leur capacité à favoriser la croissance neuronale [246], dans des microsphères d'acide poly-lactique-glycolique (PLGA en anglais pour Poly-Lactic-Glycolic Acid) afin de les protéger de l'environnement, d'augmenter leur demi-vie et de maintenir leur libération pendant le temps nécessaire à la régénération neuronale.

Le PLGA est un copolymère synthétique d'acide lactique (LA en anglais pour Lactic Acid) et d'acide glycolique (GA en anglais pour Glycolic Acid), comme le montre la figure 5.2. Le PLGA est l'un des polymères synthétiques biodégradables les plus couramment utilisés pour l'administration de médicaments ou la libération de facteurs, approuvé par la FDA (Food and Drug Administration) et l'EMA (European Medicines Agency) [247]. La biodégradabilité, qui est basée sur l'hydrolyse de ce polymère en deux monomères, l'acide lactique et l'acide glycolique, qui sont métabolisés par l'organisme, peut être contrôlée en ajustant le rapport entre l'acide lactique et l'acide glycolique dans la chaîne du copolymère [248].

En raison de cette propriété, l'utilisation de PLGA présente le grand avantage de permettre la modulation de la libération des facteurs encapsulés en modifiant uniquement la composition du polymère. En particulier, une quantité plus élevée en LA, par rapport à celle de GA, conduit à une dégradation plus lente et par conséquent à une libération plus lente des facteurs encapsulés [223]. Il existe principalement cinq types de copolymères de PLGA donnés par la combinaison de LA et

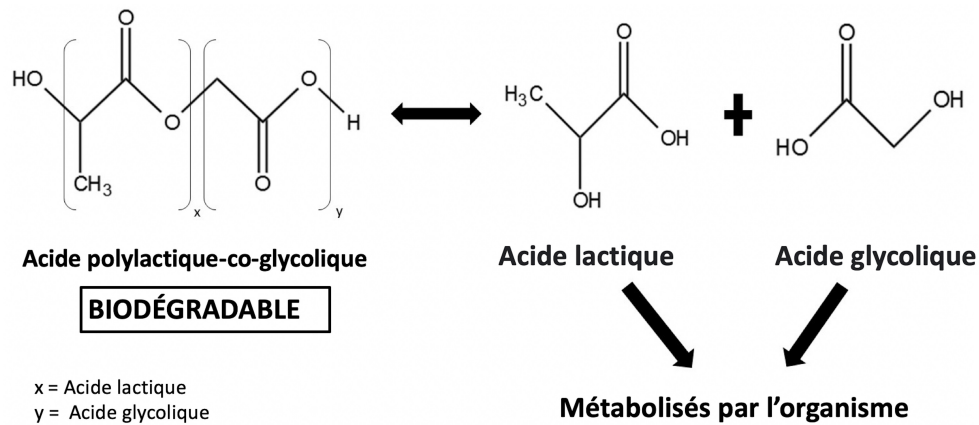


**Figure 5.2.** Structure du copolymère PLGA. Figure reproduite de nanovexbiotech.com.

GA en ratio 50/50, 65/35, 75/25, 85/15 et 95/5. Le PLGA 50/50 représente le copolymère qui se dégrade le plus rapidement (environ 30 jours) et le PLGA 95/5 représente le copolymère qui se dégrade le plus lentement (environ 60 jours) [249].

Nous avons choisi d'utiliser des micro-sphères de PLGA 50/50 comme système de libération des NFs. Ce choix s'explique par le fait que la libération des NFs doit être assez rapide (pour accélérer le phénomène d'innervation avant la formation du tissu cicatriciel) mais de manière soutenue pour rendre les NFs disponibles pendant le temps nécessaire à la régénération.

*NB: Il faut noter que, même si le chitosane n'a pas été utilisé pour cette étude comme composant principal des structures bio-imprimés, les micro-sphères de PLGA comme système de délivrance peuvent être facilement introduites dans les encres à base de chitosane développée précédemment. Par conséquent, les travaux menés au WFIRM s'inscrivent parfaitement dans l'objectif général de cette thèse.*

# Towards innervation of bioengineered muscle constructs: Development of a sustained neurotrophic factor delivery and release system

*The content of this part of the chapter is nearly identical to the following work which will be submitted shortly:*

**Title: Towards innervation of bioengineered muscle constructs: Development of a sustained neurotrophic factor delivery and release system**

**Authors: Aurelia Poerio, Vladimir Mashanov, Dehui Lai, Michale Kim, Young Min Ju, Ji Hyun Kim, Sang Jin Lee, Franck Cleymand, João F. Mano, Anthony Atala, and James Yoo**

## 5.1 Abstract

Surgical implantation of biomanufactured skeletal muscle constructs has recently emerged as a promising strategy to treat volumetric muscle defects. However, due to the slow rate of neural regeneration and integration, timely innervation of the implanted constructs with the host peripheral nerves remains an unresolved challenge. This study aims to develop a sustained release neurotrophic factor (NF) delivery system to accelerate peripheral nerve regeneration and innervation of three-dimensional (3D) bioprinted skeletal muscle constructs. Poly (lactic-co-glycolic acid) (PLGA) microspheres were selected as a delivery system for efficient loading and sustained release of two potent NFs: ciliary neurotrophic factor (CNTF) and glial cell line-derived neurotrophic factor (GDNF). We demonstrate that the NFs can be loaded within the PLGA microspheres with a high encapsulation efficiency ( $75.4\% \pm 12.6\%$ ). The NF-loaded microspheres were incorporated into the fibrinogen-based bioink used to produce biomanufactured skeletal muscle constructs and tested for printability. The microspheres did not change the viscoelastic properties of the bioink, nor did they affect the viability of human muscle progenitor cells. The release kinetic test confirmed that the bioprinted muscle constructs with the NFs-loaded microspheres released the NFs in a sustained manner compared to the bioprinted muscle construct without microspheres. The released NFs maintained their biological activities. In an *in vitro* neurite outgrowth assay, the NFs released from the PLGA microspheres facilitated the neurite growth over a longer time scale than the NFs directly loaded in the hydrogel. These results demonstrate the feasibility of incorporating the microsphere-based NF delivery system for accelerating neural regeneration in future *in vivo* applications involving biomanufactured muscle constructs.

## 5.2 Introduction

Extensive skeletal muscle tissue injuries are frequently accompanied by nerve damage, leading to atrophy and permanent functional disability of denervated muscle [241]. Current



reconstructive options for treating muscle loss include physical exercise, intramuscular injection of progenitor cells and autologous muscle grafts. However, these treatment approaches are limited by many factors, including donor tissue availability, graft failure, donor site morbidity, and difficulties in regulating progenitor cell proliferation and differentiation, and are not suitable for large volumetric muscle loss (VML) [250].

Among the new strategies to treat large muscle defects, biofabrication of autologous muscle implants by three-dimensional (3D) bioprinting has emerged as a powerful tool to create complex structures using cells, bioactive factors, and biomaterials that closely mimic the natural tissue architecture [251]. However, a major challenge that hinders complete functional integration of implanted muscle constructs is achieving proper and timely innervation by the host peripheral nervous system [252]. Delayed or inappropriate innervation of the implanted muscle construct may lead to muscular atrophy and muscle contraction loss. Therefore, it is crucial to promote nerve regeneration and induce neurite growth into implanted bioengineered constructs.

For this reason, various surgical, physiological, and pharmacological strategies have been employed to enhance and accelerate reinnervation [253, 254, 255, 256], of which the use of extrinsic neurotrophic factors (NFs) has shown to be most promising [253, 257]. NFs, such as the brain-derived neurotrophic factor (BDNF), ciliary neurotrophic factor (CNTF), glial cell line-derived neurotrophic factors (GDNF), and nerve growth factor (NGF), promote neuronal development, growth, survival, regeneration, and differentiation [245]. However, rapid degradation and loss of biological activity *in vivo* pose a severe limitation to the use of NFs in therapeutic settings [258]. To overcome this limitation, efficient delivery strategies have been proposed to protect growth factors from degradation, including their entrapment in hydrogels and encapsulation in carriers [258, 259].

Another critical factor to consider is the relatively slow rate of neural regeneration and integration with implanted bioengineered constructs. Consequently, the delivery system needs to release and maintain NFs at biologically relevant levels over extended periods instead of being rapidly depleted after an initial burst release [258]. Therefore, to accelerate innervation, an optimal delivery system that can release NFs in a controlled and sustained manner is necessary [260, 261]. For example, sustained release of NGF and GDNF from poly (lactic-co-glycolic acid) (PLGA) microspheres embedded into a nerve conduit was shown to facilitate nerve regeneration across a large sciatic nerve defect in rats [262]. Despite the promising results with bridging nerve defects through conduits, few studies have been conducted on enhancing and directing targeted growth of neurites into and within non-neural bioengineered tissue constructs [263].

The purpose of the present work is to establish the feasibility of PLGA microspheres as a vehicle that enables the delivery and sustained release of the CNTF and GDNF upon incorporation into the bioprinted skeletal muscle construct. In a previous *in vitro* study [246], these two NFs were demonstrated to induce directed growth of neurites towards an intended target. In this study, we have chosen PLGA as the factor delivery vehicle. PLGA is a widely used non-toxic biocompatible polymer in a variety of drug delivery and medical applications. In aqueous environments, including *in vivo* settings, the PLGA matrix of delivery devices undergoes gradual hydrolysis, which first breaks down long polymer chains into shorter fragments. These fragments are then further hydrolyzed to monomeric lactic and glycolic acids, which enter the normal cellular metabolic pathways, thus resulting in minimal to none systemic toxicity. As the PLGA matrix dissociates, the encapsulated drugs are gradually released [248, 264, 247]. The degradation time for commercial grade PLGA

polymers is reported to vary between 1 and 2 months, which is often long enough to port the sustained release of the encapsulated bioactive cargo molecules in most experimental and treatment scenarios [247].

Here, we show that the 3D bioprinted muscle constructs with the NF-loaded PLGA microspheres are fully compatible with the previously established biomanufacturing protocols [252, 243]. The NFs encapsulated in the microspheres retain their biological activity, show a sustained temporal release pattern, and significantly enhance neurite outgrowth.

## 5.3 Methods

### 5.3.1 Preparation of PLGA microspheres

The microspheres were prepared using a standard water-in-oil-in-water (W/O/W) double emulsion technique [265], which is schematized in Figure 5.3. Briefly, the oil phase was made by dissolving PLGA 50:50 (Lactel, B6010-2) in either dichloromethane (Alfa Aesar, 39116) or chloroform (Sigma, C606-4) to yield a 10% solution. An inner water phase consisting of either pure phosphate-buffered saline (PBS) (for manufacturing of empty control microspheres) or cargo substances loaded in PBS (to create loaded microspheres, see below) was then added to the oil phase at a ratio of 1:100 (v/v) and emulsified by sonication for 30 seconds on ice at 13% amplitude using an ultrasonicator (Sonics & Materials Inc Vibra CellVCX 400). The resulting first emulsion was then added at a ratio of 1:100 (v/v) to an aqueous phase consisting of 3% polyvinyl alcohol (PVA, Sigma, 341584), and either homogenized at 10,000 rpm with a micro homogenizer (Biospec Products Tissue Tearor M-398) for 30 seconds or vortexed for the same amount of time at a maximum speed with a vortex mixer (Fisher, 02215414) to generate the second emulsion. The final W/O/W emulsion was stirred for 4 hrs at 800 rpm at room temperature to allow for organic solvent evaporation. The microspheres were then filtered through a 100  $\mu\text{m}$  filter (Falcon, 352360), washed three times with distilled water, freeze-dried for 48 hrs, and stored at  $-20^{\circ}\text{C}$  until needed. To prepare loaded microspheres, the following substances were mixed into PBS and included in the inner water phase:

1. Fluorescein isothiocyanate (FITC)-dextran (Sigma, FD20) at a concentration of 1 mg/mL (to demonstrate the distribution of the cargo throughout the inner volume of the microspheres),
2. Bovine Serum Albumin (BSA, Sigma, A2153) at a concentration of 40 mg/mL (used as a model protein to determine the encapsulation efficiency),
3. CNTF (R&D, 257-NT) and GDNF (Sigma, GF322) at a concentration of 0.1 mg/mL (for the bioactivity *in vitro* assay) or 1 mg/mL (for the release kinetic study) each mixed with a 4 mg/mL BSA solution at a ratio of 1:200 (w/w).

### 5.3.2 Characterization of PLGA microspheres

NF-loaded and empty (without NFs) microspheres were characterized in terms of their yield, size range, morphology, and cargo distribution. The yield was calculated as the ratio of the final weight of microspheres to the total weight of PLGA used in the formulation process. The

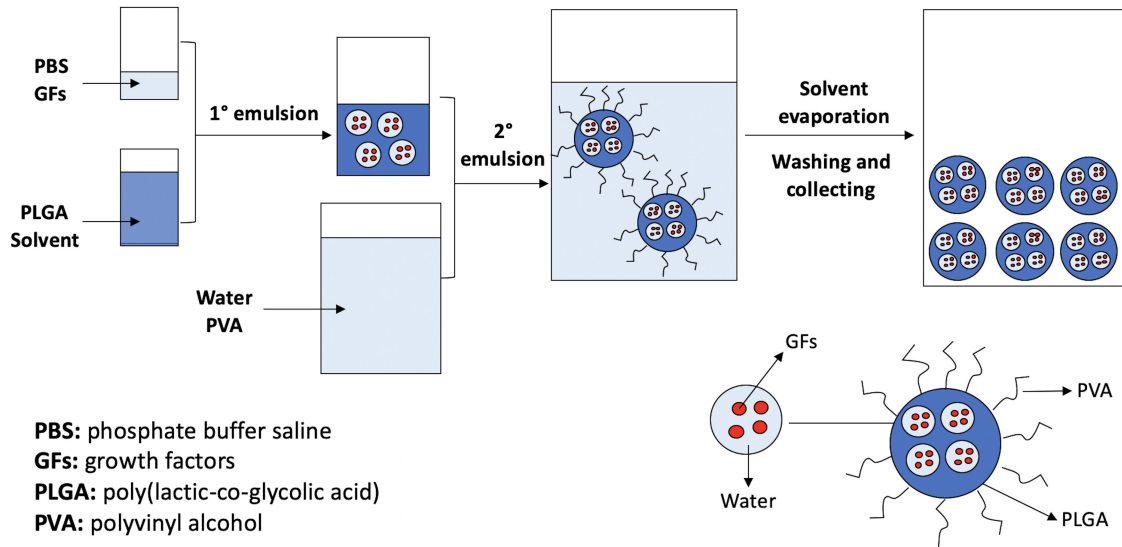


**Figure 5.3.** Preparation of PLGA microparticles by the double emulsion solvent evaporation method. Adapted with permission [266].

microspheres were weighed after filtering the final emulsion and lyophilization. The PLGA aggregates captured by the filter were not considered in the calculation of the microsphere yield. Three independent measurement were used per condition.

For microscopic examination, freeze-dried microsphere samples were sputter-coated with gold (Leica EM ACE600) and imaged with a Flex SEM 1000 scanning electron microscope (SEM, Hitachi Co., Japan). The particle size was measured on calibrated SEM images and expressed as median diameter of approximately 450–600 microspheres collected from three independent batches.

The distribution of encapsulated cargo was assessed using FITC-dextran-loaded microspheres imaged with a confocal microscope (FluoviewFV10i).

### 5.3.3 Preparation and characterization of the acellular bioink-microsphere composite materials

A fibrinogen-based bioink was prepared as previously described [243]. Briefly, hyaluronic acid (Sigma, 53747) was dissolved at 3 mg/mL in DMEM/High Glucose containing 10% (v/v) glycerol (Spectrum, G1015) by continuous overnight stirring at 37°C. Then, 20 mg/mL fibrinogen (Sigma, F8630) and 35 mg/mL gelatin (Sigma, G6144) were added to the solution by gentle shaking at 37°C for 1 hr. The final mixture was sterilized using a 0.45  $\mu\text{m}$  syringe filter (Fisher, 09-719D). The microspheres were gently mixed with the acellular bioink. Two different concentrations of microspheres (5 and 10 mg/mL) were used to evaluate the viscoelastic properties of the microspheres-loaded acellular bioink before and after crosslinking. For crosslinking, the acellular bioink was treated with thrombin (20 UI/mL) (Sigma, T4648) for 4 hrs at room temperature. The shear viscosity was assessed by a shear sweep analysis (between 0.1 and 1000  $\text{s}^{-1}$ ) at 18–19°C (pre-gel state) measured using the cone-and plate geometry (40 mm diameter, 1° cone angle, and 109  $\mu\text{m}$ -gap) on a Discovery Hybrid Rheometer DHR-2 (TA Instruments, New Castle, DE). The viscosity is presented as the average  $\pm$  standard deviation of three measurements.

The storage modulus was determined in an oscillatory amplitude sweep measurement test using the parallel plate geometry (8-mm diameter and 10- $\mu$ m gap) at a constant frequency of 1 Hz. The average storage modulus was calculated as the average  $\pm$  standard deviation of 18 data points per condition measured within the oscillatory strain range between 0.01 and 1%.

To assess the internal ultrastructure of the crosslinked hydrogels, the freshly prepared samples were washed with PBS, frozen at  $-80^{\circ}\text{C}$  overnight, and lyophilized for 48 hrs. To assess the ultrastructure of the hydrogels during their degradation, the samples were first incubated in PBS for 7 days at  $37^{\circ}$  before being processed as above. For morphological evaluation, the samples were gold sputter-coated and imaged by SEM using an acceleration voltage of 5 kV.

### 5.3.4 Encapsulation efficiency and *in vitro* release kinetics of cargo molecules

The encapsulation efficiency (EE) was determined using BSA as a model protein [267]. A total of 10 mg of BSA-loaded microspheres were hydrolyzed in 1 mL of 0.1N NaOH (Fisher, S318) containing 5% SDS (Sigma, L3771) for 72 hrs at  $37^{\circ}\text{C}$  under continuous mixing on a rotary shaker. The dissolved protein content was measured with the BCA Protein Assay kit (ThermoFisher, 23225). The EE was then calculated as the ratio between the actual and theoretical BSA content.

To determine whether the PLGA microspheres provide sustained release of NFs in 3D bioprinted constructs, we compared the *in vitro* NF release kinetics between the two different construct designs: (i) constructs containing CNTF/GDNF-loaded microspheres (5 mg/mL) embedded in the hydrogel (hydrogel + NF-loaded MSs) and (ii) microsphere-free constructs with the CNTF/GDNF directly loaded in the hydrogel (hydrogel + NFs). In both sample types, the total load of each NF (either encapsulated in microspheres or directly loaded in the bioink) was 0.5  $\mu\text{g}$  per mL of the bioink. The constructs were bioprinted as described below. After printing, the constructs were crosslinked with thrombin treatment in the presence of 40 mM  $\text{CaCl}_2$  for 30 min at room temperature. Each crosslinked construct was then incubated in 1.5 mL of the release medium (PBS with 20 mg/mL of aprotinin) at  $37^{\circ}\text{C}$ . On days 1, 3, 5, and 7, the entire release medium was collected for ELISA and replaced with an equal volume of the fresh medium. The released GDNF was quantified with the Human GDNF Quantikine ELISA kit (R&D, DG00). Results are presented as mean  $\pm$  standard deviation of three independent replicates per condition.

### 5.3.5 3D bioprinting of skeletal muscle constructs and human muscle progenitor cells (hMPCs) viability

hMPCs were generated by the Regenerative Medicine Clinical Center at the Wake Forest Institute for Regenerative Medicine. For bioprinting, the cells were expanded up to passage five ( $\sim 6$  cumulative population doublings) in a growth medium composed of DMEM/High Glucose, 20% fetal bovine serum (FBS), 2% chicken embryo extract, and 1% penicillin/streptomycin [243].

All bioprinted constructs were fabricated using the 3D Integrated Tissue-Organ Printing (ITOP) system developed at the Wake Forest Institute for Regenerative Medicine [251]. The

bioprinting was performed as previously described [243]. Briefly, it involved three components: a cell-laden fibrinogen-based bioink (described above), an acellular sacrificial material (identical in composition to the bioink without fibrinogen and cells), and a supporting polycaprolactone (PCL, MW 43,000-50,000, Polysciences, Inc., Warrington, PA) pillar structure. For each printed layer, a PCL square pillar was first created on the outside perimeter of the construct, followed by the deposition, in the inner part, of alternated filaments of the cell-laden bioink and sacrificial material. When necessary, empty or NF-loaded microspheres were included to the cell-laden bioink. A one layer design of the printed structure is shown in Figure 5.4.

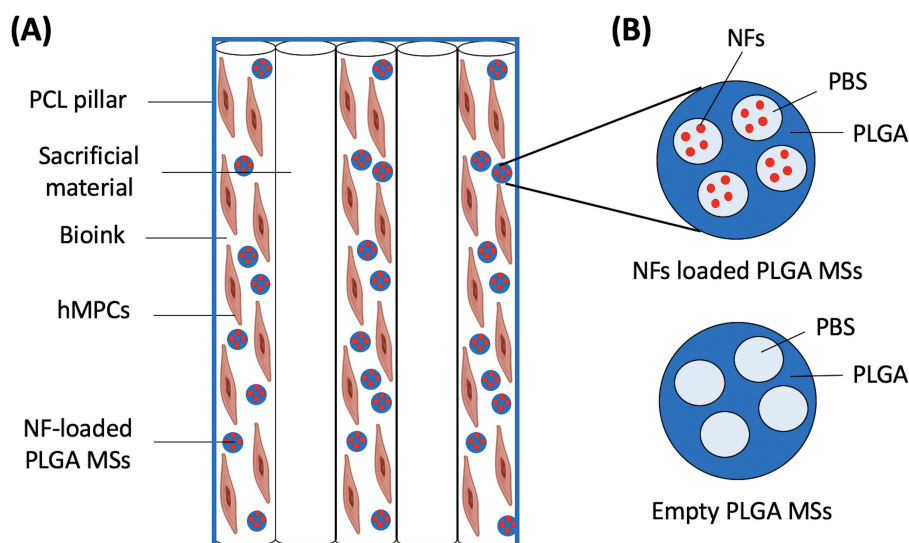


**Figure 5.4.** Representative image showing the design of a one layer bioprinted construct. Each layer is made of a PCL pillar on the outside perimeter of the construct. Inside, a filament of cell-laden bioink is alternated by a sacrificial material (that has the same composition of the cell-laden bioink, without fibrinogen and cells). (B) Higher magnification of NF-loaded and empty PLGA microspheres.

To assess the effect of PLGA microspheres on cell viability in bioprinted constructs, single layer constructs containing hMPCs at a density of  $30 \times 10^6$  cells/mL were manufactured without and with microspheres (5 mg/mL). All bioprinted constructs were crosslinked with thrombin as described above (section 5.3.4) and incubated in the growth medium for 24 hrs. Cell viability was then evaluated using a Live/Dead Viability/Cytotoxicity Assay (ThermoFisher, L3224), reported as the percentage of live cells relative to the total cell number, and presented as average  $\pm$  standard deviation of three individual constructs.

### 5.3.6 Dorsal root ganglia (DRGs) neurite growth assay

To assess the bioactivity of the released NFs and determine the effect of their sustained release on neurite outgrowth, we developed the following *in vitro* assay. To prepare hydrogels, 40  $\mu$ m cell strainers were placed into wells of a 6 well plate and filled with 1 mL of acellular bioink crosslinked with thrombin as above. DRGs were extracted from stage 33 ( $\sim$ E8) chick embryos and collected in the culture medium (DMEM/High Glucose with 2% horse serum and 1% penicillin/streptomycin). They were then positioned on top of the crosslinked acellular fibrin hydrogel layer and covered with 5 mL of the culture medium (figure 5.5a and b). The assay

involved four different hydrogel formulations: (a) pure hydrogel containing no NFs and no microspheres (hydrogel - negative control); (b) a positive control with the CNTF/GDNF combination directly dissolved into the hydrogel at a concentration of 18.75 ng/mL each (hydrogel + NFs); (c) another negative control comprised of the hydrogels loaded with 5 mg/mL of empty microspheres without CNTF/GDNF (hydrogel + empty MSs); (d) and the experimental group containing 5 mg/mL of CNTF/GDNF-loaded microspheres (hydrogel + NF-loaded MSs). The amount of NFs in groups (b) and (d) was the same and was determined based on the EE of 75% (see the Results section). The plates were incubated at 37°C for 2, 7, and 14 days, with the medium being changed every other day.

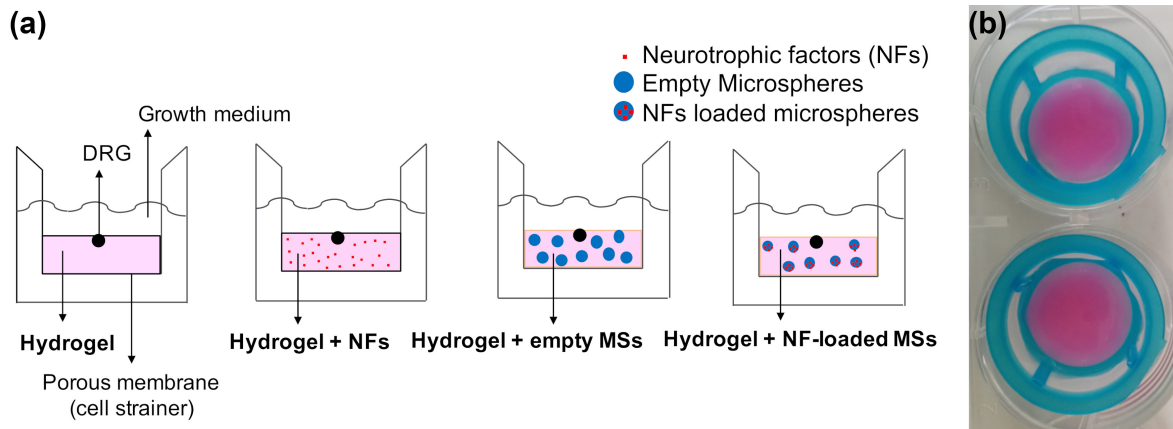


**Figure 5.5.** (a) Design of the DRG neurite growth assay. Four preparations were involved: the control hydrogel (*Hydrogel*), the hydrogel with freely loaded neurotrophic factors (*Hydrogel + NFs*), the hydrogel containing suspended empty microspheres (*Hydrogel + empty MSs*), and the hydrogel containing suspended microspheres loaded with the neurotrophic factors (*Hydrogel + NF-loaded MSs*). The hydrogels were cast into inserts manufactured from 40  $\mu\text{m}$  cell strainers, which were then placed into wells of a 6-well plate containing the culture medium. (b) Representative picture of the crosslinked hydrogel on the top of which DRGs were positioned.

At each time point, the samples were fixed in 10% neutral buffered formalin with 0.1% Triton X-100 at 4°C overnight. After extensive PBS washes ( $5 \times 1$  hr), the samples were blocked in the Protein Block solution (Dako, X0909) for 2 hrs at 4°C, followed by an overnight incubation at 4°C with the anti-neurofilament heavy polypeptide antibody (Abcam, AB4680) diluted to 1:1,000 with the Antibody Diluent (Dako, D3022). After washing the samples ( $5 \times 1$  hr) with PBS, the secondary Alexa Fluor 488-conjugated antibody (ThermoFisher, A-11039) was applied at a 1:200 dilution overnight at 4°C. After the washes, the samples were mounted in the Vectashield medium with DAPI (Vector Laboratories, H-1200) diluted with PBS at a ratio 1:1. Imaging was performed using a macro confocal microscope (Leica TCS LSI).

Maximum intensity Z-projections were generated from confocal stacks using the Fiji/ImageJ software [268, 269]. Neurites were traced and measured using the NeuronJ ImageJ plugin (figure C1) [270]. Four growth parameters were calculated: (a) total neurite outgrowth, (b) average neurite length, (c) longest neurite length, and (d) number of neurites growing out from a given DRG. Each metric was measured on at least three ganglia per treatment at least three ganglia per treatment. In particular, the following number of individual DRGs were quantified on day 2, day 7, and day 14, respectively, for each of the experimental cohorts:

the *Hydrogel* cohort – 17, 12, and 3; the *Hydrogel+NFs* cohort – 15, 10, and 4; the *Hydrogel + Empty MSs* cohort – 5, 5, and 3; and the *Hydrogel + NF-MSs* cohort – 6, 5, and 6.

### 5.3.7 Statistical analysis

The datasets were analyzed for normality with the Shapiro-Wilk test. Statistical significance was tested with Welch’s t-test (which does not assume equal sample sizes or variances), ANOVA (one-way or two-way), Mann-Whitney test, and Kruskal-Wallis test, as appropriate. All tests were performed in the R statistical environment [271]. Data were plotted either using the ggplot2 library in R [272] or Microsoft Office Excel.

## 5.4 Results

### 5.4.1 Optimization of the microsphere manufacturing protocol

Properties of microspheres are affected by both the fabrication method and the type of organic solvent used in their preparation [273, 274]. Therefore, we tested two different second emulsion generation methods – homogenization vs. vortexing – and two different organic solvents – dichloromethane vs. chloroform – in all four combinations. The microsphere manufacturing protocol was optimized in terms of morphology, yield, and size distribution, all of which determine the microsphere performance as a delivery system [275]. Although all four protocols consistently generated microspheres with a regularly spherical shape, their characteristics varied with different techniques (table 5.1, figure 5.6). Compared with homogenization, the vortexing method produced microspheres with a smoother (less porous) surface, smaller median diameter, narrower size distribution, and a significantly higher yield. Compared with dichloromethane, using chloroform resulted in a smoother surface, higher yield, and more homogenous size distribution. The presence of pores on the surface of microspheres influences the release of the embedded molecules. In particular, higher porosity leads to higher burst release and a more rapid overall loss of the cargo molecules than in less porous microspheres [276]. Because of the lower porosity of the surface, the highest yield, and a more homogeneous size distribution within a narrower range, the microspheres prepared using the vortexing method and chloroform as an organic solvent were chosen for our further studies.

Characteristic	Homogenization		Vortexing	
	Dichloromethane	Chloroform	Dichloromethane	Chloroform
Shape	Spherical	Spherical	Spherical	Spherical
Surface	High porosity	High porosity	Low porosity	Smooth
Yield, %	$1.4 \pm 0.9$	$14.6 \pm 8.3$	$41.8 \pm 0.7$	$66.1 \pm 2.7$
Median size, $\mu\text{m}$	14.3	28.2	12	23.4
Size distribution, $\mu\text{m}$	2 – 98.1	2 – 40	1.9 – 47	1.8 – 44.6

**Table 5.1.** Characteristic of empty (*i.e.* without cargo) PLGA microspheres produced with different emulsification techniques (homogenization vs. vortexing) and different organic solvents (dichloromethane vs. chloroform).

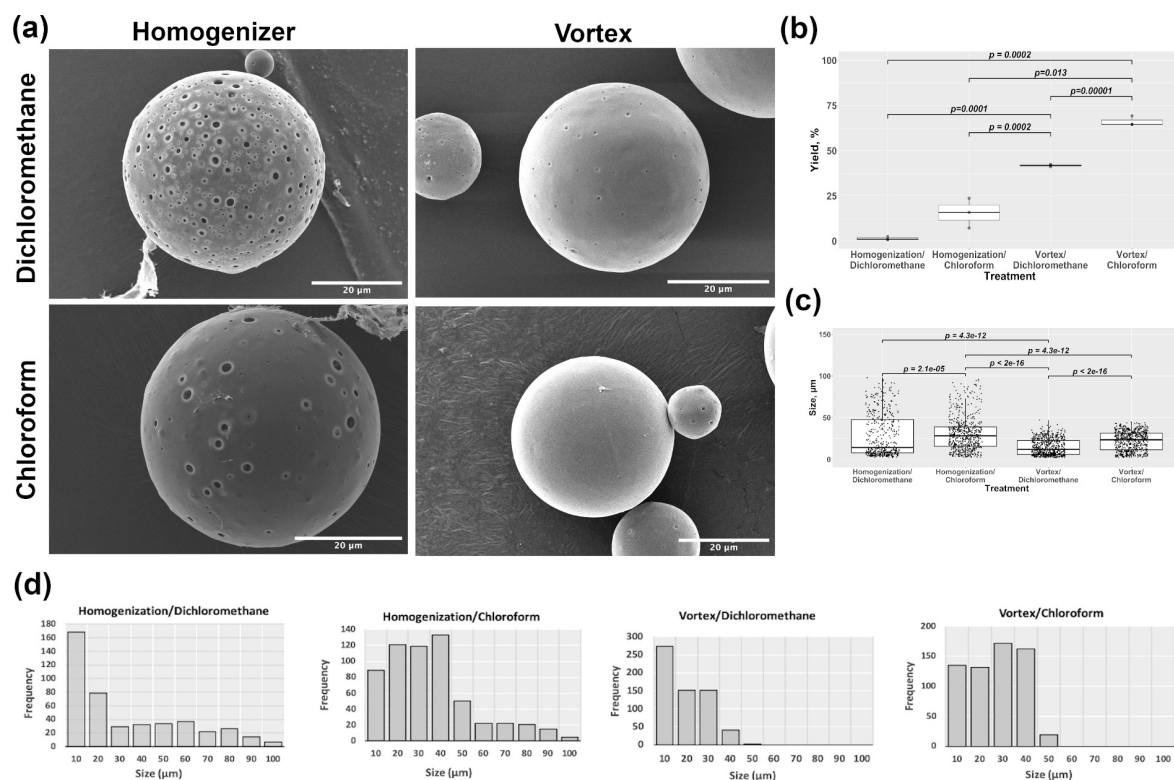


**Figure 5.6.** Empty PLGA microspheres produced with four different fabrication protocols. The emulsification technique involved either homogenization or vortexing, while the solution for the organic phase was either dichloromethane or chloroform. (a) SEM images showing the surface morphology of microspheres. (b) Yield of the fabricated microspheres calculated as the percentage of the initial PLGA weight used in each protocol. Three independent measurements were tested per condition. Two-way ANOVA indicates that both the emulsification method and solvent significantly affect the yield ( $F = 322.15, p = 9.52 \times 10^{-8}$  and  $F = 57.79, p = 6.29 \times 10^{-5}$ , respectively). There is no significant interaction between these two factors that would create a synergistic effect ( $p = 0.08$ ). (c) Boxplot showing the size of microspheres generated with each of the four protocols. The horizontal lines correspond to the median size in each population of particles. Boxes show the central 50% of the measurements, while the top and bottom whiskers correspond to the top 25% and bottom 25% of the data, respectively. Individual measurements are plotted as dots overlaying the respective plots. A Kruskal-Wallis detected a significant effect of the emulsification method (both the emulsification technique and solvent type) on the median size of microspheres ( $H(3) = 258.52, p = 2.2 \times 10^{-16}$ ). The number of particles measured in the four different preparations were as follows: 448 (homogenization/dichloromethane), 597 (homogenization/chloroform), 621 (vortex/dichloromethane), and 620 (vortex/chloroform). (d) Histograms showing the size distribution of the microspheres.

#### 5.4.2 Effect of cargo encapsulation on the characteristics of the microspheres

The effect of the loaded cargo molecules on the morphology, yield, average size, and size distribution of PLGA microspheres was assessed by incorporating the CNTF/GDNF and FITC-dextran. The cargo encapsulation did not affect the yield of the loaded microspheres (Welch's t-test,  $p = 0.6$ ), but slightly increased the surface porosity (compare figure 5.7(a)



and figure 5.6(a). On the other hand, the median size of the loaded microspheres was significantly ( $\sim 2.1$ -fold, Mann-Whitney test  $p = 2.2 \times 10^{-16}$ ) smaller than that of the empty microspheres (figure 5.7(b)) due to a more left-skewed size distribution profile (figure 5.7(c)). The loaded microspheres had fairly evenly spaced spherical internal microcavities (average size  $1.1 \mu\text{m}$ ), which presumably contain the cargo molecules that had been dissolved in the aqueous phase during the microsphere production (figure 5.7(d)). These ultrastructural observations of the internal morphology are corroborated by confocal images of FITC dextran-loaded microspheres (figure 5.7(e and e')). The fluorescently labeled cargo was evenly distributed as small spherical aggregates throughout the internal volume of the microspheres.

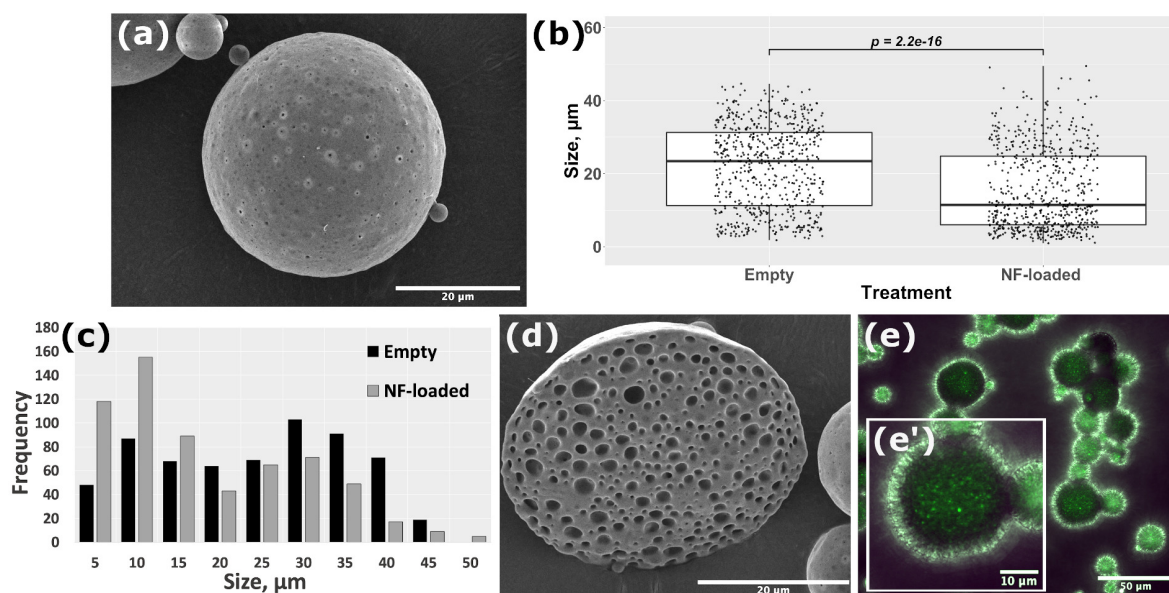


**Figure 5.7.** Characteristics of loaded microspheres. (a) External morphology of FITC-loaded microspheres (SEM). (b) Boxplot showing the size (diameter) of the loaded and empty microspheres. The boxes represent the central 50% of the data, the horizontal lines correspond to the median, and the whiskers represent the top 25% and bottom 25% of the data. Individual measurements are plotted as dots overlaying the respective boxplots. The empty microspheres are  $\sim 2.1$  times larger than the loaded microspheres. Sample size: 620 empty and 621 NF-loaded microspheres were analyzed. Three independent replicates were tested per condition. (c) Size distribution of empty and CNTF/GDNF-loaded microspheres. (d) Internal morphology of FITC-dextran loaded microspheres (SEM). (e) FITC-dextran (*green*) distribution within microspheres, maximum intensity Z-projection of a confocal stack. (e') Higher magnification of a single microsphere showing the distribution of the fluorescent signal.

Furthermore, we wanted to evaluate the effect of the lyophilization on the cargo. Figure 5.8 shows FITC dextran-loaded microspheres immediately after fabrication (a), after lyophilization (b) and after lyophilization and subsequent immersion in water for 4 hours (c). We can conclude that the lyophilization process does not affect the cargo, which is released, as expected, when microspheres are hydrated, as suggested by the presence of fluorescence in the solvent (Figure 5.8(c)).

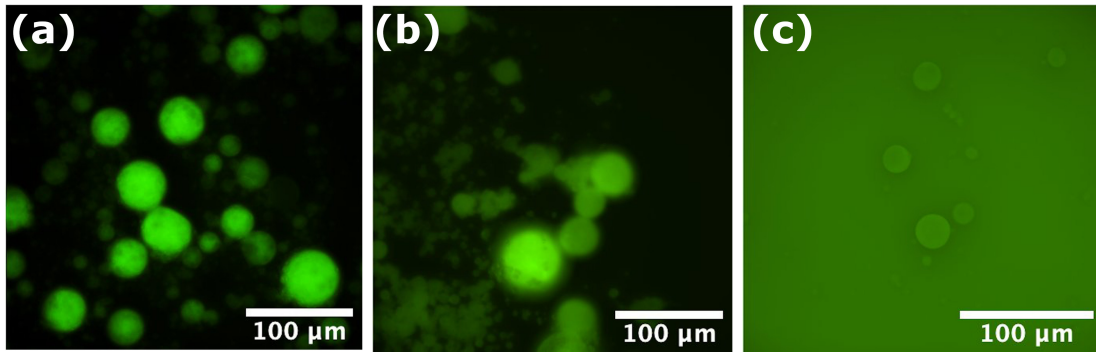


**Figure 5.8.** FITC dextran-loaded PLGA microspheres before lyophilization (a), after lyophilization (b) and after lyophilization and subsequent immersion in water for 4 hours.

### 5.4.3 Effect of microspheres on viscoelastic properties and morphology of the acellular bioink

Viscosity is a critical characteristic of the bioink that affects its printability and the cell viability in the biomanufactured construct [277]. The effect of PLGA microsphere incorporation on the viscoelastic properties of the acellular bioink is shown in figure 5.9(a–c). In a shear sweep test (figure 5.9(a)), the bioink samples loaded with 5 and 10 mg/mL of microspheres showed the same shear-thinning dynamics (*i.e.* decreasing viscosity under increasing shear rates) as the microsphere-free bioink. Therefore, the inclusion of microspheres into the bioink at a range of 0 – 10 mg/mL did not significantly affect the viscosity dynamics. The microspheres-loaded bioink can thus be easily ejected from a nozzle when pressure is applied during the bioprinting process [275].

However, at any given stress value, higher loads of microspheres do affect the viscosity of the bioink-microsphere composites. For example, there is a clear variation in the average viscosity among the three formulations (0, 5, and 10 mg/mL) at the shear rate of  $0.1 \text{ s}^{-1}$  (One-way ANOVA,  $F(2, 6) = 27.84$ ,  $p = 9.21 \times 10^{-4}$ ), as shown in figure 5.9(b). The microsphere-laden bioink with the higher microsphere content (10 mg/mL) showed a significantly higher viscosity in comparison with both the microsphere-free bioink ( $p = 8 \times 10^{-4}$ ) and the microspheres-laden bioink with the lower (5 mg/mL) microsphere content ( $p = 5 \times 10^{-3}$ ). Importantly, the viscosity levels of the microsphere-laden bioink with the lower microsphere content (5 mg/mL) were not statistically different from those of the microsphere-free bioink.

Elasticity is another property of hydrogels that affects the behavior of the encapsulated cells and the interactions between the cells and the extracellular matrix [278]. A standard metric used to characterize the sample's elastic behavior is the storage modulus ( $G'$ ), a measure of the sample's elastic or recoverable energy [279]. We measured the storage modulus of the microspheres-loaded bioinks (0, 5, and 10 mg/mL) after crosslinking (hydrogel state). One-way ANOVA detected a significant variability in the storage modulus among different formulations of hydrogels ( $F(2, 6) = 12.45$ ,  $p = 7 \times 10^{-3}$ ). The hydrogels containing the higher microsphere load (10 mg/mL), but not the lower load (5 mg/mL), had a significantly ( $p = 6 \times 10^{-3}$ ) higher storage modulus than the microsphere-free hydrogels (figure 5.9(c)), suggesting that microspheres at high concentrations increase the elasticity of the hydrogel-microsphere composite.

These data indicate that the higher microsphere load (10 mg/mL) significantly changes the viscosity of the bioink and the elasticity of the resulting crosslinked fibrin hydrogel. On

the other hand, the properties of the microsphere-laden formulations with the lower load (5 mg/mL) remain similar to those of the microsphere-free formulation previously developed to support the viability and differentiation of hMPCs [243]. Therefore, this lower microsphere load (5 mg/mL) was used in our subsequent experiments.

To determine how microspheres interact with the crosslinked fibrin hydrogel at the structural level, we compared the microscopic characteristics of both the microsphere-free and microsphere-laden hydrogels. The microsphere-laden hydrogels preserve the highly porous structure that is similar to the microsphere-free hydrogels (compare figure 5.9(d) and (e)), providing interconnected pore networks essential for cell nutrition, proliferation, and migration [280]. Furthermore, the microspheres embedded in the hydrogel appear to be firmly attached to the fibrin network and to remain attached even when the hydrogel matrix starts degrading at the later time points (*e.g.* day 7, figure C2). These results support our strategy to use the microspheres as a NF delivery system.

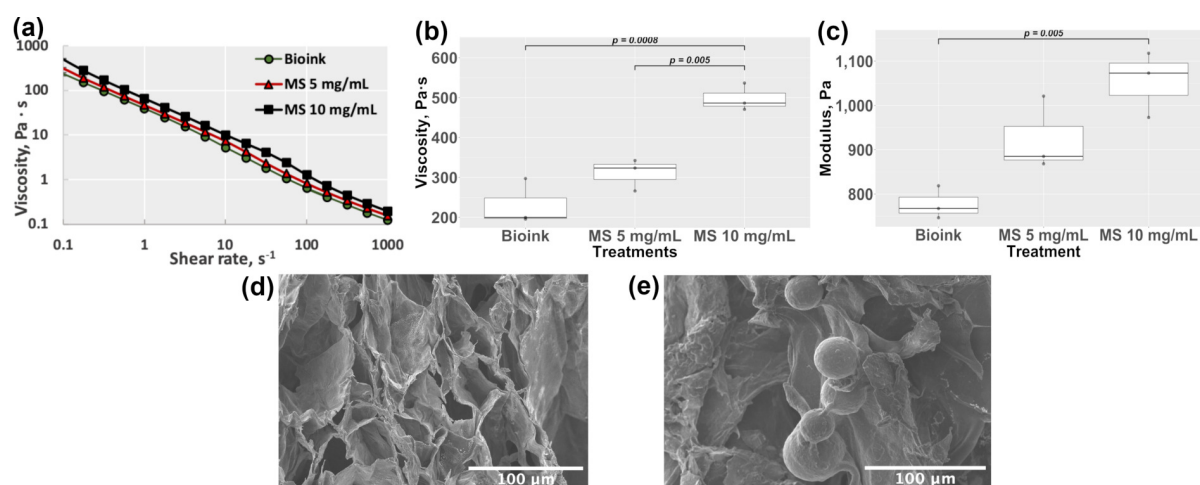


**Figure 5.9.** Viscoelastic properties and morphology of the microsphere-free hydrogels and the hydrogels loaded with microspheres at 5 mg/mL and 10 mg/mL. (a) Shear viscosity of the microsphere-free bioink (circles) and bioink loaded with 5 mg/mL (triangles) and 10 mg/mL (squares) of microspheres. (b) Average viscosity of the bioink formulations at a share rate of  $0.1 \text{ s}^{-1}$ . One-way ANOVA was used to compare the average viscosity across the three groups. Three independent replicates were used per bioink formulation. (c) The storage modulus of the cross-linked hydrogel samples. One-way ANOVA was used to compare the average storage modulus across the three different types of microspheres. Three replicates were used per condition. (d) and (e) SEM morphologies of the crosslinked microsphere-free (d) and microsphere-laden (10 mg/mL) (e) hydrogels.

#### 5.4.4 PLGA microspheres are capable of robust encapsulation efficiency and sustained release of cargo molecules

The encapsulation efficiency calculated with a direct method using BSA as a model protein was  $75.4 \pm 12.6\%$ .

To determine how encapsulation of the NFs into microspheres affects their temporal release pattern in bioprinted constructs, we compared two types of samples: (a) bioprinted constructs with CNTF and GDNF directly mixed into the hydrogel (Hydrogel + NFs) and (b) bioprinted constructs containing CNTF/GDNF-loaded PLGA microspheres in the hydrogel (hydrogel + NF-loaded MSs). Constructs of both designs showed an initial burst release of

the cargo (assessed by the GDNF release) after 1 day (figure 5.10(a)). However, while the amount of the NFs released from the hydrogel + NFs group rapidly declined over time, the release from the hydrogel + NF-loaded MSs was more stable. For example, in the former group, the released amount dropped from  $16.0 \pm 5.0\%$  on day 5 to  $5.6 \pm 2.5\%$  on day 7, whereas in the latter group, it remained at about the same level –  $16.6 \pm 0.9\%$  and  $18.2 \pm 1.1\%$  on day 5 and 7, respectively (figure 5.10(a)). The  $\sim 3.3$ -fold difference in the amount of the released NFs on day 7 between the two groups was statistically significant (Welch's t-test,  $p = 0.02$ ). The relative cumulative release profile also showed a clear difference between the two groups. The hydrogel + NF-loaded MSs group consistently released the NFs at a significantly slower rate than the hydrogel + NFs group (figure 5.10(b)).

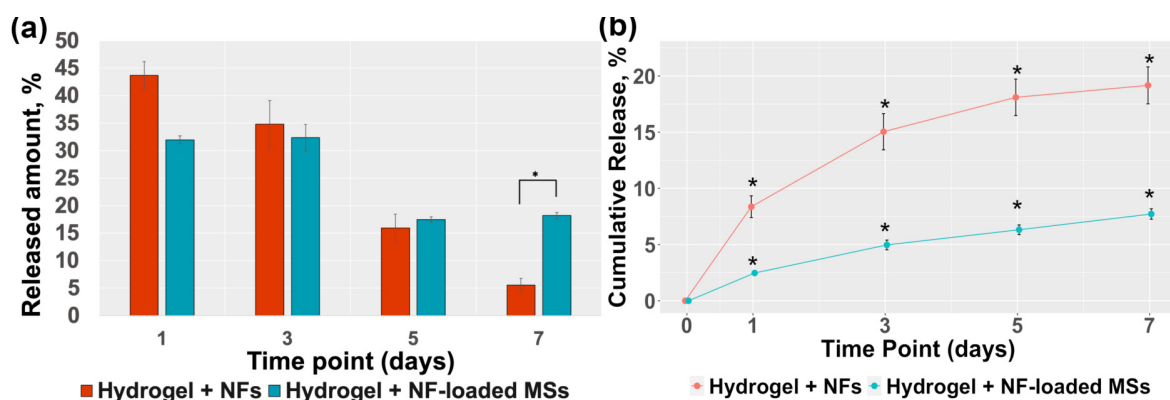


**Figure 5.10.** Release kinetics of GDNF from bioprinted construct containing either CNTF/GDNF directly incorporated into the hydrogel (*Hydrogel + NFs*) or encapsulated in PLGA microspheres (*Hydrogel + NF-loaded MSs*). (a) Release of the recovered GDNF at each time point (normalized to the total recovered GDNF). (b) Cumulative release of GDNF (normalized to the amount of encapsulated GDNF). Three independent samples of each hydrogel type were used at each time point. Statistical significance between the two different formulations of hydrogel was tested at each time point with Welch's t-test, followed by p-value adjustment for multiple comparisons with the Benjamini and Hochberg method.

#### 5.4.5 Effect of PLGA microspheres on hMPC viability in bioprinted muscle constructs

The effect of the PLGA microspheres on cell viability after extrusion-based bioprinting was evaluated in a live/dead cytotoxicity assay after one day in culture (figure 5.11(a, b)). hMPCs were mixed at the concentration of 30 million/mL before bioprinting into either the microsphere-free bioink (Bioink - control group) or the bioink containing 5 mg/mL microspheres (Bioink + MSs). No significant difference (Welch's t-test,  $p = 0.71$ ) in cell viability was detected between these two groups ( $86.5 \pm 5.2\%$  vs  $87.8 \pm 2.4\%$ , respectively) (figure 5.11(b)). Thus, the presence of PLGA microspheres at a 5 mg/mL concentration does not affect cell viability in the biomanufactured muscle constructs.

Notably, the microspheres at 5 mg/mL do not interfere with the bioprinting process and are evenly distributed throughout the extruded hydrogel (figure 5.11(c, c')). On the other hand, loading the bioink with higher concentrations of microspheres (10 mg/mL) often leads to nozzle obstruction and makes bioprinting challenging.

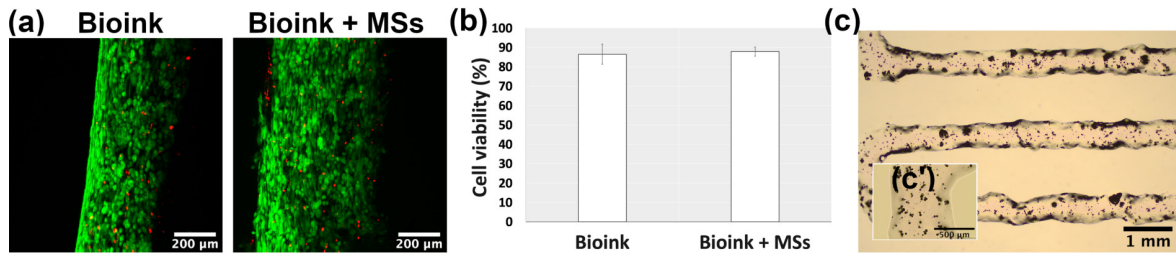


**Figure 5.11.** Cell viability and microsphere distribution in bioprinted constructs. (a) Live/Dead cell viability assay on day 1 post-bioprinting. Maximum intensity Z-projection of confocal stacks. Live and dead human muscle progenitor cells are shown in *green* and *red*, respectively, in crosslinked microsphere-free hydrogels (*Bioink*) and hydrogels containing 5 mg/mL microspheres (*Bioink + MSs*). (b) Cell viability quantified as a percentage of live cells relative to the total number of cells. Three replicates for each treatments were used. (c) Microsphere (dark dots) distribution in the bioink at a lower (c) and higher (c') magnification.

#### 5.4.6 NFs released by PLGA microspheres retain their bioactivity and facilitate neurite outgrowth

To assess the biological activity of the CNTF and GDNF released from the microspheres embedded into the hydrogel, we employed an *in vitro* neurite growth assay with chick embryonic DRG explants (figure 5.5). Our design involved four treatment groups: (a) hydrogel containing no NFs and no microspheres (hydrogel - control group); (b) microsphere-free hydrogel with CNTF and GDNF directly mixed into the hydrogel (hydrogel + NFs - positive control); (c) hydrogel with empty microspheres (hydrogel + empty MSs - microsphere control group) and (d) hydrogel containing CNTF/GDNF-loaded microspheres (hydrogel + NF-loaded MSs - test group) with the overall load of the CNTF/GDNF matching that in group b. The DRG explants were cultured on top of the hydrogels for 2, 7, and 14 days (figure 5.12, C1), and a range of growth parameters were assessed, including: (1) the total neurite outgrowth, (2) average neurite length, (3) longest neurite, and (4) number of neurites per ganglion (figure 5.13).

The statistical analysis detected a significant effect of the treatment on the above growth metrics (tables C2 – C5). On day 2, the total neurite outgrowth in the hydrogel + NFs group was significantly higher compared to the other three groups (figures 5.12(a – d), 5.13(a)). In addition, the most extended neurites in this group were significantly longer than in the hydrogel group and the hydrogel + NF-loaded MSs group (figure 5.13(c)). Notably, at this early time point, no difference was observed between the two negative control groups (hydrogel and hydrogel + empty MSs) and the hydrogel + NF-loaded MSs group (figure 5.12(d), 5.13).

On day 7, the DRGs in the hydrogel + NF-loaded MSs group started to surpass the other three groups in the growth metrics. The total neurite outgrowth in this group was significantly more extensive than in the hydrogel group and the hydrogel + empty MSs group. Also, it showed a trend ( $p = 0.078$ ) to be higher than in the hydrogel + NFs group (figures 5.12(e – h), 5.13(a)). The average neurite length in this group also significantly exceeded that of the hydrogel and hydrogel + NFs groups (figure 5.13(b)).

On day 14 (figures 5.12(i – l)), the total outgrowth in the hydrogel + NF-loaded MSs group was significantly higher than that in the hydrogel + empty MSs group (figure 5.13(a)).

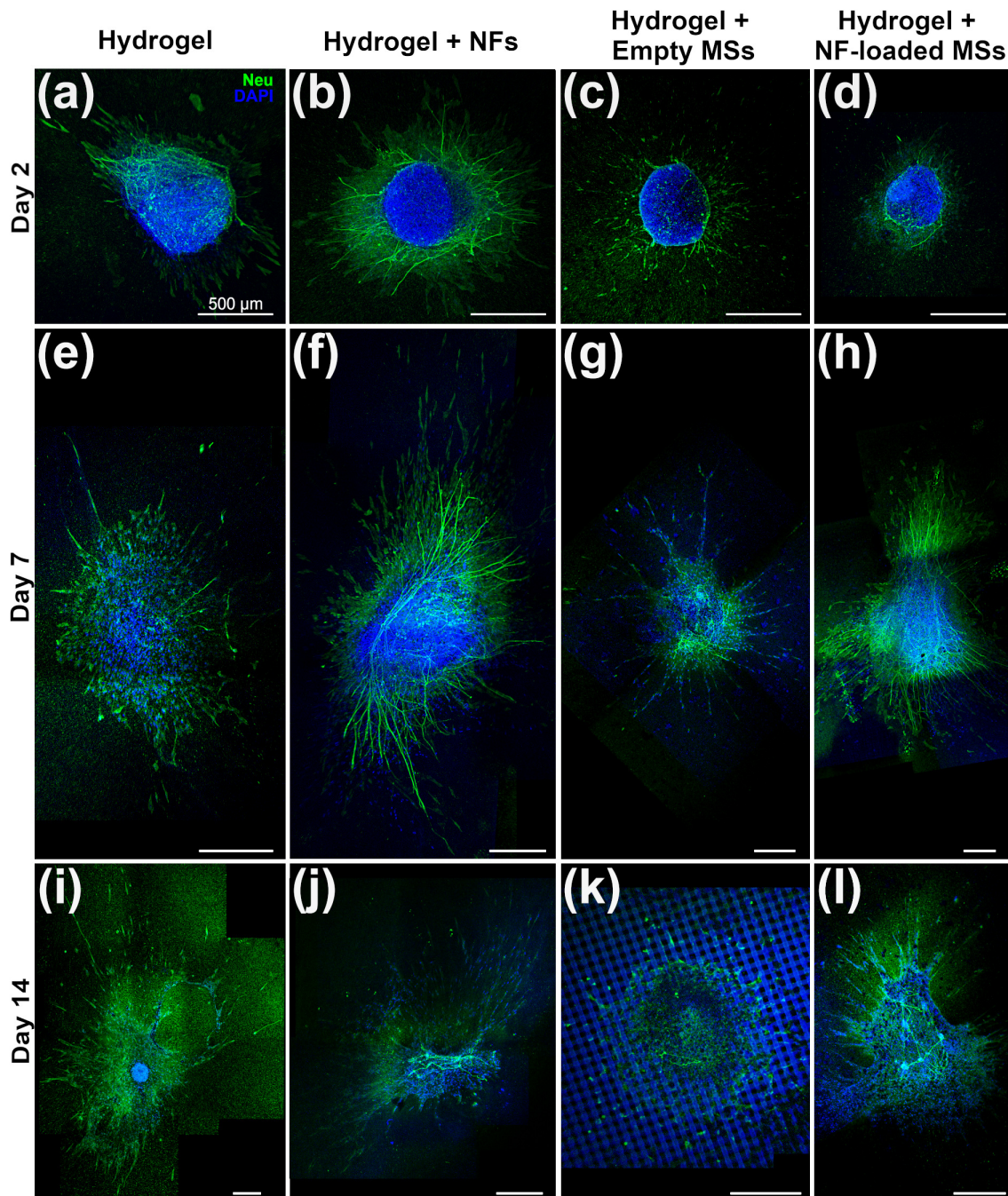


**Figure 5.12.** Representative microscopic images of DRGs in the *in vitro* neurite outgrowth assay. Four treatment groups were involved: microsphere-free hydrogel with no NFs (*Hydrogel*) (a, e, i); microsphere-free hydrogel with CNTF and GDNF directly mixed into the hydrogel (*Hydrogel + NFs*) (b, f, j); hydrogel with empty microspheres (*Hydrogel + empty MSs*); and hydrogel containing CNTF/GDNF-loaded microspheres (*Hydrogel + NF-loaded MSs*) (d, h, l). The DRGs were fixed at three time points: day 2 (a – d), day 7 (e – h), and day 14 (i – l). The DRGs were stained with antibodies recognizing neurofilaments (*NF*, *green*). Nuclei were stained with DAPI (*blue*). All images are maximum intensity Z-projections of confocal stacks. All scale bars represent 500  $\mu\text{m}$ .

This group also surpassed the other three groups in the maximum neurite length (figure 5.13(c)).

In addition to the effect of treatment on the growth metrics at individual time points, the

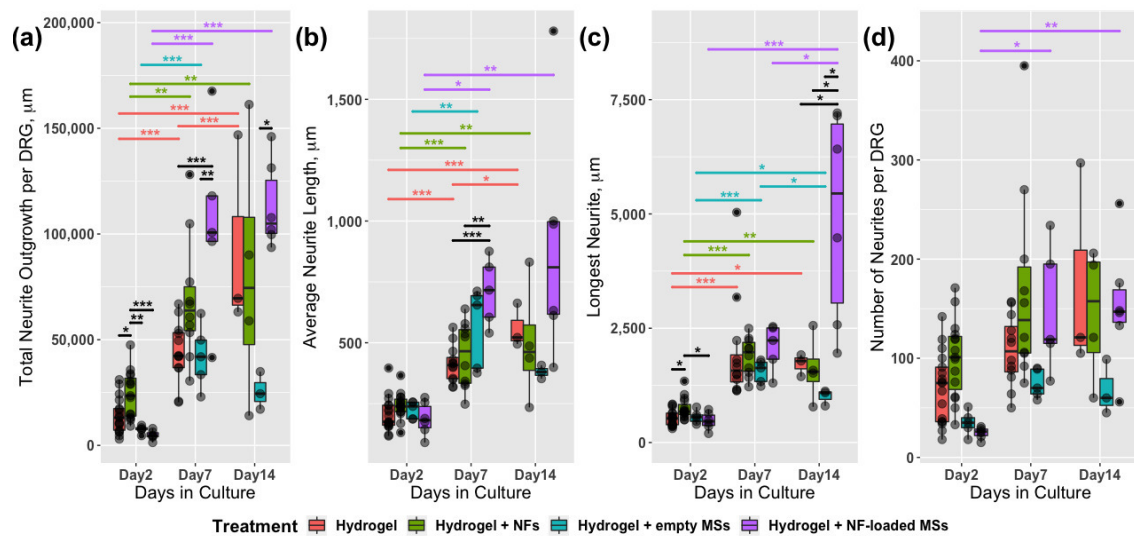


**Figure 5.13.** The quantitative analysis of the CNTF/GDNF either directly dissolved in the hydrogel (*Hydrogel + NFs*) or encapsulated in PLGA microspheres (*Hydrogel + NF-loaded MSs*) on the DRG neurite outgrowth. The two control cohorts involved the microsphere-free hydrogel with no NFs (*Hydrogel*) and the hydrogel loaded with empty microspheres (*Hydrogel + Empty MSs*). (a) Total neurite outgrowth per ganglion. (b) Average neurite length. (c) Length of the longest neurite in DRGs. (d) Number of neurites per ganglion. The significance level annotations are shown in black for the treatments cohorts at each time point, and in the respective color for each cohort across the time points.

two-factor ANOVA test also showed a significant variation in the temporal growth dynamics among the groups (tables C2 – C5). Although all four groups experienced an increase in the total neurite outgrowth and average neurite length between day 2 and day 7 (figures 5.13(a and b)), the temporal growth pattern of the DRGs in the hydrogel + NF-loaded MSs group was distinct from that of the other groups. Only this group showed a significant increase in neurite number over time (figure 5.13(d)) (between day 2 and day 7) and also an increase in the maximum neurite length over the later phase of the experiment (between days 7 and 14) (figure 5.13(c)).

Taken together, these data suggest that the NFs directly loaded into the hydrogel accelerate the early neurite outgrowth. In contrast, NFs delivered in the PLGA microspheres facilitate neurite growth over a longer time scale and significantly increase the maximum neurite length and the number of neural processes per ganglion. It is also worth noting that PLGA microspheres had no adverse effect on the neurite growth, as there is no statistical difference between the hydrogel and hydrogel + empty microspheres in any of the growth metrics at any time point.

## 5.5 Discussion

Proper and timely innervation of implanted bioengineered skeletal muscle constructs is essential for the implant's complete functional maturation. Innervation can be accelerated via a two-pronged approach: (a) induction of pre-formed post-synaptic acetylcholine receptor (AChR) clusters on the differentiated muscle cells in the skeletal muscle construct and (b) directing and enhancing the growth of the host peripheral axons to the pre-formed

AChR clusters in the implanted skeletal muscle construct. Earlier studies demonstrated that the induction of AChR clusters could be accomplished before implantation by treating the biomanufactured muscle construct with the proteoglycan agrin [281, 282]. In contrast, the acceleration of the directed growth of the host neurites towards the implanted muscle cells has remained a significant challenge.

In previously published works [262, 283], neurotrophic factor-loaded PLGA microspheres were employed to facilitate the regeneration of peripheral nerves across a surgically created gap. In these studies, a conduit was loaded with the microspheres and used to bridge the gap between the proximal and distal stumps of a damaged nerve. Our study is different in that the microspheres are integrated into the intended terminal target that needs to be innervated (*i.e.* the biomanufactured muscle construct). To our knowledge, this approach has never been utilized before. In addition, the neurotrophic factors previously delivered with PLGA microspheres [262, 283] included NGF, NT-3, GDNF, and BDNF, but not the combination of CNTF and GDNF, which were identified in a previous study as an effective morphogen inducing directed neurite growth [246] and used in the present study.

The previously published efforts that used bioengineered constructs to treat volumetric muscle defects have been primarily focused on vascular in-growth and muscle cell differentiation in the implant [282]. There have been also some limited efforts to accelerate the innervation of engineered muscle construct. One common strategy has involved surgical suturing of host nerves to muscle implants [251, 284, 285]. In other studies, neuronal stem/progenitor cells or motor neurons were directly incorporated into the engineered muscle construct [252, 286]. However, these approaches are not clinically practical due to several technical challenges, *e.g.* limited autologous cell sources, the difficulty of obtaining enough neuronal cells/tissue for transplantation, and low cell quality. Our concept of using direct incorporation of neurotrophic factors into the bioengineered muscle construct is more clinically relevant for facilitating rapid nerve growth, migration, and integration, as it is free from the above limitations. Our approach is also novel, since there has been no published designs that incorporated pharmacological agents to directly facilitate the directed growth of the host nerves into the implanted biofabricated muscle.

Recent *in vitro* experiments demonstrated that two NFs, CNTF and GDNF, acted synergistically to induce directed neurite growth [246]. The main limitation of that study was that the NFs were directly loaded into the hydrogel matrix. As shown here and in the previously published works [287], such delivery system designs may not be efficient in *in vivo* settings due to the initial burst release of NFs and their short-term biological activity due to rapid degradation [288].

To overcome these challenges, this study investigated the feasibility of using PLGA microspheres as a vehicle for sustained release of NFs required for complete nerve integration into the bioengineered scaffold. The emulsification method and the type of organic solvent used in microsphere fabrication affect the physical characteristics (porosity, size, size distribution) of the microspheres and, ultimately, the release kinetics of the encapsulated cargo molecules [267, 289, 290, 291, 292]. This study employed a W/O/W double-emulsion protocol with vortexing as the emulsification method and chloroform as the organic solvent to generate PLGA microspheres with the desired characteristics (regular spherical shape, smooth external surface, homogenous size distribution) and at a consistently high yield.

We established that, at moderate loads (5 mg/mL), these microspheres could be incorporated into the hydrogel-based extracellular matrix of bioprinted muscle constructs. At these moderate loads, the microspheres suspended in the fibrinogen-based bioink were fully



compatible with the downstream extrusion during the bioprinting process, as they neither significantly changed the viscosity of the bioink nor obstructed the nozzle. Upon completing the bioprinting and crosslinking with thrombin, the microspheres did not affect the mechanical properties of the fibrin hydrogel, nor did they interfere with the viability of the hMPCs in the constructs. The crosslinked hydrogel showed a highly porous structure that could provide a suitable interconnected network essential for cell nutrient penetration, proliferation, and migration [280]. We also found that increasing the load of the microspheres in the bioink should be avoided, as it leads to significant changes in viscoelastic properties of both the bioink and the resulting hydrogel that may affect cell behavior, viability [275, 277], migration [293], neurite outgrowth [294] and often leads to nozzle clogging during bioprinting.

The PLGA microspheres incorporated the cargo molecules with high efficiency. In the hydrogel, the NF-loaded PLGA microspheres released the NFs in a sustained manner compared to the hydrogel with the directly loaded NFs (microsphere-free hydrogel). In our *in vitro* assay, the sustained release of NFs using microspheres facilitated neurite outgrowth differently from the early burst release of the NFs directly loaded into the hydrogels. The NFs released from the microsphere-free hydrogels enhanced the neurite outgrowth at the early time points (up to day 2). In contrast, the slower and more sustained release of the NFs encapsulated in microspheres was more conducive to the neurite outgrowth at a longer time scale (*i.e.* day 7 through day 14). The most extended neurites were also produced by the DRGs cultured in the presence of the CNTF/GDNF-loaded microspheres after 14 days in culture. These results suggest that the sustained release of NFs using microspheres has the potential to accelerate the peripheral nerve growth and their integration into the skeletal muscle construct. The microspheres persisted in the hydrogels throughout the duration of the *in vitro* assay (14 days), suggesting that their degradation rate is slow and that they can be potentially used for sustained NF delivery even in longer experiments in the future.

Overall, our results show that NF-loaded PLGA microspheres can be efficiently incorporated into fibrin-based bioprinted skeletal muscle constructs. The sustained release of NFs from these microspheres accelerates neurite outgrowth *in vitro*. Previously, 3D bioprinted skeletal muscle constructs containing no NFs were shown to form robust AChR clusters in differentiated muscle cells in response to agrin treatment [281, 295]. Consequently, in future work, bioprinted constructs with pre-formed AChR clusters and NF-loaded PLGA microspheres will be used *in vivo* to evaluate the effect of these two combined strategies on the host nerve integration and restoration of the muscle function.

## 5.6 Conclusions

This study demonstrates the feasibility of PLGA microspheres as a vehicle for the delivery and sustained release of NFs in biomanufactured skeletal muscle constructs. The microspheres can be incorporated into the fibrin-based bioprinted skeletal muscle construct without affecting the viability of hMPCs or interfering with extrusion bioprinting. The encapsulated NFs are released from microspheres embedded in hydrogels in a sustained manner, retain their biological activity for at least 14 days, and significantly enhance neurite growth. Further investigations are needed to examine the long-term effect of the bioprinted muscle construct with NF-loaded microspheres on accelerating innervation and functional muscle regeneration *in vivo*.

## 5.7 Supplementary information

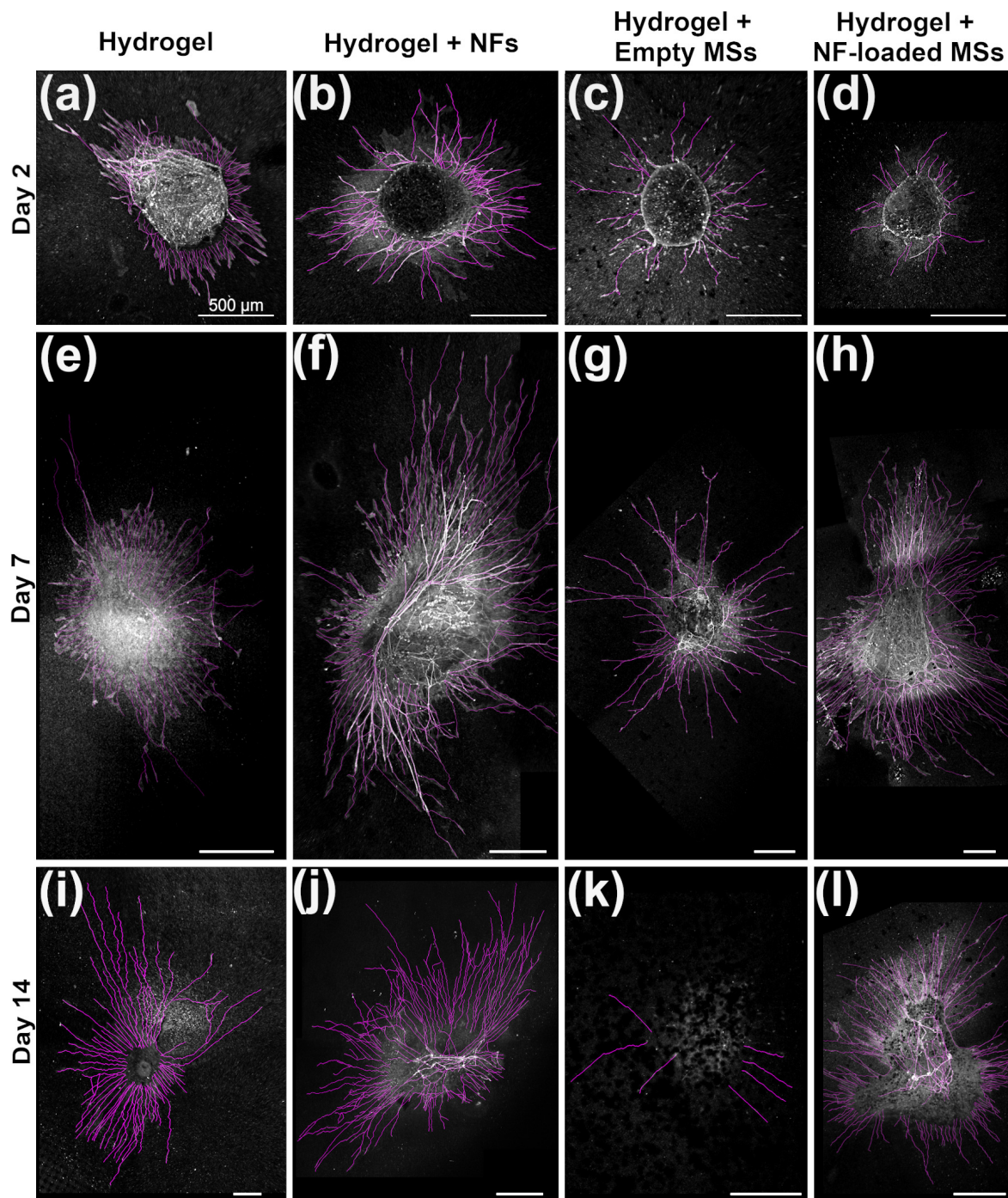


**Figure C1.** Neurite tracings (magenta) with the NeuronJ plugin on representative micrographs of DRGs in the *in vitro* neurite outgrowth assay. All images are maximum intensity Z-projections of confocal stacks. All scale bars represent 500  $\mu\text{m}$ .

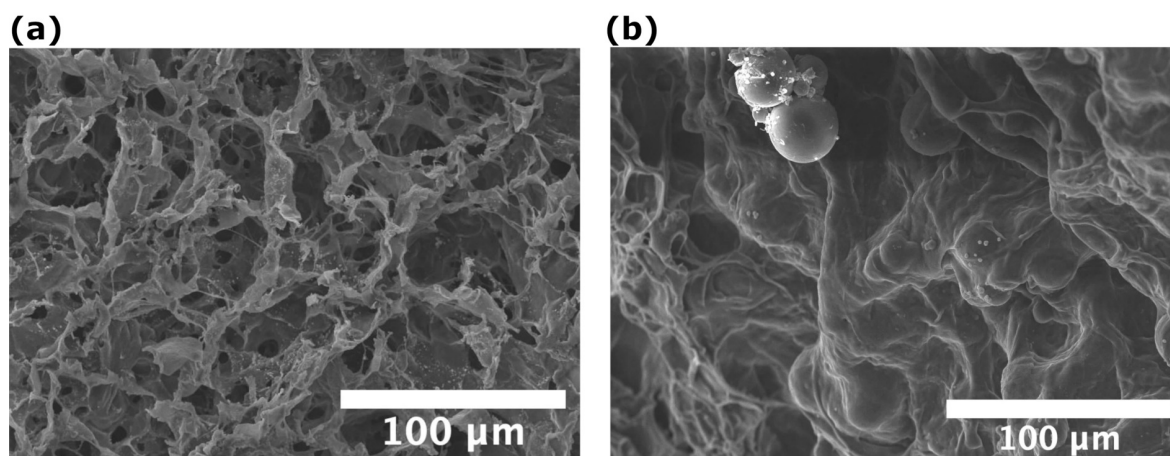


**Figure C2.** Ultrastructure (SEM) of the crosslinked microsphere-free (a) and microsphere-laden (10 mg/mL) (b) hydrogels after 7 days in PBS at 37°C.

	Df	Sum Sq	Mean Sq	F-value	P-value
Treatment	3	22938220837.36	7646073612.45	15.11	$7.36 \times 10^{-8}$
Time Point	2	64575406710.87	32287703355.43	63.79	$2 \times 10^{-16}$
Treatment:Time Point	6	16844864506.58	2807477417.76	5.55	$7.73 \times 10^{-5}$
Residuals	79	39987193023.20	506167000.29		

**Table C2.** *In vitro* outgrowth assay. Total outgrowth. ANOVA summary table  
Df – degrees of freedom; Sum Sq – sums of squares; Mean Sq – mean squares

	Df	Sum Sq	Mean Sq	F-value	P-value
Treatment	3	927250.58	309083.53	12.46	$9.41 \times 10^{-7}$
Time Point	2	2161508.48	1080754.24	43.56	$1.77 \times 10^{-13}$
Treatment:Time Point	6	614510.08	102418.35	4.13	$1.17 \times 10^{-3}$
Residuals	79	1959844.10	24808.15		

**Table C3.** *In vitro* outgrowth assay. Average neurite length. ANOVA summary table

	Df	Sum Sq	Mean Sq	F-value	P-value
Treatment	3	25468090.34	8489363.45	14.26	$1.63 \times 10^{-7}$
Time Point	2	55191185.50	27595592.75	46.36	$4.80 \times 10^{-14}$
Treatment:Time Point	6	32744367.94	5457394.66	9.17	$1.31 \times 10^{-7}$
Residuals	79	47028358.86	595295.68		

**Table C4.** *In vitro* outgrowth assay. Length of the longest neurite in DRGs. ANOVA summary table

	Df	Sum Sq	Mean Sq	F-value	P-value
Treatment	3	50425.54	16808.51	6.03	$9.38 \times 10^{-4}$
Time Point	2	98817.57	49408.78	17.74	$4.34 \times 10^{-7}$
Treatment:Time Point	6	28237.49	4706.25	1.69	0.13
Residuals	79	220051.81	2785.47		

**Table C5.** *In vitro* outgrowth assay. Number of neurites per ganglion. ANOVA summary table

## Conclusions clé:

- Des micro-sphères de PLGA peuvent être fabriquées par une méthode de double émulsion - évaporation solvant. Nous avons montré que deux méthodes différentes de génération d'émulsion (homogénéisation vs. vortex) et deux solvants organiques différents (dichlorométhane vs. chloroforme), testés dans les quatre combinaisons possibles peuvent être utilisées pour la préparation de micro-sphères. Toutefois, bien que les quatre protocoles génèrent des micro-sphères de forme régulièrement sphérique, leurs caractéristiques tels que la morphologie, le rendement de la production et la distribution de taille, qui sont les paramètres déterminant les performances des micro-sphères en tant que système de libération, variaient selon les différentes techniques. La combinaison vortex-chloroforme est celle qui a permis la formation de micro-sphères avec la porosité de surface la moins élevée, un rendement plus élevé et une distribution de taille plus homogène.
- Deux facteurs neurotrophiques (NFs), CNTF et GDNF, sélectionnés au cours d'une étude précédente en tant que facteurs capables de diriger la croissance neuronale, peuvent être encapsulés efficacement dans les micro-sphères de PLGA. Ces micro-sphères, ayant une taille médiane de 23,4  $\mu\text{m}$  et à une concentration de 5 mg/mL, peuvent être incorporées dans une bio-encre à base de fibrine contenant des cellules progénitrices musculaires humaines et utilisées pour la bio-impression 3D sans affecter ni la viabilité des cellules ni le processus de bio-impression.
- Les NFs encapsulés dans les micro-sphères, elles-mêmes intégrées dans les structures bio-imprimées en 3D, sont libérés de manière plus soutenue que les NF simplement encapsulés dans la bio-encre. Ces NFs encapsulés dans les micro-sphères conservent leur activité biologique pendant 14 jours et améliorent significativement la croissance des neurites, comme le montre notre étude *in vitro* utilisant des ganglions de la racine dorsale (DRGs en anglais pour Dorsal Root Ganglions) extraits des embryons de poulet, comme modèle de croissance neuronale.

## Perspectives:

Dans cette étude *in vitro* nous avons utilisés des ganglions de la racine dorsale (DRGs en anglais pour Dorsal Root Ganglions) comme modèle de neurites. Ce modèle était suffisant pour démontrer que les NFs encapsulés dans les micro-sphères conservent leur activité biologique pour au moins 14 jours et que leur libération soutenue améliore la croissance de neurites. Cependant, ce modèle n'est pas représentatif de la réalité car l'innervation est un mécanisme très complexe dont le succès s'évalue par la formation de points de contact entre les motoneurones et les fibres musculaires, qui sont les jonctions neuromusculaires (NMJs). Par conséquent, d'autres études *in vitro* et *in vivo* sont en cours pour déterminer l'effet de la libération soutenue des NFs sur la formation de structures de type NMJs. En particulier, l'étude *in vitro* vise à déterminer la formation de NMJs entre les neurites provenant des DRGs et cellules musculaires contenues dans le scaffold bio-imprimé. L'étude *in vivo* implique l'implantation du muscle bio-imprimé dans le rat, choisi comme animal modèle et donc l'évaluation de la formation de NMJs entre le système périphérique nerveux du rat

et le scaffold implanté. Cette étude *in vivo* vise également à évaluer la régénération de la fonctionnalité musculaire à travers des tests fonctionnels.

## Chapter 6

# Conclusions and future perspectives

### 6.1 Conclusions

The studies conducted in this thesis have brought contributions and new understandings in the field of biomaterials, especially the naturally-derived ones, as well as their application to tissue engineering.

In Chapter 2, Cicada *Orni* sloughs collected in the south-east of France were evaluated as a new alternative renewable source of chitin and its derivative chitosan. We found that cicada sloughs are very rich in chitin, which compose more than 40% of the mass of the sloughs. For the first time to our knowledge, we characterized the physicochemical properties, using simple methods such as FTIR and XRD, not only the final product of the extraction, chitin, but also of the raw material (i.e., cicada sloughs) and the intermediary products deriving from the extraction of chitin (i.e., demineralized and deproteinized products). The characterization of these products has allowed us to: i) determine the physicochemical properties of chitin, (i.e., its degree of acetylation and index of crystallinity) and ii) to propose a new method to evaluate the effectiveness of the extraction process. Subsequently, we extracted chitin from cicada sloughs harvested in two more years, and used the same characterization methods to assess the repeatability of the extraction process and the stability of the natural source over the years. We found that the physicochemical properties of the final products obtained varied from year to year, and that these differences could already be detected by analysis of the raw material (i.e., cicada sloughs) using the above-mentioned simple methods. Indeed, by comparing the FTIR spectra of the cicada sloughs harvested in three different years among them, rather than the final product, i.e. chitin, we were able to conclude that these differences are not due to the extraction process but to intrinsic differences within the source. Then, we transformed chitin into chitosan and we used the same characterization methods to assess the efficiency of the transformation process (i.e., deacetylation). We determined the physicochemical properties of chitosan and found that it has a low degree of deacetylation, which can be attributed to the deacetylation process which is probably not appropriate for this source.

In Chapter 3 we showed that two natural gums (i.e guar gum and tamarind gum) can efficiently be combined with chitosan for the development of new inks for extrusion-based bioprinting. Through a dual gelation strategy, based on: i) the inclusion of gelatin whose role is to improve the bioprinting process, and ii) the treatment of the bioprinted constructs with a solution of ethanol-NaOH to induce their gelation, it was possible to develop self-supporting biomaterial inks and stable 3D printed constructs without the use of chemical

crosslinkers. Gelatin enables all the three inks respectively made of chitosan, chitosan and guar gum and chitosan and tamarind gum to be printable and to generate self-supporting structures. Long-term stability was obtained through a gelation mechanism based on the immersion in ethanol and NaOH. Printed 3D constructs made of chitosan and gums degraded slowly compared to the constructs made of chitosan alone. This behavior may depend on the possible interactions between chitosan and the gums as well on the interactions induced by the treatment of gelation. We also found that, based on the type of chitosan-gum ink, either containing guar gum or tamarind gum, 3D printed constructs had different mechanical properties and abilities to deliver entrapped substances. For instance, constructs comprising guar gum showed improved mechanical properties while constructs comprising tamarind gum showed a more sustained release of BSA, used as a model protein. The mechanical properties of the chitosan-gum inks were comparable with those of the heart, and are currently being tested for the fabrication of cardiac patches for the treatment of myocardial infarction.

Finally, in Chapter 5, we presented the strategy that we adopted to control the release of neurotrophic factors (NFs) from bioprinted skeletal muscle constructs. We demonstrated that PLGA microspheres can be efficiently used as a vehicle for the delivery and sustained release of NFs in biomanufactured skeletal muscle constructs. This sustained release showed promising results *in vitro* in improving the neurite outgrowth from dorsal root ganglions (DRGs) as compared to the faster release obtained through the simple entrapment of NFs directly within the bioink employed to fabricate the 3D construct. The NF-loaded microspheres can be incorporated into the fibrin-based bioprinted skeletal muscle construct without affecting the viability of human muscle progenitor cells or interfering with extrusion bioprinting. This suggests that the previously developed fibrin-based bioink, now functionalized with the inclusion of NF-loaded microspheres, could be used for the biofabrication of critical size skeletal muscle constructs and improve their innervation.

## 6.2 Future perspectives

Altogether, these results pave the way to many developments in the field of biomaterials. For instance, the framework developed in this thesis, used in the evaluation of the temporal reliability of cicada sloughs as a source of chitin, could also be extended to the evaluation of the quality of other sources, or the effectiveness of different extraction processes. The deacetylation process used for the transformation of chitin to chitosan, led to a chitosan with a low degree of deacetylation, which has a low solubility. In fact, the lower the degree of deacetylation, the more chitosan acts as chitin and thus is insoluble in water or in commonly used organic solvents, such as acetic acid. Solutions to overcome this limitation may involve the use of alternative solvents, such as ionic liquids, already used to dissolve chitin [9], or involve different deacetylation conditions, such as the use of higher concentrations of NaOH, higher temperatures or longer reaction times. However, such an environment would lead to the hydrolysis of chitosan. As a consequence, it would lower its molecular weight, which, together with the degree of acetylation, strongly influence the rheological, biological and other physicochemical properties of chitosan such as its biodegradability. A design of experiments involving different extraction conditions could be carried out in order to relate the degree of deacetylation and molecular weight and select the desired characteristics.



In this thesis we also showed that chitosan can be efficiently used in combination with other components such as guar gum and tamarind gum, allowing for the thickening and gelling of the resulting inks. Nevertheless, we found that these increased properties are still not allowing for the fabrication of 3D objects. Consequently, in order to obtain the required self-supportiveness, we simply added gelatin to the mix. On the other hand, while they did not improve the printing capabilities, the inclusion of guar gum and tamarind gum had a strong effect on the long-term stability of the constructs by drastically reducing the degradation rate of the constructs, as compared to those solely made of chitosan. As a consequence, different combinations of these three polysaccharides could allow us to engineer the properties of 3D constructs, such as their mechanical properties and their degradation rate, and allow them to fulfill very specific roles in an optimized fashion. For instance, the mechanical properties displayed by these constructs motivated us to consider their use for the 3D printing of anisotropic cardiac patches for the repair of myocardial infarction. In fact, we found that constructs made of chitosan and gums had Young's modulus close to that of sections of the heart wall with specific myofiber orientations. The latter could probably be even more optimized by using different combinations of the aforementioned polymers in the ink. The next short-term step will be the fabrication of different pattern designs by 3D printing in order to mimic the myofibers orientations. Then, it will be necessary to perform biocompatibility tests and evaluate the ability of these constructs to support cell growth and differentiation into myocardial tissue. In addition, the functionalization of cardiac patches for the delivery of growth factors might be considered as well in order to improve the repair process. In this context, PLGA microspheres, which were developed in Chapter 5 as a neurotrophic factor delivery system in order to accelerate the innervation of a bioprinted skeletal muscle construct, could be easily loaded with, for example, with cardiac growth factors and added to different inks and bioinks, including the above-mentioned ones. Furthermore, considering the low degradation rate displayed by chitosan-gums based constructs, and their ability to release BSA in a more or less sustained manner, these inks could be used for the release of encapsulated factors, in different forms. For example, they could be manufactured in form of microspheres through microfluidic techniques. To this end, different combinations of the three polysaccharides, as well as different gelation conditions (i.e, concentration of NaOH, ratio ethanol-NaOH etc.) could also be used in this framework. Microspheres made of natural hydrogels could present several advantages over synthetic ones. In fact, even if, due to their tunable properties of degradation and, consequently, of the release of entrapped factors, PLGA microspheres represent one of the most used delivery systems, they are rigid. Consequently, when included within a bioink, they can cause nozzle clogging when present at high concentrations, while chitosan-natural gums microspheres, by being soft materials, could elude this problem.



## Appendix A

# Development of novel chitosan / guar gum inks for extrusion-based 3D bioprinting: Process, printability and properties



## Development of novel chitosan / guar gum inks for extrusion-based 3D bioprinting: Process, printability and properties



F. Cleymand<sup>a,d,\*</sup>, A. Poerio<sup>a</sup>, A. Mamanov<sup>a</sup>, K. Elkhoury<sup>b</sup>, L. Ikhelf<sup>a</sup>, J.P. Jehl<sup>a</sup>, C.J.F. Kahn<sup>b</sup>, M. Ponçot<sup>a</sup>, E. Arab-Tehrany<sup>b</sup>, João F. Mano<sup>a,c</sup>

<sup>a</sup> Université de Lorraine, Institut Jean Lamour, UMR CNRS 7198, 2 allée André Guinier, Campus Artem, BP 50840, F-54011, Nancy Cedex, France

<sup>b</sup> Université de Lorraine, Laboratoire Ingénierie des Biomolécules, TSA 40602, Vandoeuvre-lès-Nancy, F-54518, France

<sup>c</sup> University of Aveiro, CICECO—Aveiro Institute of Materials, Department of Chemistry, 3810-193, Aveiro, Portugal

<sup>d</sup> Mines Nancy, Campus ARTEM, 92 rue du sergent Blandan, BP 14234, 54042, Nancy Cedex, France

### ARTICLE INFO

#### Keywords:

Chitosan  
Guar gum  
Ink  
3D bioprinting  
Hydrogel

### ABSTRACT

The major limitation of 3D bioprinting is the availability of inks. In order to develop new ink formulations, both their rheological behavior to obtain the best printability and the target bio-printed objects conformities must be studied. In this paper, for the first time in our knowledge, the preparation and the characterization of novel ink formulations based on two natural biocompatible polysaccharides, chitosan (CH) and guar gum (GG), are presented. Five ink formulations containing different proportions of CH and GG were prepared and characterized in terms of rheological properties and solvent evaporation. Their printability was assessed (by varying the nozzle diameter, pressure and speed) using an extrusion-based 3D bioprinting process performed directly in air at 37 °C. Results showed that the incorporation of GG improved both the printability of the pure chitosan ink by increasing the viscosity of the solution and the shape fidelity by accelerating the solvent evaporation. We showed that the ink containing 15% (w/w) of GG and 85% (w/w) of CH had the best printability. This formulation was therefore used for the preparation of membranes that were characterized by infrared spectroscopy (FTIR) and X-Ray Diffraction (XRD) before and after gelation as well as for their mechanical properties (Young modulus, strength and strain at break). The optimal process printing parameters were determined to be: 27 G micronozzle, extrusion pressure below 2 bars and robot head speed between 20 and 25 mm/s. This novel ink formulation is a guideline for developing 2D scaffolds (such as auto-supported membranes) or 3D scaffolds for biomedical applications.

### 1. Introduction

Due to the persistent problem of organ shortage, new artificial methods have been developed in order to find alternative solutions to transplantation [1–3]. 3D bioprinting has emerged as a promising method to fabricate complex devices to regenerate or replace tissues and organs that could be processed using natural polymers [4]. Among the different technologies, extrusion-based 3D bioprinting is the most commonly used in the field of health care applications [5]. Different approaches can be used for the extrusion-based bioprinting and novel strategies to improve the current existing methodologies are constantly under investigation. The most used approach for extrusion-based 3D bioprinting consists on the deposition of the ink on a flat surface in air. A more recent promising approach consists in the extrusion of the ink into a

suspension bath that prevent the material to collapse, particularly used for the printing of low-viscosity fluids [6]. However, the first method offers lower cost processability and less complexity. Despite the great progresses that have already been made, extrusion-based 3D bioprinting is still at its early stages and there are still lots of improvements to be made concerning the bioink availability and development [7]. One of the biggest limitations of this technology is the development of inks that, in form of hydrogels, present adequate mechanical properties to ensure a good printability and shape fidelity post-printing [8] without compromising the cell viability [9]. Either synthetic or natural materials can be used to prepare bioinks, which generally show opposite characteristics. In fact, while synthetic materials present strong mechanical properties simplifying the printing process and shape fidelity of the printed constructs, the natural ones present low immunogenicity and higher

\* Corresponding author. Université de Lorraine, Institut Jean Lamour, UMR CNRS 7198, 2 allée André Guinier, Campus Artem, BP 50840, F-54011, Nancy Cedex, France.

E-mail address: [franck.cleymand@univ-lorraine.fr](mailto:franck.cleymand@univ-lorraine.fr) (F. Cleymand).

<https://doi.org/10.1016/j.bprint.2020.e00122>

Received 6 July 2020; Received in revised form 25 November 2020; Accepted 7 December 2020

2405-8866/© 2020 Published by Elsevier B.V.

# Bibliography

- [1] M. Brovold et al. “Naturally-derived biomaterials for tissue engineering applications”. In: *Novel Biomaterials for Regenerative Medicine* (2018), pp. 421–449.
- [2] E. Marin, F. Boschetto, and G. Pezzotti. “Biomaterials and biocompatibility: An historical overview”. In: *Journal of Biomedical Materials Research Part A* 108.8 (2020), pp. 1617–1633.
- [3] R. Langer. “Biomaterials in drug delivery and tissue engineering: one laboratory’s experience”. In: *Accounts of Chemical Research* 33.2 (2000), pp. 94–101.
- [4] R Langer. “eta VACANTI JP 1993.«” In: *Tissue engineering»*. *Science* 260 (), pp. 920–926.
- [5] S. Barrientos et al. “Growth factors and cytokines in wound healing”. In: *Wound repair and regeneration* 16.5 (2008), pp. 585–601.
- [6] J. Groll et al. “A definition of bioinks and their distinction from biomaterial inks”. In: *Biofabrication* 11.1 (2018), p. 013001.
- [7] A. Schwab et al. “Printability and shape fidelity of bioinks in 3D bioprinting”. In: *Chemical Reviews* 120.19 (2020), pp. 11028–11055.
- [8] D. Elieh-Ali-Komi and M. R. Hamblin. “Chitin and chitosan: production and application of versatile biomedical nanomaterials”. In: *International journal of advanced research* 4.3 (2016), p. 411.
- [9] S. S. Silva et al. “Alternative methodology for chitin–hydroxyapatite composites using ionic liquids and supercritical fluid technology”. In: *Journal of bioactive and compatible polymers* 28.5 (2013), pp. 481–491.
- [10] A. J. Russell and T. Bertram. “Moving into the clinic”. In: *Principles of Tissue Engineering*. Elsevier, 2014, pp. 57–81.
- [11] S. V. Murphy and A. Atala. “3D bioprinting of tissues and organs”. In: *Nature biotechnology* 32.8 (2014), pp. 773–785.
- [12] R. Landers, U. Hübner, R. Schmelzeisen, and R. Mülhaupt. “Rapid prototyping of scaffolds derived from thermoreversible hydrogels and tailored for applications in tissue engineering”. In: *Biomaterials* 23.23 (2002), pp. 4437–4447.
- [13] S. Lee, J. Yoo, and A. Atala. “Fundamentals of in situ tissue regeneration”. In: *In Situ Tissue Regeneration*. Elsevier, 2016, pp. 3–17.
- [14] A. K. Gaharwar, I. Singh, and A. Khademhosseini. “Engineered biomaterials for in situ tissue regeneration”. In: *Nature Reviews Materials* 5.9 (2020), pp. 686–705.
- [15] C. R. Correia, I. M. Bjørge, S. Nadine, and J. F. Mano. “Minimalist Tissue Engineering Approaches Using Low Material-Based Bioengineered Systems”. In: *Advanced Healthcare Materials* 10.9 (2021), p. 2002110.

- [16] X. Wan, Z. Liu, and L. Li. “Manipulation of Stem Cells Fates: The Master and Multifaceted Roles of Biophysical Cues of Biomaterials”. In: *Advanced Functional Materials* (2021), p. 2010626.
- [17] A. Skardal. “Bioprinting essentials of cell and protein viability”. In: *Essentials of 3D Biofabrication and Translation*. Elsevier, 2015, pp. 1–17.
- [18] R. M. Nerem and S. C. Schutte. “The challenge of imitating nature”. In: *Principles of tissue engineering*. Elsevier, 2014, pp. 9–24.
- [19] P. Bianco and P. G. Robey. “Stem cells in tissue engineering”. In: *Nature* 414.6859 (2001), pp. 118–121.
- [20] C. O. Urrutia et al. “Mechanical Stimulation of Cells Through Scaffold Design for Tissue Engineering”. In: *Scaffolds in Tissue Engineering Materials, Technologies and Clinical Applications* (2017), p. 147.
- [21] J. M. Pachence and J. Kohn. “Biodegradable polymers”. In: *Principles of tissue engineering* 22 (2000), pp. 263–277.
- [22] P. Gutierrez-Macias, M. d. L. H. De Jesus, and B. E. Barragan-Huerta. “The production of biomaterials from agro-industrial waste”. In: *Fresenius Environ. Bullet* 26.6 (2017), pp. 4128–4152.
- [23] M. Nowacki et al. “Are agricultural and natural sources of bio-products important for modern regenerative medicine? A review”. In: *Ann Agric Environ Med* 24.2 (2017), pp. 207–212.
- [24] S.-C. Wu et al. “Cell adhesion and proliferation enhancement by gelatin nanofiber scaffolds”. In: *Journal of Bioactive and Compatible Polymers* 26.6 (2011), pp. 565–577.
- [25] S. Gorgieva and V. Kokol. “Collagen-vs. gelatine-based biomaterials and their biocompatibility: review and perspectives”. In: *Biomaterials applications for nanomedicine* 2 (2011), pp. 17–52.
- [26] P. Jaipan, A. Nguyen, and R. J. Narayan. “Gelatin-based hydrogels for biomedical applications”. In: *Mrs Communications* 7.3 (2017), pp. 416–426.
- [27] S. Petros, T. Tesfaye, and M. Ayele. “A Review on Gelatin Based Hydrogels for Medical Textile Applications”. In: *Journal of Engineering* 2020 (2020).
- [28] L. Pighinelli et al. “Methods of chitin production a short review”. In: *Am. J. Biomed. Sci. Res* 3 (2019), pp. 307–314.
- [29] K. Mohan et al. “Recent insights into the extraction, characterization, and bioactivities of chitin and chitosan from insects”. In: *Trends in food science & technology* (2020).
- [30] H. Jahangirian et al. “Status of plant protein-based green scaffolds for regenerative medicine applications”. In: *Biomolecules* 9.10 (2019), p. 619.
- [31] S. S. Silva, J. F. Mano, and R. L. Reis. “Potential applications of natural origin polymer-based systems in soft tissue regeneration”. In: *Critical reviews in biotechnology* 30.3 (2010), pp. 200–221.
- [32] L. Fu, J. Zhang, and G. Yang. “Present status and applications of bacterial cellulose-based materials for skin tissue repair”. In: *Carbohydrate polymers* 92.2 (2013), pp. 1432–1442.

- [33] S. Zang et al. “Study of osteogenic differentiation of human adipose-derived stem cells (HASCs) on bacterial cellulose”. In: *Carbohydrate polymers* 104 (2014), pp. 158–165.
- [34] A. Saha, S. Tyagi, R. K. Gupta, and Y. K. Tyagi. “Natural gums of plant origin as edible coatings for food industry applications”. In: *Critical reviews in biotechnology* 37.8 (2017), pp. 959–973.
- [35] D. A. da Silva, G. C. M. Aires, and R. da Silva Pena. “Gums—Characteristics and Applications in the Food Industry”. In: *Innovation in the Food Sector Through the Valorization of Food and Agro-Food By-Products*. IntechOpen, 2020.
- [36] R. Mohammadinejad et al. “Recent advances in natural gum-based biomaterials for tissue engineering and regenerative medicine: a review”. In: *Polymers* 12.1 (2020), p. 176.
- [37] S. M. Joseph et al. “A review on source-specific chemistry, functionality, and applications of chitin and chitosan”. In: *Carbohydrate Polymer Technologies and Applications* 2 (2021), p. 100036.
- [38] D Raabe et al. “Discovery of a honeycomb structure in the twisted plywood patterns of fibrous biological nanocomposite tissue”. In: *Journal of Crystal Growth* 283.1-2 (2005), pp. 1–7.
- [39] H. El Knidri et al. “Extraction, chemical modification and characterization of chitin and chitosan”. In: *International journal of biological macromolecules* 120 (2018), pp. 1181–1189.
- [40] B. K. Park and M.-M. Kim. “Applications of chitin and its derivatives in biological medicine”. In: *International journal of molecular sciences* 11.12 (2010), pp. 5152–5164.
- [41] J. C. Roy et al. “Solubility of chitin: solvents, solution behaviors and their related mechanisms”. In: *Solubility of polysaccharides* 10 (2017).
- [42] H Tamura, T Furuike, S. Nair, and R Jayakumar. “Biomedical applications of chitin hydrogel membranes and scaffolds”. In: *Carbohydrate Polymers* 84.2 (2011), pp. 820–824.
- [43] C. K. Pillai, W. Paul, and C. P. Sharma. “Chitin and chitosan polymers: Chemistry, solubility and fiber formation”. In: *Progress in polymer science* 34.7 (2009), pp. 641–678.
- [44] Y. Zhao, R.-D. Park, and R. A. Muzzarelli. “Chitin deacetylases: properties and applications”. In: *Marine drugs* 8.1 (2010), pp. 24–46.
- [45] A. M. Boza. “Chitosan-based inks: 3D printing and bioprinting strategies to improve shape fidelity, mechanical properties, and biocompatibility of 3D scaffolds”. In: (2020).
- [46] S. Jana, S. J. Florczyk, M. Leung, and M. Zhang. “High-strength pristine porous chitosan scaffolds for tissue engineering”. In: *Journal of Materials Chemistry* 22.13 (2012), pp. 6291–6299.
- [47] R. C. F. Cheung, T. B. Ng, J. H. Wong, and W. Y. Chan. “Chitosan: an update on potential biomedical and pharmaceutical applications”. In: *Marine drugs* 13.8 (2015), pp. 5156–5186.

- [48] J. Kumirska, M. X. Weinhold, J. Thöming, and P. Stepnowski. “Biomedical activity of chitin/chitosan based materials—influence of physicochemical properties apart from molecular weight and degree of N-acetylation”. In: *Polymers* 3.4 (2011), pp. 1875–1901.
- [49] N. M. Alves and J. F. Mano. “Chitosan derivatives obtained by chemical modifications for biomedical and environmental applications”. In: *International journal of biological macromolecules* 43.5 (2008), pp. 401–414.
- [50] T. J. Madera-Santana, C. H. Herrera-Méndez, and J. R. Rodríguez-Núñez. “An overview of the chemical modifications of chitosan and their advantages”. In: *Green Materials* 6.4 (2018), pp. 131–142.
- [51] N Kahya. “Water soluble chitosan derivatives and their biological activities: a review”. In: *Polym. Sci* 4.2 (2018), pp. 1–16.
- [52] D. Saha and S. Bhattacharya. “Hydrocolloids as thickening and gelling agents in food: a critical review”. In: *Journal of food science and technology* 47.6 (2010), pp. 587–597.
- [53] D. Wu et al. “3D bioprinting of gellan gum and poly (ethylene glycol) diacrylate based hydrogels to produce human-scale constructs with high-fidelity”. In: *Materials & Design* 160 (2018), pp. 486–495.
- [54] T. M. Aminabhavi, M. N. Nadagouda, S. D. Joshi, and U. A. More. “Guar gum as platform for the oral controlled release of therapeutics”. In: *Expert opinion on drug delivery* 11.5 (2014), pp. 753–766.
- [55] S. Dey et al. “Tamarind gum in drug delivery applications”. In: *Natural Polysaccharides in Drug Delivery and Biomedical Applications*. Elsevier, 2019, pp. 285–306.
- [56] F. Cleymand et al. “Development of novel chitosan/guar gum inks for extrusion-based 3D bioprinting: Process, printability and properties”. In: *Bioprinting* 21 (2021), e00122.
- [57] A. Indurkar et al. “Optimization of guar gum-gelatin bioink for 3D printing of mammalian cells”. In: *Bioprinting* 20 (2020), e00101.
- [58] K. M. Reddy et al. “Development of chitosan-guar gum semi-interpenetrating polymer network microspheres for controlled release of cefadroxil”. In: *Designed monomers and polymers* 9.5 (2006), pp. 491–501.
- [59] K Khounvilay and W Sittikijyothin. “Rheological behaviour of tamarind seed gum in aqueous solutions”. In: *Food Hydrocolloids* 26.2 (2012), pp. 334–338.
- [60] G. S. Shaw et al. “Development and characterization of gelatin-tamarind gum/carboxymethyl tamarind gum based phase-separated hydrogels: A comparative study”. In: *Designed Monomers and Polymers* 18.5 (2015), pp. 434–450.
- [61] Y. Chang et al. “Rheological properties of six plant-based seed gums”. In: *American Journal of Analytical Chemistry* 8.11 (2017), pp. 690–707.
- [62] J. P. Vacanti and C. A. Vacanti. “The history and scope of tissue engineering”. In: *Principles of tissue engineering*. Elsevier, 2014, pp. 3–8.
- [63] J. W. Park, S. R. Hwang, and I.-S. Yoon. “Advanced growth factor delivery systems in wound management and skin regeneration”. In: *Molecules* 22.8 (2017), p. 1259.



- [64] K. E. Johnson and T. A. Wilgus. “Vascular endothelial growth factor and angiogenesis in the regulation of cutaneous wound repair”. In: *Advances in wound care* 3.10 (2014), pp. 647–661.
- [65] G. S. Schultz and A. Wysocki. “Interactions between extracellular matrix and growth factors in wound healing”. In: *Wound repair and regeneration* 17.2 (2009), pp. 153–162.
- [66] K. Lee, E. A. Silva, and D. J. Mooney. “Growth factor delivery-based tissue engineering: general approaches and a review of recent developments”. In: *Journal of the Royal Society Interface* 8.55 (2011), pp. 153–170.
- [67] R. J. Klebe. “Cytoscribing: a method for micropositioning cells and the construction of two- and three-dimensional synthetic tissues”. In: *Experimental cell research* 179.2 (1988), pp. 362–373.
- [68] C. A. Vacanti, R. Langer, B. Schloo, and J. Vacanti. “Synthetic polymers seeded with chondrocytes provide a template for new cartilage formation.” In: *Plastic and reconstructive surgery* 88.5 (1991), pp. 753–759.
- [69] A. McCormack, C. B. Highley, N. R. Leslie, and F. P. Melchels. “3D printing in suspension baths: keeping the promises of bioprinting afloat”. In: *Trends in biotechnology* 38.6 (2020), pp. 584–593.
- [70] T. J. Hinton et al. “Three-dimensional printing of complex biological structures by freeform reversible embedding of suspended hydrogels”. In: *Science advances* 1.9 (2015), e1500758.
- [71] T. Bhattacharjee et al. “Writing in the granular gel medium”. In: *Science advances* 1.8 (2015), e1500655.
- [72] R. D. Ventura. “An Overview of Laser-assisted Bioprinting (LAB) in Tissue Engineering Applications”. In: *Medical Lasers; Engineering, Basic Research, and Clinical Application* 10.2 (2021), pp. 76–81.
- [73] H.-J. Jeong, H. Nam, J. Jang, and S.-J. Lee. “3D bioprinting strategies for the regeneration of functional tubular tissues and organs”. In: *Bioengineering* 7.2 (2020), p. 32.
- [74] J. Malda et al. “25th anniversary article: engineering hydrogels for biofabrication”. In: *Advanced materials* 25.36 (2013), pp. 5011–5028.
- [75] T. K. Merceron and S. V. Murphy. “Hydrogels for 3D bioprinting applications”. In: *Essentials of 3D biofabrication and translation*. Elsevier, 2015, pp. 249–270.
- [76] J. K. Carrow et al. “Polymers for bioprinting”. In: *Essentials of 3D biofabrication and translation*. Elsevier, 2015, pp. 229–248.
- [77] T. Gao et al. “Optimization of gelatin–alginate composite bioink printability using rheological parameters: a systematic approach”. In: *Biofabrication* 10.3 (2018), p. 034106.
- [78] G. Gillispie et al. “Assessment methodologies for extrusion-based bioink printability”. In: *Biofabrication* 12.2 (2020), p. 022003.
- [79] L. Ouyang, R. Yao, Y. Zhao, and W. Sun. “Effect of bioink properties on printability and cell viability for 3D bioplotting of embryonic stem cells”. In: *Biofabrication* 8.3 (2016), p. 035020.

- [80] N. Paxton et al. “Proposal to assess printability of bioinks for extrusion-based bioprinting and evaluation of rheological properties governing bioprintability”. In: *Biofabrication* 9.4 (2017), p. 044107.
- [81] C. Bergonzi et al. “Study of 3D-printed chitosan scaffold features after different post-printing gelation processes”. In: *Scientific reports* 9.1 (2019), pp. 1–11.
- [82] R. A. Muzzarelli. “Genipin-crosslinked chitosan hydrogels as biomedical and pharmaceutical aids”. In: *Carbohydrate Polymers* 77.1 (2009), pp. 1–9.
- [83] D. Lee et al. “Chitosan-catechol: a writable bioink under serum culture media”. In: *Biomaterials science* 6.5 (2018), pp. 1040–1047.
- [84] C. Tonda-Turo et al. “Photocurable chitosan as bioink for cellularized therapies towards personalized scaffold architecture”. In: *Bioprinting* 18 (2020), e00082.
- [85] T. T. Demirtaş, G. Irmak, and M. Gümüşderelioglu. “A bioprintable form of chitosan hydrogel for bone tissue engineering”. In: *Biofabrication* 9.3 (2017), p. 035003.
- [86] Q. Liu et al. “Preparation and properties of 3D printed alginate–chitosan polyion complex hydrogels for tissue engineering”. In: *Polymers* 10.6 (2018), p. 664.
- [87] W. L. Ng, W. Y. Yeong, and M. W. Naing. “Development of polyelectrolyte chitosan-gelatin hydrogels for skin bioprinting”. In: *Procedia Cirp* 49 (2016), pp. 105–112.
- [88] H. M. Butler et al. “Optimization of starch-and chitosan-based bio-inks for 3D bioprinting of scaffolds for neural cell growth”. In: *Materialia* 12 (2020), p. 100737.
- [89] T. Ang et al. “Fabrication of 3D chitosan–hydroxyapatite scaffolds using a robotic dispensing system”. In: *Materials science and engineering: C* 20.1-2 (2002), pp. 35–42.
- [90] L. Elviri et al. “Highly defined 3D printed chitosan scaffolds featuring improved cell growth”. In: *Biomedical Materials* 12.4 (2017), p. 045009.
- [91] T. Hahn et al. “Current state of chitin purification and chitosan production from insects”. In: *Journal of Chemical Technology & Biotechnology* 95.11 (2020), pp. 2775–2795.
- [92] Q. Luo et al. “Comparison of the physicochemical, rheological, and morphologic properties of chitosan from four insects”. In: *Carbohydrate Polymers* 209 (2019), pp. 266–275.
- [93] W. Sajomsang and P. Gonil. “Preparation and characterization of  $\alpha$ -chitin from cicada sloughs”. In: *Materials Science and Engineering: C* 30.3 (2010), pp. 357–363.
- [94] D. L. Bertuzzi et al. “General Protocol to Obtain D-Glucosamine from Biomass Residues: Shrimp Shells, Cicada Sloughs and Cockroaches”. In: *Global Challenges* 2.11 (2018), p. 1800046.
- [95] S.-J. Wu, S.-K. Pan, H.-B. Wang, and J.-H. Wu. “Preparation of chitooligosaccharides from cicada slough and their antibacterial activity”. In: *International journal of biological macromolecules* 62 (2013), pp. 348–351.
- [96] N. A. Zainol Abidin et al. “The potential of insects as alternative sources of chitin: An overview on the chemical method of extraction from various sources”. In: *International Journal of Molecular Sciences* 21.14 (2020), p. 4978.

- [97] R. Chandran et al. "SEM characterization of anatomical variation in chitin organization in insect and arthropod cuticles". In: *Micron* 82 (2016), pp. 74–85.
- [98] A. Mol, M. Kaya, M. Mujtaba, and B. Akyuz. "Extraction of high thermally stable and nanofibrous chitin from Cicada (Cicadoidea)". In: *Entomological Research* 48.6 (2018), pp. 480–489.
- [99] A. Ameh, M. Isa, T. Adeleye, and K. Adama. "Kinetics of demineralization of shrimp exoskeleton in chitin and chitosan synthesis". In: *Journal of Chemical Engineering and Materials Science* 4.3 (2013), pp. 32–37.
- [100] I. Younes and M. Rinaudo. "Chitin and chitosan preparation from marine sources. Structure, properties and applications". In: *Marine drugs* 13.3 (2015), pp. 1133–1174.
- [101] M.-K. Jang et al. "Physicochemical characterization of  $\alpha$ -chitin,  $\beta$ -chitin, and  $\gamma$ -chitin separated from natural resources". In: *Journal of Polymer Science Part A: Polymer Chemistry* 42.14 (2004), pp. 3423–3432.
- [102] J. Green and J. Mattick. "Fishery waste management". In: *Food processing waste management* (1979), pp. 202–227.
- [103] D. K. Youn, H. K. No, and W. Prinyawiwatkul. "Physicochemical and functional properties of chitosans prepared from shells of crabs harvested in three different years". In: *Carbohydrate Polymers* 78.1 (2009), pp. 41–45.
- [104] A. Poerio et al. "Extraction and Physicochemical Characterization of Chitin from Cicada orni Sloughs of the South-Eastern French Mediterranean Basin". In: *Molecules* 25.11 (2020), p. 2543.
- [105] J. Brugnerotto et al. "An infrared investigation in relation with chitin and chitosan characterization". In: *Polymer* 42.8 (2001), pp. 3569–3580.
- [106] D. Zhao et al. "Two-step separation of chitin from shrimp shells using citric acid and deep eutectic solvents with the assistance of microwave". In: *Polymers* 11.3 (2019), p. 409.
- [107] A. Hassainia, H. Satha, and S. Boufi. "Chitin from *Agaricus bisporus*: Extraction and characterization". In: *International journal of biological macromolecules* 117 (2018), pp. 1334–1342.
- [108] M. Rinaudo. "Chitin and chitosan: Properties and applications". In: *Progress in polymer science* 31.7 (2006), pp. 603–632.
- [109] M. Ioelovich. "Crystallinity and hydrophilicity of chitin and chitosan". In: *J. Chem* 3.3 (2014), pp. 7–14.
- [110] E. M. Dahmane, M. Taourirte, N. Eladlani, and M. Rhazi. "Extraction and characterization of chitin and chitosan from *Parapenaeus longirostris* from Moroccan local sources". In: *International Journal of Polymer Analysis and Characterization* 19.4 (2014), pp. 342–351.
- [111] N. H. Daraghmeh et al. "chitin". In: *Profiles of drug substances, excipients and related methodology*. Vol. 36. Elsevier, 2011, pp. 35–102.
- [112] Y. Zhang et al. "Determination of the degree of deacetylation of chitin and chitosan by X-ray powder diffraction". In: *Carbohydrate research* 340.11 (2005), pp. 1914–1917.

- [113] J. Xu et al. “DDA (degree of deacetylation) and pH-dependent antibacterial properties of chitin nanofibers against *Escherichia coli*”. In: *Cellulose* 26.4 (2019), pp. 2279–2290.
- [114] C. Wenling et al. “Effects of the degree of deacetylation on the physicochemical properties and Schwann cell affinity of chitosan films”. In: *Journal of biomaterials applications* 20.2 (2005), pp. 157–177.
- [115] L. J. R. Foster et al. “Chitosan as a biomaterial: Influence of degree of deacetylation on its physicochemical, material and biological properties”. In: *PLoS One* 10.8 (2015), e0135153.
- [116] T. Wu et al. “Physicochemical properties and bioactivity of fungal chitin and chitosan”. In: *Journal of agricultural and food chemistry* 53.10 (2005), pp. 3888–3894.
- [117] I. Aranaz et al. “Functional characterization of chitin and chitosan”. In: *Current chemical biology* 3.2 (2009), pp. 203–230.
- [118] S.-h. Hsu et al. “Chitosan as scaffold materials: Effects of molecular weight and degree of deacetylation”. In: *Journal of Polymer Research* 11.2 (2004), pp. 141–147.
- [119] C. Chatelet, O. Damour, and A. Domard. “Influence of the degree of acetylation on some biological properties of chitosan films”. In: *Biomaterials* 22.3 (2001), pp. 261–268.
- [120] A. Sizovs, P. M. McLendon, S. Srinivasachari, and T. M. Reineke. “Carbohydrate polymers for nonviral nucleic acid delivery”. In: *Nucleic Acid Transfection* (2010), pp. 131–190.
- [121] K. Gupta and F. H. Jabrail. “Effects of degree of deacetylation and cross-linking on physical characteristics, swelling and release behavior of chitosan microspheres”. In: *Carbohydrate polymers* 66.1 (2006), pp. 43–54.
- [122] R. Nerem. “Chapter Two-The challenge of imitating nature”. In: *Principles of Tissue Engineering* (2007), pp. 7–14.
- [123] B. Chan and K. Leong. “Scaffolding in tissue engineering: general approaches and tissue-specific considerations”. In: *European spine journal* 17.4 (2008), pp. 467–479.
- [124] A. Atala and J. J. Yoo. *Essentials of 3D biofabrication and translation*. Academic Press, 2015.
- [125] A. Panwar and L. P. Tan. “Current status of bioinks for micro-extrusion-based 3D bioprinting”. In: *Molecules* 21.6 (2016), p. 685.
- [126] C. Tai et al. “Use of anionic polysaccharides in the development of 3D bioprinting technology”. In: *Applied Sciences* 9.13 (2019), p. 2596.
- [127] T. Kean and M. Thanou. “Biodegradation, biodistribution and toxicity of chitosan”. In: *Advanced drug delivery reviews* 62.1 (2010), pp. 3–11.
- [128] N. Thombare, U. Jha, S. Mishra, and M. Siddiqui. “Guar gum as a promising starting material for diverse applications: A review”. In: *International journal of biological macromolecules* 88 (2016), pp. 361–372.
- [129] R. Singh, R. Malviya, and P. K. Sharma. “Extraction and characterization of tamarind seed polysaccharide as a pharmaceutical excipient”. In: *Pharmacognosy Journal* 3.20 (2011), pp. 17–19.

- [130] A. J. Sami et al. “Formulation of novel chitosan guar gum based hydrogels for sustained drug release of paracetamol”. In: *International journal of biological macromolecules* 108 (2018), pp. 324–332.
- [131] K. Hölzl et al. “Bioink properties before, during and after 3D bioprinting”. In: *Biofabrication* 8.3 (2016), p. 032002.
- [132] G. Tkalec, Ž. Knez, and Z. Novak. “Formation of polysaccharide aerogels in ethanol”. In: *RSC advances* 5.94 (2015), pp. 77362–77371.
- [133] J. Schindelin et al. “Fiji: an open-source platform for biological-image analysis”. In: *Nature methods* 9.7 (2012), pp. 676–682.
- [134] J.-P. Jehl et al. “Transverse isotropic modelling of left-ventricle passive filling: mechanical characterization for epicardial biomaterial manufacturing”. In: *Journal of the mechanical behavior of biomedical materials* 119 (2021), p. 104492.
- [135] R. C. Team et al. “R: A language and environment for statistical computing”. In: (2013).
- [136] C. Qiao, X. Ma, J. Zhang, and J. Yao. “Effect of hydration on water state, glass transition dynamics and crystalline structure in chitosan films”. In: *Carbohydrate polymers* 206 (2019), pp. 602–608.
- [137] J. Hankiewicz and E. Swierczek. “Lysozyme in human body fluids”. In: *Clinica chimica acta* 57.3 (1974), pp. 205–209.
- [138] A. S. Theus et al. “Bioprintability: Physiomechanical and Biological Requirements of Materials for 3D Bioprinting Processes”. In: *Polymers* 12.10 (2020), p. 2262.
- [139] X. Wang et al. “Gelatin-based hydrogels for organ 3D bioprinting”. In: *Polymers* 9.9 (2017), p. 401.
- [140] Y. He et al. “Research on the printability of hydrogels in 3D bioprinting”. In: *Scientific reports* 6.1 (2016), pp. 1–13.
- [141] J. Yin et al. “3D bioprinting of low-concentration cell-laden gelatin methacrylate (GelMA) bioinks with a two-step cross-linking strategy”. In: *ACS applied materials & interfaces* 10.8 (2018), pp. 6849–6857.
- [142] Q. He, Q. Ao, Y. Gong, and X. Zhang. “Preparation of chitosan films using different neutralizing solutions to improve endothelial cell compatibility”. In: *Journal of Materials Science: Materials in Medicine* 22.12 (2011), pp. 2791–2802.
- [143] K. Schütz et al. “Three-dimensional plotting of a cell-laden alginate/methylcellulose blend: towards biofabrication of tissue engineering constructs with clinically relevant dimensions”. In: *Journal of tissue engineering and regenerative medicine* 11.5 (2017), pp. 1574–1587.
- [144] I. M. El-Sherbiny and M. H. Yacoub. “Hydrogel scaffolds for tissue engineering: Progress and challenges”. In: *Global Cardiology Science and Practice* 2013.3 (2013), p. 38.
- [145] M. P. Nikolova and M. S. Chavali. “Recent advances in biomaterials for 3D scaffolds: A review”. In: *Bioactive materials* 4 (2019), pp. 271–292.
- [146] D. Lee, H. Zhang, and S. Ryu. “Elastic modulus measurement of hydrogels”. In: *Cellulose-Based Superabsorbent Hydrogels* (2019), pp. 865–884.

- [147] Q. L. Loh and C. Choong. “Three-dimensional scaffolds for tissue engineering applications: role of porosity and pore size”. In: *Tissue Engineering Part B: Reviews* 19.6 (2013), pp. 485–502.
- [148] M. Fernandes Queiroz et al. “Does the use of chitosan contribute to oxalate kidney stone formation?” In: *Marine drugs* 13.1 (2015), pp. 141–158.
- [149] D. Mudgil, S. Barak, and B. Khatkar. “X-ray diffraction, IR spectroscopy and thermal characterization of partially hydrolyzed guar gum”. In: *International Journal of Biological Macromolecules* 50.4 (2012), pp. 1035–1039.
- [150] S. C. Chao, M.-J. Wang, N.-S. Pai, and S.-K. Yen. “Preparation and characterization of gelatin–hydroxyapatite composite microspheres for hard tissue repair”. In: *Materials Science and Engineering: C* 57 (2015), pp. 113–122.
- [151] G Velazquez, A Herrera-Gómez, and M. Martín-Polo. “Identification of bound water through infrared spectroscopy in methylcellulose”. In: *Journal of Food Engineering* 59.1 (2003), pp. 79–84.
- [152] X. Mei and K. Cheng. “Recent development in therapeutic cardiac patches”. In: *Frontiers in Cardiovascular Medicine* 7 (2020), p. 294.
- [153] D. D. Streeter Jr et al. “Fiber orientation in the canine left ventricle during diastole and systole”. In: *Circulation research* 24.3 (1969), pp. 339–347.
- [154] F. Torrent-Guasp et al. “Spatial orientation of the ventricular muscle band: physiologic contribution and surgical implications”. In: *The Journal of Thoracic and Cardiovascular Surgery* 122.2 (2001), pp. 389–392.
- [155] C.-I. Lo et al. “Cardiac systolic mechanics in heart failure with preserved ejection fraction: new insights and controversies”. In: *Acta Cardiologica Sinica* 29.6 (2013), p. 515.
- [156] N. R. Ariyasinghe, D. M. Lyra-Leite, and M. L. McCain. “Engineering cardiac microphysiological systems to model pathological extracellular matrix remodeling”. In: *American Journal of Physiology-Heart and Circulatory Physiology* 315.4 (2018), H771–H789.
- [157] P. Tayalia and D. J. Mooney. “Controlled growth factor delivery for tissue engineering”. In: *Advanced materials* 21.32-33 (2009), pp. 3269–3285.
- [158] M. Whitaker, R. Quirk, S. Howdle, and K. Shakesheff. “Growth factor release from tissue engineering scaffolds”. In: *Journal of Pharmacy and Pharmacology* 53.11 (2001), pp. 1427–1437.
- [159] A. W. James et al. “A review of the clinical side effects of bone morphogenetic protein-2”. In: *Tissue Engineering Part B: Reviews* 22.4 (2016), pp. 284–297.
- [160] R. Subbiah and R. E. Guldberg. “Materials science and design principles of growth factor delivery systems in tissue engineering and regenerative medicine”. In: *Advanced healthcare materials* 8.1 (2019), p. 1801000.
- [161] Z. Wang et al. “Novel biomaterial strategies for controlled growth factor delivery for biomedical applications”. In: *NPG Asia Materials* 9.10 (2017), e435–e435.
- [162] A. C. Mitchell, P. S. Briquez, J. A. Hubbell, and J. R. Cochran. “Engineering growth factors for regenerative medicine applications”. In: *Acta biomaterialia* 30 (2016), pp. 1–12.

- [163] F.-M. Chen, M. Zhang, and Z.-F. Wu. “Toward delivery of multiple growth factors in tissue engineering”. In: *Biomaterials* 31.24 (2010), pp. 6279–6308.
- [164] X. Ren et al. “Growth factor engineering strategies for regenerative medicine applications”. In: *Frontiers in bioengineering and biotechnology* 7 (2020), p. 469.
- [165] L. M. C. Aguilár, S. M. Silva, and S. E. Moulton. “Growth factor delivery: defining the next generation platforms for tissue engineering”. In: *Journal of Controlled Release* 306 (2019), pp. 40–58.
- [166] H. Cui, M. Nowicki, J. P. Fisher, and L. G. Zhang. “3D bioprinting for organ regeneration”. In: *Advanced healthcare materials* 6.1 (2017), p. 1601118.
- [167] D. Beski et al. “Software for biofabrication”. In: *Essentials of 3D Biofabrication and Translation*. Elsevier, 2015, pp. 19–41.
- [168] P. S. Gungor-Ozkerim et al. “Bioinks for 3D bioprinting: an overview”. In: *Biomaterials science* 6.5 (2018), pp. 915–946.
- [169] N. Ashammakhi et al. “Bioinks and bioprinting technologies to make heterogeneous and biomimetic tissue constructs”. In: *Materials Today Bio* 1 (2019), p. 100008.
- [170] L. Wang et al. “Influence of the mechanical properties of biomaterials on degradability, cell behaviors and signaling pathways: current progress and challenges”. In: *Biomaterials science* 8.10 (2020), pp. 2714–2733.
- [171] K. Zhang et al. “Advanced smart biomaterials and constructs for hard tissue engineering and regeneration”. In: *Bone research* 6.1 (2018), pp. 1–15.
- [172] F. Pati, J. Jang, J. W. Lee, and D.-W. Cho. “Extrusion bioprinting”. In: *Essentials of 3D biofabrication and translation*. Elsevier, 2015, pp. 123–152.
- [173] G. L. Koons and A. G. Mikos. “Progress in three-dimensional printing with growth factors”. In: *Journal of Controlled Release* 295 (2019), pp. 50–59.
- [174] S. Tarafder et al. “Micro-precise spatiotemporal delivery system embedded in 3D printing for complex tissue regeneration”. In: *Biofabrication* 8.2 (2016), p. 025003.
- [175] D. Chimene, K. K. Lennox, R. R. Kaunas, and A. K. Gaharwar. “Advanced bioinks for 3D printing: a materials science perspective”. In: *Annals of biomedical engineering* 44.6 (2016), pp. 2090–2102.
- [176] M. Hospodiuk, M. Dey, D. Sosnoski, and I. T. Ozbolat. “The bioink: A comprehensive review on bioprintable materials”. In: *Biotechnology advances* 35.2 (2017), pp. 217–239.
- [177] J. Mano et al. “Natural origin biodegradable systems in tissue engineering and regenerative medicine: present status and some moving trends”. In: *Journal of the Royal Society Interface* 4.17 (2007), pp. 999–1030.
- [178] J. Gopinathan and I. Noh. “Recent trends in bioinks for 3D printing”. In: *Biomaterials research* 22.1 (2018), pp. 1–15.
- [179] S. E. Sakiyama-Elbert. “Incorporation of heparin into biomaterials”. In: *Acta biomaterialia* 10.4 (2014), pp. 1581–1587.
- [180] K. Dzobo, K. S. C. M. Motaung, and A. Adesida. “Recent trends in decellularized extracellular matrix bioinks for 3D printing: an updated review”. In: *International journal of molecular sciences* 20.18 (2019), p. 4628.

- [181] B. S. Kim et al. “3D cell printing of in vitro stabilized skin model and in vivo pre-vascularized skin patch using tissue-specific extracellular matrix bioink: a step towards advanced skin tissue engineering”. In: *Biomaterials* 168 (2018), pp. 38–53.
- [182] M. Ali et al. “A photo-crosslinkable kidney ECM-derived bioink accelerates renal tissue formation”. In: *Advanced healthcare materials* 8.7 (2019), p. 1800992.
- [183] J.-Y. Won et al. “A potential dermal substitute using decellularized dermis extracellular matrix derived bio-ink”. In: *Artificial cells, nanomedicine, and biotechnology* 47.1 (2019), pp. 644–649.
- [184] S. C. Santos, C. A. Custódio, and J. F. Mano. “Photopolymerizable platelet lysate hydrogels for customizable 3D cell culture platforms”. In: *Advanced healthcare materials* 7.23 (2018), p. 1800849.
- [185] T. Ahlfeld et al. “A novel plasma-based bioink stimulates cell proliferation and differentiation in bioprinted, mineralized constructs”. In: *ACS applied materials & interfaces* 12.11 (2020), pp. 12557–12572.
- [186] A Lubkowska, B Dolegowska, G Banfi, et al. “Growth factor content in PRP and their applicability in medicine”. In: *J Biol Regul Homeost Agents* 26.2 Suppl 1 (2012), 3S–22S.
- [187] M. Tavares et al. “Platelet lysates-based hydrogels incorporating bioactive mesoporous silica nanoparticles for stem cell osteogenic differentiation”. In: *Materials Today Bio* 9 (2021), p. 100096.
- [188] G. Irmak and M. Gümüşderelioğlu. “Photo-activated platelet-rich plasma (PRP)-based patient-specific bio-ink for cartilage tissue engineering”. In: *Biomedical Materials* 15.6 (2020), p. 065010.
- [189] Z. Li et al. “Addition of platelet-rich plasma to silk fibroin hydrogel bioprinting for cartilage regeneration”. In: *Tissue Engineering Part A* 26.15-16 (2020), pp. 886–895.
- [190] E Abelardo. “Synthetic material bioinks”. In: *3D Bioprinting for Reconstructive Surgery*. Elsevier, 2018, pp. 137–144.
- [191] F. Liu and X. Wang. “Synthetic Polymers for Organ 3D Printing”. In: *Polymers* 12.8 (2020), p. 1765.
- [192] J. Kundu, F. Pati, Y. H. Jeong, and D.-W. Cho. “Biomaterials for biofabrication of 3D tissue scaffolds”. In: *Biofabrication*. Elsevier, 2013, pp. 23–46.
- [193] J.-H. Shim et al. “Three-dimensional printing of rhBMP-2-loaded scaffolds with long-term delivery for enhanced bone regeneration in a rabbit diaphyseal defect”. In: *Tissue Engineering Part A* 20.13-14 (2014), pp. 1980–1992.
- [194] S. Bose and S. Tarafder. “Calcium phosphate ceramic systems in growth factor and drug delivery for bone tissue engineering: a review”. In: *Acta biomaterialia* 8.4 (2012), pp. 1401–1421.
- [195] A. R. Akkineni et al. “3D plotting of growth factor loaded calcium phosphate cement scaffolds”. In: *Acta biomaterialia* 27 (2015), pp. 264–274.
- [196] T. Ahlfeld et al. “Design and fabrication of complex scaffolds for bone defect healing: combined 3D plotting of a calcium phosphate cement and a growth factor-loaded hydrogel”. In: *Annals of biomedical engineering* 45.1 (2017), pp. 224–236.



- [197] T. Ahlfeld et al. “3D plotted biphasic bone scaffolds for growth factor delivery: biological characterization in vitro and in vivo”. In: *Advanced healthcare materials* 8.7 (2019), p. 1801512.
- [198] L. D. Loozen et al. “Porous bioprinted constructs in BMP-2 non-viral gene therapy for bone tissue engineering”. In: *Journal of Materials Chemistry B* 1.48 (2013), pp. 6619–6626.
- [199] G. M. Cunniffe et al. “Three-dimensional bioprinting of polycaprolactone reinforced gene activated bioinks for bone tissue engineering”. In: *Tissue Engineering Part A* 23.17-18 (2017), pp. 891–900.
- [200] T Gonzalez-Fernandez et al. “Pore-forming bioinks to enable spatio-temporally defined gene delivery in bioprinted tissues”. In: *Journal of Controlled Release* 301 (2019), pp. 13–27.
- [201] I. Y. Bozo et al. “3D Printed Gene-activated Octacalcium Phosphate Implants for Large Bone Defects Engineering”. In: *International Journal of Bioprinting* 6.3 (2020).
- [202] G. Thakur, F. C. Rodrigues, and K. Singh. “Crosslinking biopolymers for advanced drug delivery and tissue engineering applications”. In: *Cutting-Edge Enabling Technologies for Regenerative Medicine* (2018), pp. 213–231.
- [203] B. N. Johnson et al. “3D printed anatomical nerve regeneration pathways”. In: *Advanced functional materials* 25.39 (2015), pp. 6205–6217.
- [204] J. Y. Park et al. “3D printing technology to control BMP-2 and VEGF delivery spatially and temporally to promote large-volume bone regeneration”. In: *Journal of Materials Chemistry B* 3.27 (2015), pp. 5415–5425.
- [205] P. Wang et al. “Controlled Growth Factor Release in 3D-Printed Hydrogels”. In: *Advanced healthcare materials* 9.15 (2020), p. 1900977.
- [206] R. Hosseinzadeh et al. “A Drug-Eluting 3D-Printed Mesh (GlioMesh) for Management of Glioblastoma”. In: *Advanced Therapeutics* 2.11 (2019), p. 1900113.
- [207] E. D. Ker et al. “Bioprinting of growth factors onto aligned sub-micron fibrous scaffolds for simultaneous control of cell differentiation and alignment”. In: *Biomaterials* 32.32 (2011), pp. 8097–8107.
- [208] J. Park et al. “Three dimensional cell printing with sulfated alginate for improved bone morphogenetic protein-2 delivery and osteogenesis in bone tissue engineering”. In: *Carbohydrate polymers* 196 (2018), pp. 217–224.
- [209] M. Hajimiri, S. Shahverdi, G. Kamalinia, and R. Dinarvand. “Growth factor conjugation: strategies and applications”. In: *Journal of biomedical materials research Part A* 103.2 (2015), pp. 819–838.
- [210] B. Byambaa et al. “Bioprinted osteogenic and vasculogenic patterns for engineering 3D bone tissue”. In: *Advanced healthcare materials* 6.16 (2017), p. 1700015.
- [211] D. Chimene, R. Kaunas, and A. K. Gaharwar. “Hydrogel bioink reinforcement for additive manufacturing: a focused review of emerging strategies”. In: *Advanced materials* 32.1 (2020), p. 1902026.
- [212] T Ahlfeld et al. “Development of a clay based bioink for 3D cell printing for skeletal application”. In: *Biofabrication* 9.3 (2017), p. 034103.

- [213] C. Chu et al. “Nanoparticles combined with growth factors: recent progress and applications”. In: *Rsc Advances* 6.93 (2016), pp. 90856–90872.
- [214] K. Elkhoury et al. “Soft-Nanoparticle Functionalization of Natural Hydrogels for Tissue Engineering Applications”. In: *Advanced healthcare materials* 8.18 (2019), p. 1900506.
- [215] C. W. Peak et al. “Printing therapeutic proteins in 3D using nanoengineered bioink to control and direct cell migration”. In: *Advanced healthcare materials* 8.11 (2019), p. 1801553.
- [216] B. Sun et al. “A 3D-Bioprinted dual growth factor-releasing intervertebral disc scaffold induces nucleus pulposus and annulus fibrosus reconstruction”. In: *Bioactive materials* 6.1 (2021), pp. 179–190.
- [217] F. E. Freeman et al. “3D bioprinting spatiotemporally defined patterns of growth factors to tightly control tissue regeneration”. In: *Science advances* 6.33 (2020), eabb5093.
- [218] S.-J. Lee et al. “Development of novel 3-D printed scaffolds with core-shell nanoparticles for nerve regeneration”. In: *IEEE Transactions on Biomedical Engineering* 64.2 (2016), pp. 408–418.
- [219] K. M. Z. Hossain, U. Patel, and I. Ahmed. “Development of microspheres for biomedical applications: a review”. In: *Progress in biomaterials* 4.1 (2015), pp. 1–19.
- [220] N. K. Varde and D. W. Pack. “Microspheres for controlled release drug delivery”. In: *Expert opinion on biological therapy* 4.1 (2004), pp. 35–51.
- [221] K. K. Kim and D. W. Pack. “Microspheres for drug delivery”. In: *BioMEMS and biomedical nanotechnology*. Springer, 2006, pp. 19–50.
- [222] M. T. Poldervaart et al. “Prolonged presence of VEGF promotes vascularization in 3D bioprinted scaffolds with defined architecture”. In: *Journal of controlled release* 184 (2014), pp. 58–66.
- [223] H. K. Makadia and S. J. Siegel. “Poly lactic-co-glycolic acid (PLGA) as biodegradable controlled drug delivery carrier”. In: *Polymers* 3.3 (2011), pp. 1377–1397.
- [224] G. Dawes et al. “Size effect of PLGA spheres on drug loading efficiency and release profiles”. In: *Journal of Materials Science: Materials in Medicine* 20.5 (2009), pp. 1089–1094.
- [225] D. Klose et al. “How porosity and size affect the drug release mechanisms from PLGA-based microparticles”. In: *International journal of pharmaceutics* 314.2 (2006), pp. 198–206.
- [226] E. Swider et al. “Customizing poly (lactic-co-glycolic acid) particles for biomedical applications”. In: *Acta biomaterialia* 73 (2018), pp. 38–51.
- [227] C. H. Lee et al. “Protein-releasing polymeric scaffolds induce fibrochondrocytic differentiation of endogenous cells for knee meniscus regeneration in sheep”. In: *Science translational medicine* 6.266 (2014), 266ra171–266ra171.
- [228] Y. Sun et al. “3D bioprinting dual-factor releasing and gradient-structured constructs ready to implant for anisotropic cartilage regeneration”. In: *Science Advances* 6.37 (2020), eaay1422.

- [229] D. Kilian et al. “3D Bioprinting of osteochondral tissue substitutes—in vitro-chondrogenesis in multi-layered mineralized constructs”. In: *Scientific reports* 10.1 (2020), pp. 1–17.
- [230] E. B. Petcu et al. “3D printing strategies for peripheral nerve regeneration”. In: *Biofabrication* 10.3 (2018), p. 032001.
- [231] A. R. Amini, C. T. Laurencin, and S. P. Nukavarapu. “Bone tissue engineering: recent advances and challenges”. In: *Critical Reviews™ in Biomedical Engineering* 40.5 (2012).
- [232] T. Genova et al. “The crosstalk between osteodifferentiating stem cells and endothelial cells promotes angiogenesis and bone formation”. In: *Frontiers in physiology* 10 (2019), p. 1291.
- [233] R. C. Gonçalves, A. Banfi, M. B. Oliveira, and J. F. Mano. “Strategies for Revascularization and Promotion of Angiogenesis in Trauma and Disease”. In: *Bio-materials* (2020), p. 120628.
- [234] É. R. Oliveira et al. “Advances in Growth Factor Delivery for Bone Tissue Engineering”. In: *International Journal of Molecular Sciences* 22.2 (2021), p. 903.
- [235] V. E. Santo, M. E. Gomes, J. F. Mano, and R. L. Reis. “Controlled release strategies for bone, cartilage, and osteochondral engineering—part I: recapitulation of native tissue healing and variables for the design of delivery systems”. In: *Tissue Engineering Part B: Reviews* 19.4 (2013), pp. 308–326.
- [236] T.-M. De Witte, L. E. Fratila-Apachitei, A. A. Zadpoor, and N. A. Peppas. “Bone tissue engineering via growth factor delivery: from scaffolds to complex matrices”. In: *Regenerative biomaterials* 5.4 (2018), pp. 197–211.
- [237] S. Chen, Y. Shi, X. Zhang, and J. Ma. “Evaluation of BMP-2 and VEGF loaded 3D printed hydroxyapatite composite scaffolds with enhanced osteogenic capacity in vitro and in vivo”. In: *Materials Science and Engineering: C* 112 (2020), p. 110893.
- [238] D. H. Kempen et al. “Effect of local sequential VEGF and BMP-2 delivery on ectopic and orthotopic bone regeneration”. In: *Biomaterials* 30.14 (2009), pp. 2816–2825.
- [239] Q. Wang, Y. Zhang, B. Li, and L. Chen. “Controlled dual delivery of low doses of BMP-2 and VEGF in a silk fibroin–nanohydroxyapatite scaffold for vascularized bone regeneration”. In: *Journal of Materials Chemistry B* 5.33 (2017), pp. 6963–6972.
- [240] S. Young et al. “Dose effect of dual delivery of vascular endothelial growth factor and bone morphogenetic protein-2 on bone regeneration in a rat critical-size defect model”. In: *Tissue Engineering Part A* 15.9 (2009), pp. 2347–2362.
- [241] S.-B. Kang, J. L. Olson, A. Atala, and J. J. Yoo. “Functional recovery of completely denervated muscle: implications for innervation of tissue-engineered muscle”. In: *Tissue Engineering Part A* 18.17-18 (2012), pp. 1912–1920.
- [242] S. R. Guarino, A. Canciani, and F. Forneris. “Dissecting the extracellular complexity of neuromuscular junction organizers”. In: *Frontiers in molecular biosciences* 6 (2020), p. 156.
- [243] J. H. Kim et al. “3D bioprinted human skeletal muscle constructs for muscle function restoration”. In: *Scientific Reports* 8.1 (2018), pp. 1–15.

- [244] M. Sondell, G. Lundborg, and M. Kanje. “Vascular endothelial growth factor stimulates Schwann cell invasion and neovascularization of acellular nerve grafts”. In: *Brain research* 846.2 (1999), pp. 219–228.
- [245] N. Xiao and Q.-T. Le. “Neurotrophic factors and their potential applications in tissue regeneration”. In: *Archivum immunologiae et therapiae experimentalis* 64.2 (2016), pp. 89–99.
- [246] V. Mashanov et al. “Synergistic effect of CNTF and GDNF on directed neurite growth in chick embryo dorsal root ganglia”. In: *PloS ONE* 15.10 (2020), e0240235.
- [247] D. N. Kapoor et al. “PLGA: a unique polymer for drug delivery”. In: *Therapeutic delivery* 6.1 (2015), pp. 41–58.
- [248] A. Kumari, S. K. Yadav, and S. C. Yadav. “Biodegradable polymeric nanoparticles based drug delivery systems”. In: *Colloids and surfaces B: biointerfaces* 75.1 (2010), pp. 1–18.
- [249] E. Vey et al. “Degradation kinetics of poly (lactic-co-glycolic) acid block copolymer cast films in phosphate buffer solution as revealed by infrared and Raman spectroscopies”. In: *Polymer degradation and stability* 96.10 (2011), pp. 1882–1889.
- [250] J. Liu et al. “Current methods for skeletal muscle tissue repair and regeneration”. In: *BioMed Research International* 2018 (2018).
- [251] H.-W. Kang et al. “A 3D bioprinting system to produce human-scale tissue constructs with structural integrity”. In: *Nature Biotechnology* 34.3 (2016), pp. 312–319.
- [252] J. H. Kim et al. “Neural cell integration into 3D bioprinted skeletal muscle constructs accelerates restoration of muscle function”. In: *Nature Communications* 11.1 (2020), pp. 1–12.
- [253] P. J. Kingham and G. Terenghi. “Bioengineered nerve regeneration and muscle reinnervation”. In: *Journal of Anatomy* 209.4 (2006), pp. 511–526.
- [254] S. Tanaka, A. Tsubaki, and K. Tachino. “Effect of exercise training after partial denervation in rat soleus muscles”. In: *Journal of Physical Therapy Science* 17.2 (2005), pp. 97–101.
- [255] T. Gordon. “Electrical stimulation to enhance axon regeneration after peripheral nerve injuries in animal models and humans”. In: *Neurotherapeutics* 13.2 (2016), pp. 295–310.
- [256] M. P. Willand. “Electrical stimulation enhances reinnervation after nerve injury”. In: *European Journal of Translational Myology* 25.4 (2015), p. 243.
- [257] R. Guy et al. “Human muscle progenitor cells overexpressing neurotrophic factors improve neuronal regeneration in a sciatic nerve injury mouse model”. In: *Frontiers in Neuroscience* 13 (2019), p. 151.
- [258] H. Liu et al. “Current sustained delivery strategies for the design of local neurotrophic factors in treatment of neurological disorders”. In: *Asian journal of pharmaceutical sciences* 8.5 (2013), pp. 269–277.
- [259] N. K. Mohtaram, A. Montgomery, and S. M. Willerth. “Biomaterial-based drug delivery systems for the controlled release of neurotrophic factors”. In: *Biomedical materials* 8.2 (2013), p. 022001.

- [260] S. Madduri et al. “Collagen nerve conduits releasing the neurotrophic factors GDNF and NGF”. In: *Journal of Controlled Release* 143.2 (2010), pp. 168–174.
- [261] N. B. Fadia et al. “Long-gap peripheral nerve repair through sustained release of a neurotrophic factor in nonhuman primates”. In: *Science Translational Medicine* 12.527 (2020).
- [262] W. A. Lackington et al. “Controlling the dose-dependent, synergistic and temporal effects of NGF and GDNF by encapsulation in PLGA microparticles for use in nerve guidance conduits for the repair of large peripheral nerve defects”. In: *Journal of Controlled Release* 304 (2019), pp. 51–64.
- [263] S. Das et al. “Innervation: the missing link for biofabricated tissues and organs”. In: *npj Regenerative Medicine* 5.1 (2020), pp. 1–19.
- [264] F. Danhier et al. “PLGA-based nanoparticles: an overview of biomedical applications”. In: *Journal of controlled release* 161.2 (2012), pp. 505–522.
- [265] M. Iqbal, N. Zafar, H. Fessi, and A. Elaissari. “Double emulsion solvent evaporation techniques used for drug encapsulation”. In: *International Journal of Pharmaceutics* 496.2 (2015), pp. 173–190.
- [266] T. K. Giri et al. “Prospects of pharmaceuticals and biopharmaceuticals loaded microparticles prepared by double emulsion technique for controlled delivery”. In: *Saudi Pharmaceutical Journal* 21.2 (2013), pp. 125–141.
- [267] S Ravi et al. “Development and characterization of polymeric microspheres for controlled release protein loaded drug delivery system”. In: *Indian Journal of Pharmaceutical Sciences* 70.3 (2008), p. 303.
- [268] J. Schindelin et al. “Fiji: an open-source platform for biological-image analysis”. In: *Nature Methods* 9.7 (2012), pp. 676–682.
- [269] C. T. Rueden et al. “ImageJ2: ImageJ for the next generation of scientific image data”. In: *BMC Bioinformatics* 18.1 (2017), p. 529.
- [270] E. Meijering et al. “Design and validation of a tool for neurite tracing and analysis in fluorescence microscopy images”. In: *Cytometry Part A: The Journal of the International Society for Analytical Cytology* 58.2 (2004), pp. 167–176.
- [271] R Core Team. *R: A Language and Environment for Statistical Computing*. R Foundation for Statistical Computing. Vienna, Austria, 2019.
- [272] H. Wickham. *ggplot2: Elegant Graphics for Data Analysis*. Springer-Verlag New York, 2016. ISBN: 978-3-319-24277-4.
- [273] F. Ito et al. “Study of types and mixture ratio of organic solvent used to dissolve polymers for preparation of drug-containing PLGA microspheres”. In: *European Polymer Journal* 45.3 (2009), pp. 658–667.
- [274] H. K. Makadia and S. J. Siegel. “Poly lactic-co-glycolic acid (PLGA) as biodegradable controlled drug delivery carrier”. In: *Polymers* 3.3 (2011), pp. 1377–1397.
- [275] G. Gillispie et al. “Assessment methodologies for extrusion-based bioink printability”. In: *Biofabrication* 12.2 (2020), p. 022003.
- [276] C. Cai et al. “Influence of morphology and drug distribution on the release process of FITC-dextran-loaded microspheres prepared with different types of PLGA”. In: *Journal of microencapsulation* 26.4 (2009), pp. 334–345.

- [277] O. Chaudhuri. “Viscoelastic hydrogels for 3D cell culture”. In: *Biomaterials Science* 5.8 (2017), pp. 1480–1490.
- [278] A. Vedadghavami et al. “Manufacturing of hydrogel biomaterials with controlled mechanical properties for tissue engineering applications”. In: *Acta Biomaterialia* 62 (2017), pp. 42–63.
- [279] C. W. Peak et al. “Printing therapeutic proteins in 3D using nanoengineered bioink to control and direct cell migration”. In: *Advanced Healthcare Materials* 8.11 (2019), p. 1801553.
- [280] Q. L. Loh and C. Choong. “Three-dimensional scaffolds for tissue engineering applications: role of porosity and pore size”. In: *Tissue Engineering Part B: Reviews* 19.6 (2013), pp. 485–502.
- [281] I. K. Ko et al. “The effect of in vitro formation of acetylcholine receptor (AChR) clusters in engineered muscle fibers on subsequent innervation of constructs in vivo”. In: *Biomaterials* 34.13 (2013), pp. 3246–3255.
- [282] J. Gilbert-Honick et al. “Engineering 3D skeletal muscle primed for neuromuscular regeneration following volumetric muscle loss”. In: *Biomaterials* 255 (2020), p. 120154.
- [283] D. Santos et al. “Focal release of neurotrophic factors by biodegradable microspheres enhance motor and sensory axonal regeneration in vitro and in vivo”. In: *Brain research* 1636 (2016), pp. 93–106.
- [284] L. M. Larkin, J. H. Van Der Meulen, R. G. Dennis, and J. B. Kennedy. “Functional evaluation of nerve-skeletal muscle constructs engineered in vitro”. In: *In Vitro Cellular & Developmental Biology-Animal* 42.3 (2006), pp. 75–82.
- [285] M. L. Williams, T. Y. Kostrominova, E. M. Arruda, and L. M. Larkin. “Effect of implantation on engineered skeletal muscle constructs”. In: *Journal of tissue engineering and regenerative medicine* 7.6 (2013), pp. 434–442.
- [286] S. Das et al. “Pre-innervated tissue-engineered muscle promotes a pro-regenerative microenvironment following volumetric muscle loss”. In: *Communications biology* 3.1 (2020), pp. 1–14.
- [287] M. D. Wood et al. “Fibrin gels containing GDNF microspheres increase axonal regeneration after delayed peripheral nerve repair”. In: *Regenerative medicine* 8.1 (2013), pp. 27–37.
- [288] H.-y. Zhao et al. “Research advances in tissue engineering materials for sustained release of growth factors”. In: *BioMed Research International* 2015 (2015).
- [289] D. Klose et al. “How porosity and size affect the drug release mechanisms from PLGA-based microparticles”. In: *International Journal of pharmaceuticals* 314.2 (2006), pp. 198–206.
- [290] S. Mao et al. “Effect of WOW process parameters on morphology and burst release of FITC-dextran loaded PLGA microspheres”. In: *International Journal of Pharmaceutics* 334.1-2 (2007), pp. 137–148.
- [291] G. Dawes et al. “Size effect of PLGA spheres on drug loading efficiency and release profiles”. In: *Journal of Materials Science: Materials in Medicine* 20.5 (2009), pp. 1089–1094.

- 
- [292] Y. Xia and D. W. Pack. “Uniform biodegradable microparticle systems for controlled release”. In: *Chemical Engineering Science* 125 (2015), pp. 129–143.
- [293] M. Ehrbar et al. “Elucidating the role of matrix stiffness in 3D cell migration and remodeling”. In: *Biophysical Journal* 100.2 (2011), pp. 284–293.
- [294] A. J. Man et al. “Neurite outgrowth in fibrin gels is regulated by substrate stiffness”. In: *Tissue Engineering Part A* 17.23-24 (2011), pp. 2931–2942.
- [295] J. H. Kim et al. “Pelvic floor muscle function recovery using biofabricated tissue constructs with neuromuscular junctions”. In: *Acta Biomaterialia* 121 (2021), pp. 237–249. ISSN: 1742-7061.





# List of publications

**Comparison of the Physicochemical Properties of Chitin Extracted from Cicada orni Sloughs Harvested in Three Different Years and Characterization of the Resulting Chitosan.**

*Appl. Sci.* 2021, 11(23), 11278

A.Poerio, T. Girardet, C. Petit, S. Fleutot, J.P. Jehl, E. Arab-Tehrany, J.F. Mano and F. Cleymand.

**Development of novel chitosan / guar gum inks for extrusion-based 3D bioprinting: Process, printability and properties.**

*Bioprinting*, 21 (2021) e00122

F. Cleymand, A. Poerio, A. Mamanov, K. Elkhoury, L. Ikhelf, J.P. Jehl, C.J.F. Kahn, M. Ponçot, E. Arab-Tehrany, J.F. Mano.

**Synergistic effect of CNTF and GDNF on directed neurite growth in chick embryo dorsal root ganglia.**

*PloS one* 15 (10), e0240235, 2020

V. Mashanov, A. Alwan, M.W. Kim, D. Lai, A. Poerio, Y.M. Ju, J.H. Kim, J.J. Yoo.

**Extraction and Physicochemical Characterization of Chitin from Cicada orni Sloughs of the South-Eastern French Mediterranean Basin.**

*Molecules*, 2020, 25 (11), 2543

A.Poerio, C. Petit, J.P. Jehl, E. Arab-Tehrany, J.F. Mano, F. Cleymand.

**Neurotrophic effect of fish-lecithin based nanoliposomes on cortical neurons.**

*Marine drugs*, 2019, 17 (7), 406

C. Malaplate, A. Poerio, M. Huguet, C. Soligot, E. Passeri, C.J.F. Kahn, M. Linder, E. Arab-Tehrany, F.T Yen.